Strukturelle Analyse der Transmembran-Domäne des Ethylenrezeptors ETR1 aus *Arabidopsis thaliana*

Inaugural-Dissertation

zur Erlangung des Doktorgrades

der Mathematisch-Naturwissenschaftlichen Fakultät

der Heinrich-Heine-Universität Düsseldorf

vorgelegt von

Buket Rüffer

aus Mettmann

Düsseldorf, September 2024

aus dem Institut für Biochemische Pflanzenphysiologie

der Heinrich-Heine-Universität Düsseldorf

Gedruckt mit der Genehmigung der

Mathematisch-Naturwissenschaftlichen Fakultät der

Heinrich-Heine-Universität Düsseldorf

Berichterstatter:

1. Univ.-Prof. Dr. Georg Groth

2. Univ.-Prof. Dr. Holger Gohlke

Tag der mündlichen Prüfung: 11.12.2024

„Wünsche und Träume mit deinem kleinen Herzen, aber denk immer dran, Tiana, dass der alte Stern dich nur einen Teil des Wegs bringt.

Du musst auch was dazu tun und wenn du dich anstrengst und hart arbeitest, dann wird dir alles gelingen, was du dir vorgenommen hast."

- James, The Princess and The Frog

Inhaltsverzeichnis

1 Abstract

For more than 450 million years the ethylene signaling pathway has been highly conserved in the plant kingdom. The phytohormone ethylene is involved in a number of plant processes, including germination, leaf abscission and fruit ripening. In the presence of the copper cofactor ethylene is capable of binding to the transmembrane domains (TMDs) of the ethylene receptors (ETRs), which are located in the membrane of the endoplasmic reticulum (ER). Through this a reaction cascade is activated and results in the ethylene response. The used model system is *Arabidopsis thaliana*, which contains five ETRs. Only the cytosolic domains of the ETRs have been crystallized so far. The mechanism of the conformational change in the receptor is still unknown.

In this thesis, the structural analysis of the TMD was carried out using a combination of mutants and the following methods: Electron paramagnetic resonance (EPR) spectroscopy and comparative molecular dynamics (MD) simulation was used to analyze the arrangement of the three TM helices of the ETR1 monomer with two different computer-based models. Additionally, copper binding experiments were done. To resolve the structure of ETR1 lipidic cubic phase (LCP) crystallization was used in combination with different additives (metals, peptides).

The EPR results indicate that the TMD is more flexible than it was predicted by the two comparative computer-based models. In addition, mutation studies and copper binding experiments demonstrate that the amino acid positions D25 and K91 exhibit additional stabilization *in vivo* and *in vitro*, while copper is complexed by positions C65 and H69. This copper coordination is a crucial aspect of ethylene binding.

The results of the mutation studies and copper binding experiments enabled the refinement of the copper coordination in the structural model of ETR1 which was published by Schott-Verdugo *et al.* (2019). Furthermore, crystals of the TMD could be produced for the first time, leading to first diffraction patterns. Optimizations in crystallization and the application of a combination of other methods could facilitate the elucidation of the structure of the ETR1 receptor and thus enable a deeper understanding of copper coordination, ethylene binding, conformational changes of the receptor and its signal transduction.

2 Zusammenfassung

Der Ethylensignalweg ist im Pflanzenreich seit mehr als 450 Millionen Jahren hoch konserviert. Das Phytohormon Ethylen ist an einer Reihe von Pflanzenprozessen beteiligt. Dazu gehören u. a. die Keimung, Blattabszission und die Fruchtreife. In Anwesenheit des Kupfer-Cofaktors ist Ethylen in der Lage an die Transmembran-Domänen (TMDs) der Ethylenrezeptoren (ETRs) zu binden, die in der Membran des endoplasmatischen Retikulums (ER) lokalisiert sind. Dadurch wird eine Reaktionskaskade ausgelöst, welche zu der sogenannten Ethylenantwort führt. Das verwendete Modellsystem *Arabidopsis thaliana* enthält fünf Ethylenrezeptoren (ETRs). Der genaue Mechanismus, welcher zu der Konformationsänderung im Rezeptor führt, ist unbekannt, da bisher nur die zytosolischen Domänen der ETRs kristallisiert werden konnten. Aus diesem Grund wurde eine Strukturanalyse der TMD mit einer Kombination aus ausgewählten Mutanten und folgender Methoden durchgeführt: Mithilfe von *Electron Paramagnetic Resonance* (EPR) Spektroskopie und vergleichender molekulardynamischer (MD) Simulation wurde die Anordnung der drei TM-Helices des ETR1-Monomers mit zwei verschiedenen computerbasierten ETR1-Modellen analysiert. Zudem wurden Kupferaffinitätsexperimente durchgeführt. Ein weiteres Ziel war die Strukturaufklärung von ETR1 mittels *Lipidic Cubic Phase* (LCP)-Kristallisation in Kombination mit diversen Additiven (Metallen, Peptide). Die EPR-Ergebnisse deuten darauf hin, dass die TMD flexibler ist als in den vergleichenden computerbasierten Modellen angenommen wurde. Darüber hinaus zeigen Mutations- und Kupferbindungsexperimente *in vivo* und *in vitro*, dass die Aminosäurepositionen D25 und K91 zu einer zusätzlichen Stabilisierung führen, während Kupfer durch C65 und H69 komplexiert wird. Diese Kupferkoordination spielt eine wesentliche Rolle bei der Ethylenbindung. Die Resultate der Mutationsstudien, sowie der Kupferbindungsexperimente, ermöglichten eine detailliertere Darstellung der Kupferkoordination im von Schott-Verdugo *et al.* (2019) veröffentlichten Strukturmodell von ETR1. Darüber hinaus konnten erstmals Kristalle von der TMD gebildet werden, die erste Diffraktionsmuster erzeugen. Optimierungen in der Kristallisation und die Anwendung einer Kombination anderer Methoden könnten die Aufklärung der Struktur des ETR1-Rezeptors erleichtern und damit ein tieferes Verständnis der Kupferkoordination, der Ethylenbindung, der Konformationsänderungen des Rezeptors und seiner Signaltransduktion ermöglichen.

3 Einleitung

3.1 Hintergrundinformationen – Ethylen

Die Samenkeimung, Blütenentwicklung, Abszission, Seneszenz und Fruchtreifung sind pflanzliche Prozesse, die durch ein gasförmiges Phytohormon reguliert werden - Ethylen (Abbildung 1; Burg und Burg 1962; Johnson und Ecker 1998; Abeles *et al.* 2012; Mattoo 2018). Aufgrund des vielfältigen Einflusses in Pflanzen, spielt dieses einfache Alken eine wichtige Rolle in der Agrarökonomie. Hierbei wird Ethylen beispielsweise zur beschleunigten Reifung von klimakterischen Früchten wie Tomaten, Bananen oder Äpfeln eingesetzt (Abbildung 1; Burg und Burg 1962; Abeles *et al.* 2012).

Abbildung 1*:* Reifung einer Tomate unter Einfluss von Ethylen. Modifiziert nach Kessenbrock *et al.* 2017.

Das unpolare Gas kann ungehindert intra- und interzellulär durch Pflanzenzellen und -organe, sowie zwischen Pflanzen diffundieren (Yang und Hoffman 1984; Abeles *et al.* 2012). Die Produktion von Ethylen wird nicht nur durch Entwicklungsprozesse in der Pflanze gesteuert, sondern auch durch biotische und abiotische Faktoren. Dazu zählen u. a. Pathogenbefall, hohe Salzkonzentrationen im Boden, Überflutungen und Trockenstress durch Hitze (Williamson 1950; Dubouzet *et al.* 2003; Goel *et al.* 2010; Abeles *et al.* 2012; Arraes *et al.* 2015). Ethylen diffundiert in Wasser zwar 10. 000 - fach langsamer als in Luft, dies hat jedoch den Vorteil, dass das Gas z. B. in semiaquatischen Pflanzen physikalisch in den Blättern eingeschlossen wird. Dadurch wird bei Überflutung ein Auftrieb der Blätter gewährleistet (Jackson 1985; Bleecker und Kende 2000). Synthetisiert wird Ethylen in der Vakuole der Pflanzenzelle im Yang–Zyklus. Dabei wird die Aminosäure Methionin (M) über katalytische Prozesse zu dem Ethylenvorläufer 1 - Aminocyclopropancarbonsäure (ACC) umgesetzt. Danach erfolgt die Katalyse in Ethylen (Guy und Kende 1984; Yang und Hoffman 1984).

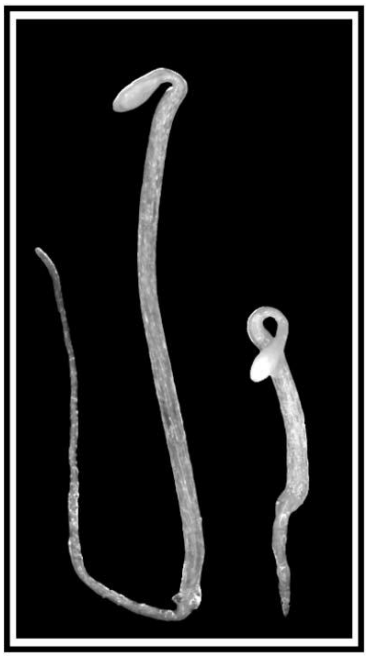

Abbildung 2: Vergleich der *Triple Response* von *Arabidopsis*-Keimlingen, die im Dunkeln angezogen wurden. Links ist das Wachstum eines Keimlings ohne den Einfluss von Ethylen. Rechts ist der *Triple Response*-Phänotyp nach Zugabe und Inkubation von 10 µM des Ethylenvorläufers 1 - Aminocyclopropancarbonsäure (ACC) erkennbar (Benavente und Alonso 2006).

Dokumentiert wurde der Einfluss von Ethylen erstmals 1901 durch im Dunkeln gehaltene Erbsensamen (Neljubow 1901). Keimlinge, die unter dem Einfluss von Ethylen standen, zeigten verkürzte und dicke Hypokotyle und Wurzeln, sowie eine Krümmung an der Spitze der Keimlinge - die Apikalhaken (Abbildung 2; Neljubow 1901; Guzmán und Ecker 1990). Diese erstmalige Beschreibung der typischen Ethylenantwort, auch *Triple Response* (Dreifachantwort) genannt, bildet die Grundlage für diverse genetische Studien, die mit der Modellpflanze *Arabidopsis thaliana* (*A. thaliana*) durchgeführt wurden. Durch Mutagenese und Experimente an Früchten, wie z. B. Tomaten, konnte man zwischen Komponenten der Ethylenbiogenese, -wahrnehmung und der -signalweiterleitung unterscheiden (Kende und Boller 1981; Yang und Hoffman 1984; Privalle und Graham 1987; Bleecker *et al.* 1988; Kieber *et al.* 1993; Hua *et al.* 1995; Schaller und Bleecker 1995; Chao *et al.* 1997; Hua *et al.* 1998; Johnson und Ecker 1998; Sakai *et al.* 1998; Bleecker und Kende 2000; Jafari *et al.* 2013).

3.2 Ethylenrezeptoren und – Unterfamilien

Das Phytohormon Ethylen wird durch eine Familie membrangebundener Rezeptoren (ETRs) im Endoplasmatischen Retikulum (ER)-Golgi-Netzwerk wahrgenommen, was zur Signaltransduktion und Auslösung des Ethylensignalweges führt (Chen *et al.* 2002; Gao *et al.* 2003; Grefen *et al.* 2008; Dong *et al.* 2010; Binder 2020). Die Proteinsequenzen dieser Rezeptoren sind im Pflanzenreich hoch konserviert (Ju *et al.* 2015; Kessenbrock *et al.* 2017; Klein *et al.* 2019; Hoppen *et al.* 2019b). In *A. thaliana* konnten fünf Rezeptoren identifiziert werden, die sich in zwei Unterfamilien unterteilen lassen (Hua *et al.* 1998; Bleecker 1999). Unterfamilie 1 setzt sich aus dem *Ethylene Receptor 1* (ETR1) und dem *Ethylene Response Sensor 1* (ERS1) zusammen (Abbildung 3; Bleecker 1999; Hall *et al.* 2000). Zu der Unterfamilie 2 gehören *Ethylene Receptor 2* (ETR2), *Ethylene Response Sensor 2* (ERS2) und *Ethylene Insensitive 4* (EIN4; Abbildung 3; Hua *et al.* 1998; Bleecker 1999).

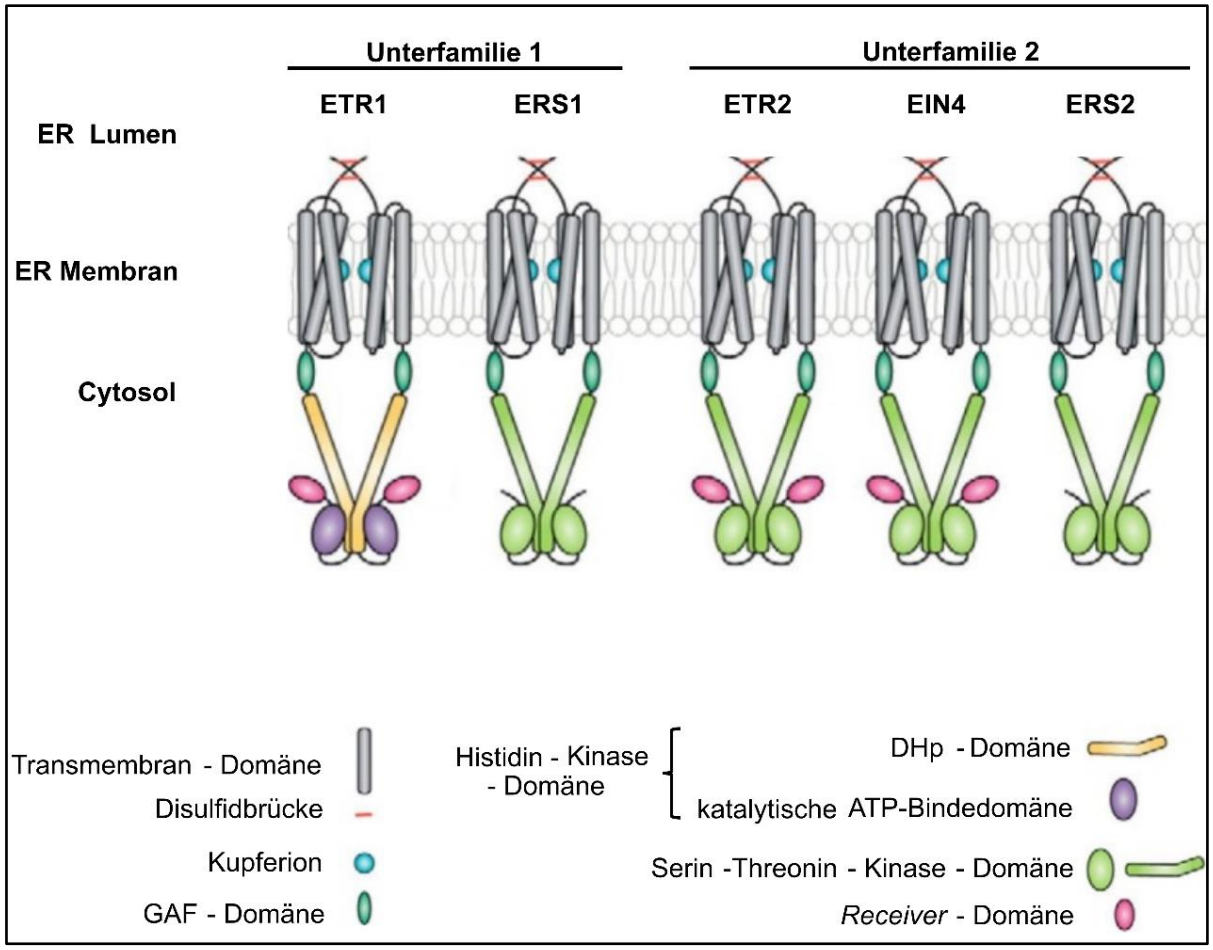

Abbildung 3: Schematische Darstellung der Ethylenrezeptorfamilie aus *Arabidopsis thaliana*. *Ethylene Receptor 1* (ETR1) und *Ethylene Response Sensor 1* (ERS1) gehören zur ersten Unterfamilie (links). Unterfamilie 2 setzt sich aus *Ethylene Receptor 2* (ETR2), *Ethylene Insensitive 4* (EIN4) und *Ethylene Response Sensor 2* (ERS2) zusammen (rechts). Alle Rezeptoren haben einen gemeinsamen Aufbau, beginnend mit einer Transmembran-Domäne (TMD; grau) in der ER-Membran. Pro TMD-Monomer wird ein Kupferion (Cu(I); blau) gebunden. Im Zytosol folgt eine *cGMP-Specific Phosphodiesterases, Adenyl Cyclases, Formate Hydrogen Lyase Transcriptional Activator*-Domäne (GAF-Domäne; dunkelgrün). Daran schließt sich eine Kinase-Domäne an. Analog zu anderen Histidin-Kinasen ist auch beiETR1 die Histidin-Kinase-Domäne (HK) in eine dimerisierende Histidin-Phosphotransfer-Domäne (DHp; gelb) und in eine katalytische ATP-Bindedomäne (CA; violett) unterteilt. Die anderen ETRs besitzen eine degenerierte HK-Domäne mit einer Serin-Threonin-Kinase-Aktivität (hellgrün). ETR1, ETR2 und EIN4 haben am C-Terminus eine *Receiver*-Domäne (RD; pink). Dimere sind über die TMD und GAF-Domäne vermittelt. Zusätzlich werden die Dimere am N-Terminus über C4 und C6 stabilisiert (rot). Modifiziert nach Binder (2020).

Alle Isoformen haben einen ähnlichen modularen Aufbau (Abbildung 3; Lacey und Binder 2014; Binder 2020). Die Transmembran-Domäne (TMD) verankert die Rezeptoren in der ER-Membran (Abbildung 3 und 4). Zudem können durch Disulfidbrückenbindungen an den Aminosäurepositionen C4 und C6 durch zwei Monomere ein funktionelles ETR-Dimer gebildet werden (Abbildung 3 und 4; Schaller und Bleecker 1995; Schaller *et al.* 1995).

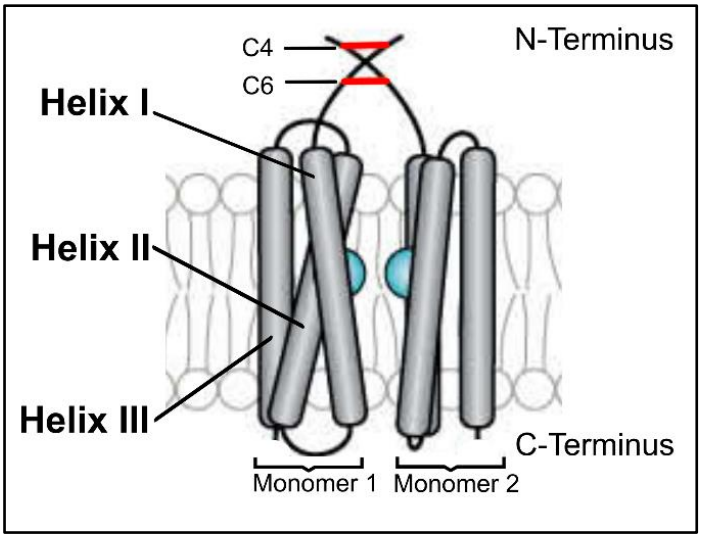

Abbildung 4: Vergrößerte Darstellung einer dimerisierten TMD (grau) eines Ethylenrezeptors. N-terminal ist das Dimer über die Aminosäurepositionen C4 und C6 eines Monomers mit denen eines zweiten Monomers kovalent über Disulfidbrücken (rot) verbunden. Die Nummerierung der transmembranen Helices eines Rezeptor-Monomers beginnt am N-terminalen Bereich (Helix I), fortlaufend mit Helix II, an welche der Cu(I)-Kofaktor (blau) bindet. Die Nummerierung endet mit Helix III. Modifiziert nach Binder (2020).

Die TMD besteht bei Unterfamilie 1 aus drei α-Helices (Rodríguez *et al.* 1999). Unterfamilie 2 verfügt möglicherweise über eine vierte Helix, die vermutlich der Signaltransduktion dient (Hua *et al.* 1998; Sakai *et al.* 1998). Pro Rezeptor-Monomer kann ein Cu(I)-Kofaktor an die ersten beiden Helices gebunden werden, wodurch wiederum Ethylen gebunden werden kann (Abbildung 3 und 4). Durch Mutagenese konnte nachgewiesen werden, dass die Aminosäuren an den Positionen C65 und H69 im direkten Zusammenhang mit der Bindung des Cu(I)-Kofaktor stehen. Des Weiteren wird vermutet, dass D25 einen stabilisierenden Effekt auf die Kupferkoordinierung haben könnte (Rodríguez *et al.* 1999; Wang *et al.* 2006; Schott-Verdugo *et al.* 2019).

Die *cGMP-Specific Phosphodiesterases, Adenyl Cyclases, Formate Hydrogen Lyase Transcriptional Activator*-Domäne (GAF-Domäne) ist für die Bildung von Hetero- und Homodimeren, sowie höherer Oligomere der ETRs verantwortlich (Abbildung 3; Gao *et al.* 2008; Chen *et al.* 2010; Berleth *et al.* 2019). Die Histidin-Kinase-Domäne (HK) ist für die Signalweiterleitung innerhalb des Rezeptors verantwortlich. Diese setzt sich bei ETR1 aus der dimerisierenden Histidin-Phosphotransfer-Domäne (DHp) und der

katalytischen ATP-Bindedomäne (CA) zusammen (Abbildung 3). Während die Unterfamilie 1 eine HK-Aktivität aufweist, verfügt die Unterfamilie 2 über eine degenerierte HK mit einer Serin-Threonin-Kinaseaktivität (Abbildung 3). ERS1 weist *in vitro* beide Aktivitäten auf (Moussatche und Klee 2004).

Die HK-Domäne und die *Receiver*-Domäne (RD) sind homolog zum Zwei-Komponenten-System aus Bakterien (Chang *et al.* 1993; Grefen und Harter 2004). Innerhalb der HK-Domäne wird ein Histidin autophosphoryliert. Dieser Phosphorylrest wird auf die RD eines Asparaginsäurerestes übertragen, falls der Rezeptor eine RD aufweist (Grefen und Harter 2004; Gao und Stock 2009). Die flexible RD phosphoryliert das dimere *Constitutive Triple Respone 1* (CTR1), eine *Rapidly Accelerated Fibrosarcoma* (*Raf*) - ähnliche Serin-Threonin-Proteinkinase, und verstärkt die Interaktion zwischen den Ethylenrezeptoren (Clark *et al.* 1998; Chang und Stadler 2001; Shakeel *et al.* 2015).

3.3 Ethylensignalweg

Die membrangebundenen Ethylenrezeptoren (ETRs; vgl. Kapitel 3.2) stellen einen integralen Bestandteil des Ethylensignalweges dar, bei dem die Bindung von Ethylen durch die Interaktion mit zwei Cu(I)-Ionen erfolgt (Schott-Verdugo *et al.* 2019).

Die Kupferchaperone *Antioxidant 1* (ATX1) und *Copper Chaperone* (CCH) transportieren Cu(I) bevorzugt zu der P_{1B}-Typ ATPase *Response To Antagonist 1* (RAN1), welches die ETRs belädt. In Abhängigkeit von der Kupferhomöostase in der Zelle erfolgt die Beladung der Rezeptoren mit dem Metallion direkt durch die Chaperone (Abbildung 5; Hoppen *et al.* 2019a).

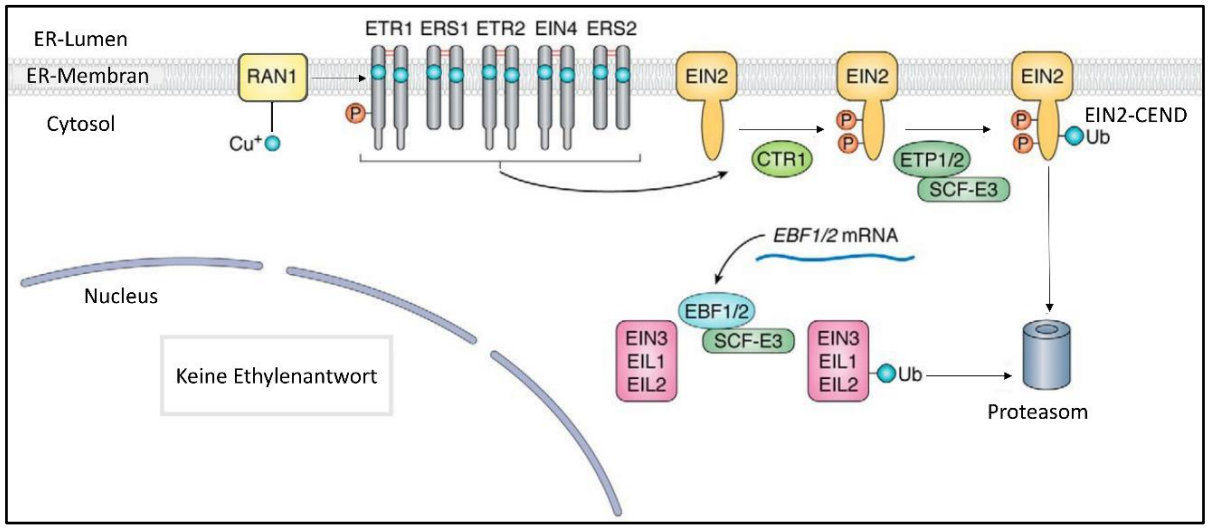

Abbildung 5: **Schematische Darstellung des Ethylensignalweges in Abwesenheit von Ethylen.** In Abwesenheit von Ethylen sind die kupferbeladenen Ethylenrezeptoren (ETR1, ETR2, ERS1, ERS2, EIN4) aktiv und aktivieren das dimere *Constitutive Triple Response 1* (CTR1), eine *Rapidly Accelerated Fibrosarcoma* (Raf) - ähnliche Serin-Threonin-Proteinkinase. Diese phosphoryliert das C-terminale Ende von *Ethylene Insensitive 2* (EIN2-CEND). Der *Skp 1 Cullen F-Box* E3-Ubiquitin-Ligase- *EIN2-Targeting Protein 1* und *2* (SCF-E3-ETP 1/2) -Komplex ubiquitiniert das C-terminale Ende von EIN2. Ebenfalls erfolgt dies mit den Transkriptionsfaktoren *Ethylene Insensitive 3* (EIN3) und *EIN 3-Like 1* und *2* (EIL1/2), welche durch den SCF-E3- *EIN 3 Binding F-Box 1* und *2* (EBF1/2) -Komplex ubiquitiniert werden. Diese werden durch das 26 S Proteasom abgebaut. Somit wird keine Ethylenantwort ausgelöst. Modifiziert nach Binder (2020).

Die Rezeptordimere sind aktiv, wenn sie in Abwesenheit von Ethylen kupferbeladen sind (Abbildung 5; Zhao *et al.* 2002). Über Autophosphorylierung aktivieren die ETRs die CTR1-Kinase (vgl. Kapitel 3.2; Abbildung 5; Mayerhofer *et al.* 2012). CTR1 phosphoryliert über ATP-Verbrauch das zytosolische C-terminale Ende des Membranproteins *Ethylene Insensitive 2* (EIN2), welches N-terminal ebenfalls am ER gebundenen ist (Abbildung 5; Ju *et al.* 2012). Der C-Terminus von EIN2 (EIN2-CEND) wird durch den *Skp 1 Cullen F-Box* E 3-Ubiquitin-Ligase-Komplex (SCF-E3), der die F-Box-Proteine *EIN2-targeting Protein 1* (ETP1) und ETP2 enthält, ubiquitiniert und vom 26S Proteasom abgebaut (Abbildung 5; Qiao *et al.* 2009; An *et al.* 2010). Im Zellkern liegen die Transkriptionsfaktoren *Ethylene Insensitive 3* (EIN3), *EIN 3-Like 1* (EIL1) und *EIN 3-Like* 2 (EIL2) vor. Diese werden mithilfe des anderen E3-Ubiquitin-Ligase-Komplexes, bestehend aus der SCF-Box und der *EIN 3 Binding F-Box 1* und *2* (EBF1/2),

ubiquitiniert und ebenfalls im 26S Proteasom abgebaut (Abbildung 5; Guo und Ecker 2003; Binder *et al.* 2007; An *et al.* 2010; Binder 2020). Als Ergebnis wird keine Ethylenantwort ausgelöst (Abbildung 5).

ETR1 und CTR1 sind Negativregulatoren. Die Bindung des Liganden, wie in diesem Fall Ethylen, führt zur Inaktivierung des Proteins. In Anwesenheit von Kupfer wird Ethylen gebunden und die Autokinaseaktivität der HK-Domäne von ETR1 inaktiviert (Abbildung 6; Schaller und Bleecker 1995; Zhao *et al.* 2002; Voet-van-Vormizeele und Groth 2008). Aufgrund der fehlenden Phosphorylierungskaskade erfolgt bei CTR1 ebenfalls eine Inaktivierung durch Konformationsänderung oder durch Ablösen vom ETR1-CTR1 Komplex (Clark *et al.* 1998; Hua und Meyerowitz 1998; Gao *et al.* 2003; Voet-van-Vormizeele und Groth 2008). EIN2-CEND wird nicht phosphoryliert. Es erfolgt die Abspaltung des EIN2-CENDs mittels einer unbekannten Protease (Abbildung 6; Ju *et al.* 2012). EIN2-CEND enthält eine *Nuclear Localization Sequence* (NLS), welche für den Transport in den Nukleus verantwortlich ist (Wen *et al.* 2012). Importin β erleichtert vermutlich den Transport von EIN2-CEND in den Nukleus (Lu *et al.* 2023). Im Nukleus bindet EIN2-CEND an das *EIN2 Nuclear Associated Protein 1* (ENAP1), welches für die Regulation der Transkriptionsfaktoren (TKF) von *Ethylene Insensitive 3* (EIN3) und *EIN 3-Like 1* (EIL1) verantwortlich ist (Abbildung 6). Durch die Akkumulierung dieser TKFs wird eine Transkriptionskaskade ausgelöst, die u. a. den TKF *Ethylene Response Factor 1* (ERF1) aktiviert (Abbildung 6; Chao *et al.* 1997; An *et al.* 2010; Ju *et al.* 2012; Wen *et al.* 2012; Zhang *et al.* 2017). Durch die ERFs wird die sogenannte Ethylenantwort ausgelöst, die physiologisch zu den oben genannten Effekten führt (vgl. Kapitel 3.1; Solano *et al.* 1998).

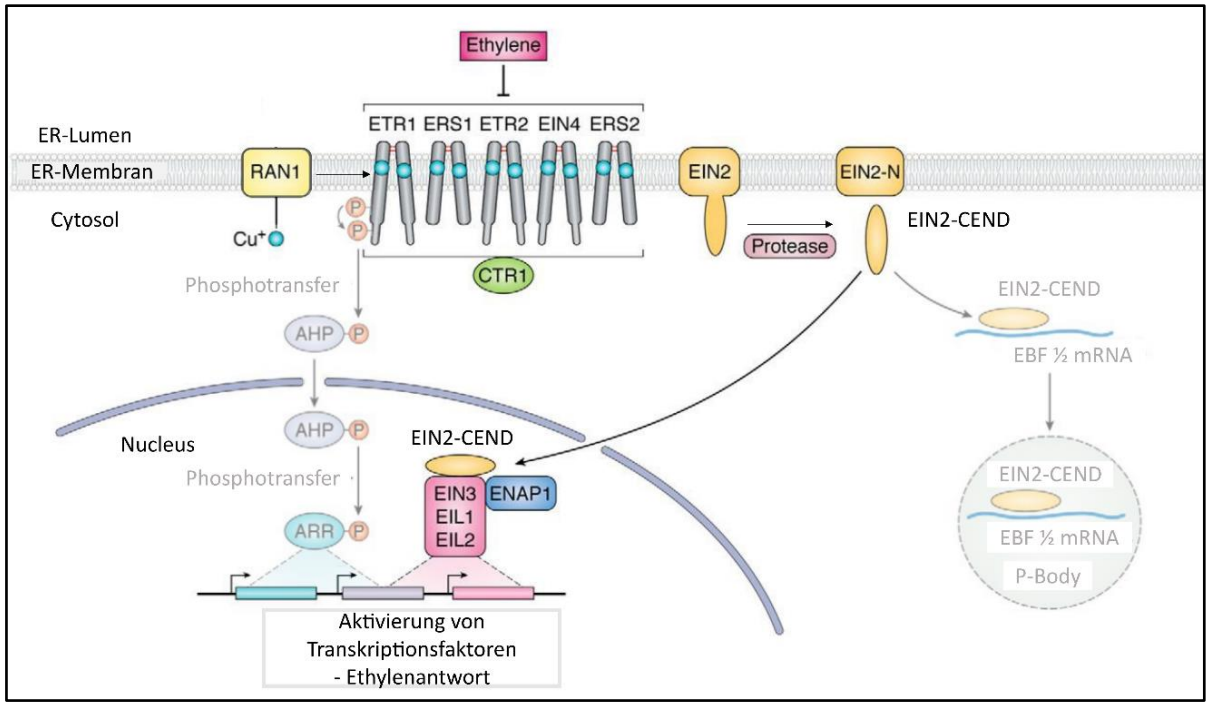

Abbildung 6: Schematische Darstellung des Ethylensignalweges in Anwesenheit von Ethylen. Durch die Bindung von Ethylen an die die kupferbeladenen Ethylenrezeptoren (ETR1, ETR2, ERS1, ERS2, EIN4) werden diese, sowie das dimere *Constitutive Triple Respone 1* (CTR1), eine R*apidly Accelerated Fibrosarcoma* (Raf) - ähnliche Serin-Threonin-Proteinkinase, inaktiviert. Durch eine unbekannte Protease wird das C-terminale Ende von *Ethylene Insensitive 2* (EIN2-CEND) abgespalten und wandert in den Nukleus. Dort wird EIN2-CEND von dem *Nuclear Associated Protein 1* (ENAP1) stabilisiert und eine stromabwärts gerichtete Kette von den Transkriptionsfaktoren *Ethylene Insensitive 3* (EIN3) und *EIN3-Like 1* und *2* (EIL1/2) gebildet, die wiederum die Ethylenantwort auslöst. EIN2-CEND kann abgesehen von der Bindung an ENAP1, auch an die *Messenger-RNA* (mRNA) von SCF-E3- *EIN 3 Binding F-Box 1* und *2* (EBF 1/2) binden. Diese mRNAs werden in Prozessierungskörperchen, auch *P-Bodies* genannt, eingeschlossen. Dadurch können EIN3 und EIL1/2 im Zellkern akkumulieren, welches zur Ethylenantwort führen. Ein weiterer Signalweg kann über die Übertragung eines Phosphorylrestes der ETRs an die *Arabidopsis Histidine Phosphotransfer Proteins* (AHPs) zu den *Response Regulator Proteins* (ARRs) erfolgen. Dabei wandert das phosphorylierte AHP in den Nukleus und transferiert den Phosphorylrest an ARR, welches wiederum Transkriptionsfaktoren bildet. Modifiziert nach Binder (2020).

Eine zusätzliche Funktion von EIN2-CEND ist die Bindung an die *Messenger-RNA* (mRNA) von EBF 1/2 (Abbildung 6). Die mRNA von EBF 1/2 werden in Prozessierungskörperchen (*P-Bodies*) sequestriert d. h. EIN3 und EIL1 können im Zellkern akkumulieren anstatt ubiquitiniert und abgebaut zu werden (Abbildung 6; Zhang und Wen 2015). Die *P-Bodies* dagegen werden durch Exoribonuklease 4 (XRN4, auch EIN5 genannt) abgebaut (Olmedo *et al.* 2006; Potuschak *et al.* 2006). Dafür interagiert EIN5

zusätzlich mit EIN2-CEND, *Poly(A)-Binding Proteins* (PABs), *Untranslated Region* (UTR) und *Up-Frameshift Surpressor 1* (UPF1; Li *et al.* 2015).

Ein weiterer Signalweg wird über die *Arabidopsis Histidine Phosphotransfer Proteins* (AHPs) und *Response Regulator Proteins* (ARRs) vermittelt (Abbildung 6). Dabei wird eine Phosphorylgruppe der ETRs auf die AHPs übertragen (Scharein *et al.* 2008; Scharein und Groth 2011; Zdarska *et al.* 2019). Die phosphorylierten AHPs wandern in den Nukleus und transferieren den Phosphorylrest an ARRs, welche TKFs sind und u. a. zur Schließung der Stomata oder zur Hemmung des Wurzelwachstums führen (Sakai *et al.* 2000; Mira-Rodado *et al.* 2012; Street *et al.* 2015; Binder 2020).

3.4 NOP-1 und andere Inhibitoren

NLS Octapeptide 1 (NOP-1) ist ein Peptid, das der Aminosäuresequenz 1262-1269 von EIN2 entspricht (Bisson und Groth 2011, 2015). Die Proteinsequenz LKRYKRRL von NOP-1 konnte anhand einer Kombination aus Mutagenese- und Interaktionsstudien zwischen EIN2 und ETR1, sowie aus Computeranalysen ermittelt werden (Bisson *et al.* 2009; Bisson und Groth 2010, 2011, 2015). Die erhaltenden Informationen sind für dieses NLS-Motiv und den Transport von EIN2-CEND in den Nukleus von Bedeutung, da Ethylen, dessen Signalweg und somit auch die NLS-Reste und NOP-1 Bindestellen in unterschiedlichsten Pflanzenorganismen seit über 450 Millionen Jahren im Pflanzenreich konserviert sind (Bisson und Groth 2011; Ju *et al.* 2012; Qiao *et al.* 2012; Wen *et al.* 2012; Ju *et al.* 2015; van de Poel *et al.* 2015; Bisson *et al.* 2016; Hoppen *et al.* 2019b).

Interaktionsstudien zwischen ETR1, EIN2 und NOP-1 haben gezeigt, dass dieses Peptid als Inhibitor von ETR1 agiert (Bisson und Groth 2015; Bisson *et al.* 2016). NOP-1 bindet hoch affin an die ETR1-GAF-Domäne mit einer Dissoziationskonstante (K_D) von 104 nM. Das Peptid bindet aufgrund seiner positiven Ladung, bedingt durch die vielen Lysine und Arginine, bevorzugt an negativ geladene Asparagin- und Glutaminsäurereste. Durch die Bindung an die GAF-Domäne wird vermutlich die Konformationsänderung und die Signalweiterleitung von der TMD zur HK-Domäne blockiert. Daher wird die Interaktion mit EIN2 gestört, wodurch es keine bzw. eine verzögerte Ethylenantwort gibt (Bisson und Groth 2015; Milić *et al.* 2018; Hoppen 2020). Eine Verzögerung der Fruchtreife und Blütenseneszenz in Schnittblumen konnte in verschiedenen Spezies

nachgewiesen werden (Abbildung 7; Bisson *et al.* 2016; Kessenbrock *et al.* 2017; Hoppen *et al.* 2019b; Klein *et al.* 2019; Aghdam und Razavi 2021).

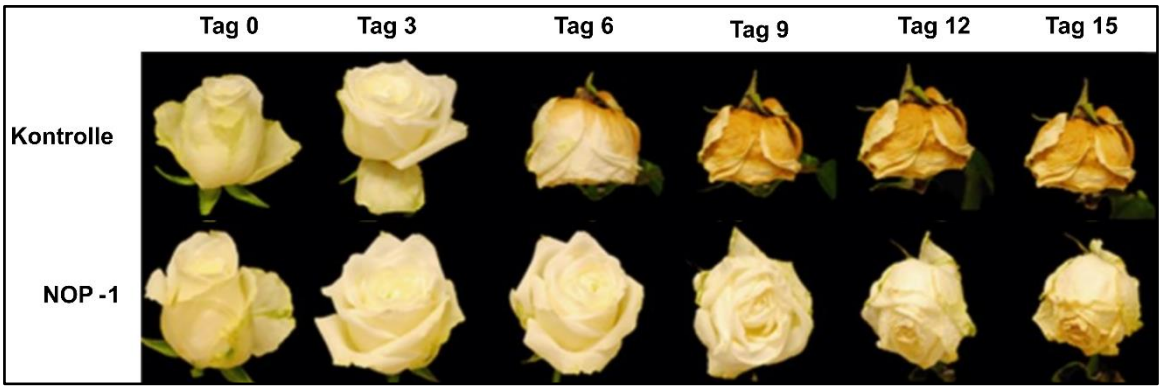

Abbildung 7: Verzögerung der Blütenseneszenz von Rosen. In der oberen Reihe wurden Rosen nur mit Tris-Acetat-Puffer pH 8 behandelt. Die Rosen verwelkten bereits nach sechs Tagen und zeigten deutlich verfärbte und eingerollte Blütenblätter. In der unteren Reihe wurden die Rosen mit 0,5 mM des Peptids *Nuclear Localization Sequence Octapeptide 1* (NOP-1) behandelt, welche eine deutliche Verzögerung der Seneszenz um sechs bis acht Tage zeigten. Modifiziert nach Hoppen *et al.* (2019b).

Neben NOP-1 wurden weitere von der NLS abgeleitete Inhibitoren analysiert wie das *NLS Icosapeptide 1* (NIP-1). NIP-1 (AFPKGKENLASVLKRYKRRL) entspricht der Aminosäuresequenz 1250–1269 von EIN2 (Bisson und Groth 2015). Die Affinität des Peptids zur ETR1-GAF ist um 36 nM stärker als zu NOP-1(Milić *et al.* 2018).

Weitere Inhibitoren sind bekannt, welche die Ethylenproduktion hemmen (1-Aminoethoxyvinylgylcin (AVG), Aminooxyessigsäure (AOA) und Cobaltsalze). *Trans*-Cycloocten (TCO), 1-Methylcyclopropan (1-MCP), 2,5-Norbornadien (NBD) und Silbersalze dagegen inhibieren die ETRs (Abbildung 8).

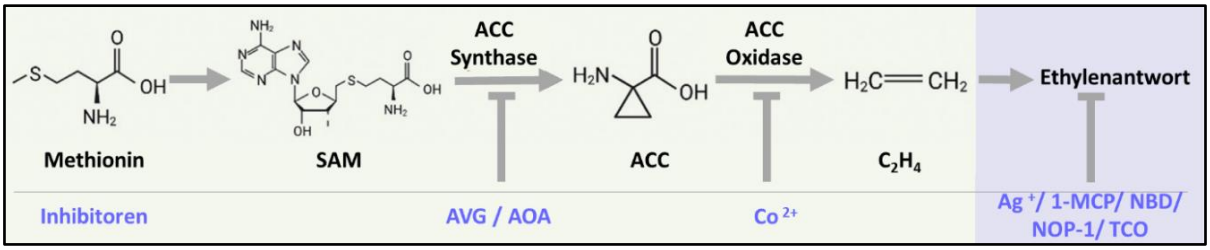

Abbildung 8: Vereinfachte schematische Darstellung der Ethylenbiosynthese, sowie deren Inhibitoren. S-Adenosylmethionin (SAM) wird aus der Aminosäure Methionin synthetisiert. Die 1-Aminocyclopropancarbonsäure (ACC) Synthase katalysiert die Umwandlung von SAM zu ACC. ACC wiederum wird durch die ACC Oxidase in Ethylen umgewandelt. Ethylen kann an die ETRs (Abbildung 3) binden und löst eine Ethylenantwort aus. Es gibt Inhibitoren, die die Enzyme in der Ethylenbiosynthese beeinflussen (grüner Hintergrund). 1-Aminoethoxyvinylgylcin (AVG) und Aminooxyessigsäure (AOA) hemmen die ACC-Synthase, während Cobalt (Co(II)) einen Einfluss auf die ACC Oxidase hat. Zudem kann die Ethylenantwort (blauer Hintergrund) durch die Substanzen Silber (Ag(I)), 1-Methylcyclopropan (1-MCP), 2,5-Norbornadien (NBD) und das Oktapeptid *Nuclear Localization Sequence Octapeptide 1* (NOP-1), *trans*-Cycloocten (TCO) beeinflusst werden. Modifiziert nach Depaepe und van der Straeten 2020; Li *et al.* 2022).

AVG und AOA beeinflussen die Produktion der Ethylenvorstufe ACC, indem die ACC-Synthase, welche S-Adenosylmethionin (SAM) in ACC umwandelt, inhibiert wird (Abbildung 8). Dadurch wird die endogene Ethylenproduktion unterbunden. Physiologische Effekte wie die Blütenseneszenz, sowie die Blattabszission werden verzögert (Yu *et al.* 1979; Yu und Yang 1979; Amrhein und Wenker 1979; Sagee *et al.* 1980).

Cobalt (Co(II)) ist ein Inhibitor, der an die ACC-Oxidase bindet und dadurch die Katalyse von ACC zu Ethylen inhibiert (Abbildung 8). Es konnte gezeigt werden, dass obwohl Auxin die Ethylenproduktion anregt, unter dem Einfluss des Schwermetallions Co(II) nur eine Anreicherung von ACC stattfindet. Der genaue Mechanismus ist jedoch unbekannt (Yu und Yang 1979).

Ein weiteres Schwermetall, das anstelle von Cu(I) als nicht-kompetitiver Inhibitor an die ETRs bindet, ist Silber (Ag(I)). Es besteht die Vermutung, dass, obwohl Ethylen in Gegenwart von Ag(I) gebunden werden kann, keine Konformationsänderung stattfindet, wodurch die Signalweiterleitung und Ethylenantwort unterbrochen wird (Rodríguez *et al.* 1999; Zhao *et al.* 2002; McDaniel und Binder 2012). Die Wirkung des Ag(I) kann durch die Zugabe von Cu(I) aufgehoben werden (Knee 1995). Es konnte gezeigt werden, dass Ag(I) vor allem die Ethylenbindung an ETR1 und ERS1 beeinflusst, während bei den Rezeptoren der Unterfamilie 2 keine Ethylenbindung nachgewiesen werden

konnte (McDaniel und Binder 2012). Häufig wird Ag(I) in Form von Silbernitrat ($AgNO_3$) oder Silberthiosulfat (STS, $Ag_2S_2O_3$) als Zusatzstoff zur Verlängerung der Haltbarkeit von Schnittblumen eingesetzt (Beyer 1976; Veen und van de Geijn 1978).

Ein Ethylen-Analogon, das an den Rezeptor bindet, ist das geruchlose und ungiftige Cyclopropen 1-MCP (Sisler und Serek 1997; Serek *et al.* 2006). 1-MCP wird mithilfe des cyclischen Zuckerkomplexes Cyclodextrin umschlossen und kann so gelagert werden. Gelangt dieser Zuckerkomplex in eine wässrige Lösung, wird 1-MCP als Gas freigesetzt und konkurriert vermutlich mit Ethylen um die Bindestelle (Blankenship und Dole 2003). Bereits geringe Mengen 1-MCP in geschlossenen Räumen reichen für eine effektive Wirkung aus, welche bei verschiedenen Schnitt- und Topfblumen, sowie Obst- und Gemüsesorten angewendet werden kann (Serek *et al.* 1995; Sisler und Serek 1997; Fan *et al.* 1999; Sisler *et al.* 1999; Martínez-Romero *et al.* 2003; Serek *et al.* 2006; Watkins 2006; Reid und Çelikel 2008).

Weitere volatile, allerdings giftige Stoffe, die an den Rezeptor binden und die Ethylenantwort in Schnittblumen unterdrücken, sind 2,5–Norbornadien und *trans*-Cycloocten. Durch verschiedene Enantiomere von *trans*-Cycloocten konnte festgestellt werden, dass die Ethylenbindungsstelle asymmetrisch ist, obwohl Ethylen selbst ein symmetrisches Molekül darstellt (Sisler *et al.* 1983; Sisler *et al.* 1986; Sisler *et al.* 1990; Sisler und Serek 1999; Pirrung *et al.* 2008).

3.5 Kupfer als Kofaktor

Kupfer (Cu) ist eins der 25 am häufigsten vorkommenden Metalle in der Erdkruste (Conry 2006). Dieses Übergangsmetall wird zusammen mit den Elementen Silber, Gold und Röntgenium im Periodensystem der Nebengruppe 11 zugeordnet (Cao *et al.* 2020). Eine Vielzahl von Prozessen in der Pflanze wird durch den Mikronährstoff Kupfer als Kofaktor beeinflusst.

Einige Proteine, die Kupfer als Kofaktor nutzen, sind z. B. die Cytochrom-c-Oxidase sowie die ETRs (Rodríguez *et al.* 1999; Raven *et al.* 1999). Kupfer ist in den zwei Oxidationsstufen Cu(I) und Cu(II) verfügbar. Ein Wechsel des Redoxzustandes des Metalls kann in der Zelle die Bildung reaktiver Sauerstoffspezies (ROS = *Reactive Oxygen Species*) zur Folge haben wie z. B. Wasserstoffperoxide, Hydroxylradikale oder Hyperoxidanionen (Halliwell und Gutteridge 1984; Han 2023). Diese ROS können DNA, Lipide, Proteine und andere Biomoleküle schädigen und schließlich zerstören (Halliwell und Gutteridge 1984; Kehrer 2000; Yruela 2005).

Zur Vermeidung der Kupferzytotoxizität wird das Metallion in Organismen mithilfe von Chaperonen in gebundener Form im Zytosol zu den entsprechenden Proteinen in den verschiedenen Zellkompartimenten transportiert. Beispielsweise wurde bei *Saccharomyces cerevisiae* (*S. cerevisiae*) festgestellt, dass bei einer intrazellulären Kupferkonzentration von 70 µM der Gehalt an freien Kupferionen weniger als ein Ion pro Zelle beträgt (Rae *et al.* 1999). Es gibt auch Proteine, die Kupfer als Kofaktor benötigen und in der Lage sind die gebildeten ROS zu Wasser und Sauerstoff zu katalysieren wie beispielsweise die Kupfer-Zink-Superoxiddismutase (Cu-Zn-SOD; Rodríguez *et al.* 1999; Raven *et al.* 1999; Alscher 2002; Festa und Thiele 2011; Rubino und Franz 2012; Dluhosch *et al.* 2024).

Die Komplexierung von Cu(I) als Kofaktor erfolgt mit vier bis fünf Substituenten, während das Metall beim Transport und Transfer auf andere Proteine zwischen zwei und vier Atomen koordiniert ist. Dementsprechend kann Cu(I) linear, trigonal-planar oder tetraedrisch koordiniert sein (Conry 2006; Rubino und Franz 2012).

Cu(II) hingegen kann durch vier bis sechs Atome gebunden sein. Die Geometrien, die sich ausbilden können, sind quadratisch-planar und quadratisch-pyramidal bzw. oktaedrisch (Conry 2006; Rubino und Franz 2012).

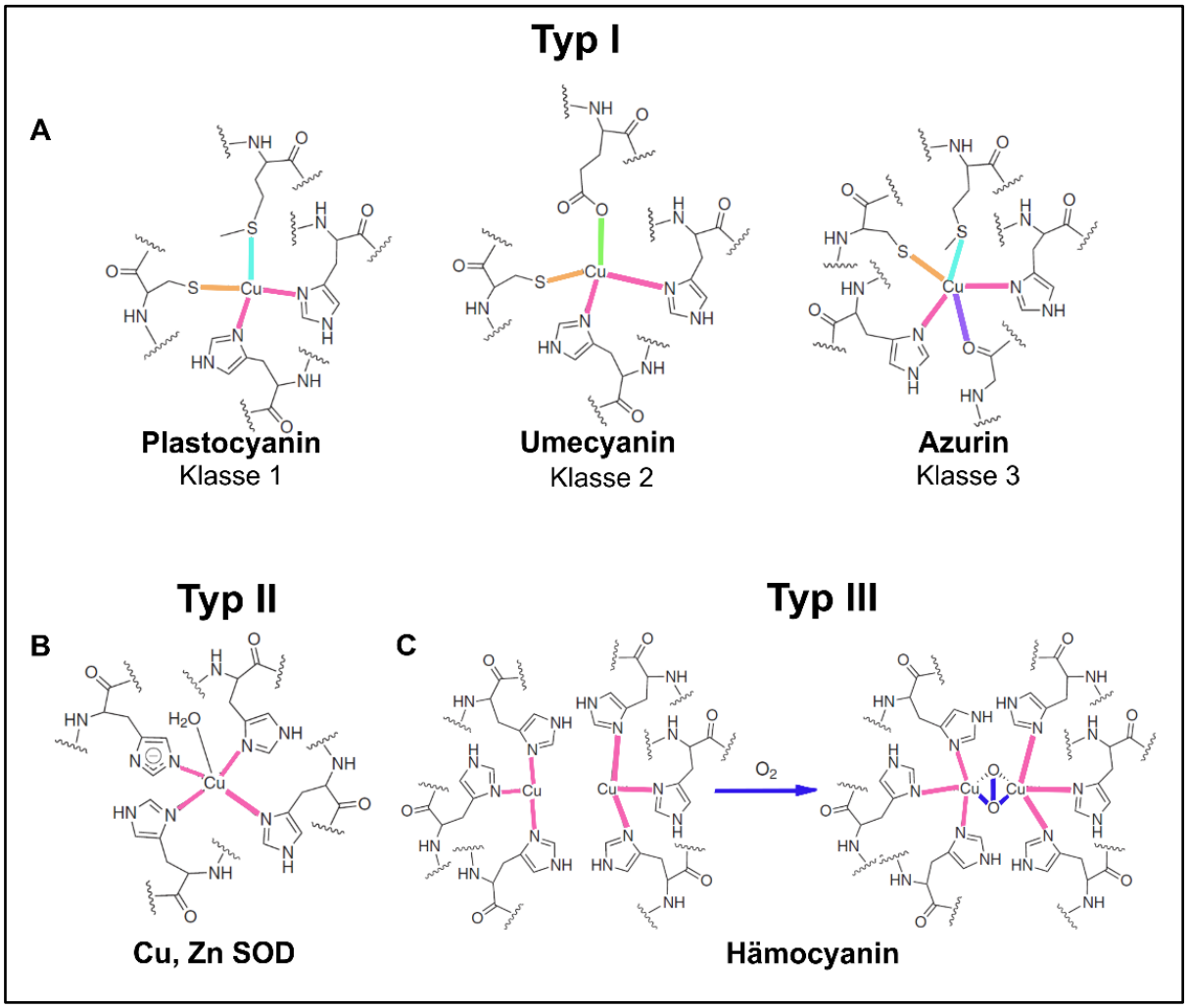

Abbildung 9 : Darstellung verschiedener Kupferkoordinationszentren anhand verschiedener Proteine. A) Das Kupferzentrum TypI wird in drei Klassen unterteilt. Hier ist Klasse 1 und 2 tetraedrisch koordiniert, während bei Klasse 3 eine trigonal-bipyramidale Anordnung durch fünf Atome zur Stabilisierung verwendet wird. In allen drei Klassen sind jeweils die Stickstoffatome zweier Histidine (pink) und das Schwefelatom eines Cysteins (orange) an der Koordinierung beteiligt. In Klasse 1 wird bei Plastocyanin zusätzlich das Schwefelatom eines Methionins (türkis) zur Stabilisierung hinzugezogen. In Klasse 2 wird bei dem Protein Umecyanin anstelle von Methionin das Sauerstoffatom einer Aminosäure verwendet, hier Glutaminsäure (grün). In der dritten Klasse wird ebenfalls ein Sauerstoffatom, im Fall von Azurin als fünfter Koordinationspartner verwendet. Hier ist es Glycin (violett). **B)** Kupferzentren des TypII koordinieren das Kupfer beispielweise in der Cu-Zn-SOD mithilfe von vier Histidinen. **C)** Dagegen besitzen Kupferzentren des Typ III zwei Kupferatome, wobei jedes Kupferatom von drei Histidinen trigonal-planar koordiniert wird. Durch die Bindung des Liganden Sauerstoff (blau) ändert sich die Konformation von trigonal-planar in trigonal-bipyramidal. Die Typen und Klassen der Kupferkoordinationszentren sind unabhängig von dem Oxidationszustand des Kupfers. Anhand von **C)** sieht man auch, dass sich die Kupferkoordinierung auch innerhalb eines Proteins ändern kann. Modifiziert nach (Rubino und Franz 2012).

Es gibt drei verschiedene Typen von Kupferzentren, die das Metallion in Proteinen komplexieren. Zu den Kupferzentren des Typ I gehören hauptsächlich Elektronentransferproteine wie Azurin und Plastocyanin (Abbildung 9A). Die trigonal-planare Koordinierung des Kupferions erfolgt von den Stickstoffatomen des Imidazolrings zweier Histidine und dem Schwefelatom eines Cysteins (Choi und Davidson 2011; Rubino und Franz 2012). Darüber hinaus sind die Kupferzentren des Typ I in drei weitere Klassen aufgespalten, die mit der Anzahl zusätzlich axialer Koordinationsstellen zusammenhängen (Rubino und Franz 2012). In der ersten Klasse wird Kupfer zusätzlich durch das Schwefelatom eines Methionins axial stabilisiert, wie in Plastocyanin (Abbildung 9A). In der zweiten Klasse hingegen wird anstelle von Methionin eine andere nicht-schwefelhaltige Aminosäure wie z. B. das Sauerstoffatom der Glutaminsäure zur Komplexierung verwendet (Abbildung 9A). In Klasse drei ist im Vergleich zur zweiten Klasse eine weitere Aminosäure an der Komplexierung des Kupfers beteiligt wie z. B. in Hämocyanin. Hier bindet zusätzlich das Schwefelatom des Methionins und das Carbonylsauerstoff des Glycins (Abbildung 9A). Daraus ergibt sich für die ersten beiden Klassen eine tetraedrische und für die dritten Klasse eine trigonal bipyramidale Geometrie zum Kupfer (Abbildung 9A; Rubino und Franz 2012).

Beim Typ II der Kupferzentren bildet sich hauptsächlich durch die Stickstoffatome der Histidine eine quadratisch-planare Geometrie aus (Abbildung 9B). Zum Teil erfolgt eine zusätzliche Koordination des Kupferkomplexes über Sauerstoffatome, die meist von Arginin- (R) oder Tyrosinresten (Y) stammen. Dazu zählen beispielsweise Oxidoreduktasen wie die Cu-Zn-SOD (Abbildung 9B; Choi und Davidson 2011; Rubino und Franz 2012).

Kupferzenten des Typ III binden zwei Kupferionen innerhalb eines Proteins, bei der jedes Kupfer durch drei Histidine gebunden wird wie z. B. in Oxidasen und Hämocyanin (Abbildung 9C). Durch die Ligandenbindung des Sauerstoffes verändert sich die Koordination aus einer trigonal-planaren zu einer bipyramidalen Geometrie (Abbildung 9C; Choi und Davidson 2011; Rubino und Franz 2012).

Der Mikronährstoff Kupfer kann in der Wurzel von *A. thaliana* über zwei verschiedene Transportsysteme aus der Erde aufgenommen werden. Zum einen wird Cu(II) zusammen mit Zink über *Zinc Transporter 2* und *4* (ZIP 2/4) aufgenommen und durch *Copper Transporter 1* und *2* (COPT 1/2) in die Pflanzenzelle transportiert. Zum anderen kann

Kupfer in reduzierter Form als Cu(I) bereitgestellt werden. Dies erfolgt durch die *Ferric Reductase Oxidase 4* und *5* (FRO 4/5; Wintz *et al.* 2003; Festa und Thiele 2011; Jain *et al.* 2014). Danach wird das Kupfer beispielsweise für den Ethylensignalweg genutzt, da für die Wahrnehmung des Ethylens Kupfer benötigt wird (vgl. Kapitel 3.3; Rodríguez *et al.* 1999).

Im Zytosol von *Arabidopsis* befinden sich Metallochaperone aus der *Antioxidant 1* (ATX1) - Familie. Zu dieser Familie gehören ATX1 und *Copper Chaperone* (CCH). Diese besitzen hoch konservierte Kupferbindemotive mit dem Sequenzmotiv MxCxxC. Durch die zwei Cysteine im Kupferbindemotiv wird ein Kupferion gebunden (Abdel-Ghany *et al.* 2005). Die beiden Chaperone haben einen ähnlichen strukturellen Aufbau. Im Vergleich zu ATX1 besitzt CCH einen zusätzlichen, ungefalteten, pflanzenspezifischen Bereich im C-Terminus. Dieser besteht aus 40 Aminosäuren (Mira *et al.* 2001a; Mira *et al.* 2004; Puig *et al.* 2007; Hoppen 2020; Hoppen und Groth 2020). Dieses C-terminale Ende spielt eine indirekte Rolle bei der Stabilisierung der Dimerisierung von CCH (Mira *et al.* 2001a; Dluhosch *et al.* 2024).

Ist Kupfer gebunden und liegt kein Ethylen vor, ist der ETR1 aktiv und hemmt den Signalweg (vgl. Kapitel 3.3). Die Expression der ER–Membran gebundenen P_{1B}-Typ-ATPase *Response To Antagonist 1* (RAN1) wird negativ reguliert, wenn eine erhöhte Kupferkonzentration in der Zelle vorliegt. Dadurch wird möglicherweise eine direkte Interaktion zwischen ETR1 und ATX1 bzw. CCH möglich (Del Pozo *et al.* 2010; Hoppen *et al.* 2019a). Es besteht die Annahme, dass ATX1 direkt an den Rezeptor bindet und Kupfer verteilt (Shin *et al.* 2012), während CCH eine gegensätzliche Rolle spielt. Dabei könnte CCH beispielweise bei der Entfernung des Kupferkofaktors beteiligt sein, bevor der Rezeptor proteasomal abgebaut wird (Mira *et al.* 2001a; Hoppen 2020; Hoppen und Groth 2020). Eine andere Möglichkeit ist, dass CCH an der Mobilisierung von Kupfer aus alten, absterbenden Pflanzenteilen beteiligt ist, da CCH auch bei hohen Kupferkonzentrationen stabil ist (Mira *et al.* 2001a; Mira *et al.* 2001b; Printz *et al.* 2016; Hoppen 2020; Dluhosch *et al.* 2024).

Durch die Dimerisierung von CHH, wird zum einen das Metallbindemotiv vor Oxidation geschützt. Zum anderen wird Kupfer selbst bei der Bindung und einem möglichen Langstreckentransport von CCH vor äußeren Einflüssen abgeschirmt, um die Zelle zu

schützen (Dluhosch *et al.* 2024; Mira *et al.* 2001b; Hoppen 2020; Hoppen und Groth 2020).

Die kupferbeladenen Metallochaperone transportieren das Kupfer zu RAN1 (Festa und Thiele 2011; Hoppen *et al.* 2019a). P_{1B}-Typ-ATPasen, wie RAN1, katalysieren den Transport von Schwermetallionen unter ATP-Verbrauch (Mira *et al.* 2002). Als Schwermetalltransporter (HMA = *Heavy Metal P-Type ATPases*) besitzt RAN1, auch HMA7 genannt und einer von acht HMAs in *Arabidopsis*, wie die ATX1-Familie Kupferbindemotive am C-terminalen Ende. Dieser Bereich wird deshalb auch als Metallbindedomäne (MBD) oder als ATX-ähnliche Faltungsmuster (*ATX-Like-Folds*) bezeichnet (Andrés-Colás *et al.* 2006; Hoppen und Groth 2020). Sie binden hoch affin an die TMD von ETR1, übertragen das Kupfer an den Rezeptor und wirken vermutlich stabilisierend. Zudem ist RAN1 am Crosstalk zwischen Ethylen und der Kupferhomöostase, sowie bei der Rekrutierung der Kupferchaperone in der Zelle beteiligt (Mira *et al.* 2002; Binder *et al.* 2010; Del Pozo *et al.* 2010).

Eine Kupferdetoxifizierung, durch den Export des Schwermetalls aus der Zelle, wird durch HMA5 ausgeführt, wenn ein Kupferüberschuss in der Zelle vorliegen sollte. Dabei wird Kupfer entweder in den extrazellulären Raum oder in den Tonoplasten transportiert (Andrés-Colás *et al.* 2006; Pilon *et al.* 2006; Festa und Thiele 2011; Huang *et al.* 2016; Khoudi 2021). Sollte ein Kupfermangel in der Zelle vorliegen, kann Kupfer mithilfe von COPT5 aus der Vakuole ins Zytosol transportiert werden und ist somit für die Chaperone verfügbar (Festa und Thiele 2011).

Phänotypisch können Symptome eines Kupfermangels oder –überschusses beobachtet werden. Biomoleküle werden bei einem Kupferüberschuss durch die Bildung von ROS geschädigt, was mit einer reduzierten Enzymaktivität einhergehen kann (Halliwell und Gutteridge 1984; Kehrer 2000; Yruela 2005). Dadurch werden Wurzel und Blattgewebe stark beschädigt und Grana- und Stromalamellen in den Chloroplasten bauen sich ab. Daraus resultieren vor allem in Keimlingen kleine und verkümmerte Pflanzen mit inhibiertem Wurzelwachstum, sowie vergilbtes (Chlorose) und absterbendes Blattgewebe (Nekrose; Lequeux *et al.* 2010; Yruela 2005). Bei einem Kupfermangel sinkt die Enzymaktivität in juvenilen Pflanzen um 70-95 %. Dies führt zu einem gehemmten Wachstum der gesamten Pflanze und zur mangelhaften Ausbildung von Früchten und Blüten (Walker und Loneragan 1981). Außerdem bildet sich an den Blatträndern der

juvenilen Pflanze Chlorose aus, welche anschließend zum Zusammenrollen, Verwelken und Absterben von Blättern führen kann (Yruela 2005).

3.6 GFP

Das grün fluoreszierende Protein (GFP), ein natürlich vorkommender Fluoreszenzreporter, hat einen großen Einfluss in der Forschung an Pro- und Eukaryoten wie z. B. in der Entwicklungs-, Molekular-, Zellbiologie und Proteinbiochemie (Chalfie 1995; Chalfie und Kain 2005). Häufig dient GFP als Fusionsprotein, wodurch nach erfolgreicher Expression und Reinigung eine grüne Färbung der Fusionsproteine erkennbar ist. Eine GFP-Fusion führt häufig zu einer besseren Stabilität, Faltung und Löslichkeit von unlöslichen Proteinen (Phillips 1997; Waldo *et al.* 1999; Pédelacq *et al.* 2006), weshalb GFP für die Kristallisation in dieser Arbeit verwendet wurde. Darüber hinaus korreliert die Fluoreszenz des GFPs meistens mit der richtigen Faltung des Zielproteins und somit auch mit der Proteinausbeute während der Expression (Phillips 1997; Waldo *et al.* 1999). In der Bakterienzelle liegt GFP nativ gefaltet im Zytosol vor (Feilmeier *et al.* 2000).

Die cDNA des natürlich vorkommenden Fluoreszenzreporters GFP wurde erstmals 1992 aus der Qualle *Aequorea victoria* (*A. victoria*) isoliert (Prasher *et al.* 1992). Die heterologe Expression und Reinigung erfolgte in bzw. aus verschiedensten Organismen wie *A. victoria*, *Caenorhabditis elegans* (*C. elegans*) und *Escherichia coli* (*E. coli*; Morise *et al.* 1974; Chalfie *et al.* 1994; Yang *et al.* 1996). Kovalente GFP-Dimere werden bei einem K_D-Wert von 100 µM ausgebildet (Phillips 1997).

GFP besteht aus 238 Aminosäuren und hat eine Größe von 26,9 kDa (Prasher *et al.* 1992). Die Strukturaufklärung des GFPs erfolgte im Jahr 1996 mithilfe von Röntgenstrukturanalyse, mit einer Auflösung von 1,9 Å (Ormö *et al.* 1996; Yang *et al.* 1996). Elf β-Faltblätter bilden die Struktur eines β-Fasses mit einem Durchmesser von 30 Å und einer Länge von ca. 40 Å. Im Zentrum des β-Fasses, befindet sich eine α-Helix. Diese Helix enthält einen grünen Chromophor, welcher für die Farbgebung des Proteins verantwortlich ist (Chalfie *et al.* 1994; Yang *et al.* 1996). Dieser Chromophor setzt sich aus einem Imidazolon- und einem Phenolring zusammen, welche durch kovalente Bindungen miteinander verbunden sind. Die Aminosäuren Serin 65 (S65), Tyrosin 66 (Y66) und Glycin (G67) bilden durch eine autokatalytische Reaktion innerhalb der α-Helix diesen Chromophor (Shimomura 1979; Prasher *et al.* 1992; Cody *et al.* 1993).

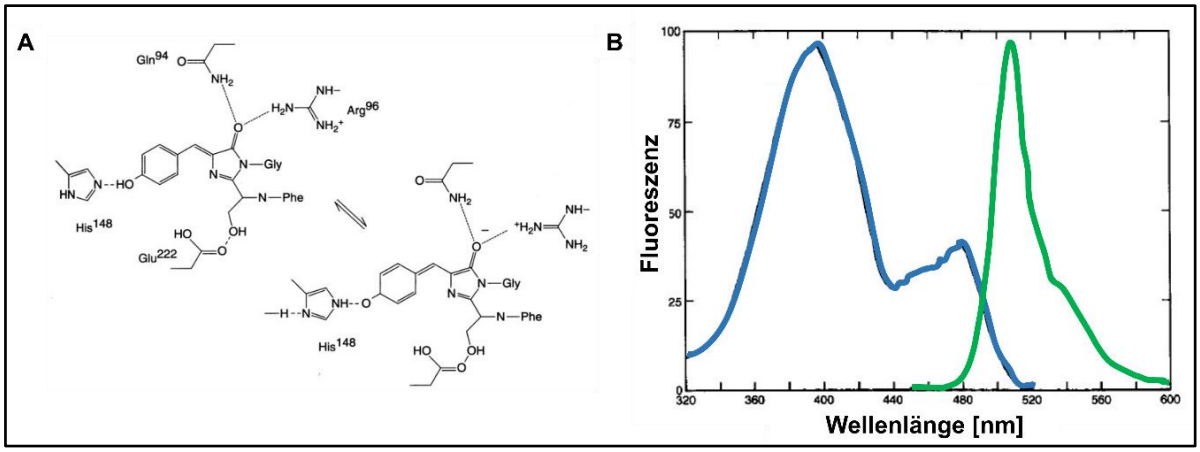

Abbildung 10: Fluoreszenz von GFP. A) Chromophor in deprotonierter (links) und protonierter Form (rechts). **B)** Anregungs- (blau) und Emissionsspektrum (grün). Modifiziert aus Chalfie und Kain 2005.

GFP hat zwei verschiedene Anregungs- und Emissionsspektren, welche auf zwei verschiedene Ladungszustände des Chromophors zurückzuführen sind (Abbildung 10A). Ist der Chromophor negativ geladen (protoniert), wird GFP bei 395 nm angeregt und emittiert bei 508 nm (Abbildung 10B). Wird ein Proton dagegen abgegeben, kann die deprotonierte Form des Chromophors bei 475 nm angeregt werden und emittiert bei 503 nm (Abbildung 10B; Heim *et al.* 1994; Chalfie und Kain 2005).

Durch Mutationen der Aminosäuren innerhalb des farbgebenden Chromophors konnten weitere Varianten erzeugt werden, deren Anregungs- und Emissionsspektren sich vom GFP-Wildtyp unterscheiden wie z. B. *mTurquoise2* (mT2). Zu diesen Mutanten zählen auch GFP-Homologe, welche aus verschiedensten Korallen isoliert wurden (Heim und Tsien 1996; Matz *et al.* 1999; Shaner *et al.* 2004; Chalfie und Kain 2005; Goedhart *et al.* 2012).

4 Zielsetzung

ETRs lösen in Anwesenheit von Kupfer und Ethylen eine Reaktionskaskade aus, die in einer Ethylenantwort wie z. B. der Fruchtreife resultiert (vgl. Kapitel 3.3). Diese Rezeptoren sind für die Agrarökonomie hinsichtlich des Transportes und der Lagerung von Gemüse, Obst und Schnittblumen wichtig, da eine zu schnelle Reifung zum Verderb führt (Reid und Wu 1992; Bleecker und Kende 2000; Barry und Giovannoni 2007; Binder 2020). Vor kurzem wurde der Kupfertransport aus der Zelle zum Rezeptor aufgeklärt (Hoppen *et al.* 2019a). Zusätzlich wurde die ETR1 Kupferkoordination – Kupferstöchiometrie experimentell, sowie über molekulardynamische (MD) Simulationen ermittelt. Anhand der Ergebnisse konnte das erste ETR1-Strukturmodell dazu entwickelt werden (Schott-Verdugo *et al.* 2019).

Eine experimentell bestimmte Struktur des ETR1-Volllängenrezeptors existiert nicht. Bisher gelang über Röntgenkristallographie und *Small Angle X-Ray Scattering* (SAXS) die Strukturaufklärung der zytosolischen Domänen von ETR1 $^{306\text{-}738}$ (Grantz *et al.* 1998; Panneerselvam *et al.* 2013; Mayerhofer *et al.* 2015). Die Struktur der TMD ist weiterhin unbekannt. Dieses Ziel sollte mit den nachfolgend genannten Methoden erreicht werden.

Lipidic Cubic Phase (LCP)-Kristallisation ist eine bewährte Methode für die Kristallisation von Membranproteinen. Sie eignet sich insbesondere für Membranproteine mit einer großen extrazellulären Domäne, wie auch ETRs sie aufweisen. Mittels LCP konnten beispielsweise bereits die Struktur verschiedener *G-Protein Coupled* Rezeptoren (GPCRs; Wadsten *et al.* 2006; Caffrey und Cherezov 2009; Zabara *et al.* 2017a; Zabara *et al.* 2017b). Entsprechend sollen verschiedene Mutanten von *A. thaliana* ETR1 und ETR2 mit und ohne GFP-Derivat *mTurquoise2* (mT2) generiert, exprimiert und über eine Immobilisierende-Metall-Ion-Affinitätschromatographie (IMAC) gereinigt werden. Diese sollen mit verschiedenen für die LCP geeigneten Lipiden und Kristallisation *Screening Kits* kristallisiert werden. Eine ggf. erforderliche Stabilisierung der Rezeptoren wäre über die Zugabe geeigneter Liganden wie z. B. NOP-1 und Cu(I) möglich.

Die Topologie der TMD und die im Modell von Schott-Verdugo *et al.* (2020) und Alphafold vorgeschlagene Orientierung der TMHs soll mithilfe von Elektronenspinresonanz

(EPR) Spektroskopie untersucht werden. Dafür sollen alle natürlich vorkommenden Cysteine in der TMD mittels Polymerase-Kettenreaktion (PCR) entfernt und durch Serine ersetzt werden. Danach sollen anhand des ETR1- Modells an ausgewählten Stellen über Klonierung andere Aminosäuren durch Cysteine in die TMD erneut eingefügt werden. Der Zweck dieser Vorgehensweise besteht darin, die chemische Markierung durch *Methanethiosulfonate Spin Label* (MTSSL), welches spezifisch an Cysteine bindet, für die EPR-Spektroskopie einzusetzen.

Dadurch werden intra- und interhelikale Abstandsmessungen in der TMD möglich. Zudem soll der Einfluss von Kupfer im Zusammenhang mit einer möglichen Konformationsänderung in der TMD evaluiert werden. Die Ergebnisse werden mit den Resultaten des bereits vorhandenen Strukturmodells von Schott-Verdugo *et al.* (2019; Modell 1), sowie dem Strukturmodell, welches mit Alphafold (Jumper *et al.* 2021, Modell 2) erstellt wurde, verglichen.

Ein weiteres Ziel ist die Untersuchung der Kupferkoordination in der TMD. Aus dem Modell von Schott-Verdugo *et al.* (2019) war bekannt, dass die Aminosäurestellen Cystein 65 (C65) und Histidin 69 (H69) für die Kupferkomplexierung verantwortlich sind. Aus dem Strukturmodell wurde abgeleitet, dass die Aminosäuren an den Position Asparaginsäure 25 (D25) und Lysin 91 (K91) eine zusätzliche Stabilisierung bei der Komplexierung des Kupfers haben könnten (Schott-Verdugo *et al.* 2019). Um diese Hypothese experimentell zu überprüfen wurden die Klonierung, Expression und Reinigung entsprechender Mutanten vorgesehen. Zudem sollen der Einfluss der genannten Positionen mithilfe von Kupferbindungsstudien ermittelt werden. Die vorliegende Arbeit befasst sich mit der Analyse der TMD unter Ausnutzung verschiedener Techniken. Als Methoden wurden LCP-Kristallisation, EPR-Spektroskopie und Kupferbindungsstudien eingesetzt.

5 Ergebnisse

5.1 Kartierung der Helixanordnung der Transmembran-Domäne des ETR1-Ethylenrezeptors durch EPR-Spektroskopie

Titel: Mapping the helix arrangement of the reconstituted ETR1 ethylene receptor transmembrane domain by EPR spectroscopy

Autoren: Anandi Kugele, Buket Uzun, Lena Müller, Stephan Schott-Verdugo, Holger Gohlke, Georg Groth und Malte Drescher

Eigener Anteil:

35 % Planung, Durchführung und Auswertung der Experimente:

Veröffentlicht in:

Royal Society of Chemistry advances 12, 04.03.2022, Artikelnummer: 12, Creative Commons Attribution 3.0 Unported Licence

DOI: 10.1039/D2RA00604A

RSC Advances

PAPER

View Article Online
View Journal | View Issue

Cite this: *RSC Adv.*, 2022, **12**, 7352

Mapping the helix arrangement of the reconstituted ETR1 ethylene receptor transmembrane domain by EPR spectroscopy†

Anandi Kugele,[a‡] Buket Uzun,[b‡] Lena Müller,[b] Stephan Schott-Verdugo,[c] Holger Gohlke,[cd] Georg Groth*[b] and Malte Drescher*[a]

The plant ethylene receptor ETR1 is a key player in the perception of the phytohormone and subsequent downstream ethylene signal transmission, crucial for processes such as ripening, senescence and abscission. However, to date, there is sparse structural knowledge about the transmembrane sensor domain (TMD) of ETR1 that is responsible for the binding of the plant hormone and initiates the downstream signal transmission. Sequence information and *ab initio* modelling suggest that the TMD consists of three transmembrane helices. Here, we combined site-directed spin labelling with electron paramagnetic resonance spectroscopy and obtained distance restraints for liposome-reconstituted ETR1_TMD on the orientation and arrangement of the transmembrane helices. We used these data to scrutinize different computational structure predictions of the TMD.

Received 28th January 2022
Accepted 23rd February 2022

DOI: 10.1039/d2ra00604a

rsc.li/rsc-advances

Introduction

Plant hormones (phytohormones) are the key players in integrating developmental signals and responses to the environment. In particular, the gaseous ethylene stimulates several physiological processes such as growth, senescence, pathogen responses, and fruit ripening, and is perceived by the ethylene receptor family.[1] Ethylene sensing leads to suppression of a downstream signalling cascade and subsequent activation of gene expression responsible for ethylene-induced biological responses.[2,3] In *Arabidopsis thaliana* (*A. thaliana*) five ethylene receptor isoforms (ETR1, ERS1, ETR2, ERS2, EIN4) have been identified.[4] They share a conserved modular structure, consisting of an N-terminal ethylene binding transmembrane sensor domain (TMD), a GAF (cGMP-specific phosphodiesterases, adenylyl cyclase and FhlA), and a catalytic transmitter domain;[4–7] ETR1, ETR2 and EIN4 additionally possess a receiver domain at the C-terminus (Fig. 1A).[8] All ethylene receptors are involved in ethylene signalling with partially overlapping roles.[9] However, more detailed structural and mechanistic knowledge is required to answer open questions including receptor output and downstream signalling, which are still largely unknown.

While a structural model of the complete cytosolic domains of receptors ERS1 and ETR1 has been obtained by crystal structure analysis and low-resolution SAXS,[10,11] the structure of the TMD has not been resolved experimentally yet. Notably, the first *ab initio* structural model of the ETR1_TMD was recently predicted and refined by tryptophan substitution scanning mutagenesis (Fig. 1B and C).[12] It is generally agreed, that the hydrophobic TMD monomer is composed of three membrane-spanning α-helices,[12,13] that, besides ethylene sensing,[14] also serve for localization of the ethylene receptor at the endoplasmic reticulum,[15] and for generation of higher-order complexes.[16,17]

In this study, Electron Paramagnetic Resonance (EPR) spectroscopy was introduced as a tool to investigate ethylene receptors, in particular the ETR1_TMD (residues 1–157). EPR spectroscopy in combination with site-directed spin labelling (SDSL) is a valuable tool to monitor protein structure and dynamics in a background-free mode,[18] and has also been applied to membrane proteins.[19–22] We employed a particular EPR technique, namely double electron–electron resonance (DEER) spectroscopy,[23] to determine distance restraints between strategically positioned spin labels in the reconstituted ETR1_TMD. We used these distance restraints to scrutinize currently available computational models of the ETR1_TMD – the dimeric *ab initio* structural model by Schott-Verdugo *et al.*[12]

[a]*Department of Chemistry and Konstanz Research School Chemical Biology (KoRS-CB), University of Konstanz, Universitätsstraße 10, 78457 Konstanz, Germany. E-mail: malte.drescher@uni-konstanz.de*

[b]*Institute of Biochemical Plant Physiology, Heinrich Heine University Düsseldorf, Universitätsstraße 1, 40225 Düsseldorf, Germany. E-mail: georg.groth@hhu.de*

[c]*John von Neumann Institute for Computing (NIC), Jülich Supercomputing Centre (JSC), Institute of Biological Information Processing (IBI-7: Structural Biochemistry), Institute of Bio- and Geosciences (IBG-4: Bioinformatics), Forschungszentrum Jülich GmbH, 52425 Jülich, Germany*

[d]*Institute for Pharmaceutical and Medicinal Chemistry, Heinrich Heine University Düsseldorf, 40225 Düsseldorf, Germany*

† Electronic supplementary information (ESI) available: Experimental details and supplementary figures. See DOI: 10.1039/d2ra00604a

‡ A. K. and B. U. contributed equally.

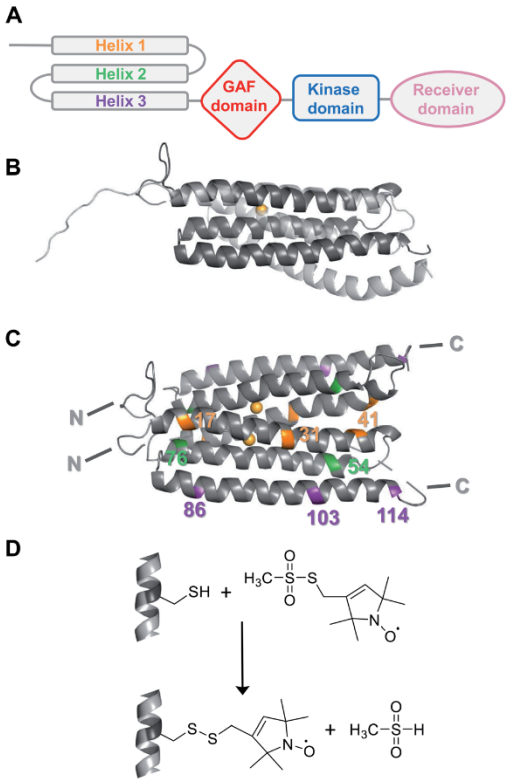

Fig. 1 (A) Schematic organization of the modular structure of an ETR1 monomer. (B) Overlaid structural models of ETR1_TMD as predicted *ab initio* by Schott-Verdugo *et al.* (2019, dark grey) and AlphaFold (2021, light grey). The copper(I) ion included in the *ab initio* model is depicted as light orange sphere. (C) Structural model of the ETR1_TMD dimer as predicted by Schott-Verdugo *et al.* (2019). Residues used in this study for cysteine mutagenesis and spin labelling were highlighted, and the copper(I) ions are depicted as light orange spheres. (D) Spin labelling of cysteines using the methanethiosulfonate spin label (MTSSL) forms the side chain R1.

and the artificial intelligence-derived AlphaFold[24] structural model (UniProt P49333, Fig. 1B).

Results and discussion

To obtain suitable ETR1_TMD constructs for thiol-mediated spin labelling, native cysteines were replaced in the *A. thaliana* ETR1 receptor by serine residues (ETR1_TMD_C4S/C6S/C65S/C99S, referred to as ETR1_ΔC in the following). Mutation of the native cysteines did not perturb the structure of ETR1_TMD (Fig. S12, ESI†). New cysteines for SDSL were installed at strategically positioned sites (Fig. 1C, 3C and S1, ESI†). Based on the knowledge about the membrane-embedded α-helix bundle,[12,13] one single and nine double cysteine-mutants were designed within the three-helix bundle of a monomer (Fig. S1 and S3,† ESI). They allow for distance determinations either within an individual helix (intrahelical) or between the three helices in the ETR1_TMD monomer (interhelical).

After expression in *Escherichia coli* and purification of ETR1_TMD,[12] disulfide bridges were reduced by dithiothreitol (DTT) to enhance subsequent labelling efficiency. Site-directed spin-labelling (SDSL) of cysteine residues with the methanethiosulfonate spin label (MTSSL) was performed in the presence of the detergent *n*-hexadecyl-phosphocholine, resulting in the spin-labelled side chain R1 (Fig. 1D; for detailed procedures see ESI†).[22,25] After removal of excess label, continuous-wave (cw)-EPR spectra of the mutants were recorded. Analysis of spin concentrations revealed no background labelling of ETR1_ΔC and virtually quantitative labelling of the cysteine variants, indicating that the selected residues are well accessible for spin labelling (Fig. S3, ESI†).

ETR1 in its functional form occurs as homo-[16] or heterodimer[26] or as part of larger protein complexes,[27] mediated by disulfide linkage[16] or in a cysteine-independent manner.[17] To assess the potentially dimeric state of our spin-labelled ETR1 constructs, we shock-froze a sample of singly spin-labelled ETR1_ΔC_L17C→R1 in the detergent-containing buffer supplemented with 20% deuterated glycerol. To detect potential intermolecular interactions, we performed a four-pulse DEER measurement, and the form factor exhibited a modulation depth deviant from zero ($\Delta \approx 8\%$, Fig. 2C, grey curve). The modulation depth is an indicator for dipolar interaction. This indicates moderate cysteine-independent interactions between neighboring ETR1 monomers or partial aggregation, even though mainly monomeric ETR1 was confirmed by non-reducing SDS-PAGE (Fig. S4, ESI†). For doubly spin-labelled

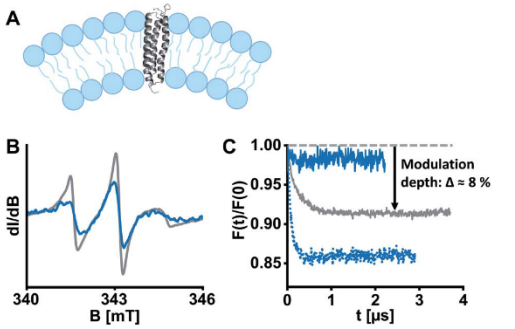

Fig. 2 ETR1 variants were reconstituted into DMPC large unilamellar vesicles for EPR experiments. (A) Schematic liposome cross section with incorporated ETR1. Possible dimer/oligomer formation was omitted in this representation for the sake of clarity. (B) Cw-EPR spectra of ETR1_L17C→R1 before (grey) and after (blue) reconstitution, normalized to the area under the curve. (C) DEER form factors after background subtraction for ETR1_L17C→R1 in detergent-containing buffer (grey, $\Delta \approx 8\%$), after reconstitution (dotted blue, $\Delta \approx 14\%$), and after diamagnetic dilution in combination with reconstitution (solid blue, $\Delta \approx 2\%$). Corresponding DEER raw data is shown in Fig. S11, ESI.†

variants, these interactions would complicate accurate evaluation of distances.

To exclude aggregation and ensure functional and structural integrity, a reconstitution approach in liposomes was pursued (Fig. 2A). Liposomes closely resemble cellular membranes, and have been applied to study membrane proteins by EPR spectroscopy several times.[28] To this aim, we prepared homogenously 100 nm-sized large unilamellar vesicles (LUVs) composed of the phospholipid 1,2-dimyristoyl-*sn*-glycero-3-phosphocholine (DMPC) by extrusion, and then partially solubilized the preformed LUVs with Triton X-100.[29] Afterwards, ETR1_ΔC_L17C→R1 was added to the LUVs in a standard molar lipid-to-protein ratio of 2000. Following stepwise removal of detergents with polystyrene beads, we collected the proteoliposomes by ultracentrifugation. Complete incorporation of ETR1 was confirmed by cw-EPR spectroscopy of the proteoliposome pellet and the supernatant (Fig. S3, ESI†). The spectra further revealed distinct broadening upon incorporation into vesicles, reflecting restricted motion of ETR1 and of the attached spin label (Fig. 2B).

To investigate the effect of reconstitution, DEER of the singly labelled variant ETR1_ΔC_L17C→R1 was measured. Interestingly, the modulation depth had even increased to $\Delta \approx 14\%$ (Fig. 2C, dotted blue curve), indicating intermolecular interactions. This implies that multimolecular species are also present in the proteoliposomes, complicating the evaluation of DEER measurements. Only when spin-labelled proteins were diamagnetically diluted with ETR1_ΔC prior to reconstitution (in a ratio of one labelled variant plus five ETR1_ΔC), the modulation depth was reduced to $\Delta \approx 2\%$ (Fig. 2C, solid blue curve). Under these conditions, multimolecular species such as oligomers consisting of ETR1_ΔC_L17C→R1 and ETR1_ΔC are still formed. The combination of diamagnetic dilution and reconstitution, however, sufficiently prevents detecting intermolecular spin–spin interactions and allows resolving only intramolecular distances. Notably, in this approach a superposition of distance distributions from monomers and dimers is measured, and the conformation of a monomer within a dimer may be different then the conformation of the monomeric ETR1.

In the next step, DEER traces were recorded for doubly labelled ETR1 diamagnetically diluted in proteoliposomes.

For verification of helix integrity, at first distance distributions between two labelled sites per helix were measured (ETR1_ΔC_L17C/Y41C→R1, ETR1_ΔC_V54C/F76C→R1 and ETR1_ΔC_V86C/L103C→R1). The modulation depths were in the expected range ($\Delta \approx 39$–46%, Fig. S6A, ESI†). To provide a reference for assessing experimentally derived distance distributions, *in silico* simulations based on current structural models of ETR1 (ref. 12 and 24) were generated using the Multiscale Modeling of Macromolecules[30] software (MMM). *In silico* labelling of sites 54 and 76 was sterically hindered (Fig. S9B, ESI†), which resulted in an artificially narrowed simulation (Fig. 3A); that was, however, not the case to such extent when taking the AlphaFold model[24] as basis (Fig. 3A and S9B, ESI†). Altogether, for the three intrahelical distance restraints the shape of the distributions and the mean distance

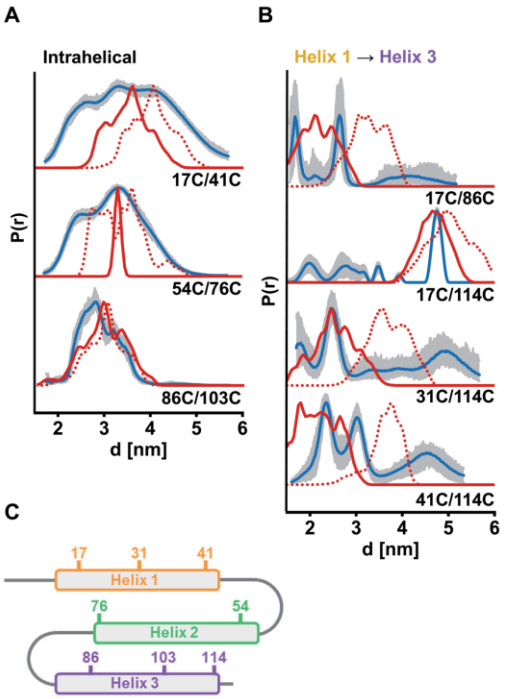

Fig. 3 Experimental distance distributions in the ETR1_TMD obtained by DEER measurements (blue) with validation (grey area). Simulated distance distributions by MMM based on the model by Schott-Verdugo *et al.* (2019, red) and by AlphaFold (2021, red dotted) are indicated. Distance distributions were scaled to their maximum. (A) Intrahelical distances. (B) Interhelical distances between helix 1 and helix 3. (C) Schematic representation of the ETR1_TMD and spin-labelled sites used for DEER distance determinations. DEER raw data and interhelical distances between helix 1 and helix 2 are given in Fig. S6, ESI.†

conform well to the expectation, although broader in shape than expected for inherently rigid α-helices (Fig. 3A). Especially for helix 1 this suggests, that it is not as structured as expected and as proposed by the models.

Moreover, interhelical distances were determined to address the topological arrangement and the orientation of the α-helices towards each other. However, the data quality for distance distributions measured between helices 1 and 2 was too low to reliably analyse the extracted distances (ETR1_ΔC_L17C/V54C→R1 and ETR1_ΔC_A31C/F76C→R1; Fig. S6B, ESI†). However, the raw data do indicate long and broad distance distributions instead of the expected short distances. Moreover, the modulation depth of these measurements was reduced to $\Delta \approx 12\%$ (Fig. S6B, ESI†), which may originate from distances too long or too short (approx. <1.8 or >5.2 nm under our experimental conditions) to be resolved by the acquired DEER traces. By cw measurements at 120 K (ref. 31) such short distances were excluded for ETR1_ΔC_L17C/V54C→R1 (Fig. S10†). Hence, the observed

DEER data could be the result of displacement of helix 2 with respect to Schott-Verdugo *et al.*[12] enabled by the flexible loops (schematically represented in Fig. 3C). The AlphaFold model also supports such a displacement.

The most significant differences between the two model structures are visible in the localization of helix 3 with respect to helix 1 (Fig. 1B). To assess this experimentally, we focused on measurements between helices 1 and 3 (ETR1_ΔC_L17C/V86C→R1, ETR1_ΔC_L17C/S114C→R1, ETR1_ΔC_A31C/S114C→R1 and ETR1_ΔC_Y41C/S114C→R1). In this series of data, especially for ETR1_ΔC_L17C/S114C→R1, the width of the distance distribution cannot be reliably extracted due to short length of the dipolar evolution time,[32] which is typical for DEER measurements in membranes.[28] However, regarding the main distance, measurements between helices 1 and 3 are in good agreement with the *ab initio* model (Fig. 3B). The AlphaFold model exhibits a looser and less parallel arrangement of the helices (Fig. 1B and S9A, ESI†), and consequently tends to longer distances (Fig. 3B).

Copper(I) is an essential cofactor to mediate high-affinity ethylene binding[33,34] and was included in the *in silico* model,[12] but absent in our experiments so far. In the field of ethylene receptors there are still open questions regarding transfer routes and coordination of copper(I).[1,35] We reasoned that bound copper(I) might have a stabilizing impact on the structure of ETR1. Consequently, we transferred copper(I) from the bicinchoninic acid (BCA)-based BCA_2-Cu(I) complex (Fig. S7A, ESI†) to selected ETR1 variants as described by Schott-Verdugo *et al.*[12] (with slight changes to protect the spin labels, see ESI†), before removing excess copper(I). To determine the copper-to-protein stoichiometry, ETR1_TMD was denatured to release the copper(I). These ions were trapped in the BCA_2–Cu(I) complex and quantified spectrophotometrically by measuring the absorption of the complex at 562 nm.[12] In analogy to previous findings,[12,36] our experiment revealed effective loading of approx. 0.75–0.97 copper(I) per ETR1 monomer (Fig. 4A and S7, ESI†). After reconstituting the copper-loaded variants, cw-EPR spectra (Fig. 4B) as well as the obtained DEER data (Fig. 4C) overlaid with the data acquired in absence of copper(I). This means, that no global changes in the ETR1 structure upon copper(I) loading were observed.

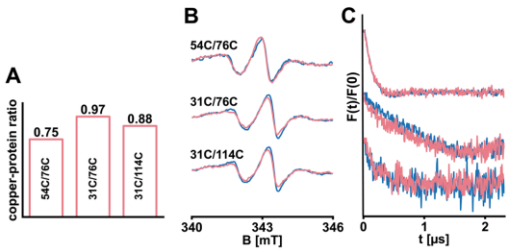

Fig. 4 Selected ETR1 variants were loaded with copper(I). (A) The copper-to-protein ratio was determined spectrophotometrically. (B) Cw-EPR spectra recorded after diamagnetic dilution and reconstitution of samples with (pink) and without (blue) copper(I). (C) Corresponding DEER-derived form factors after background subtraction, scaled to the modulation depth. DEER raw data is shown in Fig. S8, ESI.†

Conclusions

In summary, our data give rise to four key findings regarding the structure of the ETR1_TMD. First, the experimental distance restraints are altogether in better agreement with the *ab initio* structural model[12] than with the AlphaFold[24] prediction. Second, intrahelical flexibility is higher than expected from rigid models under the condition of sample preparation. Third, our data suggest displacement of helix 2 towards the C-terminal direction enabled by loop flexibility. Fourth, loading of the ETR1_TMD with copper(I) does not induce significant conformational changes.

To summarize, we have established an SDSL-EPR approach to study the TMD of ETR1, constituting a complementary tool to evaluate its structural conformation. This study reveals large potential to investigate ETR1 in the presence of its various interacting partners and represents a valuable building block towards an in-depth mechanistic understanding of ethylene signalling in plants.

Conflicts of interest

There are no conflicts to declare.

Acknowledgements

This work was funded by the Deutsche Forschungsgemeinschaft (DFG, German Research Foundation) project no. 267205415/CRC 1208 grant to GG (TP B06) and HG (TP 03).

Notes and references

1 Q. Ma and C.-H. Dong, *Plant Growth Regul.*, 2021, **93**, 39–52.
2 A. B. Bleecker, M. A. Estelle, C. Somerville and H. Kende, *Science*, 1988, **241**, 1086–1089.
3 A. N. Stepanova and J. R. Ecker, *Curr. Opin. Plant Biol.*, 2000, **3**, 353–360.
4 R. C. O'Malley, F. I. Rodriguez, J. J. Esch, B. M. Binder, P. O'Donnell, H. J. Klee and A. B. Bleecker, *Plant J.*, 2005, **41**, 651–659.
5 C. Chang, S. F. Kwok, A. B. Bleecker and E. M. Meyerowitz, *Science*, 1993, **262**, 539–544.
6 J. Hua, C. Chang, Q. Sun and E. M. Meyerowitz, *Science*, 1995, **269**, 1712–1714.
7 H. Sakai, J. Hua, Q. G. Chen, C. Chang, L. J. Medrano, A. B. Bleecker and E. M. Meyerowitz, *Proc. Natl. Acad. Sci. U.S.A.*, 1998, **95**, 5812–5817.
8 J. Ciardi and H. Klee, *Ann. Bot.*, 2001, **88**, 813–822.
9 A. Theologis, *Curr. Biol.*, 1998, **8**, R875–R878.
10 H. Mayerhofer, S. Panneerselvam, H. Kaljunen, A. Tuukkanen, H. D. Mertens and J. Mueller-Dieckmann, *J. Biol. Chem.*, 2015, **290**, 2644–2658.

11 H.-J. Müller-Dieckmann, A. A. Grantz and S.-H. Kim, *Structure*, 1999, **7**, 1547–1556.
12 S. Schott-Verdugo, L. Müller, E. Classen, H. Gohlke and G. Groth, *Sci. Rep.*, 2019, **9**, 1–14.
13 W. Wang, J. J. Esch, S.-H. Shiu, H. Agula, B. M. Binder, C. Chang, S. E. Patterson and A. B. Bleecker, *Plant Cell*, 2006, **18**, 3429–3442.
14 G. E. Schaller and A. B. Bleecker, *Science*, 1995, **270**, 1809–1811.
15 Y.-F. Chen, M. D. Randlett, J. L. Findell and G. E. Schaller, *J. Biol. Chem.*, 2002, **277**, 19861–19866.
16 G. E. Schaller, A. N. Ladd, M. B. Lanahan, J. M. Spanbauer and A. B. Bleecker, *J. Biol. Chem.*, 1995, **270**, 12526–12530.
17 M. Berleth, N. Berleth, A. Minges, S. Hänsch, R. C. Burkart, B. Stork, Y. Stahl, S. Weidtkamp-Peters, R. Simon and G. Groth, *Front. Plant Sci.*, 2019, **10**, 726.
18 P. Roser, M. J. Schmidt, M. Drescher and D. Summerer, *Org. Biomol. Chem.*, 2016, **14**, 5468–5476.
19 M. A. Hemminga and L. Berliner, *ESR spectroscopy in membrane biophysics*, Springer Science & Business Media, 2007.
20 E. Bordignon and S. Bleicken, *Biochim. Biophys. Acta, Biomembr.*, 2018, **1860**, 841–853.
21 E. Bordignon and H.-J. Steinhoff, in *ESR spectroscopy in membrane biophysics*, Springer, 2007, pp. 129–164.
22 C. Altenbach, T. Marti, H. G. Khorana and W. L. Hubbell, *Science*, 1990, **248**, 1088–1093.
23 G. Jeschke, *Annu. Rev. Phys. Chem.*, 2012, **63**, 419–446.
24 J. Jumper, R. Evans, A. Pritzel, T. Green, M. Figurnov, O. Ronneberger, K. Tunyasuvunakool, R. Bates, A. Žídek and A. Potapenko, *Nature*, 2021, **596**, 583–589.
25 E. Bordignon, in *EPR Spectroscopy*, Springer, 2011, pp. 121–157.
26 Z. Gao, C.-K. Wen, B. M. Binder, Y.-F. Chen, J. Chang, Y.-H. Chiang, R. J. Kerris, C. Chang and G. E. Schaller, *J. Biol. Chem.*, 2008, **283**, 23801–23810.
27 Y.-F. Chen, Z. Gao, R. J. Kerris III, W. Wang, B. M. Binder and G. E. Schaller, *PLoS One*, 2010, **5**, e8640.
28 I. D. Sahu and G. A. Lorigan, *Biomolecules*, 2020, **10**, 763.
29 J.-L. Rigaud and D. Lévy, in *Methods in Enzymology*, Academic Press, 2003, vol. 372, pp. 65–86.
30 G. Jeschke, *Protein Sci.*, 2018, **27**, 76–85.
31 N. Le Breton, T. Adrianaivomananjaona, G. Gerbaud, E. Etienne, E. Bisetto, A. Dautant, B. Guigliarelli, F. Haraux, M. Martinho and V. Belle, *Biochim. Biophys. Acta, Bioenerg.*, 2016, **1857**, 89–97.
32 S. G. Worswick, J. A. Spencer, G. Jeschke and I. Kuprov, *Sci. Adv.*, 2018, **4**, eaat5218.
33 F. I. Rodriguez, J. J. Esch, A. E. Hall, B. M. Binder, G. E. Schaller and A. B. Bleecker, *Science*, 1999, **283**, 996–998.
34 C. Hoppen, L. Müller, S. Hänsch, B. Uzun, D. Milić, A. J. Meyer, S. Weidtkamp-Peters and G. Groth, *Sci. Rep.*, 2019, **9**, 1–11.
35 C. Hoppen and G. Groth, *Plant Signal. Behav.*, 2020, 1716512.
36 A. B. Bleecker, J. J. Esch, A. E. Hall, F. I. Rodriguez and B. M. Binder, *Philos. Trans. R. Soc. London, Ser. B*, 1998, **353**, 1405–1412.

Electronic Supplementary Material (ESI) for RSC Advances.

Supporting Information for "Mapping the helix arrangement of the reconstituted ETR1 ethylene receptor transmembrane domain by EPR spectroscopy"

Anandi Kugele,‡ Buket Uzun,‡ Lena Müller, Stephan Schott-Verdugo, Holger Gohlke, Georg Groth* and Malte Drescher*

Table of Contents

Material and Methods

Expression and purification

Cloning of ETR1_TMD mutants, expression in *E. coli* and purification were performed as described before.[1] All oligonucleotides used for cloning are given in Figure S2.

Spin labelling

A 100 mM stock solution of MTSSL (*S*-[1-oxyl-2,2,5,5-tetramethyl-2,5-dihydro-1*H*-pyrrol-3-yl] methyl methanesulfonothioate; SIGMA) in DMSO (SIGMA) was prepared, aliquoted and stored at -80 °C. A 1 M DTT (SIGMA) stock solution was prepared in MilliQ-water, aliquoted and stored at -20 °C.
ETR1 mutants were diluted with ETR1 buffer (50 mM TRIS (SIGMA), 200 mM NaCl (Fisher Scientific), pH 8) to 30 µM, and 1 vol-% DTT stock solution was added to reduce cysteine bridges. Samples were incubated at 25 °C and 500 rpm for 1 h in an Eppendorf ThermoMixer. DTT was removed in spin filters (Amicon Ultra-0.5 mL Centrifugal Filters, 3K cutoff, Merck) by washing 12 times with ETR1 buffer at 14.000 g and 10 °C. An appropriate volume of ETR1 buffer supplemented with 0.015 % hexadecylphosphocholine (Fos-choline 16, Glycon) was added to yield 30 µM of ETR1 for spin labelling. Samples were spin labelled with a 40-fold molar excess of MTSSL[2] overnight at 4 °C and 600 rpm. Residual MTSSL was removed by washing 12 times with ETR1 buffer in spin filters as described above. After sample collection, room-temperature cw-EPR spectra were recorded to ensure complete labelling and sufficient removal of excess MTSSL. ETR1 concentration was determined photometrically with the use of an Eppendorf BioPhotometer D30 via absorption at 280 nm ($A_{280/1mm}$) using the extinction coefficients given in the table below (using ETR1 buffer as blank). Extinction coefficients were determined with the Expasy tool ProtParam.[3] Samples containing 20 vol-% glycerol (SIGMA) as cryoprotectant were frozen at -80 °C until reconstitution.

Mutant	**Molar extinction coefficient ε [M^{-1} cm^{-1}]**	**Molecular weight MW [Da]**
ETR1_ΔC	23950	20483.81
ETR1_ΔC_L17C	23950	20473.79
ETR1_ΔC_V54C/F76C	24075	20443.78
ETR1_ΔC_L17C/V54C	24075	20477.8
ETR1_ΔC_L17C/V86C	24075	20477.8
ETR1_ΔC_L17C/S114C	24075	20489.85
ETR1_ΔC_L17C/Y41C	22585	20413.75
ETR1_ΔC_V86C/L103C	24075	20477.8
ETR1_ΔC_Y41C/S114C	22585	20439.84
ETR1_ΔC_A31C/F76C	24075	20471.83
ETR1_ΔC_A31C/S114C	24075	20531.93

Preparation of Large Unilamellar Vesicles (LUVs)

For one DEER sample, 15 mg (22.14 µmol) of DMPC (1,2-dimyristoyl-*sn*-glycero-3-phosphocholine, Avanti Polar Lipids) with a molar mass of M = 677.5 g/mol were dissolved in 1.5 mL chloroform (spectroscopic grade, SIGMA) in a glass tube. While rotating by hand, the chloroform was removed under a nitrogen stream, and the resulting lipid layer was evaporated in vacuum overnight. The lipids were rehydrated in 3 mL ETR1 buffer to yield a concentration of 5 mg/mL, sonicated, and vortexed for 10 min, before incubation in the dark for 45 min at room temperature. Additionally, five freeze-thaw cycles were performed to form large unilamellar vesicles (LUVs). 100 nm-sized LUVs were then prepared by 19-fold extrusion through a layer of 100 nm polycarbonate film (Whatman) in a handheld extruder (Avanti, Polar Lipids). DLS was measured as described below to confirm size and homogeneity (DLS data is shown in Figure S5). Vesicles were stored for usually one day in the fridge until used for reconstitution.

Reconstitution

To prepare diamagnetically diluted samples, spin-labelled mutants were mixed with ETR1_ΔC in a molar ratio of 1:5. This corresponds to 1.83 nmol spin-labelled ETR1 plus 9.15 nmol ETR1_ΔC.
For one protein sample (sufficient for one cw-EPR and one DEER measurement), one portion of LUVs was prepared as described above (from 15 mg DMPC in 3 mL volume). LUVs were mixed with 191 µL of 10 % Triton X-100 (SIGMA) solution (predissolved in ETR1 buffer) for partial solubilization of the LUVs,[4] and incubated for 1 h at 22 °C without shaking. The LUVs were then merged with the ETR1 mixture in a standard lipid-to-protein ratio of 80:1 (w/w; corresponding to a molar lipid-to-protein ratio of approx. 2000), and divided into two 2 mL microcentrifuge tubes. The mixture was incubated for 1 h at 22 °C without shaking in the dark. For detergent removal, the adsorption technique using Bio-Beads SM-2 was pursued. For this purpose, 0.5 g of Bio-Beads SM-2 (BIO-RAD) per microcentrifuge tube (1 g per sample) were washed three times with methanol (SIGMA, spectroscopic grade), followed by five times washing with MQ-H_2O. The beads were stored in water and used the same day. The beads were added to the samples in four portions with a small spoon, followed by vigorous shaking for 1 h, 2 h, 2 h, and overnight. The samples became turbid during this process, as proteoliposomes are formed. The next day, the Bio-Beads SM-2 were removed in empty 0.8 mL Pierce centrifuge columns (Thermo Fisher Scientific), and the supernatant was collected in 1.5 mL ultracentrifugation tubes (Beckman Coulter Microfuge Tube Polypropylene). Proteoliposomes were collected by ultracentrifugation in a Beckman Coulter Optima MAX-XP ultracentrifuge for 1 h at 100.000 g and 4 °C. The pellet was resuspended in approx. 5 µL D_2O (SIGMA), and cw-EPR spectra of the pellet and the supernatant were measured to ensure that the nitroxide signal is found only in the pellet (Figure S3). 48 µL of the sample were mixed with 12 µL of deuterated glycerol (≙ 20 vol-%) and filled into 3 mm outer diameter quartz tubes. Samples were shock-frozen in liquid nitrogen and stored at - 80 °C until DEER measurement. Additionally, DLS was measured as described below to confirm size and homogeneity (DLS data is shown in Figure S5).

Dynamic Light Scattering (DLS)

Vesicle size was confirmed by Dynamic light scattering (DLS) in a Zetasizer nano ZS spectrometer, Malvern Instruments Ltd., at 298 K. For this purpose, 3 µL of LUVs or 1.5 µL of proteoliposomes,

respectively, were dispensed in 1 mL ETR1 buffer and filled into a 1 cm disposable polycarbonate cuvette. A refractive index of 1.44 was used and 10 scans each were accumulated. Data is shown in Figure S5.

Continuous wave (cw)-EPR

Cw-EPR spectra at room temperature (approx. 22 °C) were recorded at a Bruker EMXnano X-band continuous wave EPR spectrometer (with a cylindric cavity mode TM1110) without temperature regulation. Typical sample volumes of 30 µL were filled into a glass capillary (HIRSCHMANN ringcaps; inner diameter 1.02 mm). Spectra were recorded at a modulation amplitude of 1 G, microwave attenuation 15 dB corresponding to a power of 3.162 mW, and a sweep width of 200 G. 10 scans of 80 sec scan time each for spin-labelled protein and 30 scans of reconstituted samples were accumulated to improve the signal-to-noise ratio. Quantitative spin concentrations of samples were obtained with the use of the built-in EMXnano reference-free spin counting module (Xenon software, Bruker). The labelling efficiency was estimated as the ratio of spin/protein. Spectra were analyzed with MATLAB R2019b (The MatWorks, Inc. 3 Apple Hill Drive, Natick, MA 01760-2098, USA) and plotted with OriginLab 2018G (OriginLab Corporation, Northampton, MA, USA). Normalized spectra were obtained by dividing the spectra by area.
Cw-EPR spectra of selected mutants were recorded at 120 K to detect short distances < 2 nm (Figure S10).[5] Therefore, a Magnettech ESR5000 X-band spectrometer (Bruker) equipped with a TC H04 temperature controller was utilized. Measurements were acquired with 35 dB microwave attenuation, 0.35 mT modulation and 60 sec sweep time. 250 Scans each were accumulated to increase the signal-to-noise ratio. Spectra were baseline-corrected in Origin 2018.

Double Electron-Electron Resonance (DEER)

Distance measurements were performed in Q-band (34 GHz) using an Elexsys E580 spectrometer (Bruker Biospin) operating with a SpinJet AWG unit (Bruker Biospin) and a 150 W pulsed traveling-wave tube (TWT) amplifier (Applied Systems Engineering). The spectrometer is equipped with the EPR Flexline helium recirculation system (CE-FLEX-4K-0110, Bruker Biospin, ColdEdge Technologies) including a cold head (expander, SRDK-408D2) and a F-70H compressor (SHI cryogenics), controlled by an Oxford Instruments Mercury ITC. Samples were measured at 50 K.
For measurements of diamagnetically diluted proteoliposomes, 4-pulse DEER with a Gaussian observer pulse (pulse length optimized for every sample, ranging from $\pi_{observer}$ = 48-76 ns) and a hyperbolic secant HS(1,1) pump pulse[6] (π_{pump} = 100 ns) were employed. A frequency offset of minus 80 MHz (resulting in 33.92 GHz) was used for observer pulses. A shot repetition rate of 4 ms and the eight-step phase cycle [x](x)x_px as proposed by Tait and Stoll[7] were employed. DEER measurements were typically recorded for 22 h (up to 50 h for samples with low echo intensity) to improve the signal-to-noise ratio.

The data were processed using MATLAB R2018a and the DeerAnalysis2019 software[8]. Distance distributions were obtained by a one-step procedure as recommended by Schiemann et al.,[9] using artificial neural network analysis (DEERNet)[10].

Copper(I) loading

Buffer containing 50 mM TRIS, 200 mM NaCl and bicinchoninic acid (BCA, 2.5 mM; for BCA structure see Figure S7A) at pH 7.5 was degassed in an excicator under constant stirring to prevent oxidation of copper(I). Note that the addition of ascorbate as reducing agent would destroy nitroxide signals of spin-labelled proteins. Cu(I) (1.2 mM) was then quickly dissolved in this buffer, and spin-labelled ETR1_TMD mutants were saturated until deeply purple-stained. Samples were incubated for 5 min, before excess BCA_2-Cu(I) was removed in PD-10 columns. Samples were concentrated in spin filters (Amicon Ultra-0.5 mL Centrifugal Filters, 3K cutoff, Merck) and immediately used to determine copper-protein stoichiometry and for reconstitution, as described above. Samples loaded with Cu(I) should not be stored longer than 1 week at -80 °C containing 20 vol-% glycerol.
To determine copper-protein stoichiometries, samples were denatured with SDS (20 % w/v) and cooked at 95 °C for 20 min in the presence of 2 mM BCA to trap the Cu(I) released from the ETR1_TMD. Absorbance of the BCA_2-Cu(I) complex was then measured by absorption at 562 nm in a microplate reader (SPARK, Tecan). Cu(I) concentration was quantified by using a standard curve of BCA_2-Cu(I) (Figure S7).

Circular Dichroism (CD) Spectroscopy

CD spectra (Figure S12) of wild type and cysteine-free mutant of ETR1_TMD were recorded from 200 - 250 nm at room temperature using a Jasco-715 spectropolarimeter (Jasco GmbH, Gross-Umstadt, Germany). Both proteins were provided at 0.3 mg/ml concentration in a buffer consisting of 50 mM potassium phosphate buffer and 0.015 % (w/v) Fos-choline 16 pH 8.0. A total of 10 spectra were accumulated for each sample at 0.1 nm step resolution, 50 nm/min scan speed and 1 nm bandwidth. A cylindrical quartz cuvette (Hellma GmbH & Co. KG, Muellheim) with a path length of 1 mm and a volume of 200 µl was used in these measurements. Secondary structure was computed from the CD data obtained of both proteins by the BeStSel web server.[11-13]

Supplementary Figures

Figure S1: Primary sequence of the ETR1_TMD

```
        10         20         30         40         50
MEVCNCIEPQ WPADELLMKY QYISDFFIAI AYFSIPLELI YFVKKSAVFP

        60         70         80         90        100
YRWVLVQFGA FIVLCGATHL INLWTFTTHS RTVALVMTTA KVLTAVVSCA

       110        120        130        140        150
TALMLVHIIP DLLSVKTREL FLKNKAAELD REMGLIRTQE ETGRHVRMLT

    157
HEIRSTL
```

Amino acid sequence of residues 1-157 of wildtype *A. thaliana* ETR1_TMD (taken from UniProt P49333, ETR1_ARATH). Native cysteine residues marked in bold black were replaced with serine in this study to ensure background-free spin labelling. The residues marked in orange (helix 1), green (helix 2), and purple (helix 3) per mutant were (in different combinations) replaced with cysteine for EPR measurements.

Figure S2: Oligonucleotides used for site-directed mutagenesis

Primer	Sequence
C4S_C6S_forward	GAAGTCAGCAATAGTATTGAACCGC
C4S_C6S_reverse	CATATGACGACCTTCGATATGGC
L17C_forward	CATCTCCGATTTCTTCATTGCGATT
L17C_reverse	TATTGGTATTTCATACACAATTCATCCG
A31C_forward	TCCTCTTGAGTTGATTTACTTTGTGAA
A31C_reverse	ATCGAAAAATAGCAAATCGCAATGAAG
Y41C_forward	AATCAGCCGTGTTTCCGTATAGAT
Y41C_reverse	TCTTCACAAAGCAAATCAACTCAAGAG
V54C_forward	TCCGTATAGATGGTGTCTTGTTCAGTT
V54C_reverse	AACACGGCTGATTTCTTCACAAAGTAA
C65S_forward	TTTTATCGTTCTTTCTGGAGCAACTCATCT
C65S_reverse	GCACCAAACTGAACAAGTACCCATCTATAC
F76C_forward	AACTTATGGACTTGCACTACGCATTCG
F76C_reverse	GTTCTTTCTGGAGCACCTCATCTTATT
V86C_forward	ACCGTGGCGCTTTGTATGACTACCG
V86C_reverse	TCTCGAATGCGTAGTGAAAGTCCATAA
C99S_forward	GTTAACCGCTGTTGTCTCGTCTGCTACT
C99S_reverse	ACCTTCGCGGTAGTCATCACAAGC
L103C_forward	CGTCTGCTACTGCGTGTATGCTTGTTC
L103C_reverse	AGACAACAGCGGTTAACACCTTCG
S114C_forward	TCCTGATCTTTTGTGTGTTAAGACTCG
S114C_reverse	ATAATATGAACAAGCATCAACGCAGTAG

Figure S3: Cw-EPR spectra before and after reconstitution

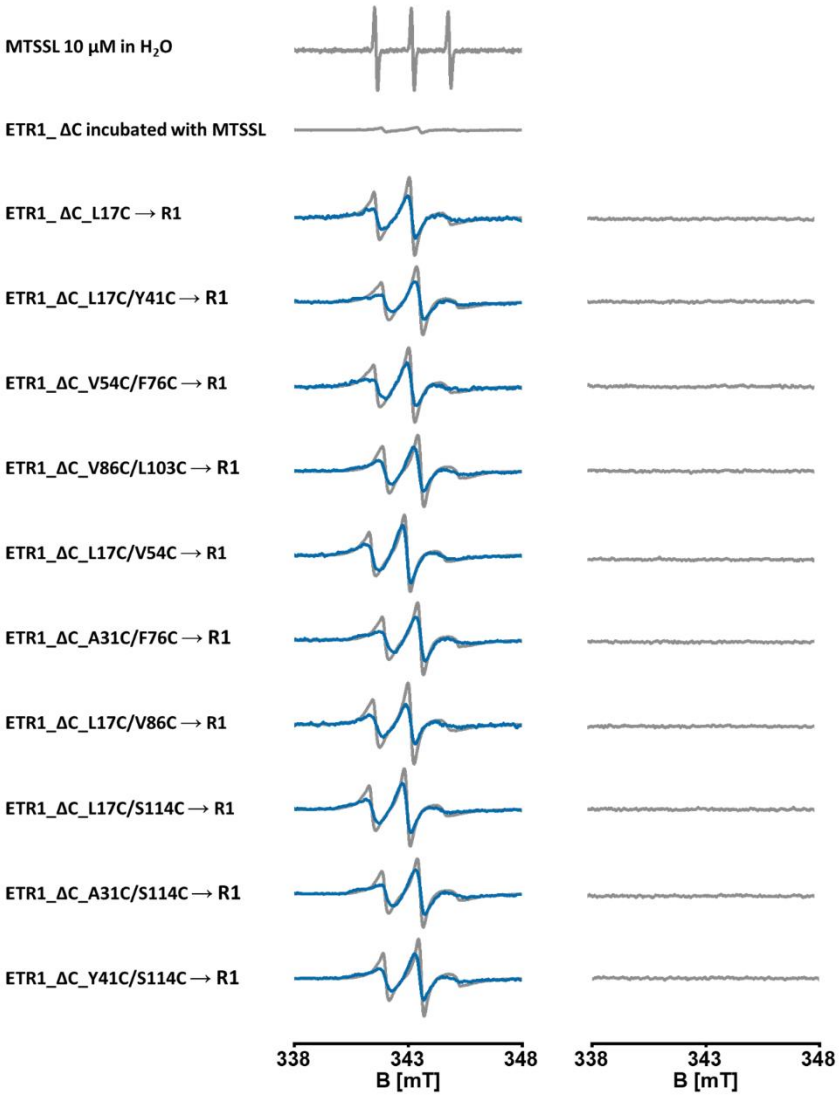

Room-temperature cw-EPR spectra of the unbound MTSSL or indicated ETR1 mutants. Left column: Spectra of the protein-detergent complex after spin labelling (grey), and after diamagnetic dilution and reconstitution (blue). The corresponding spectra on the left were normalized to the area, respectively. Right column: Spectra of the supernatant after ultracentrifugation (grey). No remaining nitroxide signal was found in the supernatant.

S8

Figure S4: Non-reducing PAGE

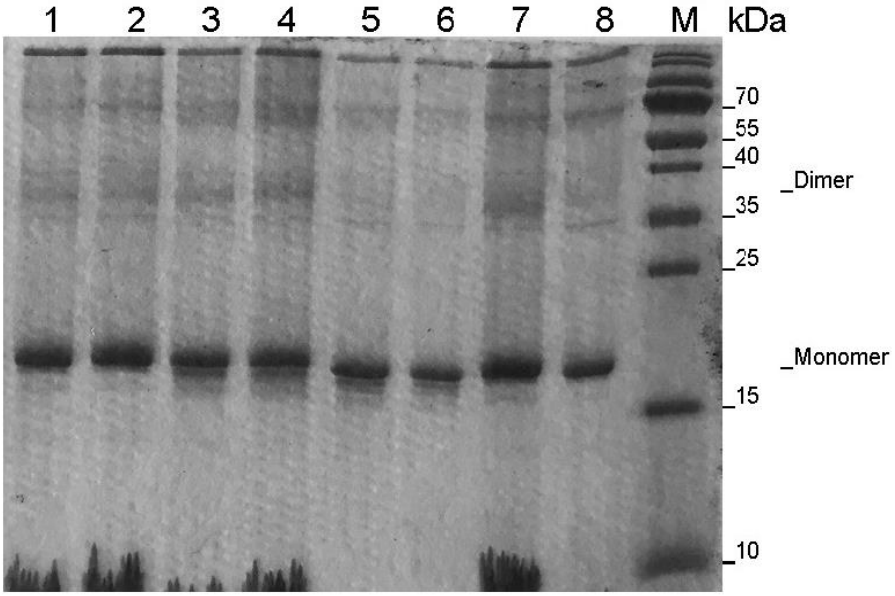

Non-reducing blue native PAGE of ETR1_TMD variants. Different combinations of spin labels (MTSSL and 3-maleimido-PROXYL) and reducing agents (TCEP and DTT) were probed for optimization of spin labelling. Lane 1-4: ETR1_ΔC_L17C, Lane 5-8: ETR1_ΔC_L17C/V54C. Lane 1 and 5: DTT + MTSSL, Lane 2 and 6: TCEP + PROXYL, Lane 3 and 7: DTT + PROXYL, Lane 54 and 8: TCEP + MTSSL. For all conditions, only insignificant dimer formation was found. Final spin labelling conditions were therefore optimized in terms of spin labelling degree. Proteins after preferred spin labelling conditions (use of DTT and MTSSL) are shown in lanes 1 and 5. Molecular weight markers for monomers and dimers are indicated.

Figure S5: DLS data of LUVs and proteoliposomes

A

Empty DMPC LUVS after extrusion

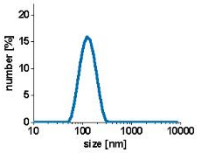

B

Proteoliposomes

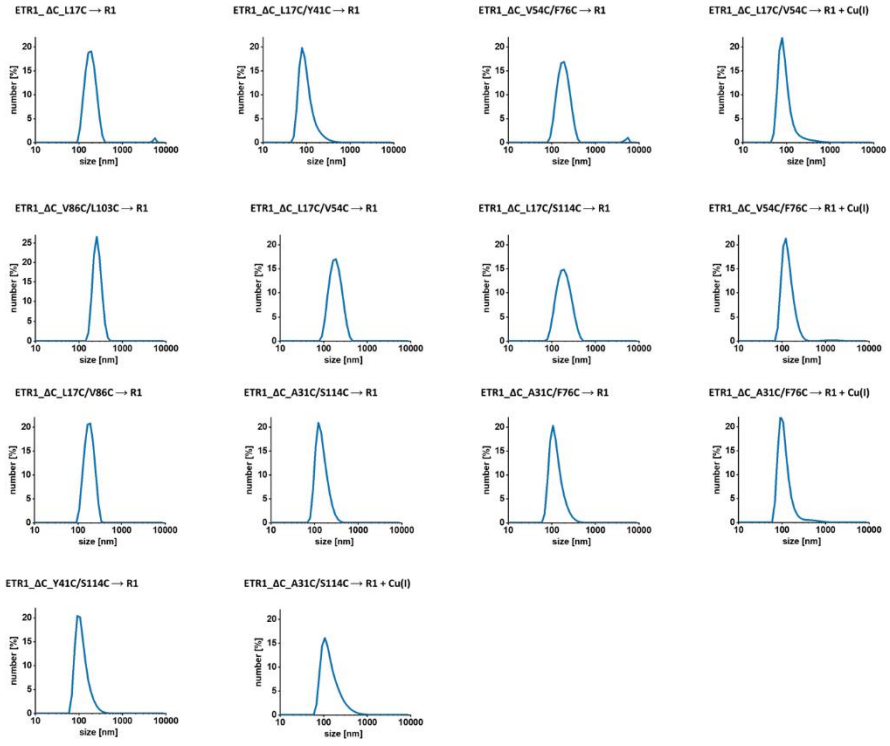

Dynamic light scattering (DLS) spectra of vesicles used in this study. The vesicle size of approx. 100 nm was confirmed by the DLS intensity. (A) DMPC vesicles extruded to 100 nm. (B) Proteoliposomes containing a mixture of spin-labelled ETR1 and ETR1_ ΔC for diamagnetic dilution.

Figure S6: DEER data of double mutants

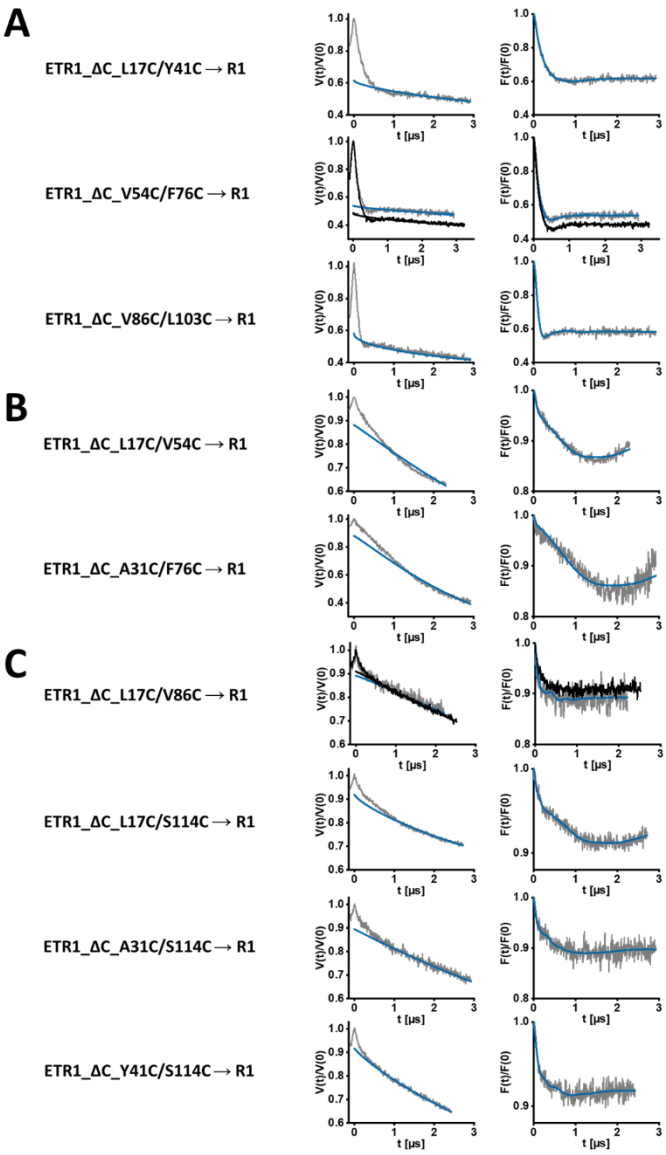

Evaluation of DEER measurements of the indicated doubly spin-labelled ETR1_TMD variants diamagnetically diluted and reconstituted. (A) intrahelical distances, (B) helix 1 ⟶ helix 2, (C) helix 1 ⟶ helix 3.Data were processed using MATLAB R2019b, the DeerAnalysis 2018a software[8], and DEERNet[10] 2019. Replicates of independently prepared samples are shown in black. Left column: Primary DEER signal (grey) and background fit (blue) as obtained by DEERNet. Right column: Background-corrected form factor (grey) and fit (blue) as obtained by DEERNet. Corresponding distance distributions for data from (A) and (C) are shown in Figure 3, main text.

S11

Figure S7: Determination of copper-protein-stoichiometry

A

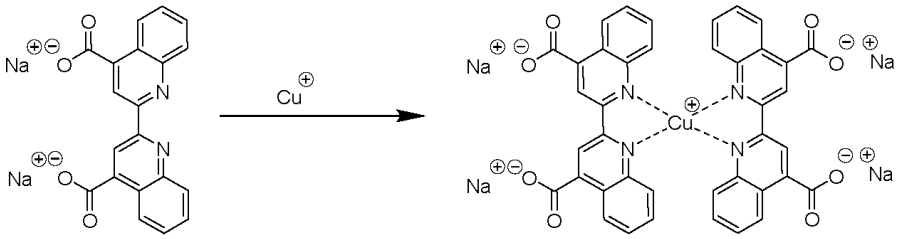

B

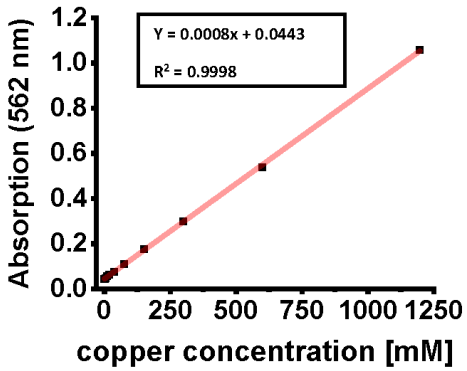

C

Mutant	Protein concentration [µM]	Cu(I) concentration [µM]	Cu(I)/protein ratio
ETR1_ΔC_V54C/F76C → R1	109	82	0.75
ETR1_ΔC_L17C/V54C → R1	521	197	0.38
ETR1_ ΔC_A31C/F76C → R1	105	102	0.97
ETR1_ ΔC_A31C/S114C → R1	146	128	0.88

A: Structural formula of Bicinchoninic acid (BCA). BCA forms a complex with Cu(I), which exhibits a strong absorption signal at 562 nm.[1]

B: Calibration curve of BCA_2-Cu(I).

C: Determination of copper-protein-stoichiometries of the indicated spin-labelled ETR1 variants.

Figure S8: DEER data of copper(I)-loaded variants

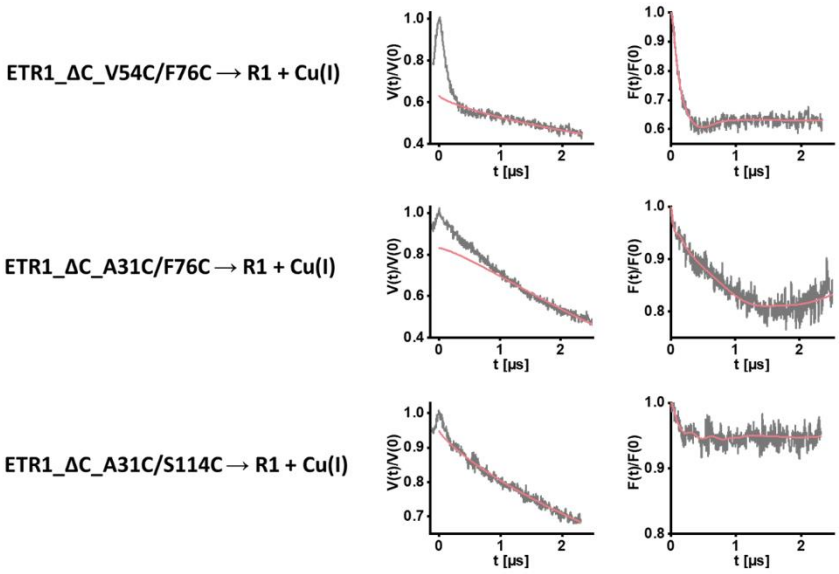

Evaluation of DEER measurements of the indicated doubly spin-labelled ETR1_TMD variants, loaded with Cu(I), diamagnetically diluted and reconstituted. Data were processed using MATLAB R2018a, the DeerAnalysis2019 software[8] and DEERNet[10]. Left column: Primary DEER signal (grey) and background fit (pink). Right column: Background-corrected form factor (grey) and fit (pink). Overlays of the form factors of samples with and without Cu(I) are shown in Figure 4C, main text.

Figure S9: Structural models used for distance simulations

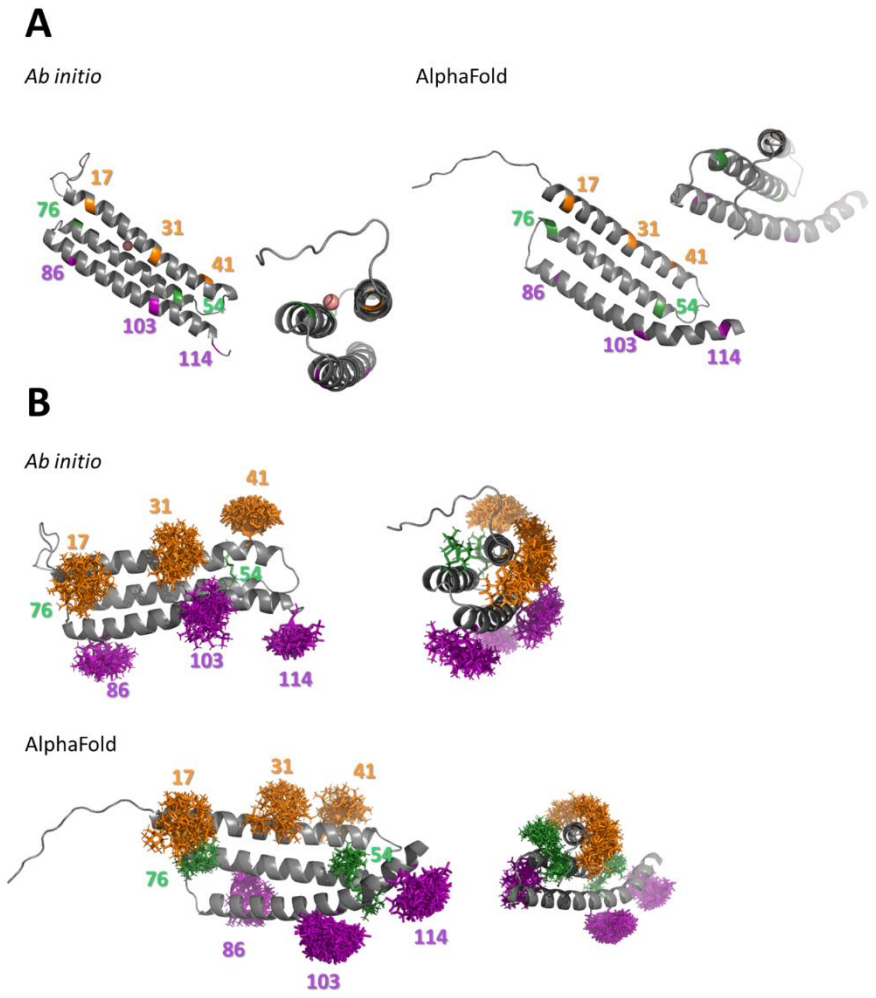

A: *Ab initio* predicted model[1] of the ETR1_TMD (left) and AlphaFold[14] structure (entry P49333, right). Side view onto the helix 1-helix 3 interface and top view onto helix 1 are shown, respectively. For the *ab initio* structure the position of the Cu(I) atom was included.

B: Possible MTSSL conformations (rotamers) attached to all labelling sites used in this study. The rotamers were calculated with the MATLAB program Multiscale Modeling of Macromolecules (MMM, version 2018.2).[15] Colour code: Helix 1 (orange), Helix 2 (green), Helix 3 (purple). Two different perspectives from the side (left) and top (right) are displayed. The resulting expected distance distributions are shown in Figure 3, main text.

Figure S10: Low-temperature cw-EPR spectra

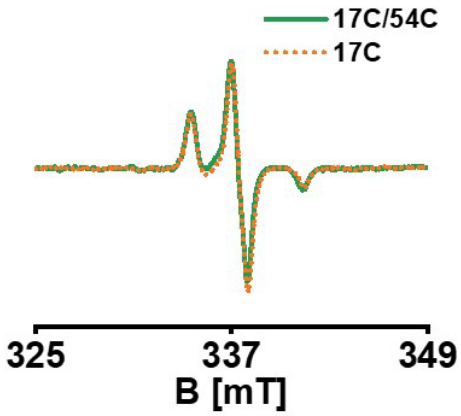

Cw-EPR spectra of the singly labelled variant (17C, orange dotted line) and the doubly labelled variant (17C/54C, green) were recorded at 120 K. After baseline-correction, the spectra were normalized to their integrated intensity. No deviations in peak amplitude were observed.

Figure S11: DEER data of single mutant

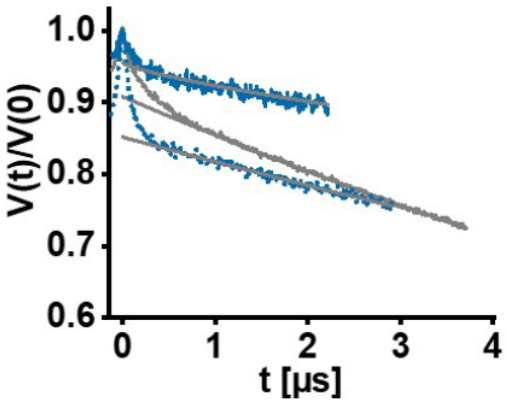

Primary DEER signal and background fit (grey) of ETR1_AC_L17C⟶R1 in detergent (grey line), after reconstitution (dashed blue line) and after diamagnetic dilution and reconstitution (solid blue line). Data were processed using MATLAB R2018a, the DeerAnalysis2019 software[8] and DEERNet[10]. The resulting form factors are shown in Figure 2C, main text.

Figure S12: CD spectra

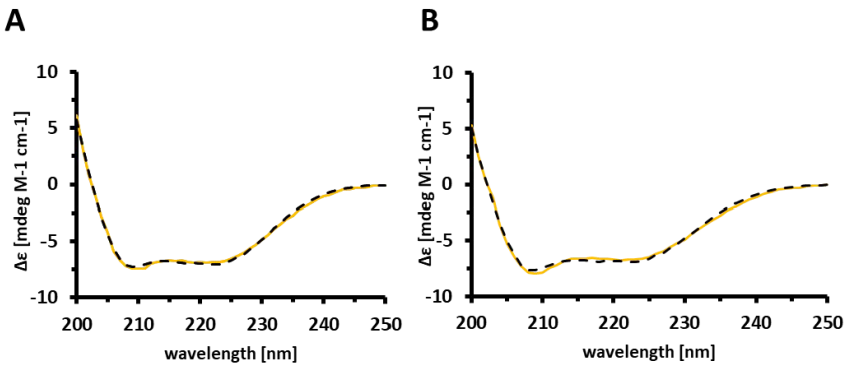

C

BESTSEL	α-Helix	β-Sheet	β-Turn	Random
ETR1_TMD wild type	66.4 %	0 %	11.6 %	22 %
ETR1_TMD_ΔC	63.7 %	0 %	8.4 %	27.9 %

Circular Dichroism (CD) spectra of purified ETR1_TMD wild type (A) and ETR1_TMD_ΔC (B). Spectra shown (orange lines) were recorded on a Jasco-715 spectropolarimeter (Jasco GmbH, Gross-Umstadt, Germany) at 0.1 nm resolution, 0.1 cm path length, 10 accumulations with a wavelength range from 250 to 200 nm. Secondary structures summarized in (C) were calculated from these spectra with BeSTSel.[11-13] Overall, the spectra of wild type and cysteine mutant are highly similar and correspond to previous CD data on receptor orthologs from Arabidopsis and tomato.[16, 17]

Supplementary References

1. S. Schott-Verdugo, L. Müller, E. Classen, H. Gohlke and G. Groth, *Sci. Rep.*, 2019, **9**, 1-14.
2. E. Bordignon, in *EPR Spectroscopy*, Springer, 2011, 121-157.
3. E. Gasteiger, C. Hoogland, A. Gattiker, M. R. Wilkins, R. D. Appel and A. Bairoch, *The proteomics protocols handbook*, 2005, 571-607.
4. J.-L. Rigaud and D. Lévy, in *Methods Enzymol.*, Elsevier, 2003, vol. 372, 65-86.
5. N. Le Breton, T. Adrianaivomananjaona, G. Gerbaud, E. Etienne, E. Bisetto, A. Dautant, B. Guigliarelli, F. Haraux, M. Martinho and V. Belle, *Biochim. Biophys. Acta, Bioenerg.*, 2016, **1857**, 89-97.
6. A. Scherer, S. Tischlik, S. Weickert, V. Wittmann and M. Drescher, *Magn. Reson.*, 2020, **1(1)**, 59-74.
7. C. E. Tait and S. Stoll, *Phys. Chem. Chem. Phys.*, 2016, **18**, 18470-18485.
8. G. Jeschke, V. Chechik, P. Ionita, A. Godt, H. Zimmermann, J. Banham, C. Timmel, D. Hilger and H. Jung, *Appl. Magn. Reson.*, 2006, **30**, 473-498.
9. O. Schiemann, C. A. Heubach, D. Abdullin, K. Ackermann, M. Azarkh, E. G. Bagryanskaya, M. Drescher, B. Endeward, J. H. Freed and L. Galazzo, *J. Am..Chem. Soc.*, 2021, **143**, 17875-17890.
10. S. G. Worswick, J. A. Spencer, G. Jeschke and I. Kuprov, *Sci. Adv.*, 2018, **4**, eaat5218.
11. A. Micsonai, F. Wien, É. Bulyáki, J. Kun, É. Moussong, Y.-H. Lee, Y. Goto, M. Réfrégiers and J. Kardos, *Nucleic Acids Res.*, 2018, **46**, W315-W322.
12. A. Micsonai, F. Wien, L. Kernya, Y.-H. Lee, Y. Goto, M. Réfrégiers and J. Kardos, *Proc. Natl. Acad. Sci.*, 2015, **112**, E3095-E3103.
13. A. Micsonai, É. Bulyáki and J. Kardos, in *Struct. Genomics*, Springer, 2021, 175-189.
14. J. Jumper, R. Evans, A. Pritzel, T. Green, M. Figurnov, O. Ronneberger, K. Tunyasuvunakool, R. Bates, A. Žídek and A. Potapenko, *Nature*, 2021, **596**, 583-589.
15. G. Jeschke, *Protein Sci.*, 2018, **27**, 76-85.
16. E. Classen and G. Groth, *Mol. Membr. Biol.*, 2012, **29**, 26-35.
17. M. Berleth, N. Berleth, A. Minges, S. Hänsch, R. C. Burkart, B. Stork, Y. Stahl, S. Weidtkamp-Peters, R. Simon and G. Groth, *Front. Plant Sci.*, 2019, **10**, 726.

5.2 Molekulare Grundlage der hochaffinen Ligandenbindung im Transmembranbereich des Ethylenrezeptors ETR1

Titel: Basis for high-affinity ethylene binding by the ethylene receptor ETR1 of *Arabidopsis*

Autoren: Beenish J. Azhar, Safdar Abbas, Sitwat Aman, Maria V. Yamburenko, Wei Chen, Lena Müller, Buket Uzun, David A. Jewell, Jian Dong, Samina N. Shakeel, Georg Groth, Brad M. Binder, Gevorg Grigoryan und G. Eric Schaller

Eigener Anteil:

10 % Planung, Durchführung und Auswertung der Experimente

Veröffentlicht in:

Proceedings of the National Academy of Sciences 120, 30.05.2023, Artikelnummer: 23, Creative Commons Attribution-NonCommercial-NoDerivates License 4.0

DOI: 10.1073/pnas.2215195120

PNAS RESEARCH ARTICLE | PLANT BIOLOGY

Basis for high-affinity ethylene binding by the ethylene receptor ETR1 of Arabidopsis

Beenish J. Azhar[a,b], Safdar Abbas[a,b], Sitwat Aman[a], Maria V. Yamburenko[a], Wei Chen[a], Lena Müller[c], Buket Uzun[c], David A. Jewell[d], Jian Dong[a], Samina N. Shakeel[a,b], Georg Groth[c], Brad M. Binder[e], Gevorg Grigoryan[a,d,1], and G. Eric Schaller[a,1]

Edited by Julian Schroeder, University of California San Diego, La Jolla, CA; received September 6, 2022; accepted April 14, 2023

The gaseous hormone ethylene is perceived in plants by membrane-bound receptors, the best studied of these being ETR1 from Arabidopsis. Ethylene receptors can mediate a response to ethylene concentrations at less than one part per billion; however, the mechanistic basis for such high-affinity ligand binding has remained elusive. Here we identify an Asp residue within the ETR1 transmembrane domain that plays a critical role in ethylene binding. Site-directed mutation of the Asp to Asn results in a functional receptor that has a reduced affinity for ethylene, but still mediates ethylene responses in planta. The Asp residue is highly conserved among ethylene receptor-like proteins in plants and bacteria, but Asn variants exist, pointing to the physiological relevance of modulating ethylene-binding kinetics. Our results also support a bifunctional role for the Asp residue in forming a polar bridge to a conserved Lys residue in the receptor to mediate changes in signaling output. We propose a new structural model for the mechanism of ethylene binding and signal transduction, one with similarities to that found in a mammalian olfactory receptor.

ethylene | ethylene receptor | ligand binding | copper cofactor | structural model

Significance

The gaseous hormone ethylene regulates many aspects of plant growth and development; however, the molecular basis by which ethylene receptors bind and respond to ethylene concentrations at less than one part per billion has remained an unresolved question. Here, evolutionary and computational modeling approaches were used to develop a new molecular model for the ethylene-binding site of the receptor ETR1 and key features of this model validated experimentally. Results shed light on the basis for high-affinity ethylene binding and how ethylene binding is transduced to mediate changes in signal output by the receptor. The new model is also relevant to our understanding of bacterial chemotaxis, convergent receptor evolution, and the development of ethylene nanosensors for agricultural and industrial applications.

The gaseous hormone ethylene regulates multiple aspects of plant growth and development, ripening being the best known of these, as well as responses to biotic and abiotic factors (1–3). Ethylene is perceived in plants by membrane-bound receptors, the first identified and best studied of these being ETR1 from Arabidopsis (2, 4–6). Most plants contain families of ethylene receptors, the five-member ethylene-receptor family of Arabidopsis consisting of ETR1, ETR2, EIN4, ERS1, and ERS2 (2, 6). The plant ethylene receptors have similar overall structures with transmembrane (TM) domains near their N-termini and signaling motifs in their C-terminal regions (2, 6). The N-terminal TM domains contain the ethylene-binding site (5, 7, 8), and also serve in membrane localization of the receptor, the majority of the receptors being found associated with the endoplasmic reticulum (9–12). Following the TM domain is a GAF domain (named after the proteins cGMP-specific phosphodiesterase, adenylyl cyclase, and FhlA in which it was initially identified) implicated in receptor interactions (12, 13). The C-terminal portions of each receptor contain domains with similarity to histidine kinases and in some cases the receiver domains of response regulators (14, 15). Histidine kinases and receiver domains are signaling elements originally identified as components in bacterial phosphorelays and are now known to be present in plants, fungi, and slime molds (16). The plant ethylene receptors are negative regulators of ethylene signal transduction, such that the receptors are "on" in the absence of ethylene and actively repress the ethylene response, and "off" when bound to ethylene, allowing for derepression of the ethylene response (2, 6, 17–19). As a result, higher-order loss-of-function mutants such as the *etr1 etr2 ein4* triple mutant and the *etr1 ers1* double mutant result in constitutive ethylene-response phenotypes, the *etr1 ers1* mutant resulting in infertility (17–19). Since the initial identification of ETR1 in plants, similar proteins with the conserved features of the ethylene-binding domain (EBD) have also been identified in prokaryotes, notably in cyanobacteria (7, 20, 21).

Due in part to the difficulty in obtaining high-resolution structural information from TM domains, much of what is known about the requirements for ethylene binding by the receptors comes from a coupling of biochemical and genetic analyses (5, 7, 20, 22, 23). Through these analyses, the receptors have been determined to function as homodimers, with ethylene binding mediated through an associated Cu(I) co-factor (7, 22–25). A set of highly conserved Cys and His residues in the TM domain is implicated in chelating the copper cofactor (5, 7, 25). Initial analysis indicated the existence of one copper cofactor per receptor dimer, suggesting a model in which the copper is chelated by two Cys and two His residues, thereby resulting in a single ethylene-binding site per receptor dimer (7). However, recent analysis is consistent with the existence of one copper cofactor per

Competing interest statement: A patent application related to this work has been filed (#PCT/US2023/017522. Ethylene receptors and binding domains with modified binding kinetics for ethylene).

This article is a PNAS Direct Submission.

[1]To whom correspondence may be addressed. Email: gevorg.grigoryan@gmail.com or george.e.schaller@dartmouth.edu.

This article contains supporting information online at https://www.pnas.org/lookup/suppl/doi:10.1073/pnas.2215195120/-/DCSupplemental.

Published May 30, 2023.

receptor monomer, which supports a model with two copper cofactors and potentially two ethylene-binding sites per receptor dimer (24). The well-characterized missense mutation *etr1-1* arises due to a mutation in the liganding Cys residue (Cys65Tyr), resulting in a receptor that no longer binds the copper cofactor and as a result also no longer binds ethylene (4, 5, 7, 26). The *etr1-1* mutation confers dominant ethylene insensitivity on plants because of this inability to perceive the ethylene signal. Additional missense mutations in the receptor have further refined our understanding of ethylene binding and signal transduction (20), as has computational modeling and tryptophan scanning mutagenesis (24, 27).

A major and still unresolved question is how the ethylene receptors bind ethylene with such high affinity. Ethylene binds to ETR1 with a calculated dissociation constant (K_d) of 2.4×10^{-9} M, and with a half-life for dissociation of over 12 h (5), consistent with plants responding to ethylene concentrations as low as 0.2 nL L^{-1} (28). Here we identify a highly conserved aspartate within the ETR1 TM domain (Asp25) as playing a critical role in copper and ethylene binding. Of particular interest, we determine that a natural variant of Asp25 (Asp25Asn) is still functional but has a reduced affinity for ethylene, pointing to the key role Asp25 plays in modulating high-affinity ethylene binding by the receptors. Additionally, we identify a highly conserved lysine residue (Lys91) that we propose forms a polar bridge to Asp25 to internally transduce the ethylene signal within the receptor to mediate changes in signaling output. Taking advantage of evolutionary and computational modeling approaches, combined with experimental verification, we propose a new structural model for the mechanism of ethylene binding and signal transduction, one with similarities to that found in a mammalian olfactory receptor.

Results

A Highly Conserved Asp Residue in the EBD Modulates Copper and Ethylene Binding by ETR1. The EBD of the receptor ETR1 of Arabidopsis is contained within the N-terminal TM domain of the protein (7, 22). This TM domain contains three predicted TM helixes, with the Cys65 and a His69 residues of TM helix II directly implicated in coordinating the copper cofactor required for ethylene binding (7, 22). Similar EBDs have been identified in a wide variety of organisms, including prokaryotes, the ethylene-binding capability of receptors from Arabidopsis, tomato, and the cyanobacterium *Synechocystis* sp PCC 6803 having all been confirmed (20, 22, 29, 30). Fig. 1*A* indicates the degree of amino acid conservation found in a comparison of EBDs from 1,221 eukaryotic and prokaryotic sequences related to ETR1. As predicted, the Cys and His residues of TMII implicated in coordinating the copper cofactor of ETR1 are highly conserved in EBDs.

Of particular interest are the additional conserved polar and charged residues found in the TM helixes, such as Asp25 (D25) of helix I in ETR1 (Fig. 1*A*), because such residues are likely to play significant roles in ethylene binding and/or signal transduction. Mutation of Asp25 to Ala (D25A) abolishes ethylene binding by the receptor when analyzed in a heterologous yeast expression system and also confers dominant ethylene insensitivity when expressed in Arabidopsis (20). Computational modeling places Asp25 of helix I in proximity to Cys65 and His69 of helix II (24, 27), suggesting that it could play a role in coordinating the copper cofactor. Interestingly, although Asp is found in 93.55% of the sequences examined, in some cases (3.67%) it is substituted by an Asn residue, most commonly in cyanobacteria but also in several plants, *Pyrus communis* (Pear) and *Cajanus cajan* (Pigeon pea).

To characterize the role of Asp25 in copper and ethylene binding, we generated four site-directed mutant versions of ETR1. $ETR1^{D25A}$ was previously found to eliminate ethylene binding (20). $ETR1^{D25N}$ represents a relatively conserved change of the Asp R-group from a carboxylic acid to a carboxamide, one that will preserve the general size of the side group, but which eliminates the negative charge. As noted above, although Asp25 is highly conserved in EBDs, an Asn residue is found at that position in a few EBDs (Fig. 1*A*). $ETR1^{D25E}$ preserves the carboxylic acid and its negative charge found in the Asp R-group, but Glu has a longer sidechain than does Asp. The $ETR1^{D25Q}$ mutation is analogous to that for $ETR1^{D25N}$, exchanging a carboxyamide for a carboxylic acid on the R-group of Glu, and so eliminating the negative charge of the Glu.

We tested the effects of Asp25 mutants on copper binding to the ETR1 TM domain following expression and purification from *E. coli* (24). Purified receptors lack the copper cofactor, allowing for their reconstitution with copper using this in vitro assay. Cu(I) was stabilized by the copper chelator bicinchoninic acid (BCA), and then titrated with increasing ETR1 protein concentration. As shown in Fig. 1*B*, titration with $ETR1^{wt}$ results in copper binding and a concomitant decrease in absorbance at 562 nm of the purple BCA_2-Cu(I) complex. In contrast, no copper binding was observed for $ETR1^{D25A}$ and only minimal residual binding observed for $ETR1^{D25N}$, $ETR1^{D25E}$, and $ETR1^{D25Q}$ (Fig. 1*B*). These data thus support a model in which Asp25 contributes to copper binding. Furthermore, we found that the Asp25 mutants had an additive effect on copper binding when combined with an $ETR1^{C65S;H69A}$ mutant, because the $ETR1^{C65S;H69A}$ mutant exhibited residual binding that was eliminated when combined with the Asp25 mutations ($ETR1^{D25X;C65S;H69A}$) (Fig. 1*B* and *SI Appendix*, Fig. S1).

Saturable ethylene binding of the ETR1 Asp25 mutants was examined by heterologous expression in yeast, with binding to [^{14}C]ethylene determined in the presence or absence of excess [^{12}C]ethylene (Fig. 1*C*) (5, 31). Expression in yeast results in the production of functional ethylene receptors as membrane-associated disulfide-linked homodimers containing the copper cofactor, facilitating an in vivo analysis of ethylene binding due to the cell permeability of ethylene (5, 22). Saturable binding of [^{14}C]ethylene was observed for $ETR1^{wt}$, as the positive control, and not with the pYCDE2 vector negative control (Fig. 1*C*). Binding of ethylene by $ETR1^{D25E}$ was still observed but was substantially reduced compared to that observed with $ETR1^{wt}$, likely arising due to steric problems from the larger size of the Glu R-group as well as differences in protein expression levels (Fig. 1*C*). No saturable [^{14}C]ethylene binding was detected for the other D25 mutants. This included the $ETR1^{D25A}$ mutant, consistent with previous observations (20), as well as for the $ETR1^{D25N}$ and $ETR1^{D25Q}$ mutants (Fig. 1*C*). Results from the ethylene-binding assay are therefore consistent with the negative charge at D25 playing a significant role in mediating high-affinity ethylene binding.

Functional Analysis of Asp25 Mutations on the ETR1 Responses In Planta. Functionality of the ETR1 Asp25 mutants was tested by transgenic expression in the *etr1 etr2 ein4* Arabidopsis background. The rationale for this approach is that the *etr1 etr2 ein4* triple mutant exhibits a partial constitutive ethylene-response phenotype, resulting in reduced shoot growth as well as a shorter hypocotyl in the air than is found in the wildtype (Fig. 2 *A* and *B* and *SI Appendix*, Fig. S2) (18). We can thus exploit the triple mutant to assess the ability of the *ETR1* transgenes to rescue growth in the absence of ethylene as well as their ability to mediate a response to ethylene (32). Such an analysis indicates whether the encoded receptors can assume the "on" conformation that represses the ethylene response in air, as

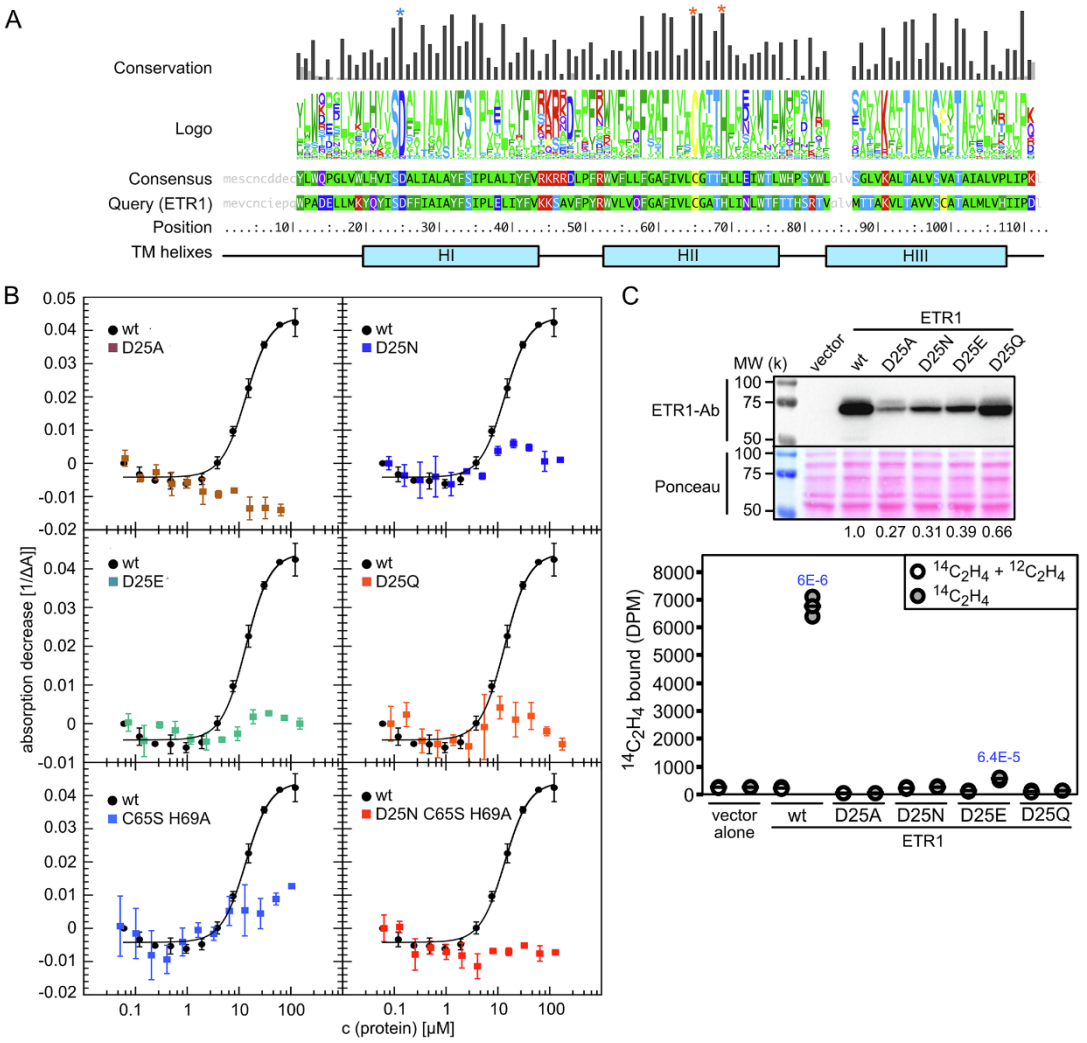

Fig. 1. Copper and ethylene binding of wildtype and Asp25 mutant versions of ETR1. (*A*) Amino acid conservation of the EBD in ETR1-like proteins. The three conserved TM (TM) helixes (HI, HII, and HIII) are indicated. Red asterisks indicate Cys65 and His69 of ETR1 HII implicated in coordinating the copper cofactor; the blue asterisk indicates the highly conserved Asp25 of HI. (*B*) Copper binding of wildtype and Asp25 mutant versions of ETR1 TM domain (ETR1-TMD; n = 3). Purified ETR1-TMD was titrated to the BCA_2-Cu(I) complex, and copper binding monitored spectrophotometrically based on the change in absorbance at 562 nm. For comparison copper binding of a Cys65Ser His69Ala mutation was examined alone and in combination with the Asp25Asn mutation. For site-directed mutations, the single letter abbreviations for the amino acids Asp (D), Ala (A), Asn (N), Cys (C), Glu (E), Gln (Q), His (H), and Ser (S) are used (*SI Appendix*, Fig. S1). (*C*) Ethylene binding to yeast transgenically expressing wildtype and Asp25 mutant versions of ETR1. ETR1 protein levels were determined by immunoblot analysis with an anti-ETR1 antibody (quantification is relative to ETR1-wt), and the proteins on the blot staining with Ponceau-S as a loading control. To analyze ethylene-binding activity, transgenic yeast samples (n = 3; horizontal line = mean) were incubated with 0.21 μL L^{-1} [^{14}C]ethylene, in the presence or absence of excess [^{12}C]ethylene, the difference between the two values representing the saturable binding; *P* values for significant saturable binding, as determined by *t* test are given for $P < 0.05$.

well as the "off" conformation that occurs in response to ethylene binding. All transgenes were expressed based on immunological detection of the tETR1 protein, and all rescued growth of the *etr1 etr2 ein4* triple mutant in air based on hypocotyl and adult shoot growth analysis, indicating that all the tETR1 proteins ($tETR1^{wt}$, $tETR1^{D25N}$, $tETR1^{D25Q}$, $tETR1^{D25E}$, $tETR1^{D25A}$) can assume the "on" conformation (Fig. 2 *A* and *B* and *SI Appendix*, Fig. S2).

Previous studies have found that the site-directed mutation of residues that result in a loss of ethylene-binding activity typically confer dominant ethylene insensitivity on the seedlings, due to an inability of the etr1 mutant protein to switch from its "on" to its "off" conformation (7, 20, 22). Based on this we anticipated that those Asp25 mutants that resulted in a loss of high-affinity ethylene binding ($tETR1^{D25N}$, $tETR1^{D25Q}$, and $tETR1^{D25A}$) would confer dominant ethylene insensitivity. Since the $tETR1^{D25E}$ protein still exhibited reduced ethylene binding, it was possible that it would respond similarly to wildtype, but it was also possible that $tETR1^{D25E}$ would confer dominant insensitivity due to the reduced ability to bind and/or the perturbation of the ethylene

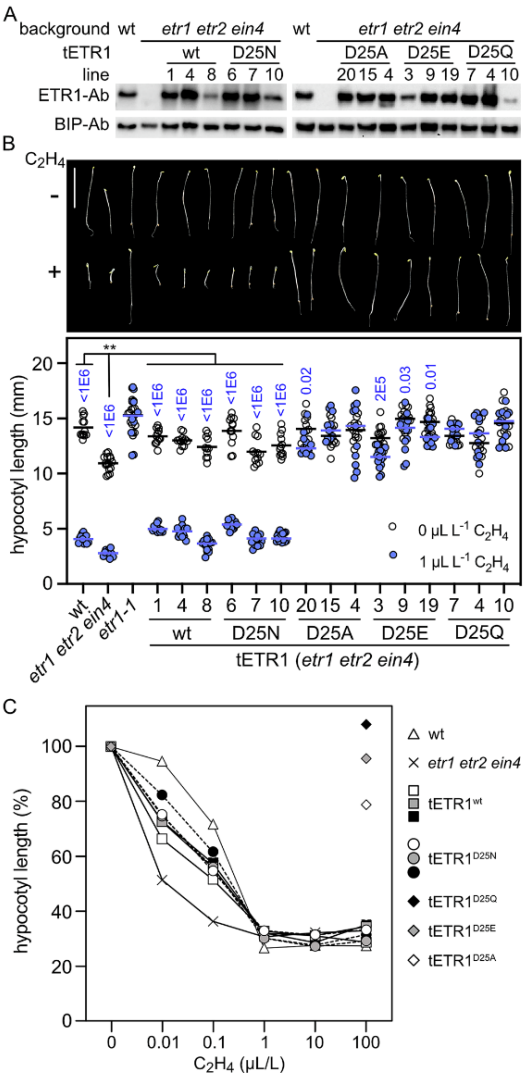

Fig. 2. Ethylene sensitivity of Arabidopsis seedlings expressing Asp25 mutants of ETR1. Wildtype (wt) and mutant versions of ETR1 were transgenically (tETR1) expressed in the *etr1 etr2 ein4* background. (*A*) ETR1 protein levels as determined by immunoblot analysis with an anti-ETR1 antibody in dark-grown seedlings. BIP serves a loading control. (*B*) Triple-response seedling growth assay to ethylene. Dark-grown seedlings were treated with 0 or 1 µL L^{-1} ethylene. Images of seedlings are shown along with quantification of the hypocotyl growth response (n ≥ 10; horizontal line = mean). The mutant *etr1-1* serves as an ethylene-insensitive control. *P* values (blue) for significant differences in the ethylene responsiveness of seedlings, as determined by *t* test, are given for $P < 0.05$. For data comparison of *etr1 etr2 ein4* to wt, tETR1(wt), and tETR1(D25N) lines grown in the absence of ethylene, ANOVA was performed with post hoc Holm multiple comparison calculation (**$P < 0.01$). (*C*) Ethylene dose response curves of hypocotyl growth in dark grown seedlings for the three lines of $ETR1^{wt}$ and $ETR1^{D25N}$ compared to wt and *etr1 etr2 ein4*. Representative ethylene-insensitive $tETR1^{D25A}$-#20, $tETR1^{D25E}$-#19, and $tETR1^{D25Q}$-#4 lines are also included and examined at 0 and 100 µL L^{-1} ethylene. The ethylene response is normalized for each line relative to its hypocotyl length at 0 µL L^{-1} ethylene (n ≥ 17; SE < 3% of hypocotyl length, not shown for clarity) (*SI Appendix*, Figs. S3 and S4).

binding site. As shown in Fig. 2 *A* and *B*, the $ETR1^{D25A}$, $ETR1^{D25E}$, and $ETR1^{D25Q}$ transgenes all conferred ethylene insensitivity based on a hypocotyl growth response analysis, consistent with predictions (i.e., less than a 20% decrease in hypocotyl growth in response to ethylene). Surprisingly, the $ETR1^{D25N}$ transgene rescued the hypocotyl growth response to ethylene to the same degree as $ETR1^{wt}$ even though, based on our previous analyses, $ETR1^{D25N}$ was compromised in its copper and ethylene-binding ability. Hypocotyl ethylene dose-response analyses confirmed a similar ethylene responsiveness for both the $ETR1^{wt}$ and $ETR1^{D25N}$ lines, their responsiveness being similar to that found with an *etr2 ein4* double mutant (Fig. 2*C* and *SI Appendix*, Figs. S3 and S4).

Based on the differences, we uncovered for the long-term ethylene growth responses for the Asp25 mutants, we also analyzed their short-term hypocotyl growth and molecular responses to ethylene. To this end, we performed a short-term kinetic analysis (28, 33), analyzing the initial hypocotyl growth inhibition in response to 10 µL/L ethylene and the growth recovery following the removal of ethylene after 2 h of treatment (Fig. 3*A*). As shown in Fig. 3*A*, both wildtype and the triple mutant *etr1 etr2 ein4* exhibit a rapid inhibition of hypocotyl growth in response to ethylene, but the growth recovery for the *etr1 etr2 ein4* mutant following removal of ethylene is substantially slower than that observed for the wildtype (33). The ethylene-insensitive mutants $ETR1^{D25A}$, $ETR1^{D25E}$, and $ETR1^{D25Q}$ all exhibit ethylene insensitivity based on the short-term kinetic analysis (Fig. 3*A*). In contrast, both the $ETR1^{wt}$ and $ETR1^{D25N}$ lines exhibit a rapid growth response to ethylene and, upon ethylene removal, a similar growth recovery intermediate between that exhibited by the wildtype and the *etr1 etr2 ein4* seedlings (Fig. 3*A* and *SI Appendix*, Fig. S5). To examine the short-term molecular response, we characterized ethylene-dependent gene expression for the ETR1 Asp25 mutants (Fig. 3*B* and *SI Appendix*, Fig. S6). The expression of *OSR1* and *ERF1* is induced, whereas the expression of *EXP5* and *EXPb1* is repressed, in response to ethylene (Fig. 3*B*). The molecular response to ethylene is similar in the $ETR1^{wt}$ and $ETR1^{D25N}$ transgenic lines for all four genes, and consistent with what is observed in the wildtype control. In contrast, the ethylene-insensitive mutants $ETR1^{D25A}$, $ETR1^{D25E}$, and $ETR1^{D25Q}$ all exhibit various levels of hyposensitivity for ethylene-dependent gene expression, this being most apparent in the analysis of *EXP5* and *EXPb1* expression. Similar effects were found on the expression of additional ethylene-regulated genes, including induction of *ARGOS*, *ERS1*, and *ERS2* and repression of *CAPE2* (*SI Appendix*, Fig. S6).

To confirm that the results obtained in the heterologous yeast expression system for $ETR1^{D25N}$ reflected the condition in planta, we compared ethylene binding of $ETR1^{wt}$ and ETR^{D25N} in the *etr1 etr2 ein4* Arabidopsis background, making use of lines that exhibited a similar seedling phenotype, ETR1 protein levels, and expression levels of the remaining receptors *ERS1* and *ERS2* (Fig. 4 *A* and *B*). [^{14}C]ethylene binding was examined in 2-week–old green seedlings grown on media containing 5 µM aminoethoxyvinylglycine (AVG) to inhibit ethylene biosynthesis. As shown in Fig. 4*C*, the triple mutant *etr1 etr2 ein4* exhibits a basal level of ethylene binding due to the presence of the receptors ERS1 and ERS2; however, transgenic expression of $ETR1^{wt}$ results in a significant increase in ethylene binding. In contrast, no increase in ethylene binding was observed following transgenic expression of ETR^{D25N}.

Mechanism by Which $ETR1^{D25N}$ Mediates Ethylene Signaling In Planta. We considered two hypotheses, not mutually exclusive, as to how $ETR1^{D25N}$ could mediate ethylene signaling in planta:

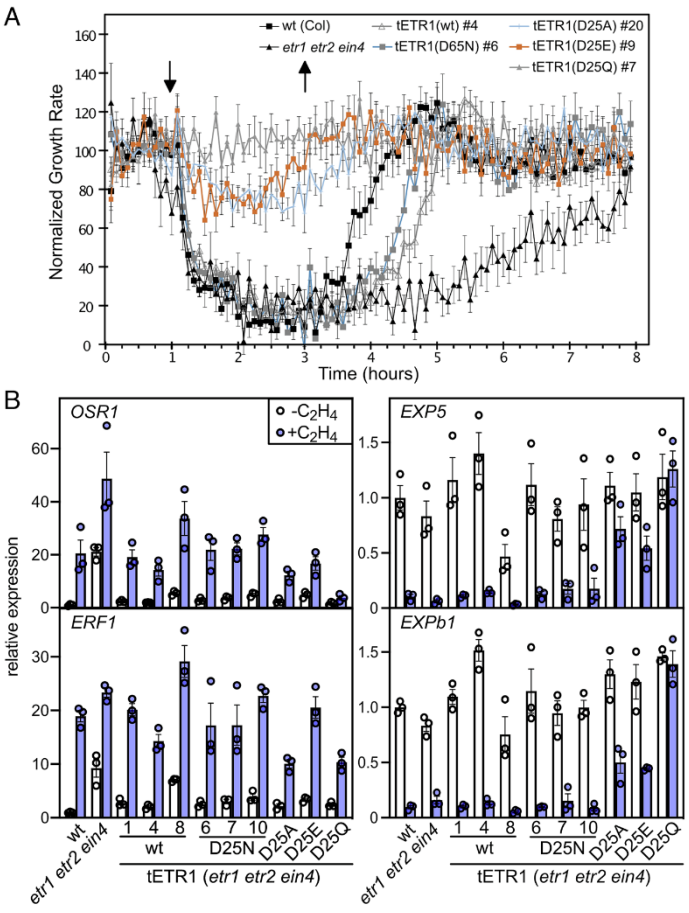

Fig. 3. Short-term ethylene responses of Arabidopsis seedlings expressing Asp25 mutants of ETR1. (*A*) Kinetics of growth response to ethylene of ETR1^{wt} and ETR1^{D25} mutant lines. Ethylene dose-response kinetics were analyzed in hypocotyls of 2-d–old etiolated seedlings for wildtype, the *etr1 etr2 ein4* triple mutant, and for the triple mutant complemented with ETR1^{wt} or various ETR1^{D25} mutants as indicated. Measurements were made in air for 1 h, followed by a 2-h exposure to 10 µL L^{-1} ethylene, and then a 5-h recovery in air. Growth rates for each line are normalized to the growth rate during the first hour in the air. Arrows indicate the time points for the addition and removal of ethylene. Error bars represent SE (n ≥ 7) (*SI Appendix*, Fig. S5). (*B*) Effect of ETR1 Asp25 mutants on ethylene-dependent gene expression. Dark-grown seedlings were treated with 0 or 1 µL L^{-1} ethylene for 2 h, and gene expression examined by qRT-PCR (n = 3). Expression was normalized to a tubulin control and is presented as relative to the untreated wildtype control. Three tETR1-wt and three tETR1^{D25N} lines were examined. The ethylene-insensitive tETR1^{D25A}#20, tETR1^{D25E}#19, and tETR1^{D25Q}#4 lines were also included. See *SI Appendix*, Fig. S6 for expression of additional genes.

residual ethylene binding of the ETR1^{D25N} mutant and/or cooperative interactions with other wildtype ethylene receptors in Arabidopsis. The first hypothesis is based on the affinity of the receptors for ethylene. ETR1 has a half-life for ethylene dissociation of over 12 h (5), allowing for the ready detection of [^{14}C]ethylene binding in yeast or in planta; however, if the ETR1^{D25N} mutant still retained the copper cofactor and bound ethylene with lower affinity (less tightly), then it would be substantially more difficult to detect with the [^{14}C]ethylene binding assays. The second hypothesis is based on the existence of ethylene receptor families in Arabidopsis. Even in the *etr1 etr2 ein4* background, used for expression of the ETR1^{D25N} mutant, the ERS1 and ERS2 wildtype receptors are still present. These could bind ethylene and, as part of a receptor complex, potentially pass on a conformational information to ETR1^{D25N}, causing it to adopt a signaling conformation even when it has not bound ethylene. This type of signaling interaction has been found for bacterial chemoreceptors, and has also been proposed to occur for the ethylene receptors which, like chemoreceptors, form higher-order receptor complexes (12, 13, 28, 34).

As an initial test for the feasibility of the first hypothesis, we asked if ETR1^{D25N} could still bind a metal cofactor, and therefore potentially ethylene, in planta. For this purpose, we examined the effects of silver (Ag) on ethylene sensitivity. Silver is thought to substitute for the copper cofactor and, although receptors containing silver can still bind ethylene, they no longer transmit the signal, resulting in ethylene insensitivity (7, 23, 35, 36). As shown in Fig. 5*A*, the dark-grown seedling response of wildtype to 10 µL/L ethylene is blocked when seedlings are grown on silver, but the *etr1 etr2 ein4* triple mutant is still responsive to ethylene in the presence of silver. We find that expression of either *tETR1^{wt}* or *tETR1^{D25N}* in the *etr1 etr2 ein4* background restores the ability of silver to block the ethylene response, consistent with ETR1^{D25N} retaining an ability to bind its metal cofactor in vivo, even though it showed reduced affinity in the in vitro assay (Fig. 1*B*).

As an alternative approach to test the two hypotheses, we used CRISPR-cas9 methodology to knock out *ERS1* and *ERS2* in the ETR1^{D25N} (*etr1 etr2 ein4*) line to generate an ETR1^{D25N} (*etr1 etr2 ein4 ers1 ers2*) line (*SI Appendix*, Fig. S7), the prediction being that signaling by ETR1^{D25N} will be lost if dependent on the presence of other wildtype receptors. Two independent ETR1^{D25N} (*etr1 etr2 ein4 ers1 ers2*) lines were generated (#11 and #15). However, contrary to the second hypothesis, the ETR1^{D25N} lines still responded to ethylene (Fig. 5*B*), consistent with an ability for ETR1^{D25N} to bind ethylene, in agreement with residual copper binding (Fig. 1*B*) and the silver sensitivity assay (Fig. 5*A*).

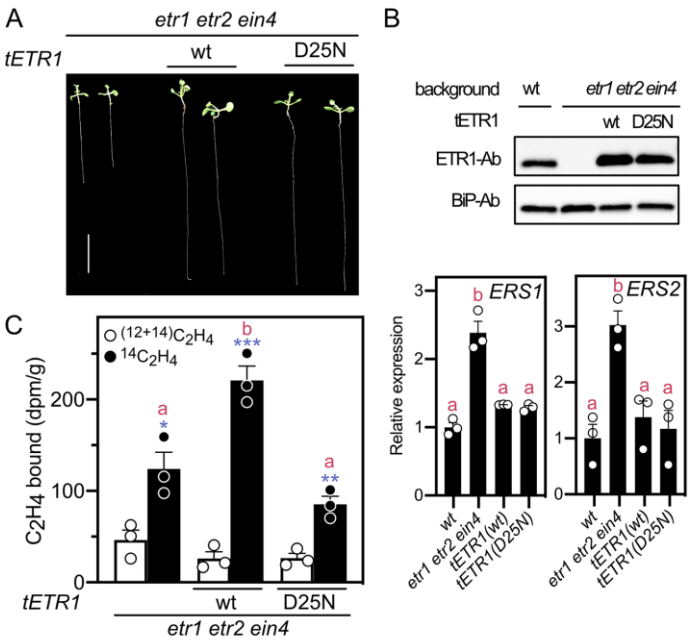

Fig. 4. Ethylene binding of Arabidopsis seedlings expressing ETR1^{wt} and ETR1^{D25N}. (*A*) Representative 2-wk-old green seedlings of the ETR1^{wt}-#4 and ETR1^{D25N}-#6 lines expressed in *etr1 etr2 ein4* background, as well as the *etr1 etr2 ein4* triple mutant itself (Scale bar, 1 cm). (*B*) Expression levels of the tETR1 receptor versions as determined by immunoblot, and of *ERS1* and *ERS2* as determined by qRT-PCR. Significant differences in gene expression between lines were determined by ANOVA with post-hoc Holm multiple comparison calculation; different red letters indicate a significant difference at $P < 0.05$. (*C*) Saturable ethylene binding (n = 3; error bar = SE) of the seedlings. Seedlings were incubated with 0.31 µL L^{-1} [^{14}C]ethylene, in the presence or absence of excess [^{12}C]ethylene, the difference between the two values representing the saturable binding. Significant saturable binding as determined by *t* test for each line is indicated (blue; $*P < 0.05$, $**P < 0.01$, $***P < 0.001$). Significant differences in expression between lines are ANOVA-based analyses (red; $P < 0.01$).

Furthermore, the ethylene response of the ETR1^{D25N} (*etr1 etr2 ein4 ers1 ers2*) lines was blocked by the competitive inhibitor 1-methylcyclopropene (1-MCP) (Fig. 5*B*) (36), also consistent with ETR1^{D25N} retaining its c opper cofactor and ability to bind its gaseous ligand. Kinetic analysis supports the ability of the ETR1^{D25N} (*etr1 etr2 ein4 ers1 ers2*) lines to rapidly mediate the ethylene response (Fig. 5*C*). These data thus support a key role for Asp25 of ETR1 in regulating the kinetics of ethylene binding by the receptor.

Effect of Lys91 Mutations of ETR1 on Seedling Growth and Ethylene Sensitivity. Coevolutionary analysis can be used to predict interactions/contacting residues in proteins (37, 38). For example, the EVCOUPLINGs algorithm derives residue–residue evolutionary couplings from deep multiple sequence alignment by a pseudolikelihood maximization method. Therefore, to gain further information about the structure of the EBD, we used the 1 to 112 amino-acid sequence of ETR1 as an input for both the EVCOUPLINGs and GREMLIN servers (37, 38). Sequence coevolution analysis predicts a coupling between Asp25 of TM helix I with Lys91 of TM helix III (GREMLIN probability of 0.960; EVcouplings probability of 0.997; Fig. 6*A* and *SI Appendix*, Table S1) (37, 38). This predicted Asp25-Lys91 coupling is of interest because, in contrast to the first and second TM helixes of ETR1 that play substantial roles in copper and ethylene binding, the third TM helix is implicated in signal transduction (20). Like Asp25, Lys91 is highly conserved (Fig. 1*A*) but Lys is not among the amino acids favored to coordinate copper ions (39, 40). A role for Asp25 in both copper binding and in forming a polar bond to TM helix III would provide a potential mechanism by which to couple ethylene binding to receptor signal output.

To examine the role of Lys91 in signaling by ETR1, we made the site-directed mutations ETR1^{K91R}, ETR1^{K91M}, and ETR1^{K91A}, and examined their copper-binding ability using the in vitro assay (*SI Appendix*, Fig. S8), their ethylene-binding ability using the yeast expression system (Fig. 6*B*) and their functionality by transgenic expression in the *etr1 etr2 ein4* Arabidopsis background (Fig. 6*C*). All three Lys91 mutants of ETR1 bound copper similarly to the wildtype control (*SI Appendix*, Fig. S8), consistent with Lys91 not playing a direct role in copper binding. In contrast, as described below, differing effects of the Lys91 ETR1 mutants were found on ethylene binding and functionality in planta.

In ETR1^{K91R}, the basic Lys91 residue is replaced with another basic residue (Arg) which should preserve the ability to form a polar bond to Asp25. The ETR1^{K91R} mutant exhibited an ethylene binding ability similar to that of ETR1^{wt} (63% of wildtype binding; Fig. 6*B*) but like some other previously characterized site-directed mutations in TM segment three (20), conferred ethylene hyposensitivity (reduced ethylene sensitivity rather than insensitivity) in Arabidopsis (Fig. 6*C*), potentially due to the larger Arg sidechain perturbing the receptor structure so that it does not effectively turn "off" upon ethylene binding.

In ETR1^{K91M}, the basic sidechain of Lys91 is replaced with a nonpolar sidechain of similar size; this mutation would no longer be able to participate in a polar bridge to mediate an ethylene-dependent change in conformation. ETR1^{K91M} exhibited substantially reduced binding of approximately 6% of that found in ETR1^{wt} (Fig. 6*B*). Interestingly, the ETR1^{K91M} mutant exhibited a seedling growth response not previously noted for ETR1 mutants (20). The ETR1^{K91M} mutant failed to rescue seedling growth efficiently but also exhibited partial ethylene hyposensitivity (Fig. 6*C*), suggesting that the receptor is less capable of maintaining the "on" and "off" conformations typically found in the absence and presence of ethylene, respectively, consistent with a lack of "communication" between the ethylene binding site involving TM helixes I and II, and the output domain of TM helix III.

In ETR1^{K91A}, as with ETR1^{K91M}, the basic sidechain of Lys is replaced with a nonpolar sidechain but one that is smaller than

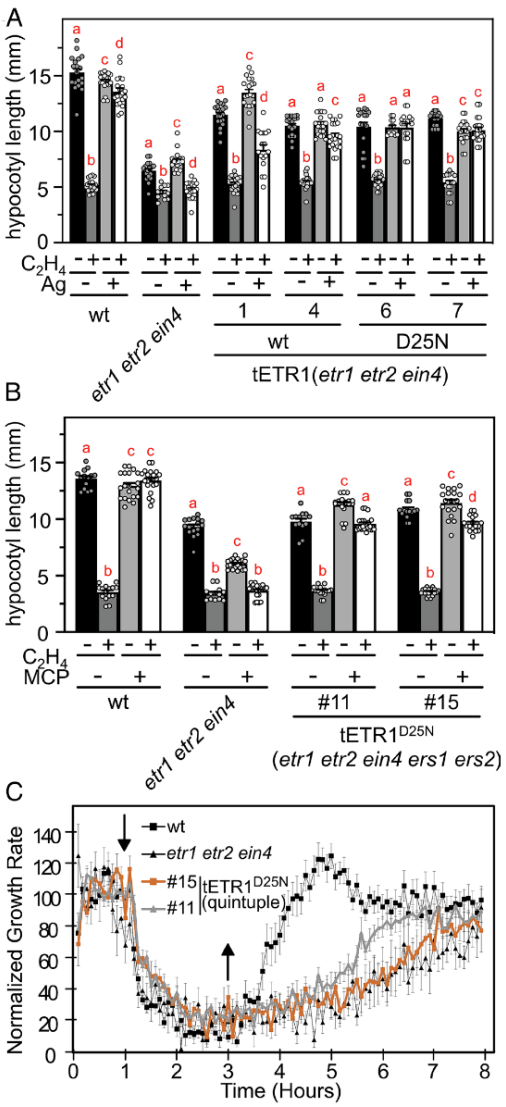

Fig. 5. Responsiveness of the ETR1^{D25N} mutant to ethylene, silver, and 1-MCP. (*A*) The ethylene responsiveness of ETR1^{wt} and ETR1^{D25N}, transgenically expressed in the *etr1 etr2 ein4* background, is blocked in the presence of 100 µM silver (Ag). The hypocotyl growth of dark-grown seedlings was analyzed in the absence or presence of 10 µM ethylene (n ≥ 11; error bars = SE). (*B*) ETR1^{D25N} responds to 1 µL L^{-1} ethylene in a background lacking all five native ethylene receptors (*etr1 etr2 ein4 ers1 ers2*), and has this response is blocked by 1 µL L^{-1} 1-MCP (n ≥ 13; error bars = SE). Loss-of-function mutations in the *ERS1* and *ERS2* genes were generated by a CRISPR-Cas9 approach in the ETR1^{D25N} (*etr1 etr2 ein4*) line #6. Significant differences in hypocotyl length following treatment were determined for each line by ANOVA with post hoc Holm multiple comparison calculation; different red letters indicate a significant difference for each line at $P < 0.05$. (*C*) Kinetics of growth response to ethylene of wildtype, *etr1 etr2 ein4*, and two lines of ETR1^{D25N} in the *etr1 etr2 ein4 ers1 ers2* (quintuple) background. Error bars represent SE (n ≥ 8).

that found with Lys; the ETR1^{K91A} mutation was previously found to confer ethylene insensitivity on Arabidopsis seedlings but still retained a low level of ethylene binding ability (20). Like ETR1^{K91M}, we found that ETR1^{K91A} retained a minimal ability to bind ethylene (only 1% of that found in ETR1^{wt}; Fig. 6*B*). Thus, preservation of the basic nature of the Lys91 sidechain is important to ethylene binding, although the finding that substitution with a nonpolar sidechain does not eliminate ethylene binding is consistent with Lys91 not playing a direct role in chelating the copper cofactor. ETR1^{K91A} conferred two different ethylene response phenotypes in the seedling lines we examined (Fig. 6*C*): a phenotype similar to that of the ETR1^{K91M} mutant (lines 9 and 14) or ethylene insensitivity (lines 10 and 11) such as previously reported for the mutation (20). The ETR1^{K91A} lines that exhibited ethylene insensitivity generally also had higher receptor protein levels (Fig. 6*C*), suggesting that insensitivity could arise due to increases in the number of misfolded receptors, these receptors potentially unable to bind ethylene or unable to change conformation upon ethylene binding.

To gain further information on the interaction of Asp25 and Lys91, we combined the Asp25Asn mutation with the ETR1^{K91X} mutations to generate ETR1$^{D25N, K91R}$, ETR1$^{D25N, K91M}$, and ETR1$^{D25N, K91A}$, and examined their functionality in the *etr1 etr2 ein4* Arabidopsis background (Fig. 6*C*). The ETR1$^{D25N, K91X}$ combinations tended to accentuate the mutant growth phenotypes noted for the ETR1^{K91X} single mutants. The ETR1$^{D25N, K91R}$ mutant is ethylene insensitive rather than hyposensitive as found in the ETR1^{K91R} mutant; the ETR1$^{D25N, K91M}$ mutant rescued seedling growth even less efficiently than the ETR1^{K91M} mutant; and the ETR1$^{D25N, K91A}$ mutant lines are all ethylene insensitive rather than just a subset as found with the ETR1^{K91A} mutant lines. The heightening of the ETR1^{K91X} phenotypes when combined with Asp25Asn indicates that the Asp25Asn mutation does affect signaling by ETR1, even though the individual ETR1^{D25N} mutant could not be distinguished from the ETR1^{wt} by standard growth response assays (Figs. 2 and 3).

Discussion

A key but unresolved structural question for the ethylene receptors is how the copper cofactor(s) required for ethylene binding are coordinated within the TM domain. The Cu(I) oxidation state is known to exist in a variety of coordination geometries, with coordination numbers anywhere from two to six (41, 42). Based on initial evidence for a single Cu(I) in the ethylene-binding site, a tetrahedral geometry for the copper binding site was proposed involving Cys65 (as the thiolate form) and His69 of ETR1: $(Cys65)_2(His69)_2$, hereafter referred to as a CCHH coordination model (7, 22). The tetrahedral geometry of the proposed CCHH copper-binding site was considered consistent with the homodimeric nature of ethylene receptors and the fact that Cys65 and His69 are on the same face of the second TM helix, one helical turn apart.

Recent data point to the existence of two coppers per receptor dimer (i.e. one copper per receptor monomer) (24), a possibility not inconsistent with data from the earlier study in which it was unclear if all the purified receptors were competent for copper binding (7), a finding that necessitates the consideration of new coordination structures for the copper cofactors. Here we implicate Asp25 of ETR1 as playing a critical role in copper binding based on the same principles that implicate Cys65 and His69. Based on our current understanding that there is one copper per monomer, we consider two potential models by which Asp25 could contribute to ethylene binding by ETR1 (Fig. 7 *A* and *B*). First, Asp25 could directly participate in copper binding along with Cys65 and His69: a tridentate Asp-Cys-His (DCH) model for copper coordination. Alternatively, Asp25 could form a

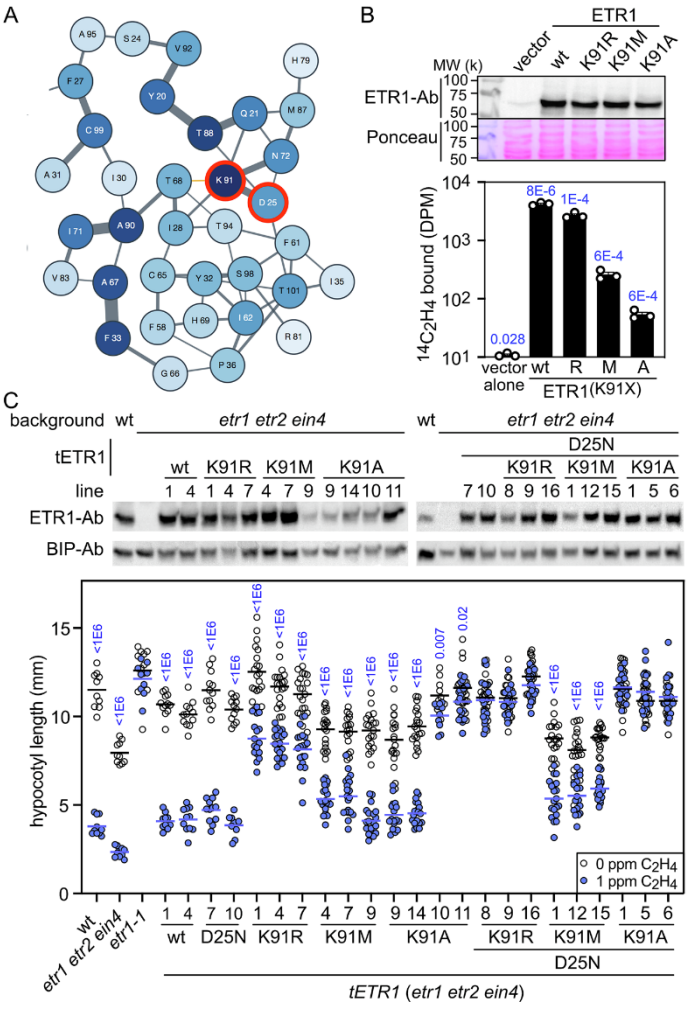

Fig. 6. Characterization of Lys91 mutants of ETR1. (*A*) Evolutionary couplings of ETR1 amino acid residues from the EBD, based on the analysis of 1,221 ETR1-related sequences using the EVcouplings framework (37). The thickness of the lines represents the strength of individual couplings. The intensity of the blue shading represents the overall strength of couplings for that specific residue. Lys91 and Asp25 are highlighted in red. (*B*) Ethylene binding to yeast transgenically expressing wildtype and Lys91 mutant versions of ETR1. Immunoblot analysis was used to determine the ETR1 protein levels with an anti-ETR1 antibody; the proteins on the blot were stained with Ponceau-S as a loading control. To determine saturable ethylene-binding activity of the ETR1 Lys91 mutants, transgenic yeast samples (n = 3) were incubated with 0.21 μL L^{-1} [^{14}C]ethylene, in the presence or absence of excess [^{12}C]ethylene, the difference between the two values representing the saturable binding; *P* values for significant saturable binding, as determined by *t* test are given for $P < 0.05$. (*C*) Characterization of Arabidopsis seedlings expressing Lys91 mutants of ETR1. Lys91 mutant versions of ETR1 alone or with Asp25Asn (D25N) were transgenically (tETR1) expressed in the *etr1 etr2 ein4* background. Immunoblot analysis was used to determine ETR1 protein levels with an anti-ETR1 antibody in dark-grown seedlings; BIP serves a loading control. For the hypocotyl growth response of dark-grown seedlings to ethylene, seedlings were treated with 0 or 1 μL L^{-1} ethylene (n ≥ 10; horizontal line = mean). *P* values (blue) for significant differences in the ethylene responsiveness of seedlings, as determined by *t* test, are given for $P < 0.05$.

hydrogen bond to His69 to orient and polarize it for copper binding: a bidentate Cys-His (CH) model for copper coordination.

In addition to results from the recent in vitro study in which one copper per ETR1 monomer was detected (24), the DCH and CH models are favored over the earlier CCHH model for the following reasons. First, chemical analysis has demonstrated that both tridentate and bidentate ancillary ligands can effectively bind Cu(I) and form a Cu(I)–ethylene complex, the primary consideration being that anionic, electron-donating ancillary ligands foster the strongest backbonding of the filled Cu(I) 3d orbital to the unfilled ethylene π^* orbital (43, 44). Second, lower coordination numbers favor Cu(I) binding over that of Cu(II) and other divalent metal ions (45), supporting the existence of two or three copper-coordinating ligands, rather than four, with the ethylene receptors. Third, modeling of Cu(I) interactions with 1-methycyclopropene (1-MCP), a potent competitive inhibitor for ethylene binding, support Cu(I) being coordinated by no more than three ligands in addition to 1-MCP (46). We note that, even should subsequent studies provide support for the CCHH model with one Cu(I) per receptor dimer, the role(s) for Asp25 identified here in copper binding are still relevant.

Structural modeling supports the CH model over the DCH model, with Asp25 playing an indirect rather than a direct role in chelation of Cu(I). Support for the CH model is found with the previous *ab initio* structural model of the EBD (24) as well as our modeling the ETR1 homodimer with AlphaFold-Multimer (Fig. 7*C* and *SI Appendix*, Fig. S9, and Movies S1 and S2) (47, 48). AlphaFold-Multimer builds on the neural network-based AlphaFold to generate structural models of protein complexes, taking advantage of related amino-acid sequences and experimentally determined protein structures (47, 48). Using AlphaFold-Multimer, we generated structural models for the ETR1 homodimer for full-length ETR1 as well as for the EBD (Fig. 7*C* and *SI Appendix*, Fig. S9). The copper cofactors were modeled under two potential coordinations involving Cys65 and His69 of the ETR1 homodimer, one in which the two coppers are bound independently and do not share an interaction with each other, and another where they are closely bonded. Both the ab initio

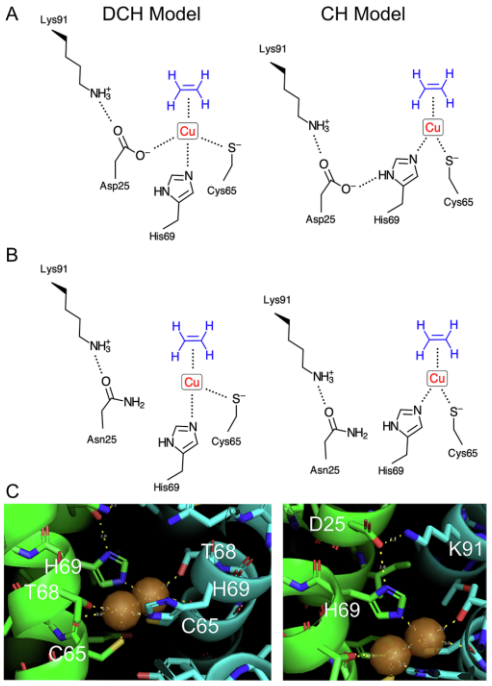

Fig. 7. Models for ETR1 interactions with copper(I) and ethylene. (*A*) Asp-Cys-His (DCH) and Cys-His (CH) models for how Asp25 contributes to copper(I) and ethylene binding and signal transmission via bonding with Lys91 in DCH and CH models. (*B*) Predicted effect of the Asn25 variant on molecular interactions at the ethylene-binding site. (*C*) AlphaFold-Multimer-based model of the ETR1 dimer (interacting coppers), with views highlighting copper-binding geometry (*Left*; H69-Cu = 2.3 Å, C65-Cu = 2.4 Å, T68-Cu = 2.7 Å, C65 backbone carbonyl-Cu = 3.0 Å) and interactions between His69, Asp25, and Lys91 (*Right*; D25-H69 = 2.8 Å, D25-K91 = 3.3 Å). (*SI Appendix*, Fig. S9 and Movies S1 and S2).

and AlphaFold models place Asp25 of helix I in proximity to Cys65 and His69 of helix II but not optimally positioned to interact with Cu(I). However, as shown in Fig. 7*C* for the AlphaFold model, the Asp25 carboxylate is well positioned to interact with the protonated nitrogen of the His sidechain. Thr68 and the backbone carbonyl of Cys65 are also close enough to potentially contribute to copper chelation, but an ETR1^{T68A} mutant still bound ethylene when expressed in yeast (20), indicating that Thr68 does not play a major role in copper chelation.

The CH model, in which the interaction of the Asp carboxylate with His contributes to Cu(I) binding may help explain the high binding affinity of the receptors for ethylene (5, 28). Such carboxylate–His–metal interactions are fairly common in proteins, being a form of indirect carboxylate–metal coordination, with the carboxylate thought to modulate the histidine to make it a more effective Lewis base and strengthen the metal complexation (49). This carboxylate-His structure is similar to that found in the well-characterized "catalytic triads" of serine proteases as well as in a host of other enzymes that also make use of an Asp–His interactions to facilitate hydrolytic and other enzymatic activities (50). The increase in the effectiveness of such enzymes may not just be due to increased nucleophilicity of the carboxylate-His, but also due to maintenance of the correct tautomer of His (e.g., N-1H vs N-3H) for the reaction (51, 52), another consideration that may apply to the ability of His69 of ETR1 to interact with the Cu(I) cofactor. Our enhanced understanding for mechanisms underlying high-affinity ethylene binding should facilitate the development of ethylene nanosensors for agricultural and industrial use (53, 54).

An unexpected but physiologically relevant finding from our studies was that the substitution of Asn for Asp25 of ETR1, unlike the other site-directed mutations examined, still allowed for ethylene binding but affected the binding kinetics. Experimental analyses of [^{14}C]ethylene binding in transgenic yeast and in planta are dependent on the extended half-life for dissociation of ethylene from the receptors, this being of over 12 h for ETR1^{wt} (5). Our inability to detect [^{14}C]ethylene binding by ETR1^{D25N} when assayed in transgenic yeast suggests a half-life for dissociation on the order of minutes or less (k_{off} increasing at least 100-fold), the consistency of the in planta results with those from yeast indicating that this difference in ethylene binding between ETR1^{wt} and ETR1^{D25N} is not an artifact of the transgenic yeast system. Interestingly, although Asp in found in 93.55% of the ETR1-like sequences examined (Fig. 1*A*), in some cases (3.67% of the sequences examined) it is substituted by an Asn residue, most commonly in cyanobacteria but also reportedly in the plants *P. communis* (Pear) and *C. cajan* (Pigeon pea). We consider it likely that the Asn-containing ethylene receptor-like proteins of cyanobacteria facilitate chemotaxis (55), the ability to rapidly detect and respond to changes in ligand concentration not being compatible with the extended binding kinetics associated with the typical plant receptors. Plants, with their slower release kinetics for ethylene, rely upon proteasome-dependent degradation of ethylene-bound receptors and transcriptional induction of new receptors to facilitate resensitization once environmental ethylene levels decrease (9, 33, 34, 56, 57).

Although deamidation of Asn and conversion to Asp has been reported to sometimes occur spontaneously in vivo (58, 59), such post-translational processing is not supported for the ETR1^{D25N} mutant based on structural and experimental considerations. First, ETR1^{D25N} lacks the Asn-Gly motif associated with deamidation but has a stabilizing Phe residue at position 26 (58, 59). Second, deamidation of Asn is suppressed in alpha-helices (60), such as are found in the TMD of ETR1. Third, we do not recover detectable ethylene binding for the ETR1^{D25N} mutant when assayed in yeast or in planta, such as would be expected if deamidation had occurred. Fourth, a small additive effect of the Asp25Asn mutation was observed when combined with the ETR1^{K91X} mutations, consistent with the presence of the Asp25Asn mutation and that it has functional consequences outside of its effect on ethylene binding.

Based on our findings, Asp25 of ETR1 plays a dual role in signaling, functioning in copper/ethylene binding as well as in internally transmitting information on ethylene binding to TM helix III through an association with Lys91 (Fig. 7). Coevolution analysis predicts a strong association between these two residues, both of which are highly conserved, the one residue acidic and the other basic, suggestive not only of physical proximity but the ability to make a strong polar bond. Mutations of Lys91did not affect copper binding of ETR1 but loss of its basic amino acid character resulted in decreased ethylene binding, potentially due to the receptor being unable to maintain the optimal conformation for ethylene binding and/or due to altered kinetics for ethylene binding as found for the Asp25Asn mutation. Of particular interest is the reduced functionality in the absence and presence of ethylene observed with the ETR1^{K91M}, ETR1$^{D25N, K91M}$, and some of the ETR1^{K91A} mutant lines, a phenotype consistent with a necessity to transmit conformational information from the ethylene binding site to TM helix

III. These mutants may be at an equilibrium between the conformations typically found in the absence ("on") and presence ("off") of ethylene, with ethylene no longer able to stabilize one conformation over the other. Alternatively, if the receptors can take on intermediate conformations, the receptors may be stuck in such an intermediate conformation. Critically, the results of these mutations indicate the importance of the basic character of Lys91 in maintaining functionality of ETR1, and how loss of this character uncouples ETR1 from the conformations needed to mediate responses in the absence and presence of ethylene.

The dual role for Asp25 supported by our study of ETR1 is remarkably like the role proposed for Asp180 in a model for the mouse olfactory receptor MOR244-3 (61). This olfactory receptor is responsive to organosulfur odorants and has a binding site with a required Cu(I) cofactor coordinated by Cys, His, and possibly an Asn residue (61, 62). Like the ethylene receptors, the copper cofactor is required for the MOR244-3 receptor to assume its active conformation, and the ligands (ethylene or methylthio-methanethiol) exert inverse agonist effects on receptor activity (18, 20, 61–64). In the model of the MOR244-3 binding site, Asp180 forms hydrogen bonds to the Cu-coordinating His105 and also to Lys269 (61). These two evolutionarily distinct receptors, both employing a Cu(I) cofactor and exhibiting high affinity for their ligands, may have converged on a similar mechanism to enhance the performance of the Cu(I)-chelating His and relaying intramolecular changes in response to ligand binding.

Materials and Methods

Detailed information is provided in *SI Appendix, Materials and Methods*. All Arabidopsis lines were of the Columbia (Col-0) accession. The *etr1-1* and *etr1-6 etr2-3 ein4-4* mutant lines have been described (4, 18, 26). Analyses of the triple response and short-term kinetic response of dark-grown Arabidopsis seedlings to ethylene were performed as described (28, 33, 65). Primers used for mutagenesis of ETR1 are listed in *SI Appendix*, Table S2. For plant transformation, constructs were introduced into *Agrobacterium tumefaciens* strain GV3101 and transformed into the *etr1-6 etr2-3 ein4-4* background (18) by the floral-dip method (66). Yeast constructs were transformed into the yeast *Saccharomyces cerevisiae* strain FY834 (MATα his3Δ200 ura3-52 leu2Δ1 lys2Δ202 trp1Δ63 GAL2+) (67).

For generation of CRISPR-Cas9 mutant lines targeting ERS1 and ERS2, guide RNAs were designed using CRISPR-P 2.0 (68) and the gRNA cassette cloned into the pCAMBIA2300-Cas9 vector (69). Heat stress treatment of transgenic lines was used to increase the efficiency of CRISPR-Cas9 mutagenesis (70). Genomic DNA was isolated (71), and the region surrounding the CRISPR target sequence sequenced using primers given in *SI Appendix*, Table S2. Characteristics of the indel mutations are given in *SI Appendix*, Fig. S7.

Copper binding of ETR1 in vitro was monitored spectrophotometrically by measuring absorbance of the purple BCA2-Cu(I) complex as described (24). Saturable ethylene binding to Arabidopsis seedlings and transgenic yeast expressing ETR1 was determined by analyzing binding to [^{14}C]ethylene in the presence or absence of excess [^{12}C]ethylene (5, 31). For ethylene-binding assays in yeast, ETR1 was expressed in the yeast *S. cerevisiae* (strain FY834) (5, 67, 72). For ethylene binding assays with Arabidopsis seedlings, 2-wk-old green seedlings were used.

Immunodetection of ETR1 in plants and transgenic yeast was performed as described (56), using an anti-ETR1 antibody generated against amino acids 401-738 of ETR1 (10). RNA isolation and RT-qPCR was performed as described (73) with three biological replicates. Relevant primers are listed in *SI Appendix*, Table S2.

For the coevolutionary analysis, we used EVCOUPLINGS and GREMLIN web servers to predict interactions/contacting residues in the EBD of ETR1 (37, 38). Results from EVCOUPLINGS are reported for the recommended result, which is based on the analysis of 1,221 sequences and an overall quality score of 9 (*SI Appendix*, Table S1). For GREMLIN, the multiple sequence alignment was performed by HHBLITS and the alignment then filtered to remove regions where the gap was greater than 75. An ab initio structural model of the EBD has been previously described (24). New structural models for the ETR1 homodimer were generated with AlphaFold-Multimer (47, 48). Coppers were modeled under two potential coordinations involving Cys65 and His69 of the ETR1 homodimer, one in which the two coppers are bound independently and do not share an interaction with each other, and another where they are closely bonded. Coordinates of the full-length ETR1 structural models with copper are available as Protein Data Bank (PDB) and PyMOL (74) files at https://digitalcommons.dartmouth.edu/facoa/4313 (75).

Statistical analyses were performed in Prism (GraphPad Software, Inc.) or using an online calculator (astatsa.com/OneWay_Anova_with_TukeyHSD/).

Data, Materials, and Software Availability. All other data are included in the manuscript and/or supporting information. Coordinates for the ETR1 structural models are available at the Dartmouth Digital Commons (https://digitalcommons.dartmouth.edu/facoa/4313) (75).

ACKNOWLEDGMENTS. This work was supported by grants from the NSF (MCB-1517032 to G.E.S., G. Grigoryan, and B.M.B..; IOS-1856513 to G.E.S.; MCB-1817304 to B.M.B.), by the Deutsche Forschungsgemeinschaft (German Research Foundation) project no. 267205415/CRC 1208 grant to G. Groth (TP B06), and by the International Research Support Initiative Program of Higher Education Commission of Pakistan to B.J.A. and S. Abbas.

Author affiliations: [a]Department of Biological Sciences, Dartmouth College, Hanover, NH 03755; [b]Department of Biochemistry, Quaid-i-azam University, Islamabad 45320, Pakistan; [c]Institute of Biochemical Plant Physiology, Heinrich Heine University Düsseldorf, 40225 Düsseldorf, Germany; [d]Department of Computer Science, Dartmouth College, Hanover, NH 03755; and [e]Department of Biochemistry and Cellular & Molecular Biology, University of Tennessee, Knoxville, TN 37996

Author contributions: G. Grigoryan and G.E.S. designed research; B.J.A., S. Abbas, S. Aman, M.V.Y., W.C., L.M., B.U., D.A.J., J.D., S.N.S., B.M.B., G. Grigoryan, and G.E.S. performed research; B.J.A., S. Abbas, S. Aman, M.V.Y., W.C., L.M., B.U., D.A.J., S.N.S., G. Groth, B.M.B., G. Grigoryan, and G.E.S. analyzed data; G. Groth, G. Grigoryan, and G.E.S. supervised research; and B.J.A., G. Grigoryan, and G.E.S. wrote the paper.

1. F. B. Abeles, P. W. Morgan, M. E. Saltveit Jr., *Ethylene in Plant Biology* (Academic Press, San Diego, ed. 2, 1992).
2. B. M. Binder, Ethylene signaling in plants. *J. Biol. Chem.* **295**, 7710–7725 (2020).
3. K. N. Chang *et al.*, Temporal transcriptional response to ethylene gas drives growth hormone cross-regulation in Arabidopsis. *eLife* **2**, e00675 (2013).
4. C. Chang, S. F. Kwok, A. B. Bleecker, E. M. Meyerowitz, Arabidopsis ethylene response gene *ETR1*: Similarity of product to two-component regulators. *Science* **262**, 539–544 (1993).
5. G. E. Schaller, A. B. Bleecker, Ethylene-binding sites generated in yeast expressing the Arabidopsis *ETR1* gene. *Science* **270**, 1809–1811 (1995).
6. B. M. Binder, C. Chang, G. E. Schaller, "Perception of ethylene by plants: Ethylene receptors" in *Annual Plant Reviews: The Plant Hormone Ethylene*, M. T. McManus, Ed. (Wiley-Blackwell, 2012), **vol. 44**, pp. 117–145.
7. F. I. Rodriguez *et al.*, A copper cofactor for the ethylene receptor ETR1 from Arabidopsis. *Science* **283**, 996–998 (1999).
8. A. E. Hall, Q. G. Chen, J. L. Findell, G. E. Schaller, A. B. Bleecker, The relationship between ethylene binding and dominant insensitivity conferred by mutant forms of the ETR1 ethylene receptor. *Plant Physiol.* **121**, 291–299 (1999).
9. Y.-F. Chen *et al.*, Ligand-induced degradation of the ethylene receptor ETR2 through a proteasome-dependent pathway in Arabidopsis. *J. Biol. Chem.* **282**, 24752–24758 (2007).
10. Y. F. Chen, M. D. Randlett, J. L. Findell, G. E. Schaller, Localization of the ethylene receptor ETR1 to the endoplasmic reticulum of Arabidopsis. *J. Biol. Chem.* **277**, 19861–19866 (2002).
11. C.-H. Dong, M. Rivarola, J. S. Resnick, B. D. Maggin, C. Chang, Subcellular co-localization of Arabidopsis RTE1 and ETR1 supports a regulatory role for RTE1 in ETR1 ethylene signaling. *Plant J.* **53**, 275–286 (2008).
12. C. Grefen *et al.*, Subcellular localization and in vivo interaction of the *Arabidopsis thaliana* ethylene receptor family members. *Mol. Plant* **1**, 308–320 (2008).
13. Z. Gao *et al.*, Heteromeric interactions among ethylene receptors mediate signaling in Arabidopsis. *J. Biol. Chem.* **283**, 23081–23810 (2008).
14. G. E. Schaller, J. J. Kieber, "Ethylene", *The Arabidopsis Book*, C. Somerville, E. Meyerowitz, Eds., 1–18 (2002).
15. R. L. Gamble, M. L. Coonfield, G. E. Schaller, Histidine kinase activity of the ETR1 ethylene receptor from Arabidopsis. *Proc. Natl. Acad. Sci. U.S.A.* **95**, 7825–7829 (1998).
16. G. E. Schaller, S. H. Shiu, J. P. Armitage, Two-component systems and their co-option for eukaryotic signal transduction. *Curr. Biol.* **21**, R320–R330 (2011).

17. W. Wang, A. E. Hall, R. O'Malley, A. B. Bleecker, Canonical histidine kinase activity of the transmitter domain of the ETR1 ethylene receptor from Arabidopsis is not required for signal transmission. *Proc. Natl. Acad. Sci. U.S.A.* **100**, 352–357 (2003).
18. J. Hua, E. M. Meyerowitz, Ethylene responses are negatively regulated by a receptor gene family in *Arabidopsis thaliana*. *Cell* **94**, 261–271 (1998).
19. X. Qu, B. P. Hall, Z. Gao, G. E. Schaller, A strong constitutive ethylene response phenotype conferred on Arabidopsis plants containing null mutations in the ethylene receptors *ETR1* and *ERS1*. *BMC Plant Biol.* **7**, 3 (2007).
20. W. Wang *et al.*, Identification of important regions for ethylene binding and signaling in the transmembrane domain of the ETR1 ethylene receptor of Arabidopsis. *Plant Cell* **18**, 3429–3442 (2006).
21. R. F. Lacey, B. Binder, Ethylene regulates the physiology of the Cyanobacterium Synechocystis sp. PCC 6803 via an ethylene receptor. *Plant Physiol.* **171**, 2798–2809 (2016), 10.1104/pp.16.00602.
22. G. E. Schaller, A. N. Ladd, M. B. Lanahan, J. M. Spanbauer, A. B. Bleecker, The ethylene response mediator ETR1 from Arabidopsis forms a disulfide-linked dimer. *J. Biol. Chem.* **270**, 12526–12530 (1995).
23. B. M. Binder, F. I. Rodriguez, A. B. Bleecker, S. E. Patterson, The effects of Group 11 transition metals, including gold, on ethylene binding to the ETR1 receptor and growth of Arabidopsis thaliana. *FEBS Lett.* **581**, 5105–5109 (2007).
24. S. Schott-Verdugo, L. Muller, E. Classen, H. Gohlke, G. Groth, Structural model of the ETR1 ethylene receptor transmembrane sensor domain. *Sci. Rep.* **9**, 8869 (2019).
25. G. Cutsail 3rd *et al.*, Spectroscopic and QM/MM studies of the Cu(I) binding site of the plant ethylene receptor ETR1. *Biophys J.* **121**, 3862–3873 (2022).
26. A. B. Bleecker, M. A. Estelle, C. Somerville, H. Kende, Insensitivity to ethylene conferred by a dominant mutation in *Arabidopsis thaliana*. *Science* **241**, 1086–1089 (1988).
27. A. Kugele *et al.*, Mapping the helix arrangement of the reconstituted ETR1 ethylene receptor transmembrane domain by EPR spectroscopy. *RSC Adv.* **12**, 7352–7356 (2022).
28. B. M. Binder, L. A. Mortimore, A. N. Stepanova, J. R. Ecker, A. B. Bleecker, Short-term growth responses to ethylene in Arabidopsis seedlings are EIN3/EIL1 independent. *Plant Physiol.* **136**, 2921–2927 (2004).
29. R. C. O'Malley *et al.*, Ethylene-binding activity, gene expression levels, and receptor system output for ethylene receptor family members from Arabidopsis and tomato. *Plant J.* **41**, 651–659 (2005).
30. R. F. Lacey, B. M. Binder, Ethylene regulates the physiology of the cyanobacterium synechocystis sp. PCC 6803 via an ethylene receptor. *Plant Physiol.* **171**, 2798–2809 (2016).
31. B. M. Binder, G. E. Schaller, Analysis of ethylene receptors: Ethylene-binding assays. *Methods Mol. Biol.* **1573**, 75–86 (2017).
32. X. Qu, G. E. Schaller, Requirement of the histidine kinase domain for signal transduction by the ethylene receptor ETR1. *Plant Physiol.* **136**, 2961–2970 (2004).
33. B. M. Binder *et al.*, Arabidopsis seedling growth response and recovery to ethylene. A kinetic analysis. *Plant Physiol.* **136**, 2913–2920 (2004).
34. B. J. Azhar, A. Zulfiqar, S. N. Shakeel, G. E. Schaller, Amplification and adaptation in the ethylene signaling pathway. *Small Methods* **4**, 1900452 (2019), 10.1002/smtd.201900452.
35. B. K. McDaniel, B. M. Binder, ETHYLENE RECEPTOR 1 (ETR1) is Sufficient and has the predominant role in mediating inhibition of ethylene responses by silver in Arabidopsis thaliana. *J. Biol. Chem.* **287**, 26094–26103 (2012).
36. G. E. Schaller, B. M. Binder, Inhibitors of ethylene biosynthesis and signaling. *Methods Mol. Biol* **1573**, 223–235 (2017).
37. T. A. Hopf *et al.*, The EVcouplings Python framework for coevolutionary sequence analysis. *Bioinformatics* **35**, 1582–1584 (2019).
38. S. Ovchinnikov, H. Kamisetty, D. Baker, Robust and accurate prediction of residue-residue interactions across protein interfaces using evolutionary information. *eLife* **3**, e02030 (2014).
39. K. A. Koch, M. M. Pena, D. J. Thiele, Copper-binding motifs in catalysis, transport, detoxification and signaling. *Chem. Biol.* **4**, 549–560 (1997).
40. A. Sharma, D. Sharma, S. K. Verma, In silico study of iron, zinc and copper binding proteins of Pseudomonas syringae pv. lapsa: Emphasis on secreted metalloproteins. *Front Microbiol.* **9**, 1838 (2018).
41. R. H. Holm, P. Kennepohl, E. I. Solomon, Structural and functional aspects of metal sites in biology. *Chem. Rev.* **96**, 2239–2314 (1996).
42. R. Balamurugan, M. Palaniandavar, R. S. Gopalan, Trigonal planar copper(I) complex: Synthesis, structure, and spectra of a redox pair of novel copper(II/I) complexes of tridentate bis(benzimidazol-2'-yl) ligand framework as models for electron-transfer copper proteins. *Inorg Chem.* **40**, 2246–2255 (2001).
43. K. M. Light, J. A. Wisniewski, W. A. Vinyard, M. T. Kieber-Emmons, Perception of the plant hormone ethylene: Known-knowns and known-unknowns. *J. Biol. Inorg Chem.* **21**, 715–728 (2016).
44. J. B. Geri, N. C. Pernicone, J. T. York, Comparing the impact of different supporting ligands on copper(I)-ethylene interactions. *Polyhedron* **52**, 207–215 (2013).
45. A. V. Davis, T. V. O'Halloran, A place for thioether chemistry in cellular copper ion recognition and trafficking. *Nat. Chem. Biol.* **4**, 148–151 (2008).
46. S. Joy, G. Periyasamy, Binding mode of 1-methylcyclopropene, an ethylene antagonist in various copper models. *Comput. Theor. Chem.* **1171**, 112662 (2020).
47. R. Evans *et al.*, Protein complex prediction with AlphaFold-Multimer. bioRxiv [Preprint] (2021). https://doi.org/10.1101/2021.10.04.463034 (Accessed 10 March 2022).
48. J. Jumper *et al.*, Highly accurate protein structure prediction with AlphaFold. *Nature* **596**, 583–589 (2021).
49. D. W. Christianson, R. S. Alexander, Carboxylate-histidine-zinc interactions in protein structure and function. *J. Am. Chem. Soc.* **111**, 6412–6419 (1989).
50. A. Rauwerdink, R. J. Kazlauskas, How the same core catalytic machinery catalyzes 17 different reactions: The serine-histidine-aspartate catalytic triad of alpha/beta-hydrolase fold enzymes. *ACS Catal.* **5**, 6153–6176 (2015).
51. K. D. Cramer, S. C. Zimmerman, Kinetic effect of a syn-oriented carboxylate on a proximate imidazle in catalysis: A model for the histidine-aspartate couple in enzymes. *J. Am. Chem. Soc.* **112**, 3680–3682 (1990).
52. S. Sprang *et al.*, The three-dimensional structure of Asn102 mutant of trypsin: Role of Asp102 in serine protease catalysis. *Science* **237**, 905–909 (1987).
53. K. Vong *et al.*, An artificial metalloenzyme biosensor can detect ethylene gas in fruits and Arabidopsis leaves. *Nat. Commun.* **10**, 5746 (2019).
54. B. Esser, J. M. Schnorr, T. M. Swager, Selective detection of ethylene gas using carbon nanotube-based devices: Utility in determination of fruit ripeness. *Angew. Chem. Int. Ed. Engl.* **51**, 5752–5756 (2012).
55. M. Mutalipassi *et al.*, Symbioses of cyanobacteria in marine environments: Ecological insights and biotechnological perspectives. *Mar. Drugs* **19**, 227 (2021).
56. S. N. Shakeel *et al.*, Ethylene regulates levels of ethylene receptor/CTR1 signaling complexes in Arabidopsis thaliana. *J. Biol. Chem.* **290**, 12415–12424 (2015).
57. B. M. Kevany, D. M. Tieman, M. G. Taylor, V. D. Cin, H. J. Klee, Ethylene receptor degradation controls the timing of ripening in tomato fruit. *Plant J.* **51**, 458–467 (2007).
58. N. E. Robinson, A. B. Robinson, Prediction of protein deamidation rates from primary and three-dimensional structure. *Proc. Natl. Acad. Sci. U.S.A.* **98**, 4367–4372 (2001).
59. N. E. Robinson, A. B. Robinson, Molecular clocks. *Proc. Natl. Acad. Sci. U.S.A.* **98**, 944–949 (2001).
60. A. A. Kosky, U. O. Razzaq, M. J. Treuheit, D. N. Brems, The effects of alpha-helix on the stability of Asn residues: Deamidation rates in peptides of varying helicity. *Protein Sci.* **8**, 2519–2523 (1999).
61. S. Sekharan *et al.*, QM/MM model of the mouse olfactory receptor MOR244-3 validated by site-directed mutagenesis experiments. *Biophys. J.* **107**, L5–L8 (2014).
62. X. Duan *et al.*, Crucial role of copper in detection of metal-coordinating odorants. *Proc. Natl. Acad. Sci. U.S.A.* **109**, 3492–3497 (2012).
63. T. Hirayama *et al.*, RESPONSIVE-TO-ANTAGONIST1, a Menkes/Wilson disease-related copper transporter, is required for ethylene signaling in Arabidopsis. *Cell* **97**, 383–393 (1999).
64. K. E. Woeste, J. J. Kieber, A strong loss-of-function mutation in RAN1 results in constitutive activation of the ethylene response pathway as well as a rosette-lethal phenotype. *Plant Cell* **12**, 443–455 (2000).
65. B. P. Hall *et al.*, Histidine kinase activity of the ethylene receptor ETR1 facilitates the ethylene response in Arabidopsis. *Plant Physiol.* **159**, 682–695 (2012).
66. S. J. Clough, A. F. Bent, Floral dip: A simplified method for Agrobacterium-mediated transformation of Arabidopsis thaliana. *Plant J.* **16**, 735–743 (1998).
67. F. Winston, C. Dollard, S. L. Ricupero-Hovasse, Construction of a set of convenient Saccharomyces cerevisiae strains that are isogenic to S288C. *Yeast* **11**, 53–55 (1995).
68. H. Liu *et al.*, CRISPR-P 2.0: An improved CRISPR-Cas9 tool for genome editing in plants. *Mol. Plant* **10**, 530–532 (2017).
69. C. J. Denbow *et al.*, Gateway-compatible CRISPR-Cas9 vectors and a rapid detection by high-resolution melting curve analysis. *Front. Plant Sci.* **8**, 1171 (2017).
70. C. LeBlanc *et al.*, Increased efficiency of targeted mutagenesis by CRISPR/Cas9 in plants using heat stress. *Plant J.* **93**, 377–386 (2018).
71. I. Kasajima, Y. Ide, N. Ohkama-Ohtsu, T. Yoneyama, T. Fujiwara, A protocol for rapid DNA extraction from *Arabidopsis thaliana* for PCR analysis. *Plant Mol. Biol. Rep.* **22**, 49–52 (2004).
72. C. Hadfield, A. M. Cashmore, P. A. Meacock, An efficient chloramphenicol-resistance marker for *Saccharomyces cerevisiae* and *Escherichia coli*. *Gene* **45**, 149–158 (1986).
73. M. I. Rai *et al.*, The ARGOS gene family functions in a negative feedback loop to desensitize plants to ethylene. *BMC Plant Biol.* **15**, 157 (2015).
74. E. F. Pettersen *et al.*, UCSF ChimeraX: Structure visualization for researchers, educators, and developers. *Protein Sci.* **30**, 70–82 (2021).
75. B. J. Azhar *et al.*, Structural files for the ETR1 ethylene-*receptor* dimer based on computational modeling. *Dartmouth Scholarship.* **4313**. (2023) https://digitalcommons.dartmouth.edu/facoa/4313.

PNAS

Supporting Information for

Basis for high-affinity ethylene binding by the ethylene receptor ETR1 of Arabidopsis

Beenish J. Azhar[1,2], Safdar Abbas[1,2], Sitwat Aman[1], Maria V. Yamburenko[1], Wei Chen[1], Lena Müller[3], Buket Uzun[3], David A. Jewell[1], Jian Dong[1], Samina N. Shakeel[1,2], Georg Groth[3], Brad M. Binder[4], Gevorg Grigoryan[1,5]*, G. Eric Schaller[1]*

G. Eric Schaller, Gevorg Grigoryan
Email: george.e.schaller@dartmouth.edu; gevorg.grigoryan@dartmouth.edu

This PDF file includes:

Supplemental Materials and Methods
Figures S1 to S9
Tables S1 to S2

Other supporting materials for this manuscript include the following:

Movies S1 to S2.

Materials and Methods

Plant materials and growth conditions
All Arabidopsis lines were of the Columbia (Col-0) accession. The *etr1-1* and *etr1-6 etr2-3 ein4-4* mutant lines have been described (1-3). Analysis of the triple response of dark-grown Arabidopsis seedlings to ethylene was performed as described (4). Briefly, seedlings were grown at 22˚C on vertically oriented plates on half-strength Murashige and Skoog basal medium with Gamborg's vitamins (pH 5.75; Sigma), 0.8% (w/v) agar, and 5 μM aminoethoxyvinylglycine (AVG) to inhibit ethylene biosynthesis. The stratified seed was exposed to light for 8 hr then moved to the dark in the presence or absence of ethylene, with analysis of the seedling growth being performed following 4 days total growth. Inhibition of seedling ethylene responses was accomplished by growth with 100 μM silver nitrate or treatment with 1 μL L^{-1} 1-methylcyclopropene (1-MCP) (5). For short-term kinetic analysis of dark-grown seedlings, time-lapse imaging and growth rate analysis of hypocotyls were carried out as described (6, 7).

Generation of site-directed mutations
ETR1 constructs used for expression in Arabidopsis were all derived from a 7.3-kb genomic ETR1 fragment containing the full-length coding sequence and native genomic promoter in the vector pCAMBIA1380 (8). Site directed mutagenesis was performed according to the manufacturers with the QuikChangeII XL Site Directed Mutagenesis Kit (Agilent Technologies) for mutations of Asp25 or with the Q5 Site-Directed Mutagenesis kit (NEB) for mutations at other sites. Primers used for mutagenesis are listed in Table S2. For plant transformation, constructs were introduced into *Agrobacterium tumefaciens* strain GV3101 and transformed into the *etr1-6 etr2-3 ein4-4* background (3) by the floral-dip method (9). Lines containing single sites of insertion for the transgene were identified based on segregation of hygromycin resistance and brought to homozygosity for analysis.

ETR1 constructs used for expression in yeast were all derived from an ETR1 cDNA driven by the ADH1 promoter in the vector pYcDE-2 (10). Site-directed mutations of Asp25 were introduced using the same primers and methodologies described above for expression of ETR1 in Arabidopsis. Mutations of Lys91 were introduced by replacing a Msc I-Sac I restriction fragment in the ETR1 cDNA with that from the genomic ETR1 mutant. Yeast constructs were transformed into the yeast *Saccharomyces cerevisiae* strain FY834 (MATα his3Δ200 ura3-52 leu2Δ1 lys2Δ202 trp1Δ63 GAL2+) (11).

Generation of CRISPR-Cas9 mutant lines targeting *ERS1* and *ERS2*
To target *ERS1* and *ERS2*, a tandem CRISPR cassette was synthesized that encoded four sgRNAs (two against *ERS1* and two against *ERS2*) driven by U6 promoters and surrounded by Hpa I and Nae I sites and cloned into pUC57 (General Biosystems) (Figure S7). The guide RNAs were designed using CRISPR-P 2.0 (12) to introduce indel mutations in the first exons of *ERS1* and *ERS2* that encode the ethylene binding site. The Hpa I/Nae I fragment containing the gRNA cassette was cloned into the Pme I site of the pCAMBIA2300-Cas9 vector, which had been generated by taking the Nsi I/Kpn I restriction fragment with Cas9 from the plasmid pMTN3164 (13) and cloning into the Nsi I/Pst I sites of pCambia2300 GenBank™ accession no. AF234315). The CRISPR-ERS1/ERS2 plasmid was transformed into the Agrobacterium strain GV3101, and the Arabidopsis line $ETR1^{D25N}$-#6 (*etr1 etr2 ein4*) transformed by the floral dip method (9). Heat stress treatment of transgenic lines was used to increase the efficiency of CRISPR-Cas9 mutagenesis (14).

For identification and genotyping of CRISPR/Cas9 mutants, genomic DNA was isolated (15), and the region surrounding the CRISPR target sequence amplified by PCR and sequenced using primers given in Table S2. The presence of the T-DNA insert containing the Cas9 cassette was determined by PCR using primers for the KanR gene (Table S2). Two independent $ETR1^{D25N}$ (*etr1 etr2 ein4 ers1 ers2*) lines were generated (#11 and #15), line #11 being Cas9 (-/-) and line #15 being Cas9(+/+). Characteristics of the indel mutations and lines used for study are given in Figure S7.

Immunoblot analysis

For yeast, total protein was extracted by bead-beating as described (16) using a Mixer Mill 400 tissue homogenizer (Retsch). For plants, microsomes were isolated from seedlings as described (17). ETR1 was identified by use of a polyclonal anti-ETR1 antibody generated against amino acids 401-738 of ETR1 (18). Immunoblot analysis was performed as described (17), using an anti-BIP antibody or Ponceau-S staining for protein as loading controls. Immunodecorated proteins were visualized and quantified by chemiluminescence using the chemiDoc MP imaging system (BIORAD).

Copper binding assay
Copper binding was monitored spectrophotometrically by measuring absorbance of the purple BCA2-Cu(I) complex as described (19). Titration curves were corrected for nonspecific binding observed with chemically and thermally denatured receptor to maximize signal to background levels.

Ethylene binding assay
[^{14}C]ethylene (specific activity = 116 mCi/mmol) was obtained from ViTrax Radiochemicals (Placentia, CA) and trapped as the mercuric perchlorate complex as described (10, 20). For ethylene binding assays in yeast, ETR1 was expressed in the yeast *Saccharomyces cerevisiae* (strain FY834) (11) using the vector pYcDE-2 and a constitutive ADC1 promoter (10, 21). The yeast growth media was supplemented with 40 µg L^{-1} copper sulfate. Saturable ethylene binding to yeast was determined by analyzing binding of 0.3 g yeast per sample to 0.21 µL L^{-1} [^{14}C]ethylene, in the presence or absence of excess [^{12}C]ethylene (10, 20).

For ethylene binding assays with Arabidopsis seedlings, two-week-old green seedlings were used that had been grown on media containing 5 µM AVG to inhibit ethylene biosynthesis, with ~1 g seedlings per sample. The fresh weight of seedlings was determined, and each sample packaged into bags formed from a layer of cheese cloth and stapled at the top. Humidity was maintained in the ethylene binding chambers by use of moistened paper towels. Saturable ethylene binding was determined by analyzing binding to 0.31 µL L^{-1} [^{14}C]ethylene, in the presence or absence of excess [^{12}C]ethylene (10, 20).

RNA Expression Analysis
RNA isolation and RT-qPCR was performed as described (22), with three biological replicates and two technical replicates of each. Primers for genes and the control tubulin gene used for normalization are listed in Table S2.

Evolutionary analysis to predict contacting residues of ETR1
For the coevolutionary analysis we used EVCOUPLINGS and GREMLIN web servers to predict interactions/contacting residues in the EBD of ETR1 (23, 24). The 1-112 amino-acid sequence of ETR1 was used as an input for both servers. The EVCOUPLINGs algorithm derives residue-residue evolutionary couplings (ECs) from deep multiple sequence alignment by pseudo-likelihood maximization method. We used the default settings for finding the evolutionary couplings between contacting residues where residue contact distance threshold was set to 5 and maximum rank was 1. Results are reported for the recommended result, which is based on the analysis of 1221 sequences and an overall quality score of 9 (Table S1). For GREMLIN, the multiple sequence alignment was performed by HHBLITS and the alignment then filtered to remove regions where the gap was greater than 75.

Structural models of the EBD
An *ab initio* structural model of the EBD has been previously described (19). New structural models for the ETR1 homodimer were generated for full-length ETR1 as well as for the EBD (amino acids 1-128) with AlphaFold-Multimer, which builds on the neural network-based AlphaFold to generate structural models of protein complexes (25, 26). Coppers were modeled under two potential coordinations involving Cys65 and His69 of the ETR1 homodimer, one in which the two coppers are bound independently and do not share an interaction with each other, and another where they are closely bonded. Molecular graphics were generated with the PyMOL Molecular Graphics System, Version 2.5 Schrödinger, LLC and with USCF ChimeraX, Version

1.4 (27). Coordinates of the full-length ETR1 structural models with copper are available as PDB and PyMOL files at https://digitalcommons.dartmouth.edu/facoa/4313.

Statistical Analysis
Unpaired T-tests were performed in Prism (GraphPad Software, Inc.), without the assumption of a consistent SD, to obtain the individual P values. ANOVA-based statistical analyses were performed using an online calculator (astatsa.com/OneWay_Anova_with_TukeyHSD/).

Gene Identifiers
ETR1 (At1g66340), *ETR2* (At3g23150), *EIN4* (At3g04580), *ERS1* (At2g40940), *ERS2* (At1g04310), *ERF1* (At3g23240), *ARGOS* (At3g59900), *OSR1* (At2g41230), *EXP5* (At3g29030), *EXPb1* (At2g20750), *CAPE2* (At4G25780), *B-TUB3* (At5G62700)

4

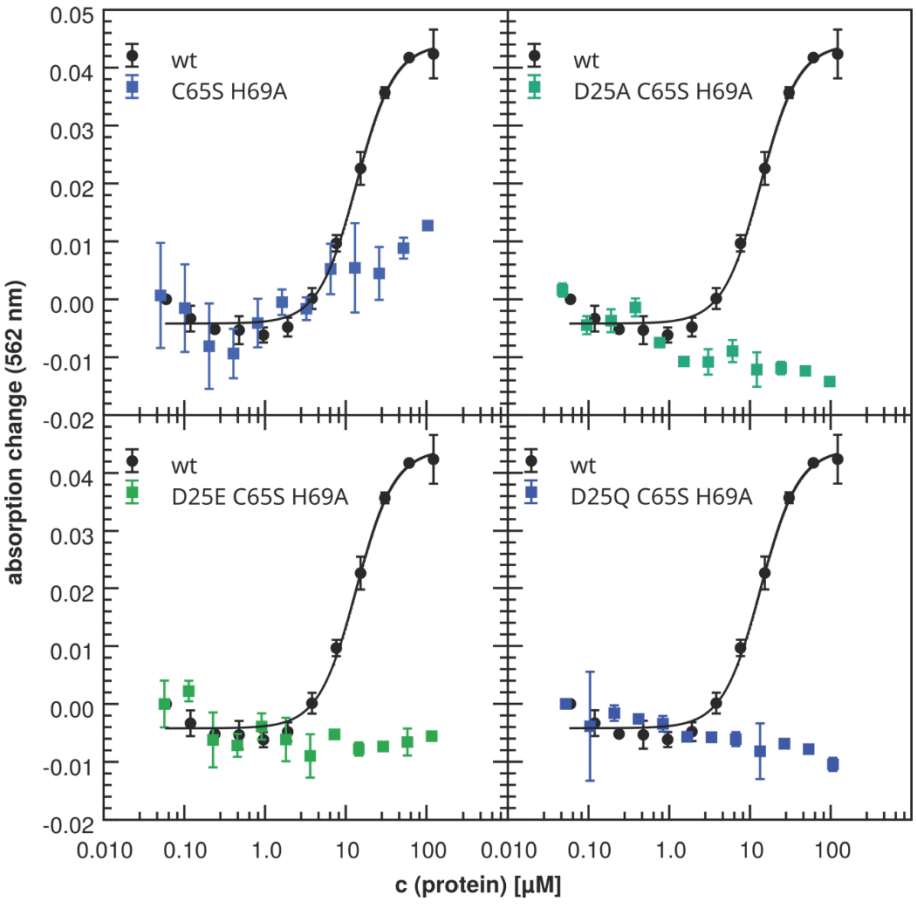

Figure S1. Copper binding by wild-type, Cys65 His69 double mutant, and Asp25 mutant versions of ETR1

Copper binding of wild-type and mutant versions of ETR1 transmembrane domain (ETR1-TMD; n = 3). Purified ETR1-TMD was titrated to the BCA_2-Cu(I) complex, and copper binding monitored spectrophotometrically based on the change in absorbance at 562 nm. For comparison, copper binding of a Cys65Ser His69Ala mutation was examined alone and in combination with the Asp25 mutations.

5

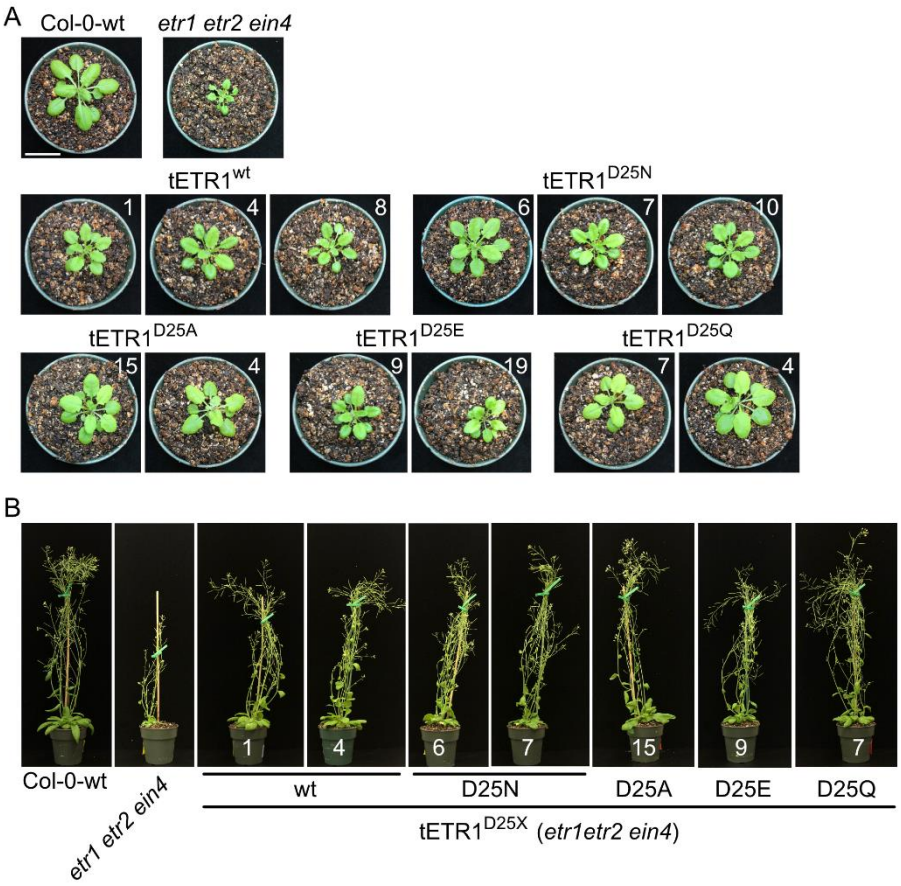

Figure S2. Adult plant phenotypes of ETR1^{D25X} mutants
The tETR1^{D25X} plants in the *etr1 etr2 ein4* background are compared to the wild type and the *etr1 etr2 ein4* mutant. The *etr1 etr2 ein4* mutant exhibits reduced growth due to its partial constitutive ethylene-response phenotype, and this can be rescued by transgenic expression of *ETR1*. The tETR1^{D25X} line numbers are indicated.
(A) Representative rosettes of 28-day-old plants. Scale bar = 2 cm.
(B) Representative adult plants with inflorescences.

6

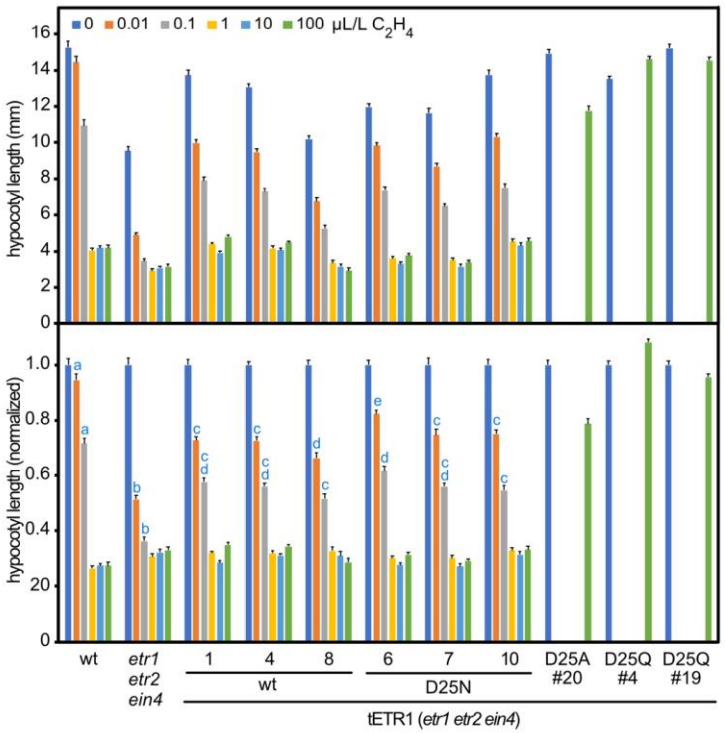

Figure S3. Ethylene dose response analysis of Arabidopsis seedlings expressing Asp25 mutants (bar graphs of data from Figure 2C). Hypocotyl growth in dark-grown seedlings for the wild type (wt), the *etr1 etr2 ein4* triple mutant, and the triple mutant complemented with $ETR1^{wt}$ or $ETR1^{D25}$ was determined at 0, 0.01. 0.1, 1, 10, and 100 µL/L ethylene. Representative ethylene-insensitive $tETR1^{D25A}$-#20, $tETR1^{D25E}$-#19, and $tETR1^{D25Q}$-#4 lines were also included and examined at 0 and 100 µL L^{-1} ethylene. The growth response is graphed based on hypocotyl length in mm (top) and normalized for each line relative to its hypocotyl length at 0 µL/L ethylene (bottom) (n ≥ 17; error bar = SE). For the normalized hypocotyl length, different blue letters indicate a significant difference between lines at 0.01 and 0.1 µL/L ethylene (ANOVA with post-hoc Holm multiple comparison calculation; P<0.05).

7

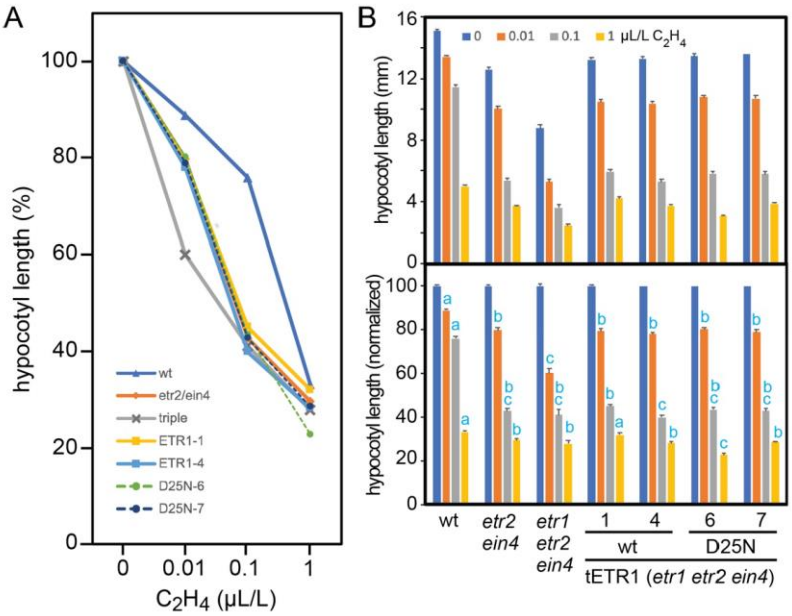

Figure S4. The ETR1^{wt} or ETR1^{D25N} transgenic lines in the *etr1 etr2 ein4* background exhibit similar ethylene sensitivity to an *etr2 ein4* mutant. Hypocotyl growth in dark-grown seedlings for the wild type (wt), the *etr2 ein4* double mutant, the *etr1 etr2 ein4* triple mutant, and two lines each for the triple mutant complemented with ETR1^{wt} or ETR1^{D25N} was determined at 0, 0.01. 0.1, and 1 µL/L ethylene (n ≥ 10). (A) Dose response curves. The ethylene response is normalized for each line relative to its hypocotyl length at 0 µL/L ethylene (SE not shown for clarity). (B) Bar graphs of data. The growth response is graphed based on hypocotyl length in mm (top) and normalized for each line relative to its hypocotyl length at 0 µL/L ethylene (bottom) (error bar = SE). For the normalized hypocotyl length, different blue letters indicate a significant difference between lines at 0.01, 0.1, and 1 µL/L ethylene (ANOVA with post-hoc Holm multiple comparison calculation; P<0.05).

8

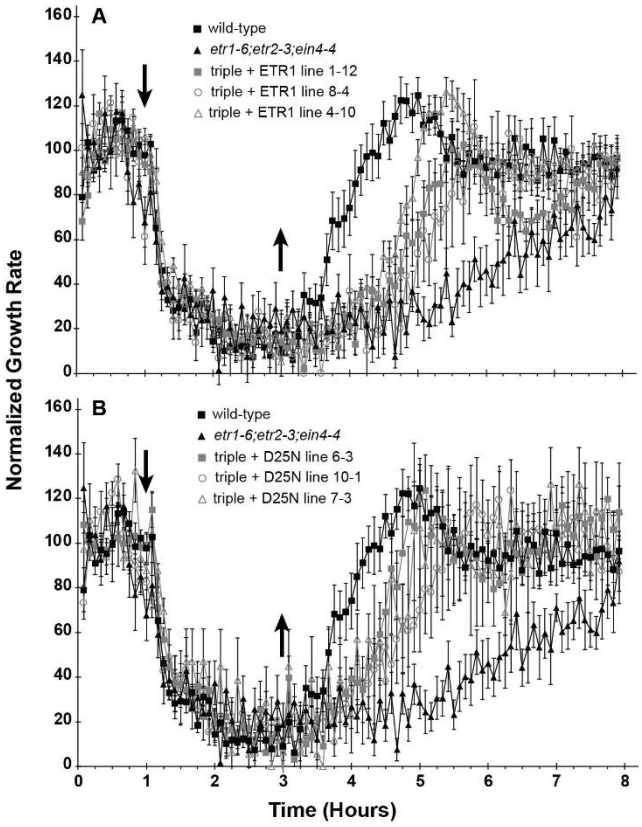

Figure S5. Kinetics of growth response to ethylene of ETR1^{wt} and ETR1^{D25N} lines
Ethylene dose response kinetics were analyzed in hypocotyls of 2-d-old etiolated seedlings for wild type, the *etr1 etr2 ein4* triple mutant, and for the triple mutant complemented with ETR1^{wt} (panel A) or ETR1^{D25N} (panel B). Measurements were made in air for 1 hr, followed by a 2-hr exposure to 10 µL L^{-1} ethylene, and then a 5-hr recovery in air. Growth rates for each line are normalized to the growth rate during the first hour in the air. Arrows indicate the time points for the addition and removal of ethylene. Error bars represent SE (n≥9 for all lines, except for ETR1 line 8, n=4).

9

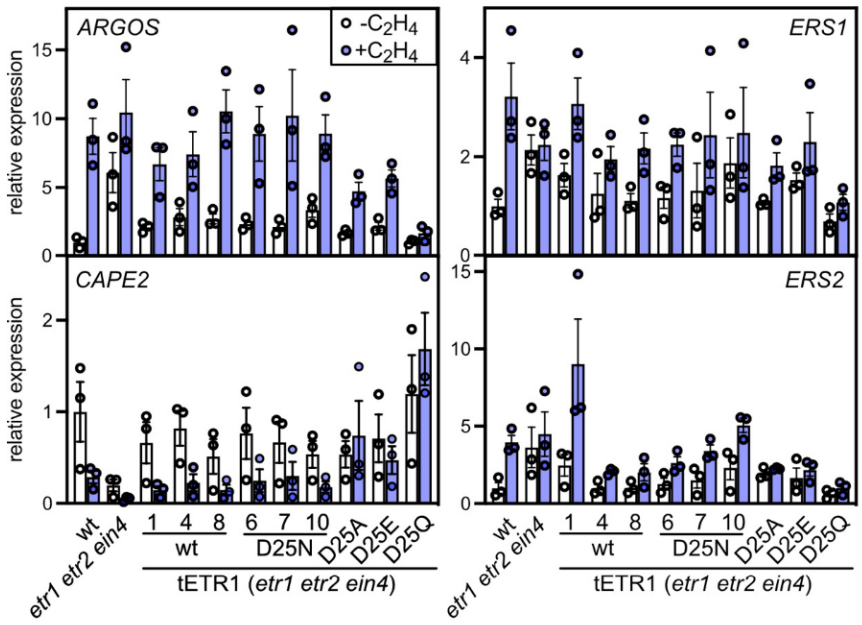

Figure S6. Effect of ETR1 Asp25 mutants on ethylene-dependent gene expression. Dark-grown seedlings were treated with 0 or 1 µL L^{-1} ethylene for 2 hr, and gene expression examined by RT-qPCR (n=3). Expression was normalized to a tubulin control and is presented as relative to the untreated wild-type control. Three tETR1-wt and three $tETR1^{D25N}$ lines were examined. The ethylene-insensitive $tETR1^{D25A}$#20, $tETR1^{D25E}$#19, and $tETR1^{D25Q}$#4 lines were also included.

10

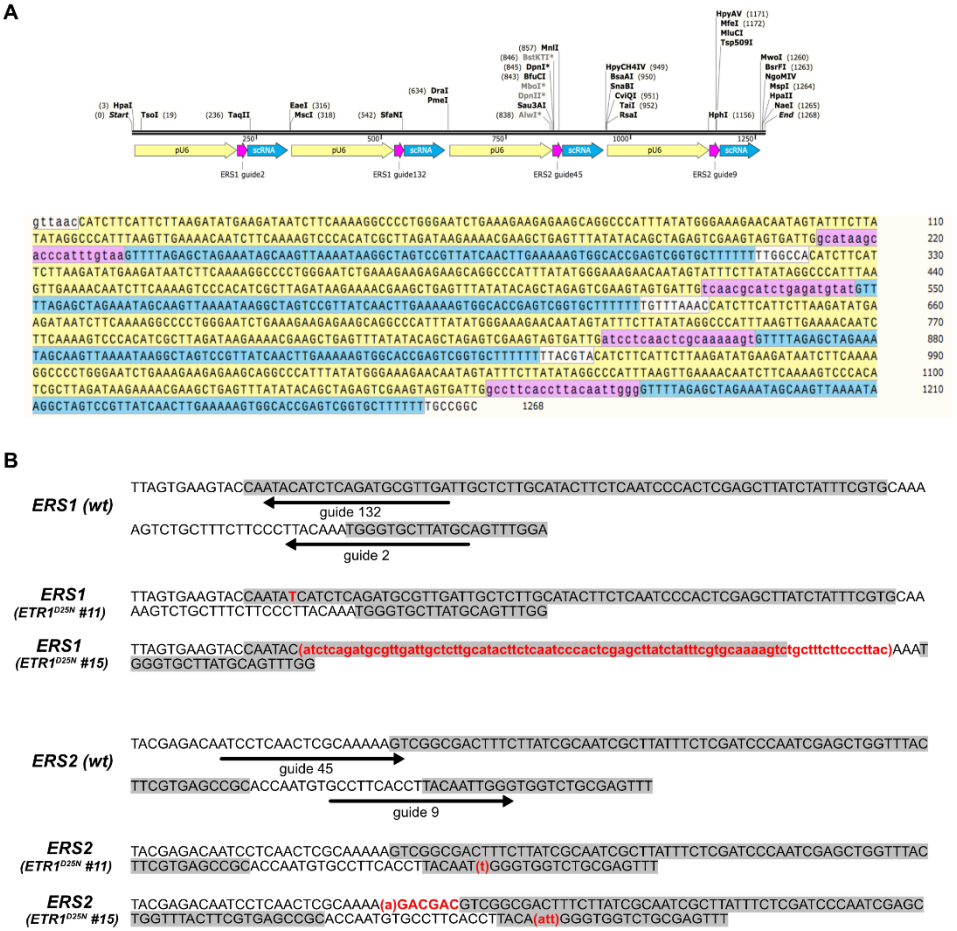

Figure S7. CRISPR-Cas9 targeting of *ERS1* and *ERS2*
(A) Diagram and sequence for CRISPR-Cas9 cassette targeting *ERS1* and *ERS2*.
(B) CRISPR-Cas9 induced mutations in *ERS1* and *ERS2*. Nucleotide sequences are given for the wild-type *ERS1* and *ERS2* sequences as well as for the *ERS1* and *ERS2* sequences found for the *ETR1^{D25N} #11* and *#15* lines in the *etr1 etr2 ers1 ers2 ein4* background. Positions of the guide RNAs are indicated for the wild-type sequences. Gray highlights indicate sequence encoding TM1 and beginning of TM2 in the receptors. Insertion sequences are capitalized, bold, and colored red. Deletion sequences are lower case, bold, colored red, and in parentheses.

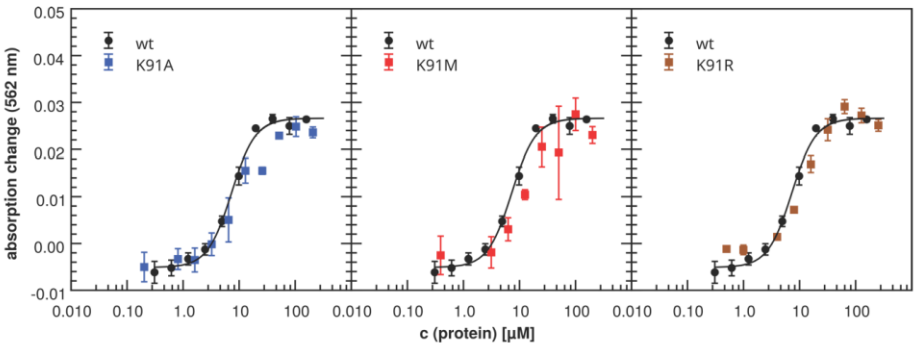

Figure S8. Copper binding by wild-type and Lys91 mutant versions of ETR1
Copper binding of wild-type and Lys91 mutant versions of ETR1 transmembrane domain (ETR1-TMD; n = 3). Purified ETR1-TMD was titrated to the BCA_2-Cu(I) complex, and copper binding monitored spectrophotometrically based on the change in absorbance at 562 nm.

12

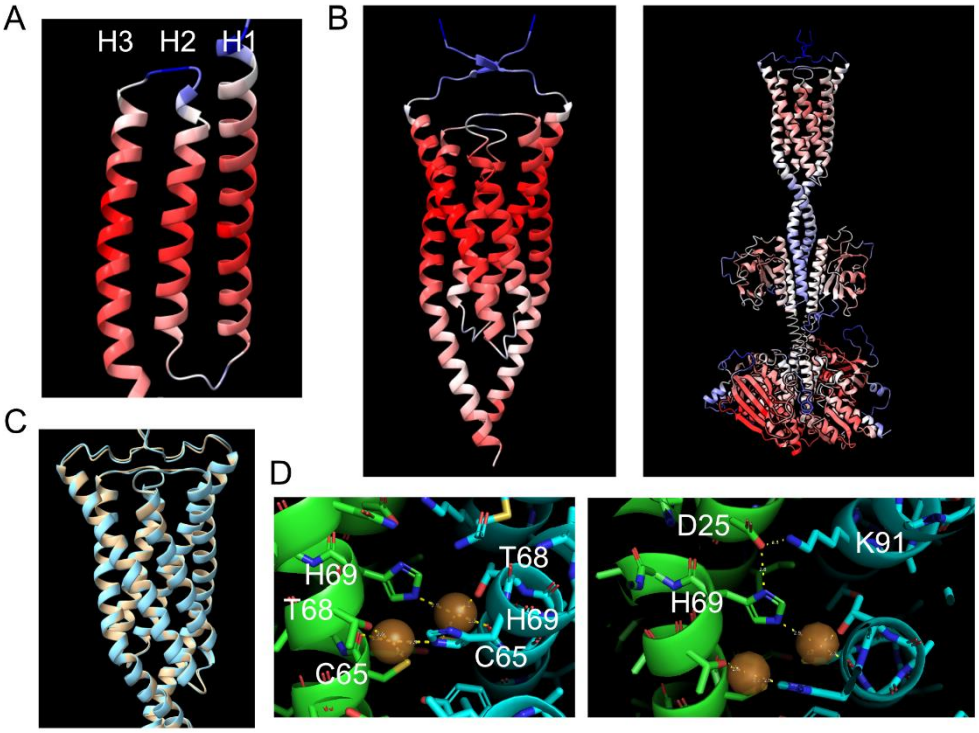

Figure S9. AlphaFold-based models of ETR1
(A) Confidence levels of AlphaFold model for ETR1 transmembrane domain with B-factor range of 56.7 (blue) to 93.7 (red)
(B) AlphaFold-Multimer models with confidence levels for homodimers of the EBD (amino acids 1-128; B factor range 37-97) and full-length ethylene receptor (B factor range 33.1-82).
(C) Overlay of 'relaxed' (cyan) and 'unrelaxed' (tan) multimer models of ETR1 homodimers.
(D) AlphaFold-Multimer-based model of the ETR1 homodimer (coppers not interacting), with views highlighting copper binding geometry (left; H69-Cu = 2.9 Å, C65-Cu = 2.2 Å, T68-Cu = 2.0 Å, C65backbone carbonyl-Cu = 2.3 Å) and interactions between His69, Asp25, and Lys91 (right; D25-H69 = 2.8 Å, D25-K91 = 3.3 Å).

13

Table S1. EVcouplings for ETR1 EBD
I and J: residue # of ETR1 amino acid sequence
A_i and A_j: amino acid identity (single letter code)
Seg_i and seg_j: Segments i and j
Prob: probability

I	A_i	j	A_j	cn	seg_i	seg_j	mad_score	prob	score
74	W	80	S	1.17	A	A	19.484	1	12.095
29	A	70	L	1.084	A	A	18.075	1	11.193
33	F	67	A	1.067	A	A	17.795	1	10.947
71	I	90	A	0.831	A	A	13.908	1	8.323
26	F	73	L	0.785	A	A	13.161	1	7.785
20	Y	88	T	0.668	A	A	11.224	0.998	6.482
21	Q	88	T	0.652	A	A	10.96	0.998	6.323
64	L	93	L	0.632	A	A	10.644	0.998	6.081
25	D	91	K	0.609	A	A	10.252	0.997	5.861
27	F	99	C	0.563	A	A	9.51	0.995	5.36
20	Y	92	V	0.559	A	A	9.437	0.995	5.295
60	A	97	V	0.554	A	A	9.347	0.995	5.249
39	L	55	L	0.536	A	A	9.053	0.993	4.957
72	N	91	K	0.533	A	A	9.005	0.992	4.869
38	E	106	V	0.498	A	A	8.427	0.99	4.637
31	A	99	C	0.482	A	A	8.166	0.987	4.312
64	L	97	V	0.46	A	A	7.805	0.985	4.183
22	Y	73	L	0.424	A	A	7.219	0.976	3.716
18	M	76	F	0.386	A	A	6.592	0.965	3.304
38	E	109	I	0.382	A	A	6.521	0.956	3.079
17	L	82	T	0.377	A	A	6.445	0.956	3.07
28	I	68	T	0.362	A	A	6.197	0.955	3.066
24	S	92	V	0.355	A	A	6.075	0.948	2.907
71	I	83	V	0.341	A	A	5.85	0.946	2.858
43	V	49	F	0.339	A	A	5.809	0.946	2.857
68	T	90	A	0.353	A	A	6.04	0.944	2.83
82	T	89	T	0.331	A	A	5.686	0.944	2.817
72	N	87	M	0.332	A	A	5.708	0.942	2.781
49	F	55	L	0.332	A	A	5.693	0.941	2.772
33	F	66	G	0.338	A	A	5.798	0.934	2.648
43	V	56	V	0.322	A	A	5.544	0.931	2.595
22	Y	76	F	0.314	A	A	5.405	0.925	2.515
40	I	59	G	0.308	A	A	5.306	0.923	2.484
58	F	65	C	0.274	A	A	4.747	0.897	2.166
36	P	62	I	0.277	A	A	4.799	0.892	2.115
41	Y	109	I	0.282	A	A	4.87	0.885	2.038
43	V	55	L	0.261	A	A	4.527	0.881	2
27	F	95	A	0.27	A	A	4.676	0.875	1.943
36	P	101	T	0.251	A	A	4.361	0.871	1.906
32	Y	98	S	0.25	A	A	4.346	0.869	1.895
79	H	87	M	0.261	A	A	4.536	0.868	1.883
45	K	52	R	0.257	A	A	4.464	0.866	1.862
38	E	105	L	0.265	A	A	4.599	0.865	1.858
32	Y	62	I	0.252	A	A	4.387	0.865	1.856
34	S	102	A	0.245	A	A	4.268	0.858	1.796
62	I	69	H	0.236	A	A	4.116	0.848	1.716
11	W	76	F	0.34	A	A	5.826	0.846	1.706
30	I	99	C	0.237	A	A	4.132	0.845	1.693

14

58	F	69	H	0.23	A	A	4.018	0.84 1.655
28	I	91	K	0.228	A	A	3.986	0.837 1.636
21	Q	91	K	0.24	A	A	4.19	0.836 1.626
35	I	101	T	0.219	A	A	3.842	0.826 1.556
57	Q	97	V	0.225	A	A	3.941	0.824 1.543
61	F	101	T	0.224	A	A	3.927	0.822 1.529
62	I	101	T	0.219	A	A	3.849	0.817 1.497
81	R	98	S	0.221	A	A	3.875	0.812 1.463
61	F	98	S	0.213	A	A	3.743	0.808 1.437
21	Q	87	M	0.216	A	A	3.794	0.801 1.39
34	S	106	V	0.212	A	A	3.73	0.798 1.376
24	S	95	A	0.209	A	A	3.675	0.798 1.375
67	A	90	A	0.207	A	A	3.636	0.795 1.352
54	V	108	I	0.212	A	A	3.719	0.791 1.334
65	C	98	S	0.204	A	A	3.588	0.791 1.332
50	P	59	G	0.196	A	A	3.46	0.78 1.264
61	F	94	T	0.2	A	A	3.524	0.776 1.245
21	Q	72	N	0.205	A	A	3.61	0.775 1.239
28	I	65	C	0.202	A	A	3.56	0.775 1.235
26	F	70	L	0.207	A	A	3.643	0.774 1.231
25	D	101	T	0.189	A	A	3.342	0.769 1.204
32	Y	69	H	0.194	A	A	3.425	0.767 1.193
40	I	56	V	0.191	A	A	3.382	0.765 1.179
25	D	88	T	0.197	A	A	3.472	0.76 1.155
32	Y	65	C	0.189	A	A	3.342	0.759 1.149
27	F	60	A	0.189	A	A	3.341	0.758 1.144
28	I	94	T	0.184	A	A	3.271	0.758 1.14
50	P	106	V	0.194	A	A	3.428	0.753 1.116
30	I	90	A	0.184	A	A	3.267	0.75 1.096
40	I	60	A	0.181	A	A	3.21	0.743 1.059
35	I	61	F	0.178	A	A	3.16	0.735 1.018
52	R	64	L	0.182	A	A	3.24	0.731 1
36	P	66	G	0.178	A	A	3.163	0.727 0.979
25	D	72	N	0.193	A	A	3.412	0.724 0.964
38	E	104	M	0.172	A	A	3.07	0.723 0.959
32	Y	101	T	0.166	A	A	2.973	0.722 0.956
62	I	94	T	0.17	A	A	3.034	0.717 0.931
26	F	54	V	0.178	A	A	3.161	0.717 0.928
36	P	58	F	0.169	A	A	3.015	0.709 0.892
11	W	18	M	0.247	A	A	4.308	0.709 0.89
67	A	83	V	0.166	A	A	2.976	0.707 0.879
57	Q	104	M	0.175	A	A	3.109	0.703 0.861
50	P	63	V	0.16	A	A	2.873	0.701 0.852
62	I	98	S	0.157	A	A	2.823	0.69 0.801
42	F	109	I	0.181	A	A	3.211	0.689 0.794
68	T	94	T	0.158	A	A	2.843	0.686 0.784
43	V	50	P	0.151	A	A	2.727	0.685 0.775
11	W	17	L	0.239	A	A	4.169	0.681 0.759
44	K	57	Q	0.159	A	A	2.849	0.68 0.754
68	T	91	K	0.153	A	A	2.75	0.679 0.751

15

Table S2. Primers used for this study.

Site Directed Mutagenesis of ETR1	
Name	**Sequence (5'-3')**
D25N-Forward	ATACATCTCCAATTTCTTCATTGCG
D25N-Reverse	TGGTATTTCATTAACAATTCATCC
D25Q-Forward	ATACATCTCCAATTTCTTCATTGCGATTG
D25Q-Reverse	TGGTATTTCATTAACAATTCATCC
D25E-Forward	ACATCTCCGAATTCTTCATTGC
D25E-Reverse	ATTGGTATTTCATTAACAATTCATC
D25A-Forward	ATACATCTCCGCTTTCTTCATTGC
D25A-Reverse	ATTGGTATTTCATTAACAATTCATC
K91R-Forward	GACTACCGCGAGAGTGTTAACCGCTG
K91R-Reverse	TGGTATTTCATTAACAATTCATCC
K91M-Forward	GACTACCGCGATGGTGTTAACCG
K91M-Reverse	ATCACAAGCGCCACGGTT
K91A-Forward	GACTACCGCGGCTGTGTTAACCGCTG
K91A-Reverse	ATCACAAGCGCCACGGTT
Sequencing Primers for ETR1 mutagenesis	
ETR1-seq for pYCDE2	CCTTCCTTCATTCACGCACAC
ETR1-seq for pCAMBIA	CACCTTCGCGGTAGTCATCAC
Primers for analysis of CRISPR-Cas9 lines	
ERS1-Forward	CCTTCCTTCATTCACGCACAC
ERS1-Reverse	CACCTTCGCGGTAGTCATCAC
ERS2-Forward	CACCTTCGCGGTAGTCATCAC
ERS2-Reverse	CCTTCCTTCATTCACGCACAC
KanR-Forward	CACCTTCGCGGTAGTCATCAC
KanR-Reverse	CACCTTCGCGGTAGTCATCAC
Quantitative real time PCR	
β-tubulin-Forward	TGGTGGAGCCTTACAACGCTACTT
β-tubulin-Reverse	TTCACAGCAAGCTTACGGAGGTCA
ERF1-Forward	TCTAATCGAGCAGTCCACGCAACA
ERF1-Reverse	AACGTCCCGAGCCAAACCCTAATA
ARGOS-Forward	GTCATGGACGTCGGAAGAAACAAC
ARGOS-Reverse	GGGAACCAATAGCAGCATAAACGG
OSR1-Forward	ATGAGGGTTCATGATCAACGGCTG
OSR1-Reverse	GGCTGGGCTCATTAGAAGGAGAAA
EXP5-Forward	CACTCATACTTTAACTTGGTGTTGG
EXP5-Reverse	GACCATTGAGATAAGAGTTGCTTTG
EXPb1-Forward	GCAAATACAGAGGGAAGAACATA
ExPb1-Reverse	CTTCATCGATATCCACTCCTTAGA
CAPE2-Forward	TGACCACGACTCCTTGCAGTTCTT
CAPE2-Reverse	ATGAAGATCCCACCATTGTCGCAC
ERS1-Forward	TTCAGTCTACAAGCGATCTTTGAAGAGG
ERS1-Reverse	AGCGCGACAAACCGTTTACAGAGA
ERS2-Forward	ACACATTCTGGGAAACAGTAATCG
ERS2-Reverse	AAGCTACCGTCGTCTTCTGC

Movie S1 (separate file). AlphaFold-Multimer-based model of the ETR1 homodimer (coppers interacting).

Movie S2 (separate file). AlphaFold-Multimer-based model of the ETR1 homodimer (coppers not interacting).

SI References

1. A. B. Bleecker, M. A. Estelle, C. Somerville, H. Kende, Insensitivity to ethylene conferred by a dominant mutation in *Arabidopsis thaliana*. *Science* **241**, 1086-1089 (1988).
2. C. Chang, S. F. Kwok, A. B. Bleecker, E. M. Meyerowitz, Arabidopsis ethylene response gene *ETR1*: Similarity of product to two-component regulators. *Science* **262**, 539-544 (1993).
3. J. Hua, E. M. Meyerowitz, Ethylene responses are negatively regulated by a receptor gene family in *Arabidopsis thaliana*. *Cell* **94**, 261-271 (1998).
4. B. P. Hall *et al.*, Histidine kinase activity of the ethylene receptor ETR1 facilitates the ethylene response in Arabidopsis. *Plant Physiol* **159**, 682-695 (2012).
5. G. E. Schaller, B. M. Binder, Inhibitors of Ethylene Biosynthesis and Signaling. *Methods Mol Biol* **1573**, 223-235 (2017).
6. B. M. Binder, L. A. Mortimore, A. N. Stepanova, J. R. Ecker, A. B. Bleecker, Short-term growth responses to ethylene in Arabidopsis seedlings are EIN3/EIL1 independent. *Plant Physiol* **136**, 2921-2927 (2004).
7. B. M. Binder *et al.*, Arabidopsis seedling growth response and recovery to ethylene. A kinetic analysis. *Plant Physiol* **136**, 2913-2920 (2004).
8. X. Qu, G. E. Schaller, Requirement of the histidine kinase domain for signal transduction by the ethylene receptor ETR1. *Plant Physiol* **136**, 2961-2970 (2004).
9. S. J. Clough, A. F. Bent, Floral dip: a simplified method for Agrobacterium-mediated transformation of Arabidopsis thaliana. *Plant J* **16**, 735-743 (1998).
10. G. E. Schaller, A. B. Bleecker, Ethylene-binding sites generated in yeast expressing the Arabidopsis *ETR1* gene. *Science* **270**, 1809-1811 (1995).
11. F. Winston, C. Dollard, S. L. Ricupero-Hovasse, Construction of a set of convenient Saccharomyces cerevisiae strains that are isogenic to S288C. *Yeast* **11**, 53-55 (1995).
12. H. Liu *et al.*, CRISPR-P 2.0: An Improved CRISPR-Cas9 Tool for Genome Editing in Plants. *Mol Plant* **10**, 530-532 (2017).
13. C. J. Denbow *et al.*, Gateway-Compatible CRISPR-Cas9 Vectors and a Rapid Detection by High-Resolution Melting Curve Analysis. *Front Plant Sci* **8**, 1171 (2017).
14. C. LeBlanc *et al.*, Increased efficiency of targeted mutagenesis by CRISPR/Cas9 in plants using heat stress. *Plant J* **93**, 377-386 (2018).
15. I. Kasajima, Y. Ide, N. Ohkama-Ohtsu, T. Yoneyama, T. Fujiwara, A protocol for rapid DNA extraction from *Arabidopsis thaliana* for PCR analysis. *Plant Mol Biol Rep* **22**, 49-52 (2004).
16. R. L. Gamble, M. L. Coonfield, G. E. Schaller, Histidine kinase activity of the ETR1 ethylene receptor from Arabidopsis. *Proc. Natl. Acad. Sci. USA* **95**, 7825-7829 (1998).
17. S. N. Shakeel *et al.*, Ethylene Regulates Levels of Ethylene Receptor/CTR1 Signaling Complexes in Arabidopsis thaliana. *J Biol Chem* **290**, 12415-12424 (2015).
18. Y. F. Chen, M. D. Randlett, J. L. Findell, G. E. Schaller, Localization of the ethylene receptor ETR1 to the endoplasmic reticulum of Arabidopsis. *J Biol Chem* **277**, 19861-19866 (2002).
19. S. Schott-Verdugo, L. Muller, E. Classen, H. Gohlke, G. Groth, Structural Model of the ETR1 Ethylene Receptor Transmembrane Sensor Domain. *Scientific reports* **9**, 8869 (2019).
20. B. M. Binder, G. E. Schaller, Analysis of Ethylene Receptors: Ethylene-Binding Assays. *Methods Mol Biol* **1573**, 75-86 (2017).
21. C. Hadfield, A. M. Cashmore, P. A. Meacock, An efficient chloramphenicol-resistance marker for *Saccharomyces cerevisiae* and *Escherichia coli*. *Gene* **45**, 149-158 (1986).

22. M. I. Rai *et al.*, The ARGOS gene family functions in a negative feedback loop to desensitize plants to ethylene. *BMC Plant Biol* **15**, 157 (2015).
23. T. A. Hopf *et al.*, The EVcouplings Python framework for coevolutionary sequence analysis. *Bioinformatics* **35**, 1582-1584 (2019).
24. S. Ovchinnikov, H. Kamisetty, D. Baker, Robust and accurate prediction of residue-residue interactions across protein interfaces using evolutionary information. *eLife* **3**, e02030 (2014).
25. R. Evans *et al.*, Protein complex prediction with AlphaFold-Multimer. *bioRxiv* https://doi.org/10.1101/2021.10.04.463034, 2021.2010.2004.463034 (2021).
26. J. Jumper *et al.*, Highly accurate protein structure prediction with AlphaFold. *Nature* **596**, 583-589 (2021).
27. E. F. Pettersen *et al.*, UCSF ChimeraX: Structure visualization for researchers, educators, and developers. *Protein Sci* **30**, 70-82 (2021).

5.3 Kristallisation und Röntgenstrukturanalyse des Ethylenrezeptors

Titel: Crystallization of Ethylene Plant Hormone Receptor – Screening for Structure

Autoren: Buket Rüffer, Yvonne Thielmann, Moritz Lemke, Alexander Minges und Georg Groth

Eigener Anteil:

35 %, Planung, Durchführung und Auswertung der Experimente

Veröffentlicht in:

Biomolecules 375, 20.03.2024, Artikelnummer:14, Creative Commons Attribution license 4.0

DOI: 10.3390/biom14030375

biomolecules

MDPI

Article

Crystallization of Ethylene Plant Hormone Receptor—Screening for Structure

Buket Rüffer †, Yvonne Thielmann †, Moritz Lemke, Alexander Minges and Georg Groth *

Institute of Biochemical Plant Physiology, Faculty of Mathematics and Natural Sciences, Heinrich Heine University Düsseldorf, 40204 Düsseldorf, Germany; yvonne.thielmann@hhu.de (Y.T.); alexander.minges@hhu.de (A.M.)
* Correspondence: georg.groth@hhu.de
† These authors contributed equally to this work.

Abstract: The plant hormone ethylene is a key regulator of plant growth, development, and stress adaptation. Many ethylene-related responses, such as abscission, seed germination, or ripening, are of great importance to global agriculture. Ethylene perception and response are mediated by a family of integral membrane receptors (ETRs), which form dimers and higher-order oligomers in their functional state as determined by the binding of Cu(I), a cofactor to their transmembrane helices in the ER-Golgi endomembrane system. The molecular structure and signaling mechanism of the membrane-integral sensor domain are still unknown. In this article, we report on the crystallization of transmembrane (TM) and membrane-adjacent domains of plant ethylene receptors by Lipidic Cubic Phase (LCP) technology using vapor diffusion *in meso* crystallization. The TM domain of ethylene receptors ETR1 and ETR2, which is expressed in *E. coli* in high quantities and purity, was successfully crystallized using the LCP approach with different lipids, lipid mixtures, and additives. From our extensive screening of 9216 conditions, crystals were obtained from identical crystallization conditions for ETR1 (aa 1-316) and ETR2 (aa 1-186), diffracting at a medium–high resolution of 2–4 Å. However, data quality was poor and not sufficient for data processing or further structure determination due to rotational blur and high mosaicity. Metal ion loading and inhibitory peptides were explored to improve crystallization. The addition of Zn(II) increased the number of well-formed crystals, while the addition of ripening inhibitory peptide NIP improved crystal morphology. However, despite these improvements, further optimization of crystallization conditions is needed to obtain well-diffracting, highly-ordered crystals for high-resolution structural determination. Overcoming these challenges will represent a major breakthrough in structurally determining plant ethylene receptors and promote an understanding of the molecular mechanisms of ethylene signaling.

Keywords: integral membrane proteins; plant hormone receptor; ethylene receptor histidine kinase; high-affinity copper binding; Cu(I) metal cofactor; transmembrane domain (TMD); biological function; metal-dependent ligand binding; LCP crystallization; protein structure

Citation: Rüffer, B.; Thielmann, Y.; Lemke, M.; Minges, A.; Groth, G. Crystallization of Ethylene Plant Hormone Receptor—Screening for Structure. *Biomolecules* **2024**, *14*, 375. https://doi.org/10.3390/biom14030375

Academic Editors: Pedro Tavares and Alice S. Pereira

Received: 8 February 2024
Revised: 16 March 2024
Accepted: 18 March 2024
Published: 20 March 2024

1. Introduction

Integral membrane proteins play crucial roles in cellular signaling and information transfer across biological membranes. These structures recognize signaling molecules ranging from small gaseous molecules to large compounds. Despite their great importance for intra- and intercellular communication and adaptation to environmental stimuli and stresses, our knowledge of the structure and biophysical properties of many receptor proteins is still limited [1–3].

The gaseous hormone ethylene regulates a wide range of essential functions in plant growth and development and is a well-known mediator of stress responses [1,4–6]. Signal perception and response to the plant hormone ethylene have been extensively studied in the model plant *Arabidopsis thaliana*. These studies have identified several mutants and the

related molecular components involved in ethylene signaling [1,7–9]. Phenotypic, molecular, and biochemical analyses suggest that ethylene perception and signaling are mediated by a family of integral membrane receptors consisting of Ethylene response 1 (ETR1) and its four isoforms ERS1 (Ethylene response sensor 1), ETR2 (Ethylene response 2), ERS2 (Ethylene response sensor 2), and EIN4 (Ethylene insensitive 4). Receptors ETR1 and ERS1 belong to subfamily I, while the other three isoforms form subfamily II [10–12]. All members of the ethylene receptor family have a similar architecture, including a transmembrane domain (TMD) that contains three helices in subfamily I (TMH1-3) and four helices in subfamily II (TMH1-4). The TMD is critical for receptor dimerization and high-affinity binding of Cu(I) cofactors, which are essential for ethylene binding and signal transfer. The TMD is followed by cGMP-specific phosphodiesterase, adenylyl cyclase, and FhlA (GAF) domains responsible for receptor dimerization and the formation of high oligomeric clusters [13–15]. Other domains include the histidine kinase (HK) domain and the receiver domain (RD). The structure of individual cytosolic subdomains of the ETR family, which are similar to bacterial two-component histidine kinases [16], has been identified by X-ray crystallography and small-angle X-ray scattering (SAXS) [17–19].

Crystallization and structural studies of full-length receptors or isolated TMD have not succeeded to date. Compared to soluble proteins, crystallization of membrane proteins is notoriously difficult and typically involves extracting the target from its native lipid membranes. In this process, commonly used detergents cover most of the membrane part (hydrophobic region), leaving only a small surface area (loops and the hydrophilic region) of the target protein for crystal contacts. Moreover, these crystals are often fragile and have low-resolution diffraction and crystallization defects. In addition, optimizing crystal packing with detergents is very time-consuming [20]. Membrane protein crystallization with LCP, where membrane proteins such as ETRs are embedded in a membrane-mimicking environment, is more suitable for high throughput screening. This method allows hydrophobic lipid-guided interactions and hydrophilic protein–protein interactions, leading to tight crystal packing. The first crystallization approaches with LCP were called bicontinuous cubic phases by Landau and Rosenbusch [21]. They intended to build a structured and flexible system where membrane proteins are incorporated into membranes using monoolein (MO) or monopalmitolein (MP). Crystals grow in three-dimensional space. In this method, called *in meso* or LCP crystallization [22], membrane proteins are mixed in detergent micelles with a lipid or lipid mixture in a specific ratio to form a homogenous mixture of reconstituted membrane proteins. Further development of *in meso* crystallization is sponge phase crystallization [23]. The solvent diameter of the solvent channels is enlarged and the high order of the cubic phase is distorted, making this method more suitable for membrane proteins with a large extracellular domain [23,24].

Another approach to enlarging the solvent channels is to use Cherezov and Caffrey's widely applied method, where the channel pores of the membrane protein of interest are occupied by different lipids or lipid mixtures, e.g., MO, MP, or MO with the addition of cholesterol or cardiolipin (Figure 1) [25]. An LCP lattice formed by MO alone has a lattice parameter of 106 Å. The lattice can be enlarged with cholesterol and cardiolipin to about 170 Å and 190 Å (Figure 1). Lattice expansion was further developed by Zabara et al. with an MP/1,2-distearoyl-sn-glycerol-3-phosphoglycerol (DSPG) mixture, which retains more water in the LCP system and forms a lattice with a maximum lattice parameter of 525 Å (Figure 1) [26].

In recent years, LCP has enabled the crystallization of a wide range of membrane proteins from enzymes [27] to transporters, channels, and receptors to structural proteins and complexes [28–35]. Its success prompted us to explore this technology for ETR1 and to foster LCP crystallization of members from the two subfamilies using different additives, screening kits, and lipid mixtures. Focusing on the structure of the TM and GAF domains, we used truncations ETR1$^{1\text{-}157}$, ETR1$^{1\text{-}316}$, ETR1$^{1\text{-}407}$, and ETR2$^{1\text{-}186}$ for *in meso* crystallization. This article reports our progress on the structural analysis of the TM and GAF domains.

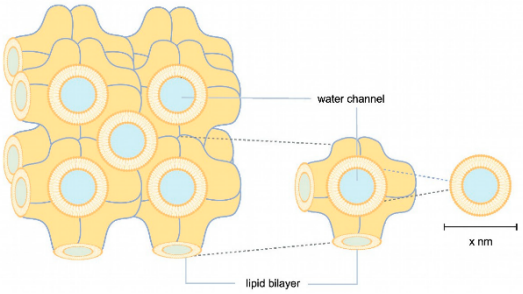

Figure 1. Schematic illustration of LCP. In orange, lipid bilayers are illustrated in highly convoluted membranes, where membrane proteins are embedded through hydrophobic interactions. Water channels, shown in blue, transport the precipitant. The size of the water channels can vary depending on the lipids, stoichiometry, additives, and precipitant used.

2. Materials and Methods

2.1. Materials

Chemicals and reagents were purchased from AppliChem (Darmstadt, Germany), Glycon (Luckenwalde, Germany), VWR International (Geldenaaksbaan, Belgium), BD (Le Pont de Claix, France), Carl Roth (Karlsruhe, Germany), BIOZOL (Eching, Germany), LIPOID (Dortmund, Germany), Jena Bioscience (Jena, Germany), Cytiva (Marlborough, MA, USA), Merck Millipore (Burlington, MA, USA), Miltenyi Biotec B.V. & Co. KG (Bergisch-Gladbach, Germany), and Molecular Dimensions (Rotherham, UK) at analytical grade. The pET16b-plasmid was purchased from MERCK/Novagen (Darmstadt, Germany), and the pGEX4T-1 plasmid was purchased from GE Healthcare (Munich, Germany). Oligonucleotides were synthesized by Sigma–Aldrich/MERCK (Steinheim, Germany). Two peptides, nuclear localization signal octapeptide 1 (NOP-1) and NLS icosapeptide 1 (NIP-1), were synthesized by Genscript (Piscataway, NJ, USA). For crystallization trial setups, ProCrysMeso (Zinsser Analytics, Eschborn, Germany) was used. A SterREO Discovery V.12 binocular (Zeiss, Oberkochen, Germany) equipped with a UV detector XtalLight100 (Xtal Concepts, Hamburg, Germany) was used for crystal detection.

2.2. Methods

2.2.1. Cloning, Heterologous Expression, and Purification

The pGEX4T-1 *ETR2*$^{1\text{-}186}$ *mT2* 10x His plasmid was derived from the pGEX4T-1 *ETR2* expression vector, as previously described [13]. The construct was truncated to remove amino acids (aa) 187-773. In addition, the fluorophore mCerulean was fused to the receptor's 10x His-tag and further modified by mutagenesis at positions T65, A145, and I146 to obtain *mTurquoise2* (mT2, see Figure 2), increasing the fluorescent reporter's brightness and photostability [36]. The primers used in this process are listed in the SI (Table S1). The pGEX4T-1 *ETR1*$^{1\text{-}157}$ *mT2* 10x His plasmid was derived from the pGEX4T-1 *ETR2*$^{1\text{-}186}$ *mT2* 10x His expression vector, as previously described (Figure 2) [13]. The coding sequence for *ETR1*$^{1\text{-}157}$ was obtained from the pETEV16b *AtETR1* expression vector by removing nucleotides encoding the soluble part of the receptor (aa 158-738, Figure 2). The pETEV16b *ETR1*$^{1\text{-}316}$ plasmid was derived from the pETEV16b *AtETR1* expression vector (Figure 2) by deleting the coding sequence for aa 317-738. The pETEV16b *ETR1*$^{1\text{-}407}$ plasmid was used as previously described (Figure 2) [37]. The sequences of all plasmids used in this study were confirmed by sequencing with T7 and T7 terminator primers. For heterologous expression, pETEV16b *AtETR1*$^{1\text{-}316}$, pETEV16b *AtETR1*$^{1\text{-}407}$, pGEX-4T-1 ETR1$^{1\text{-}157}$ mT2, or pGEX-4T-1 ETR2$^{1\text{-}186}$ mT2 were transformed into *E. coli* C41(DE3)Δ(*ompF-acrAB*) [38] and grown on 2YT agar plates containing 100 µg/mL of ampicillin at 37 °C overnight. Pre- and main cultures of pGEX-4T-1 *ETR2*$^{1\text{-}186}$ *mT2*, pGEX-4T-1 *ETR1*$^{1\text{-}157}$ *mT2*, *ETR1*$^{1\text{-}407}$, and pETEV16b

AtETR1$^{1-316}$ were prepared as previously described for the expression and purification of ETR1$^{1-157}$ [39]. pETEV16b *AtETR1*$^{1-316}$ was expressed at 30 °C and 16 °C [39]. Immobilized metal affinity chromatography (IMAC) of AtETR1$^{1-316}$ and ETR2$^{1-186}$ mT2 was conducted as described in [40]. HEPES buffer (50 mM HEPES, pH 8.0, 200 mM NaCl, 0.015 (*w*/*v*) % FosCholine 14, 0.002 (*w*/*v*) % PMSF) was used for IMAC purification of ETR2$^{1-186}$ mT2. After buffer exchange, the purified protein was concentrated to a volume $\leq$ 500 µL with a concentration $\geq$10 mg/mL. Aliquots of 60–80 µL were shock frozen with liquid nitrogen and stored at −80 °C or used directly for crystallization trials. The purity and homogeneity of all samples were analyzed and characterized by SDS-PAGE and immunodetection.

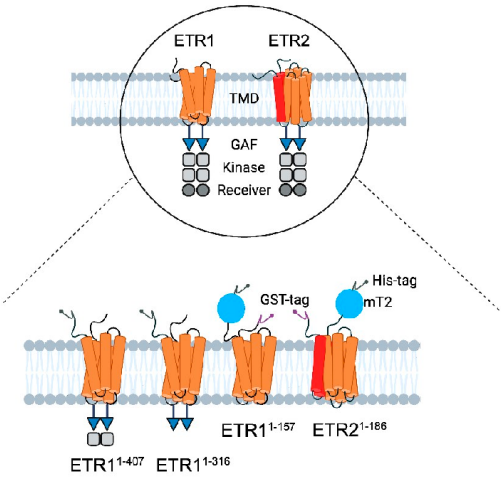

Figure 2. Schematic illustration of the modular structure of ethylene receptors and constructs used for LCP crystallization. (**Top**) ETR1 and ETR2 are two of five ethylene receptor isoforms located in the ER membrane of *Arabidopsis thaliana* [41]. They share a similar modular structure starting at their N-terminus with three transmembrane helices (orange) per monomer in ETR1. By contrast, ETR2 has a putative fourth helix (red) in the TMD monomer [1,7]. In both isoforms, the TMD is followed by the GAF domain (blue triangle), kinase domain (grey squares), and receiver domain (dark gray circle) [1]. The kinase domain of ETR2 is degenerated, and its serine–threonine kinase activity contrasts with ETR1's histidine kinase activity [1,42]. The receptors only function as dimers [1,14]. (**Bottom**) For purification and crystallization, ETR1$^{1-316}$, ETR1$^{1-407}$, ETR1$^{1-157}$ mT2, and ETR2$^{1-186}$ mT2 were used. All constructs contain a 10x His-tag (dark gray, N-terminal—ETR1$^{1-316}$, ETR1$^{1-407}$; C-terminal—ETR1$^{1-157}$ mT2 and ETR2$^{1-186}$ mT2). ETR1$^{1-157}$ mT2, and ETR2$^{1-186}$ mT2 are additionally flanked at the N-terminus by a GFP—derivative mTurquoise2 (blue) and GST tag (purple, N-terminal).

2.2.2. LCP Crystallization

Crystallization and structural studies of detergent-solubilized ethylene receptors and isolated TMDs have not been successful. Therefore, we pursued LCP crystallization as an alternative strategy to provide a more biologically native lipid environment for the ETR1 TMD. Unlike detergents, which disrupt ETR1 structure, particularly in the membrane, LCP is thought to preserve TMD structure, stability, and functionality. Compared to detergent-based crystals, LCP crystals have enhanced crystal order and diffraction quality due to their reduced solvent content. As a result, high-resolution experimental structural information can be obtained from isolated receptor proteins. LCP crystallization or *in meso* crystallization is a method where proteins are crystallized in a membrane-mimicking environment. The general setting for LCP crystallization is a protein/lipid mixture at a defined ratio mixed in a coupled syringe system to form LCP [35]. Typically, LCP crystallization experiments are

conducted in a glass sandwich setup consisting of two glass plates and a spacer. In such a setup, the LCP mixture is placed onto the lower glass plate and overlaid with a precipitant solution (Figure 3A). The upper glass plate is then placed on top of the spacer, sandwiching the LCP batch experiment between the plates (Figure 3A). To harvest the growing crystals from the LCP, the upper glass must be cut before the crystals can be removed with a loop (see Figure 3A). To facilitate handling, we used regular sitting drop plates in our setup (MPI tray [43], Figure 3B) as previously established in [44,45]. However, it should be noted that any commercially available round-bottomed sitting drop plate can be used for this protocol. The LCP (100 nL) was dispensed into the protein well and overlaid with 1.5 µL of precipitant solution (Figure 3B). The reservoir well was then filled with 35 µL of precipitant solution (Figure 3B). In this way, LCP crystallization is no longer a static batch experiment but features a diffusion-driven component. Another important benefit of the microplate setup used is that it greatly facilitates crystal harvesting. No glass cover is cut when the plate is sealed with adhesive UV-compatible foil. Previous studies showed that with such a setup, crystals can be harvested from the plates even after nine months and diffracted up to 2.0 Å [44].

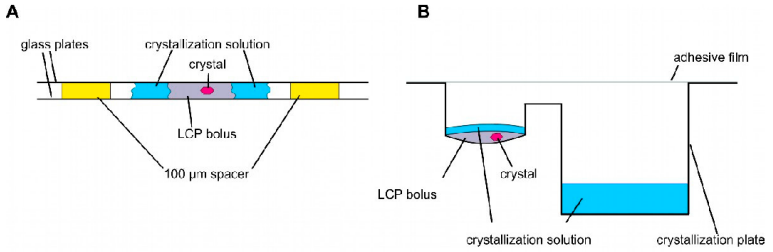

Figure 3. Schemes of different LCP crystallization approaches. (**A**) Sandwich LCP approach: the LCP bolus is covered with a crystallization solution and sandwiched between two glass plates. Spacers of 100 µm keep the glass plates apart. (**B**) Sitting drop LCP crystallization in a round-bottomed sitting drop crystallization plate. An LCP bolus is pipetted into the round cavity covered with crystallization solution. The crystallization solution is stored in the reservoir (rectangular cavity).

2.2.3. LCP—Lipid Mixture Preparation

Monoacylglycerols monoolein (MO, MAG 9.9) and monopalmitolein (MP, MAG 9.7) were heated up to 42 °C. Then, 0.12 g of the liquefied lipid was pipetted into glass vials. Thereafter, 0.013 g of lipid additives 1,2-dipalmitoyl-3-succinylglycerol (DSPG), cholesterol, 1,2-dioleoyl-sn-glycerol-3-phosphocholine (DOPC), or 57 mg cardiolipin in chloroform were added alongside 300 µL of chloroform. These lipid–chloroform mixtures were shaken frequently for 30 min at 42 °C until the lipids formed a homogeneous solution. Chloroform was removed from the glass vials under a fume hood with a stream of air. To remove the remaining solvents, the lipid mixtures were vacuumed overnight. All lipid samples were stored at −20 °C or used directly for sample preparation.

2.2.4. LCP—Sample Preparation

Normally, LCP crystallization was performed with a ratio of 60% lipid and 40% protein solution. Diverging from standard conditions, ratios of 70:30% and 50:50% (protein:lipid) were used for MP/DSPG and MP/cholesterol or MP/DOPC, respectively. For $ETR2^{1-186}$ mT2 and $ETR1^{1-157}$ mT2, the LCP was formed using the lipids MO, MO/DSPG, MO/cholesterol, MP/DOPC, and MP/DSPG. For this purpose, $ETR1^{1-316}$ and $ETR1^{1-407}$ were mixed with MO/DSPG, MO/cardiolipin, MO/cholesterol, and MP/cholesterol to obtain lipid mixtures for an LCP with enlarged lattice parameters (Figure 1) [34]. Lipid-filled glass vials were heated to 42°C. Molten lipid was filled into one Hamilton syringe of the coupled syringe system used for LCP mixtures (Innovative Labor System GmbH,

Stützerbach, Germany). Thawed protein was filtered through a 0.2 µm filter (Merck Millipore, Ultrafree-MC-GV-Centrifugal-Filter-Units, MA, USA) to remove aggregates. Lipid mixtures and protein solutions were mixed to obtain homogeneity. These LCP mixtures were pipetted onto MPI trays using the ProCrysMeso robot with humidification. The bolus contained 100 nL of LCP and was overlaid with 1.5 µL of crystallization solution (Figure 3B). The reservoir well was filled with 35 µL of crystallization solution (Figure 3B) [43]. Plates were covered with ClearVue Sheets (Molecular Dimensions, Rotherham, UK) and stored at 22 °C. In our study, crystallization screens (MemMeso HT-96, MemGold1 HT-96 Eco Screen, MemGold2 HT-96 Eco Screen, MemTrans Eco, MemChannel Eco, XP screen, BCS screen Eco, The Cubic Phase I Suite, The Cubic Phase II Suite, MIDAS, Structure screen 1 CF and 2, MemSys, MemStart and MemPlus Eco, MemStart), customized screens at pH 7.0 and 8.5, and a citrate screening kit [46] were used. In addition to various screen solutions, 2 mM of inhibitory peptides NIP-1 [37] or NOP-1 [47,48], 1 mM $ZnCl_2$, 100 µM of ammonium molybdate or 5 mM of EGTA with 50 mM ß-mercaptoethanol were added to the crystallization setup. $ETR2^{1\text{-}186}$ mT2 was saturated with Cu-BCA prior to LCP preparation to fully load the receptor with its monovalent copper cofactor, as described by Schott-Verdugo et al. [39].

3. Results and Discussion

In recent years, LCP has enabled the crystallization of a wide range of membrane proteins [44,45,49,50]. This success prompted us to explore this technology, particularly in the transmembrane and membrane-adjacent regions of ethylene receptors ETR1 and ETR2, which harbor the plant hormone binding site and the monovalent copper cofactor essential for biological function. To this end, we cloned and expressed isolated subdomains and subdomain fusions of *ETR2* in a bacterial host. Of these, $ETR2^{1\text{-}186}$ *mT2*, $ETR1^{1\text{-}157}$ *mT2*, $ETR1^{1\text{-}407}$, and $ETR1^{1\text{-}316}$ were successfully expressed in bacterial cells after chemical induction with isopropyl-β-D-1-thiogalactopyranoside (IPTG). Purification of all four protein constructs after overnight expression resulted in large amounts (0.5–2 mL) of pure (see protein gels in Figure 4) and homogeneous material ($ETR1^{1\text{-}407}$ 16 mg/mL; $ETR1^{1\text{-}316}$ 19 mg/mL; $ETR1^{1\text{-}157}$ mT2 16 mg/mL; $ETR2^{1\text{-}186}$ mT2 11 mg/mL). Analysis of these preparations by SDS-PAGE and Western blotting (Figure 4) revealed only minor impurities, indicating that samples contained related monomers and SDS-stable dimers. For $ETR1^{1\text{-}157}$ mT2, a minor degradation product of ~20 kDa was observed in addition to the correct TMD monomer. For LCP crystallization of the purified recombinant ETR1 and ETR2 protein constructs, MO and MP were applied as standard lipids. Considering the different molecular mass and membrane-adjacent extent of the four constructs, further lipids were added to the standard setup to expand the lattice parameters of the LCP (Figure 1) [25]. The addition of anionic phospholipid DSPG to the LCP mixture increases solvent channels in the LCP to 26.8 nm in diameter through electrostatic and steric remodeling [51]. By contrast, when MO is used on its own, solvent channels are limited to ~12 nm through electrostatic swelling in a sponge phase [25]. To mimic natural membrane cholesterol composition, CHS, cardiolipin, or DOPC have also been used as additives to MP or MO [25,52,53]. In particular, DOPC, expected to be a promising additive to this lipid together with other phosphatidylcholines, is highly abundant in the ER endomembrane system where ETRs reside in the plant [54–56]. In addition to their effect on lattice parameters, doped lipids can form cubic phases with different geometries and water channel sizes, respectively (Figure 1) [25]. Finally, LCP formation also depends on the length and branching of the lipids as well as on the water content of the lipid mixture used. While cholesterol and DOPC only slightly extend the lattice parameters, cardiolipin and DSPG form extended water channels [22] suitable for membrane proteins with large extracellular domains such as the *Gloeobacter violaceus* ligand-gated ion channel protein [26] or, in our case, ETRs (Figure 2).

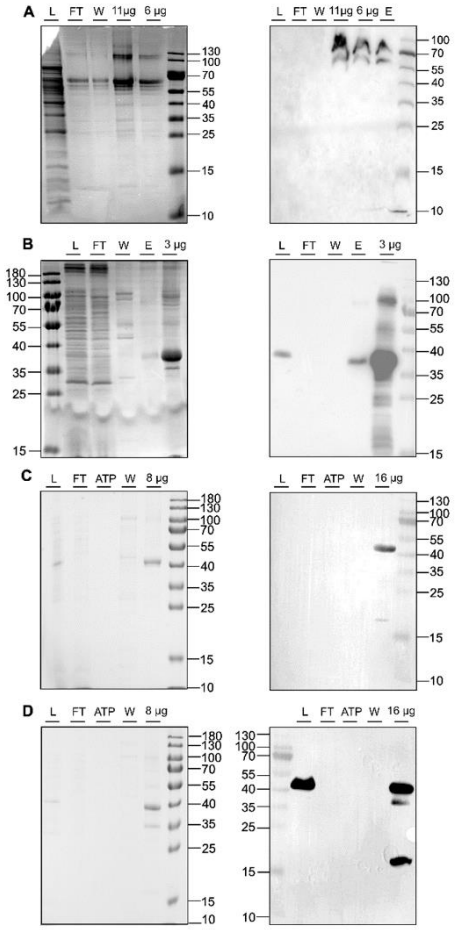

Figure 4. SDS-PAGE protein gels (**left panel**) and Western blots (**right panel**) of IMAC purifications for ETR2$^{1\text{-}186}$mT2 (**A**), ETR1$^{1\text{-}316}$ (**B**), ETR1$^{1\text{-}407}$ (**C**), and ETR1$^{1\text{-}157}$mT2 (**D**). The blots and gels were marked with sample load (L), flow-through (FT), ATP wash step (ATP), 50 mM imidazole wash step (W), 250 mM elution step (E), or x µg of the concentrated sample after imidazole removal. For immunoblotting, anti-GFP-HRP (Santa Cruz Biotechnology, Danvers, MA, USA) was used (**A**). Western blot signals in (**B**–**D**) were detected by HRP-conjugated anti-His antibody (Miltenyi Biotec B.V. & Co. KG, Bergisch-Gladbach, Germany). Colloidal Coomassie staining was used for SDS_PAGE protein gels shown on the left panel.

Quantitative evaluation of our screening trials revealed a higher number of crystal hits for MO/cholesterol MP/DOPC than corresponding setup trials for MO alone or other lipid mixtures (Figures 5 and S1). In addition to the difference in number, crystals from MO-lipid mixtures also appeared more rapidly (1–7 days) than in corresponding screenings with pure MO or MP-lipid mixtures (2–12 weeks).

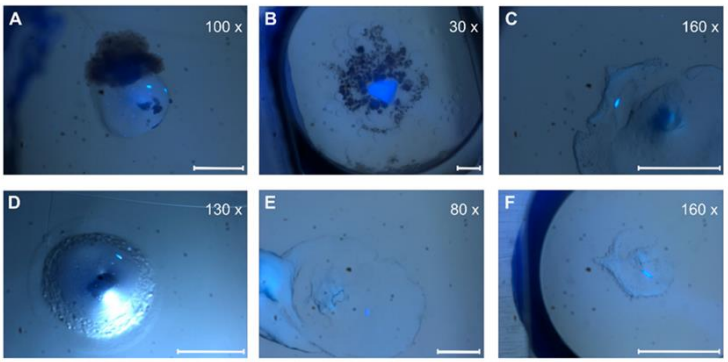

Figure 5. Crystal pictures under UV light. (**A**,**D**) ETR1$^{1\text{-}316}$; (**B**,**E**) ETR1$^{1\text{-}407}$; (**C**,**F**) ETR1$^{1\text{-}157}$ mT2. Depending on the magnification factor, the white scale bars represent a 100 µm length.

Depending on the lipid crystals obtained in our LCP screening, trials showed significant variations in size (35–200 µm) and morphology from amorphous crystals to cubes, needles, plates, and rods (Figure 5). Most of these crystals showed no diffraction on synchrotron beamlines, except for crystals from ETR1$^{1\text{-}316}$ and ETR2$^{1\text{-}186}$ mT2, which diffracted up to 4 Å and 2 Å, respectively. However, as shown in Figure 6, the overall data quality for these crystals was poor. The related diffraction pattern was rotationally blurred and showed high mosaicity, indicating disorders and poorly defined lattice packing. Peak integration and processing of the data collected for these crystals failed. Attempts to further optimize the initial crystallization conditions from the screening (0.1M $CaCl_2$, 0.1 M Tris pH 8.5; 28% (*v*/*v*) PEG300) by varying the salt or PEG concentrations have not succeeded. As a result of high salt, crystal processing and analysis were further complicated by salt crystals forming alongside the protein crystals, which interfered with harvesting protein crystals from the LCP and caused disturbing background noise in the diffraction images (Figure 6). By contrast, only non-diffracting protein crystals were obtained with low salt.

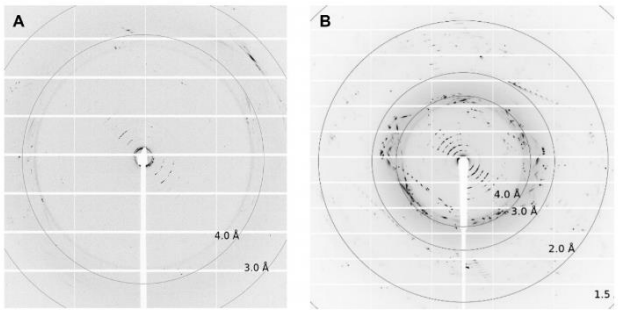

Figure 6. Diffraction pictures of (**A**) ETR1$^{1\text{-}316}$ and (**B**) ETR2$^{1\text{-}186}$ mT2. For ETR1$^{1\text{-}316}$, single spots up to 4 Å can be detected. For ETR2$^{1\text{-}186}$ mT2, diffraction spots reach up to 2Å. The crystallization conditions used for both crystals were 0.1 M $CaCl_2$, 0.1 M Tris pH 8.5; 28% *v*/*v* PEG300.

In the past, several crystallization studies revealed the significant role of protein stabilization in obtaining diffraction-quality crystals. To this end, target proteins are complexed with substrates, nucleic acids, cofactors, or small molecules. Successful examples include the bacterial two-component HK, a protein family closely related to HK-related ETRs. Similar to ETRs, many of these proteins contain a sensor domain linked to the

cytoplasmic kinase module via a transmembrane structure. While bacterial HKs' sensor domains are typically located in the periplasm, ETRs' sensor domains are fully integrated into the transmembrane structure. The sensor, transmembrane, and membrane adjacent HAMP domains of the nitrate/nitrite sensor kinase NarQ from *E. coli* have been solved by *in meso* crystallization and single-wavelength anomalous diffraction approaches in the ligand-bound form [57,58]. Structural alignment with the ligand-free apo structure of NarQ revealed that nitrate binding in the sensor domain triggers substantial rearrangements in the transmembrane structure, which are thought to reflect molecular events in HK signaling. Further examples of stabilized and structurally resolved bacterial HKs relate to the sensor domains of receptor kinases CusS and NarX from *E. coli* and CitA from *Klebsiella pneumoniae* [59–61], all of which require their stimulus (nitrate for NarX, Cu(I) for CusS and citrate for CitA) as cofactors for receptor dimerization. Dimerization is thought to induce conformational changes in the transmembrane structure, which are transferred to the kinase module.

A well-known cofactor of ETRs that is essential for their biological function is monovalent copper, which is bound to their transmembrane structure. Current data suggest that the metal cofactor is not required for receptor dimerization, but rather plays an essential role in providing a high-affinity binding site for the plant hormone ligand [13,37,62]. Studies of purified ETR1 reconstituted into unilamellar liposomes by EPR spectroscopy indicate that copper loading on the receptor does not cause major conformational changes in the transmembrane structure. However, given the spatial resolution of 1–2 nm for this technique [63], ligand-induced rearrangements of a few Angstroms, as observed for bacterial HKs [59–61], cannot be completely excluded at this stage. Therefore, to arrest the receptor in a defined and homogenous state, the copper loading state of the purified recombinant ETR must be fixed. Previous studies in our lab showed that about 20% of recombinant ETR1 produced in *E. coli* is preloaded with Cu(I) from the bacterial host. Therefore, to obtain a uniform, fully loaded preparation for LCP crystallization, recombinant ETRs were preloaded with Cu-BCA, as described previously [39,64]. Alternatively, Cu(I) was completely removed from the ETRs according to protocols described for the copper-exported P-type ATPase CopA [65]. In addition to their natural metal cofactor, purified recombinant proteins can bind to other metal ions that can maintain or even stabilize their structure. In this sense, Cu(I) has been replaced by Zn(II) in human and cyanobacterial copper chaperones for structural studies [66–68]. Thus, in addition to fixing the copper loading state of our purified ETRs, we also used zinc as a replacement in our LCP crystallization trials. In summary, our controlled metal-loading experiments revealed that many well-formed protein crystals are formed upon Zn(II) and Cu(I) addition by Cu-BCA. Conversely, the removal of the metal cofactor with TTM/EGTA/β-mercaptoethanol did not affect crystallization (Figure S1).

Previous studies from our laboratory [37,47,48,69] showed that the small synthetic peptide NOP-1 (LKRYKRRL), corresponding to an interaction sequence (NLS) in a downstream ETR binding partner, tightly binds to the ETR1 GAF domain and probably prevents conformational changes, leading to increased structural stability of the receptor dimer [37]. When applied to the plant, the peptide showed visible effects on plant ethylene responses. NOP-1 successfully delayed ripening and senescence in tomatoes [48,70], broccoli [71], and apples [72] by six to eight days. Binding studies by MST on purified ETR receptors from tomato, apple, and *Arabidopsis* demonstrated the peptide's high affinity for binding to receptors in the range of 80–100 nM [37,48,70,72]. Extending the sequence of the NOP-1 inhibitory peptide with additional residues (12 aa) adjacent to the NLS binding motif in the EIN2 downstream interaction partner (NIP peptide) further improved binding affinity [37]. Both inhibitory peptides were used for co-crystallization of our ETR constructs in the LCP screening trials to stabilize their transmembrane and membrane-adjacent domains. While the addition of NIP resulted in many well-formed rods and needles, NOP-1 addition had less effect on crystallization. However, compared to the previous metalation of the receptor by Cu(I) or Zn(II), the impact of both peptide ligands was less pronounced (Figure S1).

A total of 9216 crystallization trials were tested with four ETR constructs, lipids (MO, MP, cholesterol, cardiolipin, DSPG, DOPC), ligands (Cu-BCA, $ZnCl_2$, ammonium molybdate/EGTA/β-mercaptoethanol, NIP, NOP), and 18 different crystallization kits (for details see Material and Methods). For ETR2$^{1\text{-}186}$ mT2, more than 3900 crystallization conditions were screened with 17 crystallization kits, additives Cu-BCA and $ZnCl_2$, and lipid combinations MP/DSPG, MO/DSPG, MO, and MO/DOPC. For ETR1$^{1\text{-}316}$, lipid combinations MO/DSPG, MO/cholesterol, MO/cardiolipin, and MP/cholesterol, additives NIP, NOP, TTM/EGTA/β-mercaptoethanol, and 11 crystallization kits were used. Over 3700 crystallization conditions were screened. For ETR1$^{1\text{-}157}$ mT2, lipids (MO and MO/cholesterol) were used with six crystallization kits, resulting in 768 different crystallization conditions. Similarly, 768 crystallization conditions were tested for ETR1$^{1\text{-}407}$, which was applied using the additive NIP, seven crystallization kits, and lipid combinations MO/DSPG and MO/Cardiolipin. A total of 566 ETR crystals were screened at high-performance synchrotron beamlines (Figure S1). The formation of crystals was observed under different conditions; however, in most cases, they exhibited no or poor diffraction, possibly due to the intrinsic flexibility of ETR domains and resulting disorders in the crystal lattice. Attempts to restrict ETR flexibility by adding metal cofactors or inhibitory ligands have not succeeded.

4. Conclusions

Crystallization in lipid mesophases is a useful approach to studying and resolving membrane protein structures in a lipid-like environment. Plant ethylene receptors are a plausible target for this technique as the structure of their transmembrane sensor domain has not been resolved by other means yet. The TM domain of ethylene receptors ETR1 and ETR2, which is expressed in *E. coli* in high quantities and purity, was successfully crystallized using the LCP approach with different lipids, lipid mixtures, and additives. Of the many crystals obtained in our extensive screening, only two conditions provided crystals of ETR1$^{1\text{-}316}$ and ETR2 $^{1\text{-}186}$ mT2 with clear but blurred diffraction up to 4 Å and 2 Å, respectively. Although we tested known metal cofactors and inhibitory peptides of the receptors as additives under these conditions, we have not obtained well-diffracting highly-ordered crystals of these ETR structures. We assume that the high intrinsic flexibility of the TMD, which is supported by previous EPR studies, hampers high-resolution diffraction over a broad rotation angle. Therefore, TMD flexibility should be restrained for further crystallization attempts. Possible strategies include intra- and intermolecular cross-linking, termini-restraining, or the use of orthologous ETR1 receptors from different species [73–75]. Increased stability and rigidity of the TMD, as well as the rigidity of the receptor's membrane-adjacent domains, should improve structural determination by NMR, cryo-EM, or X-ray crystallography.

Supplementary Materials: The following supporting information can be downloaded at: https://www.mdpi.com/article/10.3390/biom14030375/s1, Figure S1: Compared data of crystallization hits between harvested and measured crystals; Table S1: Primer sequences for cloning.

Author Contributions: Conceptualization: G.G., Y.T. and B.R.; investigation: B.R., Y.T., A.M. and M.L.; project administration: Y.T. and G.G.; Visualization: B.R. and Y.T.; writing: B.R., Y.T. and G.G. All authors have read and agreed to the published version of the manuscript.

Funding: This work was supported by the Deutsche Forschungsgemeinschaft (German Research Foundation) project no. 267205415/CRC 1208 grant to G.G. (TP B06).

Institutional Review Board Statement: Not applicable.

Informed Consent Statement: Not applicable.

Data Availability Statement: Data is available from the authors upon reasonable request.

Acknowledgments: We are thankful for the permanent loan of the ProCrysMeso robot from Hartmut Michel at the Max Planck Institute of Biophysics in Frankfurt. We acknowledge the European Synchrotron Radiation Facility (ESRF) and the German Electron Synchrotron (DESY) for providing

synchrotron radiation facilities. We thank the Center for Structural Studies (CSS) at the Heinrich Heine University for their support. The CSS is funded by the Deutsche Forschungsgemeinschaft (DFG Grant number 417919780). Images were created with https://BioRender.com (accessed on 16 January 2024).

Conflicts of Interest: The authors declare no conflicts of interest.

References

1. Binder, B.M. Ethylene signaling in plants. *J. Biol. Chem.* **2020**, *295*, 7710–7725. [CrossRef]
2. Ju, C.; Chang, C. Advances in ethylene signalling: Protein complexes at the endoplasmic reticulum membrane. *AoB Plants* **2012**, *2012*, pls031. [CrossRef]
3. Cho, W.; Stahelin, R.V. Membrane-protein interactions in cell signaling and membrane trafficking. *Annu. Rev. Biophys. Biomol. Struct.* **2005**, *34*, 119–151. [CrossRef]
4. Bleecker, A.B. Ethylene perception and signaling: An evolutionary perspective. *Trends Plant Sci.* **1999**, *4*, 269–274. [CrossRef]
5. Bleecker, A.B.; Kende, H. Ethylene: A gaseous signal molecule in plants. *Annu. Rev. Cell Dev. Biol.* **2000**, *16*, 1–18. [CrossRef]
6. Ju, C.; van de Poel, B.; Cooper, E.D.; Thierer, J.H.; Gibbons, T.R.; Delwiche, C.F.; Chang, C. Conservation of ethylene as a plant hormone over 450 million years of evolution. *Nat. Plants* **2015**, *1*, 14004. [CrossRef]
7. Lacey, R.F.; Binder, B.M. How plants sense ethylene gas—The ethylene receptors. *J. Inorg. Biochem.* **2014**, *133*, 58–62. [CrossRef]
8. Grefen, C.; Harter, K. Plant two-component systems: Principles, functions, complexity and cross talk. *Planta* **2004**, *219*, 733–742. [CrossRef]
9. Shakeel, S.N.; Gao, Z.; Amir, M.; Chen, Y.; Rai, M.I.; Haq, N.U.; Schaller, G.E. Ethylene Regulates Levels of Ethylene Receptor/CTR1 Signaling Complexes in Arabidopsis thaliana. *J. Biol. Chem.* **2015**, *290*, 12415–12424. [CrossRef]
10. Hua, J.; Meyerowitz, E.M. Ethylene responses are negatively regulated by a receptor gene family in *Arabidopsis thaliana*. *Cell* **1998**, *94*, 261–271. [CrossRef]
11. Hua, J.; Sakai, H.; Nourizadeh, S.; Qianhong, G.C.; Bleecker, A.B.; Ecker, J.R.; Meyerowitz, E.M. EIN4 and ERS2 are members of the putative ethylene receptor gene family in *Arabidopsis*. *Plant Cell* **1998**, *10*, 1321–1332. [CrossRef]
12. Hall, A.E.; Findell, J.L.; Schaller, G.E.; Sisler, E.C.; Bleecker, A.B. Ethylene perception by the ERS1 protein in Arabidopsis. *Plant Physiol.* **2000**, *123*, 1449–1458. [CrossRef]
13. Berleth, M.; Berleth, N.; Minges, A.; Hänsch, S.; Burkart, R.C.; Stork, B.; Stahl, Y.; Weidtkamp-Peters, S.; Simon, R.; Groth, G. Molecular Analysis of Protein-Protein Interactions in the Ethylene Pathway in the Different Ethylene Receptor Subfamilies. *Front. Plant Sci.* **2019**, *10*, 726. [CrossRef]
14. Schaller, G.E.; Bleecker, A.B. Ethylene-binding sites generated in yeast expressing the Arabidopsis ETR1 gene. *Science* **1995**, *270*, 1809–1811. [CrossRef]
15. Gao, Z.; Wen, C.-K.; Binder, B.M.; Chen, Y.; Chang, J.; Chiang, Y.; Robert, J.K.R., III; Chang, C.; Schaller, G.E. Heteromeric interactions among ethylene receptors mediate signaling in Arabidopsis. *J. Biol. Chem.* **2008**, *283*, 23801–23810. [CrossRef]
16. Chang, C.; Kwok, S.F.; Bleecker, A.B.; Meyerowitz, E.M. Arabidopsis ethylene-response gene ETR1: Similarity of product to two-component regulators. *Science* **1993**, *262*, 539–544. [CrossRef]
17. Mayerhofer, H.; Panneerselvam, S.; Kaljunen, H.; Tuukkanen, A.; Mertens, H.D.T.; Mueller-Dieckmann, J. Structural model of the cytosolic domain of the plant ethylene receptor 1 (ETR1). *J. Biol. Chem.* **2015**, *290*, 2644–2658. [CrossRef]
18. Grantz, A.A.; Muller-Dieckmann, H.J.; Kim, S.-H. Subcloning, crystallization and preliminary X-ray analysis of the signal receiver domain of ETR1, an ethylene receptor from *Arabidopsis thaliana*. *Acta Crystallogr. D Biol. Crystallogr.* **1998**, *54*, 690–692. [CrossRef]
19. Panneerselvam, S.; Kaljunen, H.; Mueller-Dieckmann, J. Cloning, overexpression, purification and preliminary X-ray analysis of the catalytic domain of the ethylene receptor ETR1 from Arabidopsis thaliana. *Acta Crystallogr. Sect. F Struct. Biol. Cryst. Commun.* **2013**, *69*, 1307–1309. [CrossRef]
20. Birch, J.; Axford, D.; Foadi, J.; Meyer, A.; Eckhardt, A.; Thielmann, Y.; Moraes, I. The fine art of integral membrane protein crystallisation. *Methods* **2018**, *147*, 150–162. [CrossRef]
21. Landau, E.M.; Rosenbusch, J.P. Lipidic cubic phases: A novel concept for the crystallization of membrane proteins. *Proc. Natl. Acad. Sci. USA* **1996**, *93*, 14532–14535. [CrossRef]
22. Caffrey, M.; Cherezov, V. Crystallizing membrane proteins using lipidic mesophases. *Nat. Protoc.* **2009**, *4*, 706–731. [CrossRef]
23. Wadsten, P.; Wöhri, A.B.; Snijder, A.; Katona, G.; Gardiner, A.T.; Cogdell, R.J.; Neutze, R.; Engström, S. Lipidic sponge phase crystallization of membrane proteins. *J. Mol. Biol.* **2006**, *364*, 44–53. [CrossRef]
24. Zabara, A.; Meikle, T.G.; Newman, J.; Peat, T.S.; Conn, C.E.; Drummond, C.J. The nanoscience behind the art of in-meso crystallization of membrane proteins. *Nanoscale* **2017**, *9*, 754–763. [CrossRef]
25. Cherezov, V.; Clogston, J.; Misquitta, Y.; Abdel-Gawad, W.; Caffrey, M. Membrane protein crystallization in meso: Lipid type-tailoring of the cubic phase. *Biophys. J.* **2002**, *83*, 3393–3407. [CrossRef]
26. Zabara, A.; Chong, J.T.Y.; Martiel, I.; Stark, L.; Cromer, B.A.; Speziale, C.; Drummond, C.J.; Mezzenga, R. Design of ultra-swollen lipidic mesophases for the crystallization of membrane proteins with large extracellular domains. *Nat. Commun.* **2018**, *9*, 544. [CrossRef]

27. Wu, H.; Wacker, D.; Mileni, M.; Katritch, V.; Han, G.W.; Vardy, E.; Liu, W.; Thompson, A.A.; Huang, X.; Carrol, F.I.; et al. Structure of the human κ-opioid receptor in complex with JDTic. *Nature* **2012**, *485*, 327–332. [CrossRef]
28. Thomaston, J.L.; Alfonso-Prieto, M.; Woldeyes, R.A.; DeGrado, W.F. High-resolution structures of the M2 channel from influenza A virus reveal dynamic pathways for proton stabilization and transduction. *Proc. Natl. Acad. Sci. USA* **2015**, *112*, 14260–14265. [CrossRef]
29. Siu, F.Y.; He, M.; de Graaf, C.; Han, G.W.; Yang, D.; Zhang, Z.; Zhou, C.; Xu, Q.; Wacker, D.; Joseph, J.S.; et al. Structure of the human glucagon class B G-protein-coupled receptor. *Nature* **2013**, *499*, 444–449. [CrossRef] [PubMed]
30. Shimamura, T.; Shiroishi, M.; Weyand, S.; Tsujimoto, H.; Winter, G.; Katritch, V.; Abagyan, R.; Cherezov, V.; Liu, W.; Han, G.W.; et al. Structure of the human histamine H1 receptor complex with doxepin. *Nature* **2011**, *475*, 65–70. [CrossRef] [PubMed]
31. Schöppe, J.; Ehrenmann, J.; Waltenspühl, Y.; Plückthun, A. Universal platform for the generation of thermostabilized GPCRs that crystallize in LCP. *Nat. Protoc.* **2022**, *17*, 698–726. [CrossRef] [PubMed]
32. Caffrey, M. A comprehensive review of the lipid cubic phase or in meso method for crystallizing membrane and soluble proteins and complexes. *Acta Crystallogr. F Struct. Biol. Commun.* **2015**, *71*, 3–18. [CrossRef] [PubMed]
33. Zhang, T.; Liu, J.; Fellner, M.; Zhang, C.; Sui, D.; Hu, J. Crystal structures of a ZIP zinc transporter reveal a binuclear metal center in the transport pathway. *Sci. Adv.* **2017**, *3*, e1700344. [CrossRef] [PubMed]
34. Kusakizako, T.; Tanaka, Y.; Hipolito, C.J.; Kuroda, T.; Ishitani, R.; Suga, H.; Nureki, O. LCP crystallization and X-ray diffraction analysis of VcmN, a MATE transporter from Vibrio cholerae. *Acta Crystallogr. F Struct. Biol. Commun.* **2016**, *72*, 552–557. [CrossRef]
35. Cherezov, V. Lipidic cubic phase technologies for membrane protein structural studies. *Curr. Opin. Struct. Biol.* **2011**, *21*, 559–566. [CrossRef]
36. Goedhart, J.; von Stetten, D.; Noirclerc-Savoye, M.; Lelimousin, M.; Joosen, L.; Hink, M.A.; von Weeren, L.; Gadella, T.W.J., Jr.; Royant, A. Structure-guided evolution of cyan fluorescent proteins towards a quantum yield of 93%. *Nat. Commun.* **2012**, *3*, 751. [CrossRef]
37. Milić, D.; Dick, M.; Mulnaes, D.; Pfleger, C.; Kinnen, A.; Gohlke, H.; Groth, G. Recognition motif and mechanism of ripening inhibitory peptides in plant hormone receptor ETR1. *Sci. Rep.* **2018**, *8*, 3890. [CrossRef]
38. Kanonenberg, K.; Royes, J.; Kedrov, A.; Poschmann, G.; Angius, F.; Solgadi, A.; Spitz, O.; Kleinschrodt, K.; Stühler, K.; Miroux, B.; et al. Shaping the lipid composition of bacterial membranes for membrane protein production. *Microb. Cell Factories* **2019**, *18*, 131. [CrossRef]
39. Schott-Verdugo, S.; Müller, L.; Classen, E.; Gohlke, H.; Groth, G. Structural Model of the ETR1 Ethylene Receptor Transmembrane Sensor Domain. *Sci. Rep.* **2019**, *9*, 8869. [CrossRef]
40. Lemke, M.; Reiners, J.; Smits, S.H.J.; Lakomek, N.; Groth, G. Functional reconstitution and structural characterization of the plant hormone receptor ETR1 in lipid nanodiscs. *Chem. Commun.* **2023**, *59*, 9344–9347. [CrossRef]
41. Grefen, C.; Städele, K.; Růzicka, K.; Petr, O.; Klaus, H.; Jakub, H. Subcellular localization and in vivo interactions of the Arabidopsis thaliana ethylene receptor family members. *Mol. Plant* **2008**, *1*, 308–320. [CrossRef]
42. Moussatche, P.; Klee, H.J. Autophosphorylation activity of the *Arabidopsis ethylene* receptor multigene family. *J. Biol. Chem.* **2004**, *279*, 48734–48741. [CrossRef]
43. Rathmann, B.; Pais, D.Q.; Thielmann, Y. MPI tray: A versatile crystallization plate for membrane proteins. *J. Appl. Crystallogr.* **2017**, *50*, 327–330. [CrossRef]
44. Zhao, J.; Xie, H.; Mehdipour, A.R.; Safarian, S.; Ermler, U.; Münke, C.; Thielmann, Y.; Hummer, G.; Ebersberger, I.; Wang, J.; et al. The structure of the Aquifex aeolicus MATE family multidrug resistance transporter and sequence comparisons suggest the existence of a new subfamily. *Proc. Natl. Acad. Sci. USA* **2021**, *118*, e2107335118. [CrossRef]
45. Zakrzewska, S.; Mehdipour, A.R.; Malviya, V.N.; Nonaka, T.; Köpke, J.; Münke, C.; Hausner, W.; Hummer, G.; Safarian, S.; Michel, H. Inward-facing conformation of a multidrug resistance MATE family transporter. *Proc. Natl. Acad. Sci. USA* **2019**, *116*, 12275–12284. [CrossRef]
46. Joseph, J.S.; Liu, W.; Kunken, J.; Weiss, T.M.; Tsuruta, H.; Cherezov, V. Characterization of lipid matrices for membrane protein crystallization by high-throughput small angle X-ray scattering. *Methods* **2011**, *55*, 342–349. [CrossRef]
47. Bisson, M.M.A.; Groth, G. Targeting Plant Ethylene Responses by Controlling Essential Protein-Protein Interactions in the Ethylene Pathway. *Mol. Plant* **2015**, *8*, 1165–1174. [CrossRef] [PubMed]
48. Bisson, M.M.A.; Kessenbrock, M.; Müller, L.; Hofmann, A.; Schmitz, F.; Cristescu, S.M.; Groth, G. Peptides interfering with protein-protein interactions in the ethylene signaling pathway delay tomato fruit ripening. *Sci. Rep.* **2016**, *6*, 30634. [CrossRef] [PubMed]
49. Zabara, A.; Meikle, T.G.; Trenker, R.; Yao, S.; Newman, J.; Peat, T.S.; Separovic, F.; Conn, C.E.; Call, M.J.; Call, M.E.; et al. Lipidic Cubic Phase-Induced Membrane Protein Crystallization: Interplay Between Lipid Molecular Structure, Mesophase Structure and Properties, and Crystallogenesis. *Cryst. Growth Des.* **2017**, *17*, 5667–5674. [CrossRef]
50. Zabara, A.; Mezzenga, R. Plenty of room to crystallize: Swollen lipidic mesophases for improved and controlled in-meso protein crystallization. *Soft Matter* **2012**, *8*, 6535–6541. [CrossRef]
51. Engblom, J.; Miezis, Y.; Nylander, T.; Razumas, V.; Larsson, K. On the swelling of monoolein liquid-crystalline aqueous phases in the presence of distearoylphosphatidylglycerol. In *Surface and Colloid Science*; Razumas, V., Lindman, B., Nylander, T., Eds.; Springer: Berlin/Heidelberg, Germany, 2001; pp. 9–15. Volume 116.

52. Cecchetti, C.; Strauss, J.; Stohrer, C.; Naylor, C.; Pryor, E.; Hobbs, J.; Tanley, S.; Goldman, A.; Byrne, B. A novel high-throughput screen for identifying lipids that stabilise membrane proteins in detergent based solution. *PLoS ONE* **2021**, *16*, e0254118. [CrossRef] [PubMed]
53. Li, D.; Howe, N.; Dukkipati, A.; Shah, S.T.A.; Bax, B.D.; Edge, C.; Bridges, A.; Hardwicke, P.; Singh, O.M.P.; Giblin, G.; et al. Crystallizing Membrane Proteins in the Lipidic Mesophase. Experience with Human Prostaglandin E2 Synthase 1 and an Evolving Strategy. *Cryst. Growth Des.* **2014**, *14*, 2034–2047. [CrossRef] [PubMed]
54. Reszczyńska, E.; Hanaka, A. Lipids Composition in Plant Membranes. *Cell Biochem. Biophys.* **2020**, *78*, 401–414. [CrossRef] [PubMed]
55. Brown, D.J.; Dupont, F.M. Lipid Composition of Plasma Membranes and Endomembranes Prepared from Roots of Barley (*Hordeum vulgare* L.): Effects of Salt. *Plant Physiol.* **1989**, *90*, 955–961. [CrossRef] [PubMed]
56. Donaldson, R.P.; Beevers, H. Lipid composition of organelles from germinating castor bean endosperm. *Plant Physiol.* **1977**, *59*, 259–263. [CrossRef]
57. Gushchin, I.; Melnikov, I.; Polovinkin, V.; Ishchenko, A.; Yuzhakova, A.; Buslaev, P.; Bourenkov, G.; Grudinin, S.; Round, E.; Balandin, T.; et al. Mechanism of transmembrane signaling by sensor histidine kinases. *Science* **2017**, 356. [CrossRef]
58. Gordeliy, V.I.; Labahn, J.; Moukhametzianov, R.; Efremov, R.; Granzin, J.; Schlesinger, R.; Büldt, G.; Savopol, T.; Scheidig, A.J.; Klare, J.P.; et al. Molecular basis of transmembrane signalling by sensory rhodopsin II-transducer complex. *Nature* **2002**, *419*, 484–487. [CrossRef] [PubMed]
59. Gudipaty, S.A.; McEvoy, M.M. The histidine kinase CusS senses silver ions through direct binding by its sensor domain. *Biochim. Biophys. Acta* **2014**, *1844*, 1656–1661. [CrossRef]
60. Cheung, J.; Hendrickson, W.A. Structural analysis of ligand stimulation of the histidine kinase NarX. *Structure* **2009**, *17*, 190–201. [CrossRef]
61. Sevvana, M.; Vijayan, V.; Zweckstetter, M.; Reinelt, S.; Madden, D.R.; Herbst-Irmer, R.; Sheldrick, G.M.; Bott, M.; Griesinger, C.; Becker, S. A ligand-induced switch in the periplasmic domain of sensor histidine kinase CitA. *J. Mol. Biol.* **2008**, *377*, 512–523. [CrossRef]
62. Schaller, G.E.; Ladd, A.N.; Lanahan, M.B.; Spanbauer, J.M.; Bleecker, A.B. The ethylene response mediator ETR1 from Arabidopsis forms a disulfide-linked dimer. *J. Biol. Chem.* **1995**, *270*, 12526–12530. [CrossRef]
63. Kugele, A.; Uzun, B.; Müller, L.; Schott-Verdugo, S.; Gohlke, H.; Groth, G.; Drescher, M. Mapping the helix arrangement of the reconstituted ETR1 ethylene receptor transmembrane domain by EPR spectroscopy. *RSC Adv.* **2022**, *12*, 7352–7356. [CrossRef]
64. Müller, L. Kupfertransport und -koordinationschemie der Kupferbindenden Domäne des Ethylenrezeptors ETR1. Ph.D. Thesis, Universitäts und Landesbibliothek, Düsseldorf, Germany, 2019. Available online: https://docserv.uni-duesseldorf.de/servlets/DocumentServlet?id=52654 (accessed on 12 January 2024).
65. Andersson, M.; Mattle, D.; Sitsel, O.; Klymchuk, T.; Nielsen, A.M.; Møller, L.B.; White, S.H.; Nissen, P.; Gourdon, P. Copper-transporting P-type ATPases use a unique ion-release pathway. *Nat. Struct. Mol. Biol.* **2014**, *21*, 43–48. [CrossRef]
66. Mangini, V.; Belviso, B.D.; Nardella, M.I.; Natile, G.; Arnesano, F.; Caliandro, R. Crystal Structure of the Human Copper Chaperone ATOX1 Bound to Zinc Ion. *Biomolecules* **2022**, *12*, 1494. [CrossRef]
67. Badarau, A.; Baslé, A.; Firbank, S.J.; Dennison, C. Investigating the role of zinc and copper binding motifs of trafficking sites in the cyanobacterium Synechocystis PCC 6803. *Biochemistry* **2013**, *52*, 6816–6823. [CrossRef]
68. Badarau, A.; Baslé, A.; Firbank, S.J.; Dennison, C. Crosstalk between Cu(I) and Zn(II) homeostasis via Atx1 and cognate domains. *Chem. Commun.* **2013**, *49*, 8000–8002. [CrossRef]
69. Hoppen, C.; Müller, L.; Albrecht, A.C.; Groth, G. The NOP-1 peptide derived from the central regulator of ethylene signaling EIN2 delays floral senescence in cut flowers. *Sci. Rep.* **2019**, *9*, 1287. [CrossRef] [PubMed]
70. Kessenbrock, M.; Klein, S.M.; Müller, L.; Hunsche, M.; Noga, G.; Groth, G. Novel Protein-Protein Inhibitor Based Approach to Control Plant Ethylene Responses: Synthetic Peptides for Ripening Control. *Front. Plant Sci.* **2017**, *8*, 1528. [CrossRef] [PubMed]
71. Aghdam, M.S.; Razavi, F. Octapeptide NOP-1 treatment delays yellowing in broccoli floret during low temperature storage. *Postharvest Biol. Technol.* **2021**, *180*, 111628. [CrossRef]
72. Klein, S.; Fiebig, A.; Neuwald, D.; Dluhosch, D.; Müller, L.; Groth, G.; Noga, G.; Hunsche, M. Influence of the ethylene-related signal-inhibiting octapeptide NOP-1 on postharvest ripening and quality of 'Golden Delicious' apples. *J. Sci. Food Agric.* **2019**, *99*, 3903–3909. [CrossRef] [PubMed]
73. Liu, S.; Li, S.; Krezel, A.M.; Li, W. Stabilization and structure determination of integral membrane proteins by termini restraining. *Nat. Protoc.* **2022**, *17*, 540–565. [CrossRef] [PubMed]
74. Kastner, B.; Fischer, N.; Golas, M.M.; Sander, B.; Dube, P.; Böhringer, D.; Hartmuth, K.; Deckert, J.; Hauer, F.; Wolf, E.; et al. GraFix: Sample preparation for single-particle electron cryomicroscopy. *Nat. Methods* **2008**, *5*, 53–55. [CrossRef] [PubMed]
75. Lusty, C.J. A gentle vapor-diffusion technique for cross-linking of protein crystals for cryocrystallography. *J. Appl. Crystallogr.* **1999**, *32*, 106–112. [CrossRef]

Supplementary Material
for
Crystallization of ethylene plant hormone receptor – screening for the structure

Buket Rüffer [1,¶], Yvonne Thielmann [1,¶], Moritz Lemke [1], Alexander Minges [1] and Georg Groth [1,*]

Author Affiliations:

[1]Heinrich Heine University Düsseldorf, Faculty of Mathematics and Natural Sciences, Institute of Biochemical Plant Physiology, Germany

To whom correspondence should be addressed:

Email: georg.groth@hhu.de

Tel: +49 211 81 12822

Fax: +49 211 81 13569

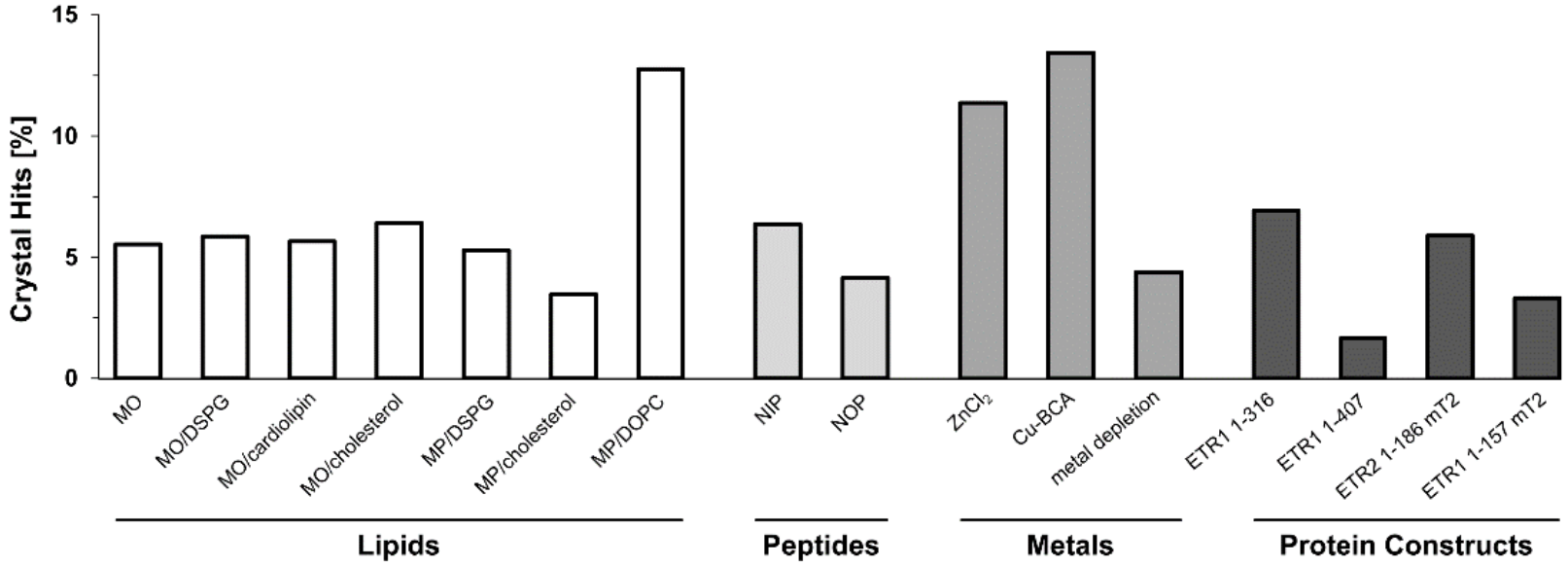

S1 Fig 1. Compared data of crystallization hits of harvested and measured crystals [%], which were evaluated with regard to the following parameters from left to right: lipids (white), peptides (light grey), metals (dark grey) and protein constructs (black).

Table S1. Primer sequences for cloning.

Primer name	Sequence
ETR2 TMD_CFP_for	ATGCTGACCCAGGAAATCCGTAAAAGTCTGATGGTGAGCAAGGGC
ETR2 TMD_CFP_rev	CAGACTTTTACGGATTTCCTG
ETR2 TMD_for	CCGCATCGTGACTGAC
CFP rev	AGGCAGATCGTCAGTCAGTCACGATGCGGCTTGTACAGCTCGTCC
mTurquoise-T65S_for	ACCACCCTGTCCTGGGGC
mTurquoise-T65S rev	CACGAGGGTGGGCCAG
mTurquoise2_A145Y-I146F_for	TACTTTAGCGACAACGTCTATATCACCG
mTurquoise2_A145Y-I146F	GTTGTACTCCAGCTTGTGCC
ETR2_c-term.-10x His-forI	CATCATCATCATCACTGACTGACGATCTGCCTCG
ETR2_CFP_10x His	ATGATGATGATGATGCTTGTACAGCTCGTCCATGC
ETR1 TMD_mT2_for	catgagattagaagcactttaatggtgagcaagggcgaggagctg
GST_TEV_rev	caatacaattgcagacttcCATACCCGGGCCCTGAAAATACAG
ETR1-TMD_for	ATGgaagtctgcaattgtattgaaccg
ETR1-TMD_rev	taaagtgcttctaatctcatgagtcaacattctc

6 Diskussion

Der Ethylensignalweg ist im Pflanzenreich hoch konserviert (Ju *et al.* 2015). Um das gasförmige Phytohormon Ethylen binden zu können werden die im ER lokalisierten Ethylenrezeptoren benötigt (vgl. Kapitel 3.2; Chen *et al.* 2002; Gao *et al.* 2003; Grefen *et al.* 2008; Dong *et al.* 2010). Die Rezeptoren, die in dieser Arbeit verwendet wurden, stammen aus dem Organismus *A. thaliana*. Bei diesen Rezeptoren handelt es sich um Negativregulatoren, die in Anwesenheit von zwei Cu(I)-Kofaktoren pro Dimer aktiv sind (Schott-Verdugo *et al.* 2019; Binder 2020). Durch Autophosphorylierungsschritte in der HK-Domäne und in der RD wird CTR1 aktiviert, welches wiederum EIN2-CEND phosphoryliert. Wenn kein Ethylen vorliegt werden in der darauffolgenden Kaskade wichtige Elemente (EIN2-CEND, EIN3, EIL1/2) die zur Ethylenantwort führen würden, proteolytisch abgebaut (vgl. Kapitel 3.3; Binder 2020). In Anwesenheit von Ethylen und Kupfer werden die Ethylenrezeptoren inaktiviert. Dadurch findet keine Autophosphorylierung der Rezeptoren statt. Somit wird EIN2-CEND nicht mehr abgebaut und kann in den Nukleus transportiert werden. Durch Transkriptionsfaktoren wird die sogenannte Ethylenantwort ausgelöst (vgl. Kapitel 3.3; Abbildung 6; Binder 2020). Beispiele hierfür sind die Blütenseneszenz und die Fruchtreife (Burg und Burg 1962; Johnson und Ecker 1998). Sowohl der genaue Mechanismus, der zur Bindung von Ethylen und der damit verbundenen vermuteten Konformationsänderung führt, als auch die Struktur der Rezeptoren sind jedoch unbekannt. Bisher sind nur die Kristallstrukturen für die HK und RD des ETR1 bekannt (Grantz *et al.* 1998; Panneerselvam *et al.* 2013; Mayerhofer *et al.* 2015). Im Jahr 2019 wurde eine ganze Reihe funktionaler Studien an ETR1 im Zusammenhang mit dem Kupferkofaktor durchgeführt, die zur Aufklärung der Kupfertransportroute führte (Hoppen *et al.* 2019a; Hoppen 2020). Dadurch konnte das erste experimentell, validierte Strukturmodell der ETR1-TMD - bestehend aus drei Helices - erstellt werden (Schott-Verdugo *et al.* 2019; Müller 2020). Mithilfe der etablierten Kupfer-Bicinchoninsäure (BCA)-Methode konnte die Kupferstöchiometrie im Rezeptor, die Kupferaffinität des Rezeptors und der Kupfertransfer der Chaperone ATX1 und CCH auf ETR1 untersucht werden (Schott-Verdugo *et al.* 2019; Hoppen *et al.* 2019a; Hoppen 2020; Müller 2020).

Diese Resultate und Methoden sollten nun weiterführend für strukturelle Analysen genutzt werden. Um weitere Informationen über die TMD zu erhalten, wurde in dieser

Arbeit die relative Anordnung der TM-Helices von ETR1 zueinander mithilfe von EPR-Spektroskopie untersucht. Dazu wurden die experimentellen Ergebnisse mit den Strukturmodellen, welche von Schott-Verdugo *et al.* (2019; Modell 1) und Alphafold (Jumper *et al.* 2021; Modell 2) vorhergesagt wurden, verglichen (vgl. Kapitel 5.1). Basierend auf der Annahme von Schott-Verdugo *et al.* (2019), dass die Aminosäureposition D25 einen Einfluss auf die Kupferbindung haben könnte, erfolgten weitere Bindungsstudien zur Kupferkoordinierung. Mit diesen konnte die Bedeutung der Aminosäuren D25 und K91 im Zusammenhang mit der Kupferkoordinierung besser eingeordnet werden (vgl. Kapitel 5.2). Darüber hinaus konnte die Methode der LCP-Kristallisation für ETR1 und ETR2 etabliert werden, welche zu ersten Kristallen und Diffraktionsbildern führte (vgl. Kapitel 5.3).

6.1 Diskussion der Ergebnisse aus der EPR-Spektroskopie

Mithilfe des chemischen Farbstoffs *Methanethiosulfonate Spin Label* (MTSSL), der kovalent an Cysteine bindet, sollten die intra- und interhelikalen Abstände der transmembranen Helices mittels EPR-Spektroskopie bestimmt werden (vgl. Kapitel 5.1; Figure 1; Altenbach *et al.* 1990). Dazu wurden Cysteine an ausgewählten Positionen in der TMD durch Substitutionen mittels PCR erfolgreich eingefügt. Um unspezifische Bindungen des Farbstoffs zu vermeiden, wurden die natürlich vorhandenen Cysteine C4, C6, C65 und C99 zu Serinen mutiert (vgl. Kapitel 5.1). Nach der erfolgreichen rekombinanten Expression und Reinigung dieser Cysteinmutanten, konnte die Methode der EPR-Spektroskopie erfolgreich genutzt werden, um Untersuchungen an der TMD des ETR1 durchzuführen (vgl. Kapitel 5.1; Supplemental Figure S4). Im direkten Vergleich weisen die experimentell gewonnenen Ergebnisse eine höhere Übereinstimmung mit der Helixanordnung des Modells von Schott-Verdugo *et al.* (2020) als in das von Alphafold generierte Modell ein (vgl. Kapitel 5.1, Figure 3).

Die intrahelikalen Abstände, welche im Experiment ermittelt wurden, stimmen bei Helix I und Helix II für beide Modelle überein. Im Vergleich zu Modell 1 und den experimentellen Ergebnissen zeigt die vorhergesagte Anordnung zwischen Helix I und Helix III von Modell 2 an den Aminosäurepositionen L17C/V86C, A31C/S114C und Y41C/S114C eine Abweichung (vgl. Kapitel 5.1; Figure 3). Dies könnte daran liegen, dass Alphafold ein Vorhersageprogramm ist, welches auf einer künstlichen Intelligenz basiert. Dabei wird die Aminosäuresequenz eines Proteins aus UniProt und oder der

homologen Struktur aus der Proteindatenbank genutzt (Jumper *et al.* 2021). Im Vergleich zu Modell 2 wurde für die Erstellung des Modell 1 von Schott-Verdugo *et al.* (2019) eine Kombination verschiedener Vorhersageprogramme verwendet. Zusätzlich wurden die Ergebnisse aus der experimentell validierten Daten Tryptophan-Scanning-Mutagenese integriert (Schott-Verdugo *et al.* 2019).

Die intrahelikale Messung an Helix II an den Aminosäurepositionen V54C/F76C ergab, dass der Abstand zwischen den beiden Positionen größer war als erwartet (vgl. Kapitel 5.1, Figure 3). Eine weitere intrahelikale Messung an Helix II an den Aminosäurepositionen V54C/F76C zeigte, dass der Abstand zwischen den beiden Positionen größer war als angenommen wurde (vgl. Kapitel 5.1, Figure 3). Der experimentell ermittelte Abstand weicht demnach von den in Modell 1 und 2 vorhergesagten Werten ab. Die Diskrepanz lässt sich vermutlich darauf zurückführen, dass MTSSL den Abstand vergrößert hat (vgl. Kapitel 5.1, Figure 3).

Zusätzlich scheint die zweite Helix eine höhere Flexibilität an den Schleifenregionen (Position V54C, F76C) aufzuweisen. Weitere Hinweise auf eine hohe Flexibilität in der TMD, abgesehen vom größeren Abstand zwischen V54C/F76C, sind die nicht messbaren Bereiche des chemischen Markers an den Positionen L17C/V54C und A31C/F76C (vgl. Kapitel 5.1). Die zu messenden Abstände lagen vermutlich außerhalb des Messbereichs für die EPR-Spektroskopie (<1,8 nm oder >5,6 nm; vgl. Kapitel 5.1; Jeschke 2012).

In einem weiteren Experiment wurden ausgewählte Mutanten mit Kupfer-BCA beladen, sowie die Kupferstöchiometrie berechnet (Schott-Verdugo *et al.* 2019; Müller 2020). Es wird angenommen, dass durch die Bindung des Kupferkofaktors und des Liganden Ethylen eine Konformationsänderung verursacht wird, wodurch die Rezeptoren von dem inaktiven in den aktiven Zustand wechseln sollten. Deshalb ist eine erhöhte Mobilität in diesen Bereichen anzunehmen (Zhao *et al.* 2002).Durch die Beladung des Rezeptors mit Kupfer-BCA könnte, anhand der chemisch markierten Cysteine, eine ligandenbedingte Konformationsänderung im Rezeptor gemessen werden. Dies würde zu detaillierteren Informationen über die Funktionalität und Anordnung der Helix führen.

Neben den Mutanten L17C/V54C und A31C/F76C, wurde die Mutante V54C/F76C für die Kupferbeladung eingesetzt, um mögliche Konformationsänderungen in der flexiblen zweiten Helix zu untersuchen. Bei der Mutante A31C/S114C wäre nach der Kupferbeladung und Konformationsänderung ebenfalls ein messbarer Unterschied zu erwarten gewesen, da Helix III für die Signaltransduktion innerhalb des Rezeptors verantwortlich ist (Wang *et al.* 2006).

Eine Kupferbindung ist zwar in diesen Experimenten nachweisbar, führt allerdings zu keiner messbaren Konformationsänderung (vgl. Kapitel 5.1, Figure 3; Supplemental Figure S7). Im Vergleich zu den übrigen mit Kupfer-BCA getesteten Mutanten zeigt die Mutante L17C/V54C eine geringere Kupferbeladung (vgl. Supplemental Figure S7C). Dies lässt sich vermutlich auf die räumliche Nähe des MTSSL- *Spin Labels* zum möglichen Kupferkoordinationszentrum D25 C65S und H69 zurückführen, wodurch die Komplexierung des Kupfers behindert wird. Zusätzlich sind die Marker an diesen Positionen eher nach innen als nach außen orientiert (vgl. Kapitel 5.1, Supplemental Figure S7 und Figure S9; vgl. Kapitel 5.2, Figure 7; Rodríguez *et al.* 1999; Wang *et al.* 2006; Schott-Verdugo *et al.* 2019).

Zusammenfassend konnte ermittelt werden, dass die Anordnung der TMH in Strukturmodell 1 von Schott-Verdugo *et al.* (2019) besser mit den experimentellen Daten übereinstimmen als die in Strukturmodell 2, welches mit Alphafold generiert wurde. Helix II ist vor allem in den C-terminalen Schleifenregionen flexibler, als in Modell 1 und 2 angenommen wurde. Cu(I) allein führte zu keiner maßgeblichen Änderung in der Konformation der TMD. Zudem konnte erfolgreich eine Methode entwickelt werden, um die Anordnung der α-Helices von ETR1 genauer zu untersuchen und mit verschiedenen computerbasierten Modellen zu vergleichen.

Durch die Ergebnisse aus der EPR haben sich neue Herausforderungen ergeben. Um einen stärkeren Effekt in der EPR in Bezug auf die Konformationsänderung zu erkennen, könnte in zukünftigen Experimenten versucht werden z. B. Ethylen hinzuzufügen (Zhao *et al.* 2002), welcher zu einem messbaren Unterschied in den Abständen der markierten Helices führen könnte. Ergänzend dazu könnten Circulardichroismus (CD) -, *Nuclear Magnetic Resonance* (NMR) - und Fluoreszenzspektroskopie angewandt werden, um eine Veränderung in der Konformation zu beobachten (Greenfield 2015; Hu *et al.* 2021; Dos Santos Rodrigues *et al.* 2023).

Es besteht die Möglichkeit, dass andere Domänen (GAF-, DHp-, HK-, RD-Domäne) einen entscheidenden Faktor bei der Konformationsänderung einnehmen. Daher könnten weitere EPR-Experimente an ausgewählten Stellen von ETR1-GAF $^{1–316}$ oder mit dem Volllängenrezeptor von *A. thaliana* durchgeführt werden, die bereits für Rekonstitution von Nanodisks verwendet wurden (vgl. Kapitel 5.3; Lemke *et al.* 2023).

Als alternative Methode zur EPR-Messung mit Proteoliposomen kann der Einsatz von Nanodisks in Betracht gezogen werden. Dies hätte den Vorteil, dass eine definierte Anzahl des ETR1 in einer festgelegten Größe in der Nanodisk vorliegen, während bei Proteoliposomen keine genaue Aussage über die Orientierung des Rezeptors und die Anzahl der Rezeptoren pro Proteoliposom getroffen werden kann (Bayburt *et al.* 2002; Bayburt und Sligar 2010). Des Weiteren besteht die Möglichkeit die Anwesenheit des ETR1 in den Nanodiscs mithilfe von *Size-Exclusion*-Chromatographie (SEC) Proben auf einem Coomassie-gefärbten SDS-Gel nachzuweisen (Lemke *et al.* 2023). Bei den Proteoliposomen wird die tatsächliche Anwesenheit von ETR1 erst bei der *continuous wave* (*cw*) -EPR-Spektroskopie über die *Spin Label* überprüft. Allerdings kann nicht ausgeschlossen werden, dass zusätzlich ein gewisser Anteil an ETR1 in Detergens vorliegt (vgl. Kapitel 5.1). Darüber hinaus konnte die Funktionalität der HK-Domäne anhand von Nukleotidbindung an ETR1 in Nanodisks nachgewiesen werden, welches zusätzlich auf die korrekte Faltung des Proteins zurückzuführen ist (Lemke *et al.* 2023). Auch bei anderen Proteinen, wie z. B. dem *Epidermal Growth Factor* Rezeptor, konnte die Rezeptorfunktionalität in Nanodisks *in vitro* nachgewiesen werden (Mi *et al.* 2008; Bayburt und Sligar 2010).

Um die Flexibilität der zweiten Helix zu reduzieren, könnten zudem chemische *Crosslinker* wie Bissulfosuccinimidylsuberat (BS^3) alleine oder in Kombination mit Cu(I) oder Ag(I) verwendet werden, welche eine kovalente-Amin-Amin-Verknüpfung herstellen. Dies konnte beispielhaft bei dem Histidin-Kinase-Rezeptor CusS gezeigt werden, bei dem die Monomere durch *Crosslinking* erfolgreich zu Dimeren und Oligomeren vernetzt wurden (Aravind 2012).

Quecksilberchlorid (Hg_2Cl) könnte ebenfalls zur Quervernetzung von ETR1 eingesetzt werden. Mithilfe von Hg_2Cl konnte ZIP stabilisiert und eine Konformation des Proteins in LCP kristallisiert werden. Dabei bindet Hg an zwei Cysteinreste (Zhang und Sui und Hu 2023). Andere Metalle, die für das *Crosslinking* verwendet werden könnten sind

Kupfer, Aluminium und Blei (Wedrychowski *et al.* 1986). Alternativ könnten die aufgelisteten *Crosslinker* ebenfalls zur Optimierung der LCP-Kristallisation dienen, um ETR1 oder ETR2 zu stabilisieren. Glutaraldehyd ist ein weiterer *Crosslinker*, welcher für die EPR-Spektroskopie verwendet werden könnte (vgl. Kapitel 6.3; Richards und Knowles 1968; Lusty 1999).

Allerdings besteht auch die Möglichkeit, dass die Auflösungsgrenze von der EPR-Spektroskopie mit 1,8 nm zu gering ist (Jeschke 2012), um kleine Konformationsänderungen oder eine Stabilisierung in ETR1 nachzuweisen. In diesem Fall können alternative Methoden wie Kryoelektronenmikroskopie (Kryo-EM) oder Kristallisation zur Strukturaufklärung eingesetzt werden. Mit Kryo-EM lässt sich eine Auflösung von bis zu 0,125 nm erreichen, mit Kristallisation von bis zu 0,27 nm (Smith *et al.* 2002; Yip *et al.* 2020).

6.2 Diskussion der Ergebnisse aus der Ligandenbindung im Transmembranbereich des Ethylenrezeptors ETR1

In Bezug auf den Ethylenrezeptor ETR1 ist bekannt, dass die ersten beiden Helices, abgesehen von der Kupferkoordination, auch die Ethylen-/Kupfer-Bindungstasche ausbilden. Es wird angenommen, dass die Ethylenbindedomäne und die Kupferbindungsdomäne benachbart sind oder sich überlappen (Wang *et al.* 2006; Azhar 2021). Die Geometrie des Komplexes, der das Cu(I) in ETR1 koordiniert, ist bislang nicht bekannt. Die bisherigen Modellierungs-, *X-ray Absorption Spectroscopy* (XAS) und *Extended X-ray Absorption Fine Structure* (EXFAS)-Analysen deuten darauf hin, dass das Kupferion in ETR1 lediglich zwischen zwei oder drei oder vier Atomen koordiniert wird. Die aktuelle Theorie besagt, dass neben dem Stickstoffatom von H69 und dem Schwefelatom von C65 auch die Sauerstoffatome von Wasser an der Koordination beteiligt sind (Schott-Verdugo *et al.* 2019; Müller 2020; Cutsail *et al.* 2022). Die Koordinierung durch zwei Cysteine und zwei Histidine oder nur durch zwei Cysteine ist beispielsweise bei der Bindung von Kupfer an dem humanen ATX1-Homologon *Antioxidant1 Copper Chaperone* (ATOX1) zu beobachten (Ansbacher und Shurki 2012). In Bezug auf dieses Thema stellt sich die Frage, ob und welche weiteren Aminosäuren neben C65 und H69 an der Kupferkoordination bei ETR1 beteiligt sind, da Cu(I) im allgemeinen linear, trigonal-planar oder tetraedrisch koordiniert sein kann (Abbildung 9; Conry 2006; Rubino und Franz 2012). Es besteht die Vermutung, dass D25

an der Kupferkoordination beteiligt sein könnte, wie durch MD-Simulationen nahegelegt wird (Abbildung 11A; Schott-Verdugo *et al.* 2019; Müller 2020).

Ein Hinweis auf die Involvierung von D25 in der Kupferkoordination ist beispielsweise, dass bei EPR-Messungen, bei denen die Stelle C65 zu Serin mutiert wurde, trotzdem eine Kupferbeladung in den Mutanten nachgewiesen werden konnte (vgl. Kapitel 5.1, Supplemental Figure S7). Zudem konnte anhand der neusten Mutagenese- und Kupferbindungsstudien gezeigt werden, dass D25 einen Einfluss auf die Kupferkoordination hat (vgl. Kapitel 5.2). Für die Mutante D25A wurde beim Kupferbindungsversuch keine Affinität zum Metallion gemessen, was in einer fehlenden Ethylenbindung resultiert (vgl. Kapitel 5.2; Figure 1B; Wang *et al.* 2006).

Theoretisch hätte eine Kupferbindung bei Glutaminsäure (E)-Mutante (E25) stattfinden müssen, da diese Aminosäure die gleiche negative Ladung wie die Asparaginsäure (D) hat, was jedoch nicht der Fall war (vgl. Kapitel 5.2, Figure 1B). Ebenfalls konnte keine Kupferbindung beim Ersatz durch das polare Glutamin (Q) D25Q nachgewiesen werden, welches im Vergleich zur Glutaminsäure über eine Amingruppe verfügt (vgl. Kapitel 5.2, Figure 1B). Im Vergleich zu den Aminosäuren Asparaginsäure und Asparagin (N) verfügen sowohl die Aminosäuren Glutaminsäure als auch Glutamin über eine zusätzliche Methyliden (CH_2)-Gruppe. Diese zusätzliche Gruppe könnte in der ETR1-TMD eine sterische Behinderung in der Bewegung des Aminosäurerestes zum Kupferion verursachen (Abbildung 11D). Andere Aminosäuren (25A, 25E, 25Q) scheinen teilweise trotz ihrer Ähnlichkeit zur Asparaginsäure nicht in der Lage zu sein, die Kupferbindung positiv zu beeinflussen. Aufgrund der vorliegenden Ergebnisse lässt sich ableiten, dass D25 spezifisch für das Kupfer ist.

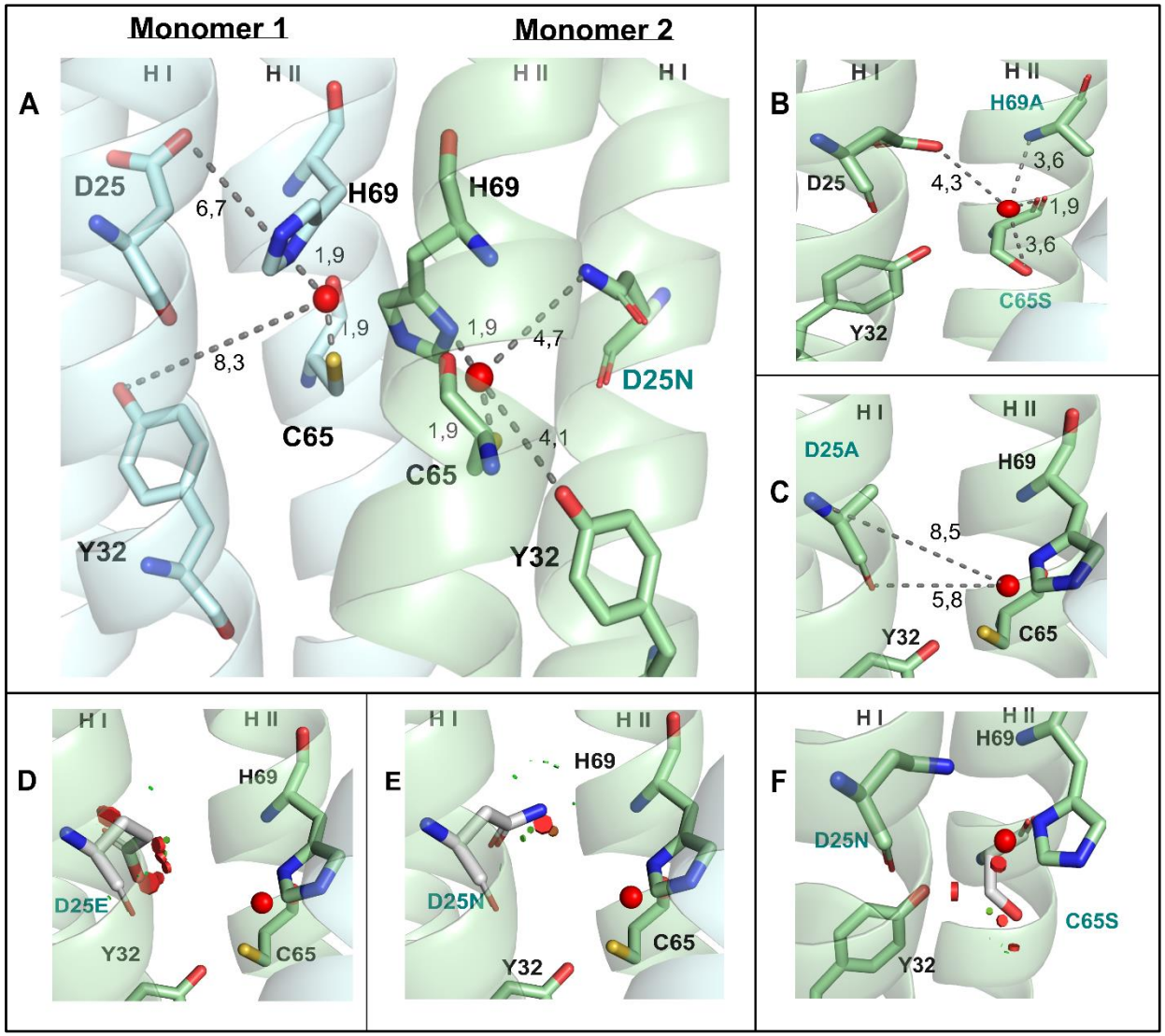

Abbildung 11: Schematischer Ausschnitt aus der Transmembran-Domäne von ETR1 vom Modell Schott-Verdugo et al. (2019). In den Aminosäuren sind Schwefel (gelbe Markierung) -, Sauerstoff (rote Markierung) - und Stickstoffatome (dunkelblaue Markierung), sowie Monomer 1 (hellblau) und Monomer 2 (hellgrün) entsprechend eingefärbt. Mutanten sind an der Schrift dunkelgrün markiert. **A)** Eingezeichnet sind die Aminosäurepositionen im TM-Dimer, die Kupfer (rote Kugel) komplexieren könnten. Der gemessene Abstand der Asparaginsäure 25 (D25) beträgt 6,7 Å zum Kupfer, zu Tyrosin 32 (Y32) 4,1 Å und 8,3 Å, zu Cystein 65 je 1,9 Å und zu Histidin 69 (H69) je 1,9 Å. In Monomer 2 wird Asparagin (*D25N*) stellvertretend für die Komplexierung des Kupfers von der Birne, Cyanobakterien und Traubenerbse dargestellt. Die Abstände zum Kupfer sind grau gestichelt. **B)** Die möglichen Abstände folgender Atome aus den Mutanten D25N, C65S und H69A betragen für Sauerstoff 3,6 Å und 1,9 Å, für Stickstoff 4,2 Å und 4,3 Å. **C)** Der Abstand von D25A zum Kupfer kann 5,8 Å oder 8,5 Å betragen, wodurch keine Kupferkomplexierung durch diese Aminosäure stattfinden kann. **D)** Darstellung der Glutaminsäure (D25E) -, **E)** der Asparagin (D25N) -, und **F)** der Serin (C65S) -Mutante. Rote Scheiben zeigen Schnittstellen und sterische Behinderungen mit anderen Molekülen auf, sowie deren Überlappungen mit Van-der-Waals-Kräften. Grüne Punkte oder Scheiben zeigen an, wenn sich Atome fast berühren oder deren Van-der-Waals-Kräfte sich leicht überlappen. Im Vergleich zu D25E, zeigen D25N und C65S eine geringere sterische Behinderung mit anderen Molekülen und Überlappung mit Van-der-Waals-Kräften an.

Eine Ausnahme bildet das strukturell zu Asparaginsäure ähnliche, polare Asparagin, das eine geringfügige Restbindung zu Kupfer aufweist (vgl. Kapitel 5.2, Figure 1B). Zudem scheint D25N im Vergleich zu D25E nur keine oder eine geringfügige, mögliche sterische Behinderung zu anderen Aminosäuren aufzuweisen (Abbildung 11D und 11E). Durch die Triple-Mutante D25N C65S H69A in der ETR1-TMD wurde gezeigt, dass D25 eindeutig an der Kupferkomplexierung beteiligt ist, da im Vergleich zur Mutante C65S H69A, kein Signal für die Kupferbindung detektiert wurde (vgl. Kapitel 5.2, Figure 1B). Die geringfügige Bindung in der D25N-Mutante ist voraussichtlich darauf zurückzuführen, dass, in manchen Organismen wie in Birnen, Cyanobakterien und Traubenerbsen die Kupferkomplexierung durch Asparagin möglich ist (vgl. Kapitel 5.2).

In diesem Zusammenhang besteht noch Unklarheit, ob D25 eine direkte oder indirekte Beteiligung an der Kupferkoordinierung durch Kupferbindung und/ oder Stabilisierung aufweist. Von Rodriguez *et al.* (1999) ist bekannt, dass durch die Mutation der metallbindenden Aminosäurereste an den Positionen C65 und H69 zu Serin und Alanin fast kein Ethylen mehr gebunden wird. Dies deutet auf die essentielle Kupferbindestelle hin (Rodríguez *et al.* 1999). In dieser Arbeit wurden anhand der erzeugten Doppelmutanten (C65S H69A) in dem Kupfer-BCA-Experiment eine geringe Kupferbeladung verzeichnet, sodass die Beteiligung eines dritten und / oder vierten Liganden an der Kupferbindung angenommen werden kann (vgl. Kapitel 5.2). Diese Erkenntnis stützt die Modellierungs-, XAS- und EXFAS-Analysen, welche besagen, dass für die Cu(I)-Koordinierung von ETR1 zwei, drei oder maximal vier Atome beteiligt sein können (Schott-Verdugo *et al.* 2019; Müller 2020; Cutsail *et al.* 2022).

Bei der Chelatierung des Kupfers von der ETR1-TMD-Doppelmutante (C65S H69A) könnte voraussichtlich Asparaginsäure 25 (D25), Alanin (H69A) und Serin 65 (C65S) beteiligt sein, da diese sich in der Nähe zum Metallion befinden. Obwohl C65S eine geringe sterische Behinderung aufweist, könnte eine Kupferbindung erfolgen (Abbildung 11F). Serin würde hier die Rolle des Cysteins übernehmen und das Alanin, die Rolle des Histidins (Abbildung 11BDie Sauerstoff- oder Stickstoffatome könnten an der Kupferkoordinierung involviert sein (Abbildung 11B). Eine ähnliche Kupferkoordination aus den Aminosäuren D25, C65S und H69 könnte bei den EPR-Experimenten vorliegen, da trotz der mutierten Stelle C65S, eine Kupferbindung nachgewiesen werden

konnte (vgl. Kapitel 5.1). Allerdings scheint das H69 in dem Fall besser an das Kupfer zu binden als das H69A aus dem Kupferbindungsexperiment (vgl. Kapitel 5.1; Supplemental Figure 7; vgl. Kapitel 5.2 Figure 1B). Dies ist wahrscheinlich auf den geringen Abstand des Stickstoffatoms des Histidins (1,9 Å), im Vergleich zu dem Stickstoffatom des H69A (3,6 Å) zurückzuführen (Abbildung 11A und 11B).

Bei dem Kupferbindungsexperiment mit D25A scheint die Distanz des Alanins mit 5,8 Å und 8,5 Å zum Kupfer zu groß zu sein, sodass dessen Stickstoff und Sauerstoffatom Kupfer nicht komplexieren kann und deshalb keine Kupferbindung stattfindet (Abbildung 11 C). In der Literatur hat Sauerstoff bei der Koordinierung mit Cu(I)-Ionen einen Abstand von ca. 1,9 - 3,3 Å und bei Stickstoff 1,9-2,5 Å. Für Schwefel konnte ein Abstand zwischen 2,1-3,3 Å ermittelt werden (Shepard *et al.* 1990; Shepard *et al.* 1993; Lyashenko *et al.* 2006).

Einige gemessen Werte für die Aminosäuren, die Kupfer binden könnten, ähneln den Literaturangaben wie z. B. das Stickstoffatom von H69 (1,9 Å; Abbildung 11A). Für C65S konnte ein Wert von 1,9 Å und 3,6 Å für die Sauerstoffatome, sowie 4,6 Å für Stickstoff gemessen werden (Abbildung 11B). Bei C65S, Y32 und D25 mit einem Wert von 3,6 Å, 4,1 Å und 8,3 Å, sowie 6,7 Å für Sauerstoff ist die gemessene Entfernung zu groß (Literaturwert Sauerstoff 1,9-3,1 Å; Abbildung 11A, und 11B). Das gleiche gilt für den gemessenen Abstand von Kupfer zu dem Stickstoffatom von C65S. Die Entfernung des Schwefelatoms von C65 für Cu(I) ist mit 0,2 Å zu kurz. Jedoch könnte man anhand von Computeranalysen feststellen, wie sich die Aminosäurereste noch ausrichten könnten und dadurch an der Kupferbindung beteiligt sind.

In ETR1 könnte versucht werden D25 zu Methionin oder Cystein zu mutieren. Wenn diese Mutante eine stärkere Affinität zu Kupfer aufweist, ist davon auszugehen, dass D25 indirekt an der Kupferkoordination beteiligt ist. Wenn die Bindung der erstellten Mutante gleichwertig zum Wildtyp oder schwächer ist, würde dies für eine direkte Koordinierung des Kupfers über H69 sprechen.

Des Weiteren wurde über Computeranalysen vorhergesagt, dass die Position K91 mit D25 interagiert (vgl. Kapitel 5.2). Anhand dessen wurden weitere Mutagenesestudien, als auch Kupferbindungsexperimente in *Arabidopsis* und Hefe als Einzel- und Doppelmutanten durchgeführt. Es wurde nachgewiesen, dass K91 keinen Einfluss auf die

Kupferbindung hat (vgl. Kapitel 5.2). Allerdings wurde beobachtet, dass diese K91-Mutanten eine verminderte Ethylenbindung aufweisen. Somit konnte gezeigt werden, dass die Position K91 eine Rolle bei der Ethylenbindung oder bei der Stabilisierung der Ethylenbindungstasche spielt (vgl. Kapitel 5.2).

In der Literatur wird Tyrosin (Y) 32 als ein weiterer potenzieller Ligand für die Kupferkoordination aufgeführt (Wang *et al.* 2006). Y32 befindet sich in der Nähe der Kupferbindestelle, sodass dessen nahe gelegenes Sauerstoffatom in Bezug auf die Kupferkoordination ein weiterer Ligand für ETR1 wäre (Abbildung 11). Anhand von Mutagenesestudien konnte gezeigt werden, dass bei den Einzelmutation, von jeweils D25 und Y32 zu Alanin (A), keine Ethylenbindung stattfindet (Wang *et al.* 2006; Cutsail *et al.* 2022). Diese Annahme müsste allerdings anhand von weiteren Experimenten untersucht werden, da bislang keine weiteren Studien zu der Position Y32 existieren. Zukünftig könnten Kupferbindungsexperimente mit Y32-Mutanten erfolgen in Kombination mit MD-Simulation, um zu ermitteln, ob diese Stelle einen Einfluss auf die Chelatierung des Metalls nimmt. Als Mutante könnte hierfür ETR1 $^{1\text{-}157}$ Y32A C65S H69A verwendet werden, um zu prüfen, ob die Kupferbindung ähnliche wie bei ETR1 $^{1\text{-}157}$ D25N C65S H69A ausbleibt. Falls dies nicht geschieht, beeinflusst Y32 voraussichtlich nicht die Kupferbindung. Stattdessen könnte die Position Y32, ähnlich zu K91, ein stabilisierender Bestandteil bei der Ethylenbindung sein, da eine hohe räumliche Nähe bzw. Überlappung zwischen der Kupferbindungsstelle und der Ethylenbindestelle angenommen werden kann (Wang *et al.* 2006).

6.3 Diskussion der Ergebnisse aus der LCP-Kristallisation

Von dem ER-ständigen Membranprotein ETR1, welches bei Bindung von Kupfer und Ethylen die Ethylenantwort initiiert, war bisher nur die Kristallstruktur der zytosolischen Domäne bekannt (vgl. Kapitel 3.3; Grantz *et al.* 1998; Panneerselvam *et al.* 2013; Mayerhofer *et al.* 2015; Binder 2020). Aufgrund dessen lag in dieser Arbeit der Fokus auf der Strukturaufklärung der ETR-TMD (ETR1 $^{1\text{-}157}$) mittels der LCP-Kristallisation unter Verwendung verschiedener Lipidmischungen und Screening Kits.

Aufgrund der beteiligten Dimerisierung der GAF-Domäne, die dadurch einen stabilisierenden Effekt haben sollte (Grefen *et al.* 2008; Milić *et al.* 2018; Berleth *et al.* 2019), wurden zusätzlich zwei verschiedene ETR1-GAF-Mutanten (ETR1-GAF$^{1\text{-}316}$, ETR1-GAF $^{1\text{-}407}$) zur Kristallisation verwendet. Aufgrund der Sequenzhomologie von 71% in

der TMD von ETR2 (Sakai *et al.* 1998), wurde parallel die ETR2-TMD (ETR2 $^{1\text{-}186}$) kristallisiert (vgl. Kapitel 5.3). Erstmals konnte mithilfe der LCP-Kristallisation Kristalle von der ETR1- und ETR2-TMD gebildet und erste Diffraktionsbilder aufgenommen und dokumentiert werden.

Zusätzlich wurde das GFP-Derivat, *mTurquoise2* (mT2) an die TMDs fusioniert. Durch die korrekte Faltung des mT2 erhält man ein Fluoreszenzsignal, welches ebenfalls indirekt einen Hinweis auf die korrekte Faltung der Fusionskonstrukte gibt. Des Weiteren könnte mT2 einen stabilisierenden Effekt auf die TMD haben und die Löslichkeit des Fusionskonstruktes erhöhen (Phillips 1997; Waldo *et al.* 1999; Pédelacq *et al.* 2006).

Aus den experimentellen Daten ist zu entnehmen, dass die meisten Kristalle mit ETR1 $^{1\text{-}316}$ gebildet (7,1 %, Supplemental S1 Figure 1) und geerntet werden konnten, d. h., dass dieses Konstrukt aufgrund des dimerisierenden Effektes der GAF-Domäne voraussichtlich am stabilsten ist. Am zweit stabilsten scheint ETR2 $^{1\text{-}186}$mT2 zu sein (6,0 %), gefolgt von ETR1 $^{1\text{-}157}$mT2 (3,4 %). Die geringste Kristallausbeute hatte ETR1 $^{1\text{-}407}$ (1,7 %, Supplemental S1 Figure 1). Vermutlich führt die Verlängerung des ETR1 $^{1\text{-}316}$ Konstruktes um 91 Aminosäuren in Richtung des C-Terminus (ETR1 $^{1\text{-}407}$) zu einer größeren Flexibilität und damit, zumindest für die Kristallisation zu einer Instabilität. Das GFP-Derivat mT2 zeigt einen stabilisierenden Effekt in den TMDs. Allerdings scheint die Stabilisierung während der Kristallisation durch das monomere *Turquoise2* u.a. aufgrund der Flexibilität der Rezeptor-TMD nicht ausreichend zu sein.

Das Detergens Foscholine-14 hat zum Zeitpunkt der Membransolubilisierung und nach der Reinigung nicht zu einer Denaturierung von mT2 geführt, da nach der Reinigung und nach dem Anmischen der LCP ein Fluoreszenzsignal beobachtet wurde. Dennoch könnten die Lipide der LCP einen Einfluss auf das mT2 haben, wodurch das Signal des Fluorophors in der LCP abgeschwächt wird. Um diesen Effekt entgegenzuwirken, könnten für zukünftige LCP-Ansätze andere GFP-Varianten wie z. B. *superfolder GFP* (sfGFP) verwendet werden. Dieser Fluoreszenzreptorer ist stabiler gefaltet (Pédelacq *et al.* 2006) und unempfindlicher gegenüber Temperaturen (Cava *et al.* 2008) und Detergenzien (Kai 2012). Durch diese Eigenschaften hat sfGFP voraussichtlich einen stärkeren stabilisierenden Effekt auf die TMD als monomeres *Turquoise2* (Kai 2012). Es gibt zwar von mT2 auch eine sfmT2-Variante, sowie eine sfmT2^{ox}-Variante vor (Meiresonne *et al.* 2019),die unempfindlicher gegenüber ROS ist, jedoch liegen keine

Informationen über die Stabilität bei unterschiedlichen pH-Werten oder über *Photobleaching* vor. Darüber hinaus könnte eine Dimerisierung von sfGFP in der LCP einen zusätzlichen stabilisierenden Effekt haben. Um eine bessere Vernetzung in der LCP und zwischen den Wasserkanälen und damit eine höhere Stabilität im Rezeptor bzw. Kristall zu erhalten, könnte sfGFP ebenfalls am N-Terminus fusioniert werden. Dies würde zu einer Dimerisierung des GFPs in den Wasserkanälen und mit ETR1-Monomeren führen.

Eine weitere Möglichkeit ist die Verwendung von split-sfGFP, wobei die GFP-Hälften an das C- und N-terminale Ende der TMD kloniert werden. Bei korrekter Faltung des gesamten Konstruktes würden die GFP-Hälften ein Fluoreszenzsignal erzeugen (Liu *et al.* 2022). Voraussetzung hierfür ist jedoch eine gerade Anzahl von TMDs, welches nur mit Rezeptoren der zweiten Unterfamilie möglich wäre, da eine vierte TMD vermutet wird (vgl. Kapitel 3.2; Liu *et al.* 2022).

Ein neuer Ansatz wäre die Generierung zweier unterschiedlicher split-GFP-ETR1-Konstrukte. Dabei würde beispielsweise das erste ETR1-Monomer mit den ersten zehn β-Faltblättern des GFPs fusioniert werden. Das zweite Monomer könnte an das GFP nur mit dem elften β-Faltblatt fusioniert werden. Beim Mischen der beiden Konstrukte sollte daraufhin ein grünes Fluoreszenzsignal entstehen, welches auf die korrekte Faltung und Expression der Proteine hinweist (Pédelacq und Cabantous 2019). Andere Proteine, die die Stabilität und Löslichkeit von ETR1 begünstigen könnten, sind z. B. Thioredoxin, Lysozym oder das Maltosebindeprotein. Diese könnten ebenfalls N- oder C-terminal oder als *Termini Restrainer* fusioniert werden (Liu und Li 2022; Liu *et al.* 2022).

Die Kristalle zeigen zwar ein Signal im UV-Licht, jedoch streuen diese nicht bei der Bestrahlung mit Röntgenstrahlen. Dies ist wahrscheinlich auf die unregelmäßige Anordnung des Proteins im Kristallgitter zurückzuführen. Des Weiteren lässt sich vermuten, dass die zweite Helix, wie bereits in Bezug auf die erwähnten EPR-Ergebnisse angenommen wurde, zu flexibel ist. (vgl. Kapitel 5.1). Hier könnten, neben den bereits bei der EPR genannten *Crosslinkern* (vgl. Kapitel 6.1), weitere verwendet werden, die für die EPR ungeeignet wären. Bei der EPR sind beispielsweise *Crosslinker* über Cysteine ungeeignet, da die Disulfidbrücken über Dithiothreitol (DTT) für das *Spin Labeling* reduziert werden müssen und sowohl MTSSL (vgl. Kapitel 5.1), als auch *Crosslinker* wie Bismaleimidohexan (BMH) an Cysteine binden. Eine erfolgreiche Stabilisierung für

die Kristallisation einer Histidin-Kinase aus Cyanobakterien konnte mit Dithiobis-succinimidylpropionate erzielt werden (Wang 2018). Auch natürliche Sulfhydryl-*Crosslinker* könnten durch gezielte Mutationen in ETR1 die Flexibilität im Rezeptor einschränken (Hiromoto *et al.* 2022). Zudem besteht die Möglichkeit Glutaraldehyd zu verwenden, um den Rezeptor für die LCP-Kristallisation zu stabilisieren. Für *Vapor Diffusion* Kristallisationsansätze konnte Glutaraldehyd bereits zielführend verwendet werden (Richards und Knowles 1968; Lusty 1999).

Um den ETR1 Rezeptor für die Kristallisation zu stabilisieren, könnte eine Kokristallisation mit RAN1 erfolgen. Der Vorteil wäre, dass das Membranprotein RAN1 ebenfalls im Lipidbereich lokalisiert wäre wie ETR1. Darüber hinaus hat RAN1 eine hohe Bindungsaffinität zu ETR1 (K_D RAN1 = 33 nM). Die alleinige Verwendung der MBDs wären für Stabilisierung von ETR1 während der Kokristallisation nicht ausreichend, da die Affinität vergleichsweise zur RAN1-Volllänge geringer ist (K_D Nter RAN1= 205 nM; K_D Cter RAN1= 2611 nM; Hoppen *et al.* 2019a).

Zudem wurde getestet, ob während der Kristallisation Zink zur Stabilisierung des ETR1 beitragen könnte, da dieses zweiwertige Metall bereits erfolgreich bei der Kristallisation von kupferbindenden Chaperonen eingesetzt wurde (Badarau *et al.* 2013; Mangini *et al.* 2022). Die Kristallisationsrate von ETR1 mit Zink lag bei 11,5 % (vgl. Kapitel 5.3, Supplemental S1 Figure 1). Aufgrund dessen wäre es sinnvoll zu prüfen, ob ETR1 auch in der Lage ist, Zn(II) zu binden. Hierfür könnte ein kolorimetrischer Assay ähnlich zum Kupfer-BCA-Assay aufgesetzt werden (Schott-Verdugo *et al.* 2019). Falls Zn(II) bindet, könnte anhand des gebundenen Zinks ebenfalls die Stöchiometrie berechnet werden. Dabei könnte ETR1 kupferfrei mit Tris-2-chlorehyl-phosphat (TCEP) gereinigt werden (Müller 2020), um bei der Zugabe und Inkubation eines Zink-komplexierenden, farbgebenden Mittels mögliche Interaktionen zu vermeiden. Danach würde der Überschuss des Zn-Farbkomplexes von der Probe abgetrennt werden. Analog zum Kupfer-BCA Assay, würde man anschließend die $ZnCl_2$ gesättigte ETR1-Probe mit 20% SDS und dem Zink-komplexierenden Mittel aufkochen (Schott-Verdugo *et al.* 2019). Wenn Zn(II) von ETR1 komplexiert wurde, sollte sich ein farbiger Zinkkomplex bilden. Bei einer bestimmten Wellenlänge kann diese Farbgebung im Photometer erfasst werden.

Wenn ein kompetitiver Assay durchgeführt werden sollte, wäre es sinnvoll kupferfreies ETR1 mit dem Zn-Farbkomplex (analog zur Kupfer-ETR1 Titration; Schott-Verdugo *et*

al. 2019) zu titrieren, um ggf. eine Entfärbungsreaktion zu beobachten. Da ETR1 in der Lage ist Cu(II) zu binden, allerdings ineffektiver und vermutlich unspezifischer als Cu(I) (Müller 2020), ist eine Zn(II) Bindung trotzdem nicht ausgeschlossen.

Ein geeigneter Zinkchelator wäre z. B. Zincon. Bei der Komplexierung von Zincon ist zu berücksichtigen, dass Zink bei 618 nm in Abhängigkeit vom pH-Wert 6-11 absorbiert und einen K_D von 2,09 x 10^{-6} M bei pH 7.4 aufweist, wodurch es für die genannten Versuche besser geeignet wäre als Kupfer. Zwar ist Zincon in der Lage Cu(I) zu binden, dieser Komplex absorbiert allerdings von pH 2-12 durchgängig und hat einen K_D von 4,68 x 10^{-17} M (Kocyła *et al.* 2017). Im Vergleich dazu bindet ETR1 an Cu(I) schwächer mit einer Affinität von 1,3 x 10^{-15} M (Schott-Verdugo *et al.* 2019). Das Detektionslimit für Zincon beträgt komplexiert mit Zn(II)- oder Cu(I)-Ionen in 50 mM Boratpuffer (pH 9,0) mit 8 M Urea liegt bei 200 nM (Säbel *et al.* 2010).

Der Bildung von Kristallen, die nicht beugen, könnte auch auf inhomogene Proteinproben zurückzuführen sein. Nach der IMAC-Reinigung könnte die Entfernung von Aggregaten und Oligomeren mithilfe eines 0,2 µm Filters nicht ausreichend sein (vgl. Kapitel 5.3), wodurch bei den Kristallisationsansätzen keine homogene Kristallisationsprobe vorliegen würde. Aus diesem Grund könnte ETR1 über eine Größenausschlusschromatographie gereinigt werden, um Aggregate, Oligomere und Dimere voneinander zu trennen und anschließend zu kristallisieren. Außerdem könnten Verunreinigungen durch beispielsweise *Outer Membrane Porins* (Omps) vorliegen, welche in der äußeren Membran von *E. coli* vorkommen. Bei der Reinigung und Kristallisation eines HK-Rezeptors in Anwesenheit von Foscholine-12 wurde beispielsweise die Verunreinigung des Porins OmpF festgestellt, welches als Monomer eine Größe von ca. 38 kDa aufweist (Kefala *et al.* 2010). Diese Größe ist ähnlich zu den kristallisierenden ETR1- bzw. ETR2-Konstrukten (vgl. Kapitel 5.3). Falls eine Verunreinigung durch Omps vorliegen würde, könnte zur Expression der *E. coli* Stamm BL21 Gold (DE3) ΔABCF eingesetzt werden, bei dem die vier Omps ABCF deletiert wurden (Meuskens *et al.* 2020).

Für die Funktionalität des Proteins, sowie für die Rekonstitution des Proteins in der LCP oder in Nanodisks, wäre ein Austausch des Detergens über die IMAC wahrscheinlich sinnvoll. Beispielsweise konnte durch den Austausch von Foscholine durch DDM, nachfolgend ein ABC-Transporter aus Bakterien erfolgreich in Nanodisks rekonstituiert werden und eine Proteinaktivität nachgewiesen werden (Kanonenberg *et al.* 2019).

Zudem ist DDM eines der am häufigsten verwendeten Detergenzien, welches in der Kristallisation verwendet wird (Stetsenko und Guskov 2017).

In dieser Arbeit entstanden die meisten Kristalle mit dem Lipid MO/DOPC (12,8 %, vgl. Kapitel 5.3, Supplemental S1 Figure 1). Phosphatidylcholine und Sterole sind in der Pflanzenmembran weit verbreitet (Donaldson und Beevers 1977; Brown und Dupont 1989). Die Verwendung des Phosphatidylcholinlipids DOPCs stellt, vermutlich eine natürlichere Umgebung für die Ethylenrezeptoren dar als DSPG, Cholesterol oder Cardiolipin. Letzteres ist zwar in Mitochondrien weit verbreitet (Donaldson und Beevers 1977), jedoch besteht durch die starke Verzweigung des Cardiolipins die Möglichkeit besonders große Wasserkanäle zu bilden (Cherezov *et al.* 2002). DSPG ist ebenfalls durch seine Struktur und die elektrostatische Ladung in der Lage stark vergrößerte Wasserkanäle zu bilden. Im Gegensatz dazu verursacht Cholesterol durch seine starre Sterolstruktur eine geringere Krümmung an der Lipidoberfläche, was vergrößerte Wasserkanäle zur Folge hat (Zabara *et al.* 2018).

Um natürlichere Bedingungen für die ETRs zu schaffen könnten MO oder MP mit kommerziell erhältlichen Lipidextrakten aus *E. coli* gemischt werden, da die heterologe Expression der ETRs in *E. coli* erfolgt (vgl. Kapitel 5.1 - 5.3). Darüber hinaus wurde beispielsweise das *E. coli polar extract* bereits zum einen für die Rekonstitution der Nanodisks von der Histidin-Kinase CusS und zum anderen nach der Rekonstitution für die EPR-Spektroskopie verwendet (Martens *et al.* 2016; Affandi und McEvoy 2019). Ein weiteres kommerziell erwerbliches Lipid, welches mit MO und MP mischbar wäre, ist das pflanzliche Sojalipidextrakt. Obwohl die Zusammensetzung vermutlich nicht exakt der Zusammensetzung der Membran von *A. thaliana* entspricht, könnte es dennoch die Kristallisation positiv beeinflussen, da die Ethylenrezeptoren- und weitere Komponenten des Signalweges in pflanzlichen Organismen hoch konserviert sind (Ju *et al.* 2015; Kessenbrock *et al.* 2017; Hoppen *et al.* 2019b) und eine natürlichere Umgebung für diese pflanzlichen Rezeptoren geschaffen wird.

Es besteht die Möglichkeit, dass die ausgewählten Lipide nach der Rekonstitution in Nanodisks besser in LCP kristallisieren, da sich das Membranprotein bereits in einer Lipidumgebung vorliegt, bevor es in die LCP eingebaut wird. Bisher wurde die LCP-Kristallisation nur mit *Styrene Maleic Anhydrid* (SMA) Nanodisks dokumentiert (Broecker *et al.* 2017).

In Anbetracht der Ähnlichkeit der ETRs mit dem Zwei-Komponenten-System wäre es eine weitere Möglichkeit, Monovaccenin zu verwenden und die gleichen Kristallisationsbedingungen zu testen, die bereits für die Histidin-Kinase NarQ verwendet wurden (Gordeliy *et al.* 2002; Gushchin *et al.* 2017).

Des Weiteren könnte eine andere Variante der LCP-Kristallisation, die LCP-Sandwich Methode ausprobiert werden. Hierbei wird die LCP mit einer Pufferlösung zwischen zwei Glasplatten gelegt und durch *Spacer* getrennt. Die Methode, die in dieser Arbeit verwendet wurde, ist jedoch einfacher in der Durchführung, da die Probe langsamer austrocknet bzw. keine Kristalle verloren gehen oder zerbrechen können (vgl. Kapitel 5.3). Erfahrungsgemäß ist es jedoch aufgrund der dreidimensionalen Anordnung der LCP teilweise schwierig, die genauen Kristallkanten und -formen im Durchlicht zu erkennen und den Kristall zu entnehmen. Für die Sandwich-Methode gibt es eine optimierte Version, bei dem die Kristallproben mit der gesamten Konstruktion aus einer 96-Well-Glasplatte herausgeschnitten werden. Durch die dünne Lipidschicht sind die Kristalle besser sichtbar. Zudem können die Kristalle direkt in den Glasplättchen vermessen werden (Huang *et al.* 2020a; 2020b).

Eine andere Kristallisationsmethode, die zur Strukturaufklärung führen könnte, ist die *Hanging Drop Vapor Diffusion,* welche für die Histidin-Kinasen NarX und CitA angewandt wurde (Sevvana *et al.* 2008; Cheung und Hendrickson 2009). Des Weiteren könnte diese Methode für stabilisierende Proteine wie sfGFP verwendet werden (vgl. S. 101). Aufgrund der großen Oberfläche und der löslichen Eigenschaft von sfGFP ist anzunehmen, dass außerhalb der Detergensmizelle bessere Kristallkontakte mit dem ETR1-TMD-Fusionskonstrukt geknüpft werden könnten als durch ETR1 ohne sfGFP (Liu und Li 2022).

6.4 Zusammenfassung und Ausblick

In der vorliegenden Arbeit wurde erstmals die Anwendung der LCP- und EPR-Methode zur Durchführung von Strukturanalysen am ETR1 etabliert. Die EPR-Ergebnisse zeigen mit dem Strukturmodell von Schott-Verdugo *et al.* (2019) eine höhere Übereinstimmung als dem mit Alphafold erstellten Alternativmodell. Des Weiteren konnte festgestellt werden, dass die TMD eine hohe Flexibilität aufweist, insbesondere an TM-Helix II. In den Cysteinmutanten, bei denen die Kupferbindungsstelle C65 mutiert war, konnte dennoch Kupfer gebunden werden, was darauf hinweist, dass weitere Aminosäuren wie D25 und H69 in die Kupferkoordination involviert sind. Die Erstellung diverser Kupfermutanten diente der Bestätigung der These, dass D25 einen Einfluss auf die Kupferbindung bzw. -koordinierung ausübt. Dies führte zu einer Verbesserung des Kupferbindungsmodells. Die genaue Rolle von D25 und K91 in der Kupferbindung muss jedoch noch weiter untersucht werden, beispielsweise anhand der Kristallstruktur. Mithilfe der LCP-Kristallisation führte zwar zur Bildung erster streufähiger Kristalle, allerdings besteht weiterhin das Problem, dass die Diffraktionsmuster bislang nicht ausreichend sind, um die Struktur der TMD zu bestimmen. Zurückzuführen ist dies ebenfalls auf die Flexibilität der TMD, die eine regelmäßige Anordnung innerhalb des Kristalls verhindert. Die besten Ergebnisse hinsichtlich der Kristallisation wurden mit ETR1-GAF $^{1\text{-}316}$ und ETR2 $^{1\text{-}186}$mT2 erzielt, was vermutlich auf die Stabilisierung durch die GAF-Domäne bzw. durch mT2 zurückzuführen sein könnte. Durch die Vielzahl möglicher Optimierungen könnte die Struktur von ETR1 mittels der hier vorgestellten Methode in den nächsten Jahren gelöst werden. Darüber hinaus könnten neben der LCP-Kristallisation weitere Methoden zur Strukturauflösung eingesetzt werden wie z. B. *Vapor Diffusion* Kristallisation oder Kryo-EM. Wenn die Struktur der TMD aufgeklärt werden kann, ist ein wichtiger Aspekt in der Kette des Ethylensignalweges gelöst, da die Ethylenantwort erst durch die Bindung von Kupfer und Ethylen ausgelöst wird. Die Struktur erlaubt eine detaillierte Analyse des Koordinationszentrums des Kupferkofaktors und der Ethylen-Bindungstasche. Möglicherweise können neue Inhibitoren innerhalb der Ethylen-Signalübertragung identifiziert werden. Darüber hinaus können detaillierte Einblicke gewonnen werden wie beispielsweise der Kupferkofaktor von den Metallochaperonen ATX1, CCH und RAN1 auf die ETR1-TMD übertragen wird. Des Weiteren kann der Signaltransduktionsmechanismus, der zur Konformationsänderung und Aktivierung der Signalkaskade führt, erklärt werden.

7 Literaturverzeichnis

Abdel-Ghany *et al.* (2005): AtCCS is a functional homolog of the yeast copper chaperone Ccs1/Lys7. In: *0014-5793* 579 (11), S. 2307–2312. DOI: 10.1016/j.febslet.2005.03.025.

Abeles *et al.* (2012): Ethylene in Plant Biology. 2nd ed. Saint Louis: Elsevier Science.

Affandi und McEvoy (2019): Mechanism of metal ion-induced activation of a two-component sensor kinase. In: *The Biochemical journal* 476 (1), S. 115–135. DOI: 10.1042/BCJ20180577.

Aghdam und Razavi (2021): Octapeptide NOP-1 treatment delays yellowing in broccoli floret during low temperature storage. In: *Postharvest Biology and Technology* 180, S. 111628. DOI: 10.1016/j.postharvbio.2021.111628.

Alscher (2002): Role of superoxide dismutases (SODs) in controlling oxidative stress in plants. In: *J Exp Bot* 53 (372), S. 1331–1341. DOI: 10.1093/jexbot/53.372.1331.

Altenbach *et al.* (1990): Transmembrane protein structure: spin labeling of bacteriorhodopsin mutants. In: *Science (New York, N.Y.)* 248 (4959), S. 1088–1092. DOI: 10.1126/science.2160734.

Amrhein und Wenker (1979): Novel inhibitors of ethylene production in higher plants. In: *Plant and Cell Physiology* 20 (8), S. 1635–1642. DOI: 10.1093/oxfordjournals.pcp.a075966.

An *et al.* (2010): Ethylene-induced stabilization of ETHYLENE INSENSITIVE3 and EIN3-LIKE1 is mediated by proteasomal degradation of EIN3 binding F-box 1 and 2 that requires EIN2 in Arabidopsis. In: *The Plant cell* 22 (7), S. 2384–2401. DOI: 10.1105/tpc.110.076588.

Andrés-Colás *et al.* (2006): The Arabidopsis heavy metal P-type ATPase HMA5 interacts with metallochaperones and functions in copper detoxification of roots. In: *The Plant journal : for cell and molecular biology* 45 (2), S. 225–236. DOI: 10.1111/j.1365-313X.2005.02601.x.

Ansbacher und Shurki (2012): Predicting the coordination number within copper chaperones: Atox1 as case study. In: *The journal of physical chemistry. B* 116 (15), S. 4425–4432. DOI: 10.1021/jp210678n.

Aravind (2012): Molecular and Biochemical Analysis of the Histidine Kinase CusS and its Role in Metal Resistance in Escherichia coli. Online verfügbar unter https://repository.arizona.edu/handle/10150/232493.

Arraes *et al.* (2015): Implications of ethylene biosynthesis and signaling in soybean drought stress tolerance. In: *BMC plant biology* 15, S. 213. DOI: 10.1186/s12870-015-0597-z.

Azhar (2021): Structural Characterization of ETR1 Receptor and Ethylene Signaling in Plants. Online verfügbar unter http://dspace.qau.edu.pk:8080/jspui/bitstream/123456789/19557/1/bio%206090.pdf.

Badarau *et al.* (2013): Investigating the role of zinc and copper binding motifs of trafficking sites in the cyanobacterium Synechocystis PCC 6803. In: *Biochemistry* 52 (39), S. 6816–6823. DOI: 10.1021/bi400492t.

Barry und Giovannoni (2007): Ethylene and Fruit Ripening. In: *J Plant Growth Regul* 26 (2). DOI: 10.1007/s00344-007-9002-y.

Bayburt *et al.* (2002): Self-Assembly of Discoidal Phospholipid Bilayer Nanoparticles with Membrane Scaffold Proteins. In: *Nano Lett.* 2 (8), S. 853–856. DOI: 10.1021/nl025623k.

Bayburt und Sligar (2010): Membrane protein assembly into Nanodiscs. In: *FEBS Letters* 584 (9), S. 1721–1727. DOI: 10.1016/j.febslet.2009.10.024.

Benavente und Alonso (2006): Molecular mechanisms of ethylene signaling in Arabidopsis. In: *Molecular bioSystems* 2 (3-4), S. 165–173. DOI: 10.1039/B513874D.

Berleth *et al.* (2019): Molecular Analysis of Protein-Protein Interactions in the Ethylene Pathway in the Different Ethylene Receptor Subfamilies. In: *Frontiers in plant science* 10, S. 726. DOI: 10.3389/fpls.2019.00726.

Beyer (1976): A potent inhibitor of ethylene action in plants. In: *Plant Physiol* 58 (3), S. 268–271. DOI: 10.1104/pp.58.3.268.

Binder *et al.* (2007): The Arabidopsis EIN3 binding F-Box proteins EBF1 and EBF2 have distinct but overlapping roles in ethylene signaling. In: *Plant Cell* 19 (2), S. 509–523. DOI: 10.1105/tpc.106.048140.

Binder *et al.* (2010): The copper transporter RAN1 is essential for biogenesis of ethylene receptors in Arabidopsis. In: *Journal of Biological Chemistry* 285 (48), S. 37263–37270. DOI: 10.1074/jbc.m110.170027.

Binder (2020): Ethylene signaling in plants. In: *The Journal of biological chemistry* 295 (22), S. 7710–7725. DOI: 10.1074/jbc.REV120.010854.

Bisson *et al.* (2009): EIN2, the central regulator of ethylene signalling, is localized at the ER membrane where it interacts with the ethylene receptor ETR1. In: *The Biochemical journal* 424 (1), S. 1–6. DOI: 10.1042/BJ20091102.

Bisson *et al.* (2016): Peptides interfering with protein-protein interactions in the ethylene signaling pathway delay tomato fruit ripening. In: *Sci Rep* 6 (1), S. 30634. DOI: 10.1038/srep30634.

Bisson und Groth (2010): New insight in ethylene signaling: autokinase activity of ETR1 modulates the interaction of receptors and EIN2. In: *Molecular Plant* 3 (5), S. 882–889. DOI: 10.1093/mp/ssq036.

Bisson und Groth (2011): New paradigm in ethylene signaling: EIN2, the central regulator of the signaling pathway, interacts directly with the upstream receptors. In: *Plant signaling & behavior* 6 (1), S. 164–166. DOI: 10.4161/psb.6.1.14034.

Bisson und Groth (2015): Targeting Plant Ethylene Responses by Controlling Essential Protein-Protein Interactions in the Ethylene Pathway. In: *Molecular plant* 8 (8), S. 1165–1174. DOI: 10.1016/j.molp.2015.03.014.

Blankenship und Dole (2003): 1-Methylcyclopropene: a review. In: *Postharvest Biology and Technology* 28 (1), S. 1–25. DOI: 10.1016/S0925-5214(02)00246-6.

Bleecker *et al.* (1988): Insensitivity to Ethylene Conferred by a Dominant Mutation in Arabidopsis thaliana. In: *Science (New York, N.Y.)* 241 (4869), S. 1086–1089. DOI: 10.1126/science.241.4869.1086.

Bleecker (1999): Ethylene perception and signaling: an evolutionary perspective. In: *Trends in plant science* 4 (7), S. 269–274. DOI: 10.1016/S1360-1385(99)01427-2.

Bleecker und Kende (2000): Ethylene: a gaseous signal molecule in plants. In: *Annual review of cell and developmental biology* 16, S. 1–18. DOI: 10.1146/annurev.cellbio.16.1.1.

Broecker *et al.* (2017): Crystallogenesis of Membrane Proteins Mediated by Polymer-Bounded Lipid Nanodiscs. In: *Biophysical journal* 112 (3), 356a-357a. DOI: 10.1016/j.bpj.2016.11.1933.

Brown und Dupont (1989): Lipid Composition of Plasma Membranes and Endomembranes Prepared from Roots of Barley (Hordeum vulgare L.) : Effects of Salt. In: *Plant physiology* 90 (3), S. 955–961. DOI: 10.1104/pp.90.3.955.

Burg und Burg (1962): Role of Ethylene in Fruit Ripening. In: *Plant physiology* 37 (2), S. 179–189. DOI: 10.1104/pp.37.2.179.

Caffrey und Cherezov (2009): Crystallizing membrane proteins using lipidic mesophases. In: *Nature protocols* 4 (5), S. 706–731. DOI: 10.1038/nprot.2009.31.

Cao *et al.* (2020): Understanding Periodic and Non-periodic Chemistry in Periodic Tables. In: *Front. Chem.* 8, S. 813. DOI: 10.3389/fchem.2020.00813.

Cava *et al.* (2008): Expression and use of superfolder green fluorescent protein at high temperatures in vivo: a tool to study extreme thermophile biology. In: *Environmental microbiology* 10 (3), S. 605–613. DOI: 10.1111/j.1462-2920.2007.01482.x.

Chalfie *et al.* (1994): Green fluorescent protein as a marker for gene expression. In: *Science (New York, N.Y.)* 263 (5148), S. 802–805. DOI: 10.1126/science.8303295.

Chalfie (1995): Green fluorescent protein. In: *Photochemistry and photobiology* 62 (4), S. 651–656. DOI: 10.1111/j.1751-1097.1995.tb08712.x.

Chalfieund Kain (2005): Methods of Biochemical Analysis, Volume 47, Green Fluorescent Protein. Properties, Applications and Protocols. 2., Auflage. New York, NY: John Wiley & Sons (Methods of Biochemical Analysis, 47).

Chang *et al.* (1993): Arabidopsis ethylene-response gene ETR1: similarity of product to two-component regulators. In: *Science (New York, N.Y.)* 262 (5133), S. 539–544. DOI: 10.1126/science.8211181.

Chang und Stadler (2001): Ethylene hormone receptor action in Arabidopsis. In: *BioEssays : news and reviews in molecular, cellular and developmental biology* 23 (7), S. 619–627. DOI: 10.1002/bies.1087.

Chao *et al.* (1997): Activation of the ethylene gas response pathway in Arabidopsis by the nuclear protein ETHYLENE-INSENSITIVE3 and related proteins. In: *Cell* 89 (7), S. 1133–1144. DOI: 10.1016/s0092-8674(00)80300-1.

Chen *et al.* (2002): Localization of the ethylene receptor ETR1 to the endoplasmic reticulum of Arabidopsis. In: *Journal of Biological Chemistry* 277 (22), S. 19861–19866. DOI: 10.1074/jbc.M201286200.

Chen *et al.* (2010): Ethylene receptors function as components of high-molecular-mass protein complexes in Arabidopsis. In: *PloS one* 5 (1), e8640. DOI: 10.1371/journal.pone.0008640.

Cherezov *et al.* (2002): Membrane protein crystallization in meso: lipid type-tailoring of the cubic phase. In: *Biophysical journal* 83 (6), S. 3393–3407. DOI: 10.1016/S0006-3495(02)75339-3.

Cheung und Hendrickson (2009): Structural analysis of ligand stimulation of the histidine kinase NarX. In: *Structure (London, England : 1993)* 17 (2), S. 190–201. DOI: 10.1016/j.str.2008.12.013.

Choi und Davidson (2011): Cupredoxins--a study of how proteins may evolve to use metals for bioenergetic processes. In: *Metallomics : integrated biometal science* 3 (2), S. 140–151. DOI: 10.1039/c0mt00061b.

Clark *et al.* (1998): Association of the Arabidopsis CTR1 Raf-like kinase with the ETR1 and ERS ethylene receptors. In: *Proceedings of the National Academy of Sciences of the United States of America* 95 (9), S. 5401–5406. DOI: 10.1073/pnas.95.9.5401.

Cody *et al.* (1993): Chemical structure of the hexapeptide chromophore of the Aequorea green-fluorescent protein. In: *Biochemistry* 32 (5), S. 1212–1218. DOI: 10.1021/bi00056a003.

Conry (2006): Copper: Inorganic & Coordination ChemistryBased in part on the article Copper: Inorganic & Coordination Chemistry by Rebecca R. Conry & Kenneth D. Karlin which appeared in the Encyclopedia of Inorganic Chemistry, First Edition: John Wiley & Sons, Ltd (Encyclopedia of Inorganic Chemistry).

Cutsail *et al.* (2022): Spectroscopic and QM/MM studies of the Cu(I) binding site of the plant ethylene receptor ETR1. In: *Biophysical journal* 121 (20), S. 3862–3873. DOI: 10.1016/j.bpj.2022.09.007.

Del Pozo *et al.* (2010): Gene expression profiling analysis of copper homeostasis in Arabidopsis thaliana. In: *Biochemical and Biophysical Research Communications* 393 (2), S. 248–252. DOI: 10.1016/j.bbrc.2010.01.111.

Depaepe und van der Straeten (2020): Tools of the Ethylene Trade: A Chemical Kit to Influence Ethylene Responses in Plants and Its Use in Agriculture. In: *Small Methods* 4 (8), Artikel 1900267, S. 1900267. DOI: 10.1002/smtd.201900267.

Dluhosch *et al.* (2024): Structure and dimerization properties of the plant-specific copper chaperone CCH. In: *Sci Rep* 14 (1), S. 19099. DOI: 10.1038/s41598-024-69532-y.

Donaldson und Beevers (1977): Lipid composition of organelles from germinating castor bean endosperm. In: *Plant physiology* 59 (2), S. 259–263. DOI: 10.1104/pp.59.2.259.

Dong *et al.* (2010): Molecular association of the Arabidopsis ETR1 ethylene receptor and a regulator of ethylene signaling, RTE1. In: *The Journal of biological chemistry* 285 (52), S. 40706–40713. DOI: 10.1074/jbc.M110.146605.

Dos Santos Rodrigues *et al.* (2023): Applications of fluorescence spectroscopy in protein conformational changes and intermolecular contacts. In: *BBA advances* 3, S. 100091. DOI: 10.1016/j.bbadva.2023.100091.

Dubouzet *et al.* (2003): OsDREB genes in rice, Oryza sativa L., encode transcription activators that function in drought-, high-salt- and cold-responsive gene expression. In: *The Plant journal : for cell and molecular biology* 33 (4), S. 751–763. DOI: 10.1046/j.1365-313x.2003.01661.x.

Fan *et al.* (1999): 1-Methylcyclopropene Inhibits Apple Ripening. In: *jashs* 124 (6), S. 690–695. DOI: 10.21273/JASHS.124.6.690.

Feilmeier *et al.* (2000): Green fluorescent protein functions as a reporter for protein localization in Escherichia coli. In: *Journal of Bacteriology* 182 (14), S. 4068–4076. DOI: 10.1128/jb.182.14.4068-4076.2000.

Festa und Thiele (2011): Copper: an essential metal in biology. In: *Current biology : CB* 21 (21), R877-83. DOI: 10.1016/j.cub.2011.09.040.

Gao *et al.* (2003): Localization of the Raf-like kinase CTR1 to the endoplasmic reticulum of Arabidopsis through participation in ethylene receptor signaling complexes. In: *Journal of Biological Chemistry* 278 (36), S. 34725–34732. DOI: 10.1074/jbc.M305548200.

Gao *et al.* (2008): Heteromeric interactions among ethylene receptors mediate signaling in Arabidopsis. In: *The Journal of biological chemistry* 283 (35), S. 23801–23810. DOI: 10.1074/jbc.M800641200.

Gao und Stock (2009): Biological insights from structures of two-component proteins. In: *Annual review of microbiology* 63, S. 133–154. DOI: 10.1146/annurev.micro.091208.073214.

Goedhart *et al.* (2012): Structure-guided evolution of cyan fluorescent proteins towards a quantum yield of 93%. In: *Nature communications* 3, S. 751. DOI: 10.1038/ncomms1738.

Goel *et al.* (2010): Overexpression of osmotin gene confers tolerance to salt and drought stresses in transgenic tomato (Solanum lycopersicum L.). In: *Protoplasma* 245 (1-4), S. 133–141. DOI: 10.1007/s00709-010-0158-0.

Gordeliy *et al.* (2002): Molecular basis of transmembrane signalling by sensory rhodopsin II-transducer complex. In: *Nature* 419 (6906), S. 484–487. DOI: 10.1038/nature01109.

Grantz *et al.* (1998): Subcloning, crystallization and preliminary X-ray analysis of the signal receiver domain of ETR1, an ethylene receptor from Arabidopsis thaliana. In: *Acta crystallographica. Section D, Biological crystallography* 54 (Pt 4), S. 690–692. DOI: 10.1107/s0907444997015023.

Greenfield (2015): Circular dichroism (CD) analyses of protein-protein interactions. In: *Methods in molecular biology (Clifton, N.J.)* 1278, S. 239–265. DOI: 10.1007/978-1-4939-2425-7_15.

Grefen *et al.* (2008): Subcellular localization and in vivo interactions of the Arabidopsis thaliana ethylene receptor family members. In: *Molecular plant* 1 (2), S. 308–320. DOI: 10.1093/mp/ssm015.

Grefen und Harter (2004): Plant two-component systems: principles, functions, complexity and cross talk. In: *Planta* 219 (5), S. 733–742. DOI: 10.1007/s00425-004-1316-4.

Guo und Ecker (2003): Plant responses to ethylene gas are mediated by SCF(EBF1/EBF2)-dependent proteolysis of EIN3 transcription factor. In: *Cell* 115 (6), S. 667–677. DOI: 10.1016/s0092-8674(03)00969-3.

Gushchin *et al.* (2017): Mechanism of transmembrane signaling by sensor histidine kinases. In: *Science (New York, N.Y.)* 356 (6342). DOI: 10.1126/science.aah6345.

Guy und Kende (1984): Conversion of 1-aminocyclopropane-1-carboxylic acid to ethylene by isolated vacuoles of Pisum sativum L. In: *Planta* 160 (3), S. 281–287. DOI: 10.1007/BF00402867.

Guzmán und Ecker (1990): Exploiting the triple response of Arabidopsis to identify ethylene-related mutants. In: *The Plant cell* 2 (6), S. 513–523. DOI: 10.1105/tpc.2.6.513.

Hall *et al.* (2000): Ethylene perception by the ERS1 protein in Arabidopsis. In: *Plant physiology* 123 (4), S. 1449–1458. DOI: 10.1104/pp.123.4.1449.

Halliwell und Gutteridge (1984): Oxygen toxicity, oxygen radicals, transition metals and disease. In: *Biochem J* 219 (219 // 1), S. 1–14. DOI: 10.1042/bj2190001.

Han (2023): Copper trafficking systems in cells: insights into coordination chemistry and toxicity. In: *Dalton transactions (Cambridge, England : 2003)* 52 (42), S. 15277–15296. DOI: 10.1039/d3dt02166a.

Heim *et al.* (1994): Wavelength mutations and posttranslational autoxidation of green fluorescent protein. In: *Proceedings of the National Academy of Sciences of the United States of America* 91 (26), S. 12501–12504. DOI: 10.1073/pnas.91.26.12501.

Heim und Tsien (1996): Engineering green fluorescent protein for improved brightness, longer wavelengths and fluorescence resonance energy transfer. In: *Current biology : CB* 6 (2), S. 178–182. DOI: 10.1016/s0960-9822(02)00450-5.

Hiromoto *et al.* (2022): Creation of Cross-Linked Crystals With Intermolecular Disulfide Bonds Connecting Symmetry-Related Molecules Allows Retention of Tertiary Structure in Different Solvent Conditions. In: *Front. Mol. Biosci.* 9, S. 908394. DOI: 10.3389/fmolb.2022.908394.

Hoppen *et al.* (2019a): Soluble and membrane-bound protein carrier mediate direct copper transport to the ethylene receptor family. In: *Scientific reports* 9 (1), S. 10715. DOI: 10.1038/s41598-019-47185-6.

Hoppen *et al.* (2019b): The NOP-1 peptide derived from the central regulator of ethylene signaling EIN2 delays floral senescence in cut flowers. In: *Scientific reports* 9 (1), S. 1287. DOI: 10.1038/s41598-018-37571-x.

Hoppen (2020): Funktionelle und strukturelle Charakterisierung der Interaktion von Kupferchaperonen mit Ethylenrezeptoren. Online verfügbar unter https://docserv.uni-duesseldorf.de/servlets/derivateservlet/derivate-56700/dissertation_final_pdf_a_1b.pdf.

Hoppen und Groth (2020): Novel insights into the transfer routes of the essential copper cofactor to the ethylene plant hormone receptor family. In: *Plant signaling & behavior* 15 (2), S. 1716512. DOI: 10.1080/15592324.2020.1716512.

Hu *et al.* (2021): NMR-Based Methods for Protein Analysis. In: *Analytical chemistry* 93 (4), S. 1866–1879. DOI: 10.1021/acs.analchem.0c03830.

Hua *et al.* (1995): Ethylene insensitivity conferred by Arabidopsis ERS gene. In: *Science (New York, N.Y.)* 269 (5231), S. 1712–1714. DOI: 10.1126/science.7569898.

Hua *et al.* (1998): EIN4 and ERS2 are members of the putative ethylene receptor gene family in Arabidopsis. In: *The Plant cell* 10 (8), S. 1321–1332. DOI: 10.1105/tpc.10.8.1321.

Hua und Meyerowitz (1998): Ethylene responses are negatively regulated by a receptor gene family in Arabidopsis thaliana. In: *Cell* 94 (2), S. 261–271. DOI: 10.1016/S0092-8674(00)81425-7.

Huang *et al.* (2016): A heavy metal P-type ATPase OsHMA4 prevents copper accumulation in rice grain. In: *Nat Commun* 7 (1), S. 12138. DOI: 10.1038/ncomms12138.

Huang *et al.* (2020a): 3D-printed holders for in meso in situ fixed-target serial X-ray crystallography. In: *J Appl Cryst* 53 (Pt 3), S. 854–859. DOI: 10.1107/S1600576720002897.

Huang *et al.* (2020b): In Meso In Situ Serial X-Ray Crystallography (IMISX): A Protocol for Membrane Protein Structure Determination at the Swiss Light Source. In: *Methods in molecular biology (Clifton, N.J.)* 2127, S. 293–319. DOI: 10.1007/978-1-0716-0373-4_20.

Jackson (1985): Ethylene and Responses of Plants to Soil Waterlogging and Submergence. In: *Annu. Rev. Plant. Physiol.* 36 (1), S. 145–174. DOI: 10.1146/annurev.pp.36.060185.001045.

Jafari *et al.* (2013): Cloning, identification and expression analysis of ACC oxidase gene involved in ethylene production pathway. In: *Molecular biology reports* 40 (2), S. 1341–1350. DOI: 10.1007/s11033-012-2178-7.

Jain *et al.* (2014): The diverse roles of FRO family metalloreductases in iron and copper homeostasis. In: *Front. Plant Sci.* 5, S. 100. DOI: 10.3389/fpls.2014.00100.

Jeschke (2012): DEER distance measurements on proteins. In: *Annual Review of Physical Chemistry* 63 (Volume 63, 2012), S. 419–446. DOI: 10.1146/annurev-physchem-032511-143716.

Johnson und Ecker (1998): The ethylene gas signal transduction pathway: a molecular perspective. In: *Annual review of genetics* 32, S. 227–254. DOI: 10.1146/annurev.genet.32.1.227.

Ju *et al.* (2012): CTR1 phosphorylates the central regulator EIN2 to control ethylene hormone signaling from the ER membrane to the nucleus in Arabidopsis. In: *Proceedings of the National Academy of Sciences of the United States of America* 109 (47), S. 19486–19491. DOI: 10.1073/pnas.1214848109.

Ju *et al.* (2015): Conservation of ethylene as a plant hormone over 450 million years of evolution. In: *Nature plants* 1, S. 14004. DOI: 10.1038/NPLANTS.2014.4.

Jumper *et al.* (2021): Highly accurate protein structure prediction with AlphaFold. In: *Nature* 596 (7873), S. 583–589. DOI: 10.1038/s41586-021-03819-2.

Kai (2012): Development and application of a high-throughput cell-free expression system. Darmstadt: Technische Universität Darmstadt. Online verfügbar unter https://tuprints.ulb.tu-darmstadt.de/3136/1/thesis_upload_for_library.pdf.

Kanonenberg *et al.* (2019): Functional Reconstitution of HlyB, a Type I Secretion ABC Transporter, in Saposin-A Nanoparticles. In: *Scientific reports* 9 (1), S. 8436. DOI: 10.1038/s41598-019-44812-0.

Kefala *et al.* (2010): Structures of the OmpF porin crystallized in the presence of foscholine-12. In: *Protein Science* 19 (5), S. 1117–1125. DOI: 10.1002/pro.369.

Kehrer (2000): The Haber-Weiss reaction and mechanisms of toxicity. In: *Toxicology* 149 (1), S. 43–50. DOI: 10.1016/S0300-483X(00)00231-6.

Kende und Boller (1981): Wound ethylene and 1-aminocyclopropane-1-carboxylate synthase in ripening tomato fruit. In: *Planta* 151 (5), S. 476–481. DOI: 10.1007/BF00386542.

Kessenbrock *et al.* (2017): Novel Protein-Protein Inhibitor Based Approach to Control Plant Ethylene Responses: Synthetic Peptides for Ripening Control. In: *Frontiers in plant science* 8, S. 1528. DOI: 10.3389/fpls.2017.01528.

Khoudi (2021): Significance of vacuolar proton pumps and metal/H+ antiporters in plant heavy metal tolerance. In: *Physiologia Plantarum* 173 (1), S. 384–393. DOI: 10.1111/ppl.13447.

Kieber *et al.* (1993): CTR1, a negative regulator of the ethylene response pathway in Arabidopsis, encodes a member of the raf family of protein kinases. In: *Cell* 72 (3), S. 427–441. DOI: 10.1016/0092-8674(93)90119-b.

Klein *et al.* (2019): Influence of the ethylene-related signal-inhibiting octapeptide NOP-1 on postharvest ripening and quality of 'Golden Delicious' apples. In: *Journal of the science of food and agriculture* 99 (8), S. 3903–3909. DOI: 10.1002/jsfa.9613.

Knee (1995): Copper reverses silver inhibition of flower senescence in Petunia hybrida. In: *Postharvest Biology and Technology* 6 (1-2), S. 121–128. DOI: 10.1016/0925-5214(94)00038-T.

Kocyła *et al.* (2017): Molar absorption coefficients and stability constants of Zincon metal complexes for determination of metal ions and bioinorganic applications. In: *Journal of inorganic biochemistry* 176, S. 53–65. DOI: 10.1016/j.jinorgbio.2017.08.006.

Lacey und Binder (2014): How plants sense ethylene gas--the ethylene receptors. In: *Journal of inorganic biochemistry* 133, S. 58–62. DOI: 10.1016/j.jinorgbio.2014.01.006.

Lemke *et al.* (2023): Functional reconstitution and structural characterization of the plant hormone receptor ETR1 in lipid nanodiscs. In: *Chemical communications (Cambridge, England)* 59 (61), S. 9344–9347. DOI: 10.1039/d3cc02619a.

Lequeux *et al.* (2010): Response to copper excess in Arabidopsis thaliana: Impact on the root system architecture, hormone distribution, lignin accumulation and mineral profile. In: *Plant physiology and biochemistry : PPB* 48 (8), S. 673–682. DOI: 10.1016/j.plaphy.2010.05.005.

Li *et al.* (2015): EIN2-directed translational regulation of ethylene signaling in Arabidopsis. In: *Cell* 163 (3), S. 670–683. DOI: 10.1016/j.cell.2015.09.037.

Li *et al.* (2022): Something old, something new: Conservation of the ethylene precursor 1-amino-cyclopropane-1-carboxylic acid as a signaling molecule. In: *Current opinion in plant biology* 65, S. 102116. DOI: 10.1016/j.pbi.2021.102116.

Liu *et al.* (2022): Stabilization and structure determination of integral membrane proteins by termini restraining. In: *Nat Protoc* 17 (2), S. 540–565. DOI: 10.1038/s41596-021-00656-5.

Liu und Li (2022): Protein Fusion Strategies for Membrane Protein Stabilization and Crystal Structure Determination. In: *Crystals* 12 (8), S. 1041. DOI: 10.3390/cryst12081041.

Lu *et al.* (2023): Importin β1 Mediates Nuclear Entry of EIN2C to Confer the Phloem-Based Defense against Aphids. In: *International journal of molecular sciences* 24 (10). DOI: 10.3390/ijms24108545.

Lusty (1999): A gentle vapor-diffusion technique for cross-linking of protein crystals for cryo-crystallography. In: *J Appl Cryst* 32 (1), S. 106–112. DOI: 10.1107/S002188989801053X.

Lyashenko *et al.* (2006): Three-dimensional structure of laccase from Coriolus zonatus at 2.6 Å resolution. In: *Crystallogr. Rep.* 51 (5), S. 817–823. DOI: 10.1134/S1063774506050117.

Mangini *et al.* (2022): Crystal Structure of the Human Copper Chaperone ATOX1 Bound to Zinc Ion. In: *Biomolecules* 12 (10). DOI: 10.3390/biom12101494.

Martens *et al.* (2016): Lipids modulate the conformational dynamics of a secondary multidrug transporter. In: *Nat Struct Mol Biol* 23 (8), S. 744–751. DOI: 10.1038/nsmb.3262.

Martínez-Romero *et al.* (2003): 1-methylcyclopropene increases storability and shelf life in climacteric and nonclimacteric plums. In: *Journal of agricultural and food chemistry* 51 (16), S. 4680–4686. DOI: 10.1021/jf034338z.

Mattoo (2018): Plant Growth Regulating Chemicals. First edition. Boca Raton, FL: CRC Press.

Matz *et al.* (1999): Fluorescent proteins from nonbioluminescent Anthozoa species. In: *Nat Biotechnol* 17 (10), S. 969–973. DOI: 10.1038/13657.

Mayerhofer *et al.* (2012): Protein kinase domain of CTR1 from Arabidopsis thaliana promotes ethylene receptor cross talk. In: *Journal of molecular biology* 415 (4), S. 768–779. DOI: 10.1016/j.jmb.2011.11.046.

Mayerhofer *et al.* (2015): Structural model of the cytosolic domain of the plant ethylene receptor 1 (ETR1). In: *The Journal of biological chemistry* 290 (5), S. 2644–2658. DOI: 10.1074/jbc.M114.587667.

McDaniel und Binder (2012): ethylene receptor 1 (etr1) Is Sufficient and Has the Predominant Role in Mediating Inhibition of Ethylene Responses by Silver in Arabidopsis thaliana. In: *Journal of Biological Chemistry* 287 (31), S. 26094–26103. DOI: 10.1074/jbc.M112.383034.

Meiresonne *et al.* (2019): Superfolder mTurquoise2ox optimized for the bacterial periplasm allows high efficiency in vivo FRET of cell division antibiotic targets. In: *Molecular Microbiology* 111 (4), S. 1025–1038. DOI: 10.1111/mmi.14206.

Meuskens *et al.* (2020): Corrigendum: A New Strain Collection for Improved Expression of Outer Membrane Proteins. In: *Front. Cell. Infect. Microbiol.* 10, S. 220. DOI: 10.3389/fcimb.2020.00220.

Mi *et al.* (2008): Functional and structural stability of the epidermal growth factor receptor in detergent micelles and phospholipid nanodiscs. In: *Biochemistry* 47 (39), S. 10314–10323. DOI: 10.1021/bi801006s.

Milić *et al.* (2018): Recognition motif and mechanism of ripening inhibitory peptides in plant hormone receptor ETR1. In: *Scientific reports* 8 (1), S. 3890. DOI: 10.1038/s41598-018-21952-3.

Mira *et al.* (2001a): Evidence for the plant-specific intercellular transport of the Arabidopsis copper chaperone CCH. In: *The Plant journal : for cell and molecular biology* 25 (5), S. 521–528. DOI: 10.1046/j.1365-313x.2001.00985.x.

Mira *et al.* (2001b): Functional and conformational properties of the exclusive C-domain from the Arabidopsis copper chaperone (CCH). In: *Biochem J* 357 (2), S. 545–549. DOI: 10.1042/bj3570545.

Mira *et al.* (2002): Copper Homeostasis in Plants. In: E. J. Massaro (Hg.): Handbook of Copper Pharmacology and Toxicology. Totowa, NJ: Humana Press, S. 543–557. Online verfügbar unter https://link.springer.com/chapter/10.1007/978-1-59259-288-3_33.

Mira *et al.* (2004): Ionic self-complementarity induces amyloid-like fibril formation in an isolated domain of a plant copper metallochaperone protein. In: *BMC Struct Biol* 4 (1), S. 7. DOI: 10.1186/1472-6807-4-7.

Mira-Rodado *et al.* (2012): Identification of two-component system elements downstream of AHK5 in the stomatal closure response of Arabidopsis thaliana. In: *Plant signaling & behavior* 7 (11), S. 1467–1476. DOI: 10.4161/psb.21898.

Morise *et al.* (1974): Intermolecular energy transfer in the bioluminescent system of Aequorea. In: *Biochemistry* 13 (12), S. 2656–2662. DOI: 10.1021/bi00709a028.

Moussatche und Klee (2004): Autophosphorylation Activity of the Arabidopsis Ethylene Receptor Multigene Family. In: *Journal of Biological Chemistry* 279 (47), S. 48734–48741. DOI: 10.1074/jbc.M403100200.

Müller (2020): Kupfertransport und-koordinationschemie der kupferbindenden Domäne des Ethylenrezeptors ETR1. Online verfügbar unter https://docserv.uni-duesseldorf.de/servlets/derivateservlet/derivate-56140.

Neljubow (1901): Uber die horizontale Nutation der Stengel von Pisum Sativum und einiger anderen Planzen. In: *Bot. Centralbl. Beih.* 10, S. 128–139. Online verfügbar unter https://cir.nii.ac.jp/crid/1570291225049293184.

Olmedo *et al.* (2006): ETHYLENE-INSENSITIVE5 encodes a 5'--3' exoribonuclease required for regulation of the EIN3-targeting F-box proteins EBF1/2. In: *Proceedings of the National Academy of Sciences of the United States of America* 103 (36), S. 13286–13293. DOI: 10.1073/pnas.0605528103.

Ormö *et al.* (1996): Crystal structure of the Aequorea victoria green fluorescent protein. In: *Science (New York, N.Y.)* 273 (5280), S. 1392–1395. DOI: 10.1126/science.273.5280.1392.

Panneerselvam *et al.* (2013): Cloning, overexpression, purification and preliminary X-ray analysis of the catalytic domain of the ethylene receptor ETR1 from Arabidopsis thaliana. In: *Acta crystallographica. Section F, Structural biology and crystallization communications* 69 (Pt 11), S. 1307–1309. DOI: 10.1107/S174430911302842X.

Pédelacq *et al.* (2006): Correction: Corrigendum: Engineering and characterization of a superfolder green fluorescent protein. In: *Nat Biotechnol* 24 (9), S. 1170. DOI: 10.1038/nbt0906-1170d.

Pédelacq und Cabantous (2019): Development and Applications of Superfolder and Split Fluorescent Protein Detection Systems in Biology. In: *International journal of molecular sciences* 20 (14). DOI: 10.3390/ijms20143479.

Phillips (1997): Structure and dynamics of green fluorescent protein. In: *Current opinion in structural biology* 7 (6), S. 821–827. DOI: 10.1016/S0959-440X(97)80153-4.

Pilon *et al.* (2006): Copper cofactor delivery in plant cells. In: *Current opinion in plant biology* 9 (3), S. 256–263. DOI: 10.1016/j.pbi.2006.03.007.

Pirrung *et al.* (2008): Ethylene receptor antagonists: strained alkenes are necessary but not sufficient. In: *Chemistry & Biology* 15 (4), S. 313–321. DOI: 10.1016/j.chembiol.2008.02.018.

Potuschak *et al.* (2006): The exoribonuclease XRN4 is a component of the ethylene response pathway in Arabidopsis. In: *Plant Cell* 18 (11), S. 3047–3057. DOI: 10.1105/tpc.106.046508.

Prasher *et al.* (1992): Primary structure of the Aequorea victoria green-fluorescent protein. In: *Gene* 111 (2), S. 229–233. DOI: 10.1016/0378-1119(92)90691-H.

Printz *et al.* (2016): Copper Trafficking in Plants and Its Implication on Cell Wall Dynamics. In: *Front. Plant Sci.* 7, S. 601. DOI: 10.3389/fpls.2016.00601.

Privalle und Graham (1987): Radiolabeling of a wound-inducible pyridoxal phosphate-utilizing enzyme: evidence for its identification as ACC synthase. In: *Archives of Biochemistry and Biophysics* 253 (2), S. 333–340. DOI: 10.1016/0003-9861(87)90186-x.

Puig *et al.* (2007): Higher plants possess two different types of ATX1-like copper chaperones. In: *Biochemical and Biophysical Research Communications* 354 (2), S. 385–390. DOI: 10.1016/j.bbrc.2006.12.215.

Qiao *et al.* (2009): Interplay between ethylene, ETP1/ETP2 F-box proteins, and degradation of EIN2 triggers ethylene responses in Arabidopsis. In: *Genes & development* 23 (4), S. 512–521. DOI: 10.1101/gad.1765709.

Qiao *et al.* (2012): Processing and subcellular trafficking of ER-tethered EIN2 control response to ethylene gas. In: *Science (New York, N.Y.)* 338 (6105), S. 390–393. DOI: 10.1126/science.1225974.

Rae *et al.* (1999): Undetectable intracellular free copper: the requirement of a copper chaperone for superoxide dismutase. In: *Science (New York, N.Y.)* 284 (5415), S. 805–808. DOI: 10.1126/science.284.5415.805.

Raven *et al.* (1999): The role of trace metals in photosynthetic electron transport in O2-evolving organisms. In: *Photosynthesis Research* 60 (2/3), S. 111–150. DOI: 10.1023/A:1006282714942.

Reid und Çelikel (2008): Use of 1-Methylcyclopropene in Ornamentals: Carnations as a Model System for Understanding Mode of Action. In: *horts* 43 (1), S. 95–98. DOI: 10.21273/HORTSCI.43.1.95.

Reid und Wu (1992): Ethylene and flower senescence. In: *Plant Growth Regul* 11 (1), S. 37–43. DOI: 10.1007/BF00024431.

Richards und Knowles (1968): Glutaraldehyde as a protein cross-linkage reagent. In: *Journal of molecular biology* 37 (1), S. 231–233. DOI: 10.1016/0022-2836(68)90086-7.

Rodríguez *et al.* (1999): A copper cofactor for the ethylene receptor ETR1 from Arabidopsis. In: *Science (New York, N.Y.)* 283 (5404), S. 996–998. DOI: 10.1126/science.283.5404.996.

Rubino und Franz (2012): Coordination chemistry of copper proteins: how nature handles a toxic cargo for essential function. In: *Journal of inorganic biochemistry* 107 (1), S. 129–143. DOI: 10.1016/j.jinorgbio.2011.11.024.

Säbel *et al.* (2010): A spectrophotometric method for the determination of zinc, copper, and cobalt ions in metalloproteins using Zincon. In: *Analytical biochemistry* 397 (2), S. 218–226. DOI: 10.1016/j.ab.2009.10.037.

Sagee *et al.* (1980): Abscission of Citrus Leaf Explants: INTERRELATIONSHIPS OF ABSCISIC ACID, ETHYLENE, AND HYDROLYTIC ENZYMES. In: *Plant physiology* 66 (4), S. 750–753. DOI: 10.1104/pp.66.4.750.

Sakai *et al.* (1998): ETR2 is an ETR1-like gene involved in ethylene signaling in Arabidopsis. In: *Proceedings of the National Academy of Sciences of the United States of America* 95 (10), S. 5812–5817. DOI: 10.1073/pnas.95.10.5812.

Sakai *et al.* (2000): Arabidopsis ARR1 and ARR2 response regulators operate as transcriptional activators. In: *The Plant Journal* 24 (6), S. 703–711. DOI: 10.1111/j.1365-313X.2000.00909.x.

Schaller *et al.* (1995): The ethylene response mediator ETR1 from Arabidopsis forms a disulfide-linked dimer. In: *The Journal of biological chemistry* 270 (21), S. 12526–12530. DOI: 10.1074/jbc.270.21.12526.

Schaller und Bleecker (1995): Ethylene-binding sites generated in yeast expressing the Arabidopsis ETR1 gene. In: *Science (New York, N.Y.)* 270 (5243), S. 1809–1811. DOI: 10.1126/science.270.5243.1809.

Scharein *et al.* (2008): Ethylene signaling: identification of a putative ETR1-AHP1 phosphorelay complex by fluorescence spectroscopy. In: *Analytical biochemistry* 377 (1), S. 72–76. DOI: 10.1016/j.ab.2008.03.015.

Scharein und Groth (2011): Phosphorylation alters the interaction of the Arabidopsis phosphotransfer protein AHP1 with its sensor kinase ETR1. In: *PloS one* 6 (9), e24173. DOI: 10.1371/journal.pone.0024173.

Schott-Verdugo *et al.* (2019): Structural Model of the ETR1 Ethylene Receptor Transmembrane Sensor Domain. In: *Scientific reports* 9 (1), S. 8869. DOI: 10.1038/s41598-019-45189-w.

Serek *et al.* (1995): Effects of 1-MCP on the vase life and ethylene response of cut flowers. In: *Plant Growth Regul* 16 (1), S. 93–97. DOI: 10.1007/BF00040512.

Serek *et al.* (2006): Controlling ethylene responses in flowers at the receptor level. In: *Biotechnology advances* 24 (4), S. 368–381. DOI: 10.1016/j.biotechadv.2006.01.007.

Sevvana *et al.* (2008): A ligand-induced switch in the periplasmic domain of sensor histidine kinase CitA. In: *Journal of molecular biology* 377 (2), S. 512–523. DOI: 10.1016/j.jmb.2008.01.024.

Shakeel *et al.* (2015): Ethylene Regulates Levels of Ethylene Receptor/CTR1 Signaling Complexes in Arabidopsis thaliana. In: *The Journal of biological chemistry* 290 (19), S. 12415–12424. DOI: 10.1074/jbc.M115.652503.

Shaner *et al.* (2004): Improved monomeric red, orange and yellow fluorescent proteins derived from Discosoma sp. red fluorescent protein. In: *Nat Biotechnol* 22 (12), S. 1567–1572. DOI: 10.1038/nbt1037.

Shepard *et al.* (1990): Copper coordination geometry in azurin undergoes minimal change on reduction of copper(II) to copper(I). In: *J. Am. Chem. Soc.* 112 (21), S. 7817–7819. DOI: 10.1021/ja00177a065.

Shepard *et al.* (1993): Structure of apo-azurin from Alcaligenes denitrificans at 1.8 Å resolution. In: *Acta Crystallographica Section D: Biological Crystallography* 49 (3), S. 331–343. DOI: 10.1107/S0907444992013544.

Shimomura (1979): Structure of the chromophore of Aequorea green fluorescent protein. In: *FEBS Letters* 104 (2), S. 220–222. DOI: 10.1016/0014-5793(79)80818-2.

Shin *et al.* (2012): Copper chaperone antioxidant protein1 is essential for copper homeostasis. In: *Plant Physiol* 159 (3), S. 1099–1110. DOI: 10.1104/pp.112.195974.

Sisler *et al.* (1983): INVESTIGATION OF THE MODE OF ACTION OF ETHYLENE IN CARNATION SENESCENCE. In: *Acta Hortic.* (141), S. 229–234. DOI: 10.17660/ActaHortic.1983.141.30.

Sisler *et al.* (1986): Effect of antagonists of ethylene action on binding of ethylene in cut carnations. In: *Plant Growth Regul* 4 (3), S. 213–218. DOI: 10.1007/BF00028164.

Sisler *et al.* (1990): Competition of cyclooctenes and cyclooctadienes for ethylene binding and activity in plants. In: *Plant Growth Regul* 9 (2), S. 157–164. DOI: 10.1007/BF00027443.

Sisler *et al.* (1999): Inhibition of ethylene responses by 1-Methylcyclopropene and 3-Methylcyclopropene. In: *Plant Growth Regul* 27 (2), S. 105–111. DOI: 10.1023/A:1006153016409.

Sisler und Serek (1997): Inhibitors of ethylene responses in plants at the receptor level: Recent developments. In: *Physiologia Plantarum* 100 (3), S. 577–582. DOI: 10.1111/j.1399-3054.1997.tb03063.x.

Sislerund Serek (1999): Compounds controlling the ethylene receptor. 40 Bände: Botanical Bulletin of Academia Sinica. Online verfügbar unter https://ejournal.sinica.edu.tw/bbas/content/1999/1/bot41-01.html.

Smith *et al.* (2002): The structure of apo human glutamate dehydrogenase details subunit communication and allostery. In: *Journal of molecular biology* 318 (3), S. 765–777. DOI: 10.1016/S0022-2836(02)00161-4.

Solano *et al.* (1998): Nuclear events in ethylene signaling: a transcriptional cascade mediated by ETHYLENE-INSENSITIVE3 and ETHYLENE-RESPONSE-FACTOR1. In: *Genes & development* 12 (23), S. 3703–3714. DOI: 10.1101/gad.12.23.3703.

Stetsenko und Guskov (2017): An Overview of the Top Ten Detergents Used for Membrane Protein Crystallization. In: *Crystals* 7 (7), S. 197. DOI: 10.3390/cryst7070197.

Street *et al.* (2015): Ethylene Inhibits Cell Proliferation of the Arabidopsis Root Meristem. In: *Plant Physiol* 169 (1), S. 338–350. DOI: 10.1104/pp.15.00415.

van de Poel *et al.* (2015): Ethylene and Hormonal Cross Talk in Vegetative Growth and Development. In: *Plant Physiol* 169 (1), S. 61–72. DOI: 10.1104/pp.15.00724.

Veen und van de Geijn (1978): Mobility and ionic form of silver as related to longevity of cut carnations. In: *Planta* 140 (1), S. 93–96. DOI: 10.1007/BF00389386.

Voet-van-Vormizeele und Groth (2008): Ethylene controls autophosphorylation of the histidine kinase domain in ethylene receptor ETR1. In: *Molecular Plant* 1 (2), S. 380–387. DOI: 10.1093/mp/ssn004.

Wadsten *et al.* (2006): Lipidic sponge phase crystallization of membrane proteins. In: *Journal of molecular biology* 364 (1), S. 44–53. DOI: 10.1016/j.jmb.2006.06.043.

Waldo *et al.* (1999): Rapid protein-folding assay using green fluorescent protein. In: *Nat Biotechnol* 17 (7), S. 691–695. DOI: 10.1038/10904.

Walker und Loneragan (1981): Effects of Copper Deficiency on Copper and Nitrogen Concentrations and Enzyme Activities in Aerial Parts of Vegetative Subterranean Clover Plants. In: *Annals of Botany* 48 (1), S. 65–73. DOI: 10.1093/oxfordjournals.aob.a086098.

Wang *et al.* (2006): Identification of important regions for ethylene binding and signaling in the transmembrane domain of the ETR1 ethylene receptor of Arabidopsis. In: *The Plant cell* 18 (12), S. 3429–3442. DOI: 10.1105/tpc.106.044537.

Wang (2018): Structural characterisation of Histidine Kinase 2. Structural characterisation of Histidine Kinase 2. Queen Mary University of London, London. Online verfügbar unter https://qmro.qmul.ac.uk/xmlui/handle/123456789/33933.

Watkins (2006): The use of 1-methylcyclopropene (1-MCP) on fruits and vegetables. In: *Biotechnology advances* 24 (4), S. 389–409. DOI: 10.1016/j.biotechadv.2006.01.005.

Wedrychowski *et al.* (1986): The in vivo cross-linking of proteins and DNA by heavy metals. In: *0021-9258* 261 (7), S. 3370–3376. DOI: 10.1016/S0021-9258(17)35792-7.

Wen *et al.* (2012): Activation of ethylene signaling is mediated by nuclear translocation of the cleaved EIN2 carboxyl terminus. In: *Cell Res* 22 (11), S. 1613–1616. DOI: 10.1038/cr.2012.145.

Williamson (1950): Ethylene, a metabolic product of diseased or injured plants: Phytopathology.

Wintz *et al.* (2003): Expression profiles of Arabidopsis thaliana in mineral deficiencies reveal novel transporters involved in metal homeostasis. In: *Journal of Biological Chemistry* 278 (48), S. 47644–47653. DOI: 10.1074/jbc.M309338200.

Yang *et al.* (1996): The molecular structure of green fluorescent protein. In: *Nat Biotechnol* 14 (10), S. 1246–1251. DOI: 10.1038/nbt1096-1246.

Yang und Hoffman (1984): Ethylene Biosynthesis and its Regulation in Higher Plants. In: *Annu. Rev. Plant. Physiol.* 35 (1), S. 155–189. DOI: 10.1146/annurev.pp.35.060184.001103.

Yip *et al.* (2020): Atomic-resolution protein structure determination by cryo-EM. In: *Nature* 587 (7832), S. 157–161. DOI: 10.1038/s41586-020-2833-4.

Yruela (2005): Copper in plants. In: *Braz. J. Plant Physiol.* 17 (1), S. 145–156. DOI: 10.1590/s1677-04202005000100012.

Yu *et al.* (1979): 1-Aminocyclopropanecarboxylate synthase, a key enzyme in ethylene biosynthesis. In: *Archives of Biochemistry and Biophysics* 198 (1), S. 280–286. DOI: 10.1016/0003-9861(79)90420-X.

Yu und Yang (1979): Auxin-induced Ethylene Production and Its Inhibition by Aminoethyoxyvinylglycine and Cobalt Ion. In: *Plant physiology* 64 (6), S. 1074–1077. DOI: 10.1104/pp.64.6.1074.

Zabara *et al.* (2017a): Lipidic Cubic Phase-Induced Membrane Protein Crystallization: Interplay Between Lipid Molecular Structure, Mesophase Structure and Properties, and Crystallogenesis. In: *Crystal growth & design* 17 (11), S. 5667–5674. DOI: 10.1021/acs.cgd.7b00519.

Zabara *et al.* (2017b): The nanoscience behind the art of in-meso crystallization of membrane proteins. In: *Nanoscale* 9 (2), S. 754–763. DOI: 10.1039/c6nr07634c.

Zabara *et al.* (2018): Design of ultra-swollen lipidic mesophases for the crystallization of membrane proteins with large extracellular domains. In: *Nature communications* 9 (1), S. 544. DOI: 10.1038/s41467-018-02996-5.

Zdarska *et al.* (2019): ETR1 Integrates Response to Ethylene and Cytokinins into a Single Multistep Phosphorelay Pathway to Control Root Growth. In: *Molecular plant* 12 (10), S. 1338–1352. DOI: 10.1016/j.molp.2019.05.012.

Zhang *et al.* (2017): EIN2 mediates direct regulation of histone acetylation in the ethylene response. In: *Proceedings of the National Academy of Sciences of the United States of America* 114 (38), S. 10274–10279. DOI: 10.1073/pnas.1707937114.

Zhangund Sui und Hu (2023): High-resolution structure of a mercury cross-linked ZIP metal transporter reveals delicate motions and metal relay for regulated zinc transport. Online verfügbar unter https://www.ncbi.nlm.nih.gov/pmc/articles/pmc10153219/.

Zhang und Wen (2015): Ethylene signalling: EIN2 dual targeting. In: *Nature Plants* 1 (12), S. 15192. DOI: 10.1038/nplants.2015.192.

Zhao *et al.* (2002): Effect of ethylene pathway mutations upon expression of the ethylene receptor ETR1 from Arabidopsis. In: *Plant physiology* 130 (4), S. 1983–1991. DOI: 10.1104/pp.011635.

8 Anhang

8.1 Abkürzungsverzeichnis

Abkürzungen	Bedeutung
α	Alpha
β	Beta
Δ	Delta
ε	Extinktionskoeffizient
π	Pi
µg	Microgramm
µm	Mikrometer
µM	mikromolar
1-MCP	1-Methylcyclopropan
%	Prozent
%-ig/er	Prozentig/er
°C	Grad
Å	Ångström
A	Alanin
aa	Aminosäuren/A*mino Acids*
Ab	*Antibody*
ABC-Transporter	*ATP-Binding Cassette Transporter*
ACC	1- Aminocyclopropancarbonsäure
acrAB	*Acridine Resistance Protein A And B*
Ag	Silber
$AgNO_3$	Silbernitrat
$Ag_2S_2O_3$/ STS	Silberthiosulfat
AHP	*Arabidopsis Histidine Phosphotransfer Protein*
Amp^{100}	Ampicillin (100 µg/ µL)
AOA	Aminooxyessigsäure
A. thaliana	*Arabidopsis thaliana*

ARGOS	*Auxin-Regulated Gene Involved In Organ Size*
ARR	*Response Regulator Protein*
ATP	Adenosintriphosphat
ATPase	Adenosintriphosphatase
ATX1	*Antioxidant1*
ATOX	*Human Antioxidant1 Copper Chaperone*
AVG	1-Aminoethoxyvinylgylcin
A. victoria	*Aequorea victoria*
BCA	Bicinchoninsäure
BMH	Bismalemidhexan
BS^3	Bis(sulfosuccinimidyl)suberat
bzw.	beziehungsweise
C	Cystein
C	Kohlenstoff
C_2H_4	Ethylen
CA	katalytische ATP-Bindedomäne
ca.	Circa
$CaCl_2$	Calciumchlorid
C. cajan	*Cajanus cajan*
CAPE	*SCP Domain-Containing Protein*
CCH	*Copper Chaperone*
cDNA	*Complementary DNA*
CD-Spektroskopie	Circulardichroismus-Spektroskopie
C. elegans	*Caenorhabditis elegans*
CH_2-Gruppe	Methyliden-Gruppe
CHS	Cholesterylhemisuccinat
CitA	Sensor-Histidin-Kinase CitA
cm	Zentimeter
cmc	*Critical Micelle Concentration*
Co(II)	zweiwertiges Cobalt-Ion

Col-0	Arabidopsis Ökotyp Columbia
COPT	*Copper Transporter*
CRISPR-Cas	*Clustered Regularly Interspaced Short Palindromic Repeats- CRISPR-Associated Protein 9*
C-terminal	Carboxy-terminal
C-Terminus	Carboxy-Terminus
CTR1	*Constitutive Triple Response1*
Cu	Kupfer
Cu(I)	Kupfer (I)-Ion
CusS	Sensor Histidine-Kinase CusS
cw	*Continuous Wave*
D	Asparaginsäure
Da	Dalton
dB	Dezibel
DHp	dimerisierende Histidin-Phosphotransfer-Domäne
$_{dd}H_2O$	demineralisiertes, steril filtriertes Wasser
DDM	n-Dodecyl-β-Maltoside
DEER	*Double Electron-Electron Resonance Spectroscopy*
d. h.	das heißt
DLS	*Dynamic Light Scattering*
DMPC	1,2-Dimyristoyl-sn-Glycero-3-Phosphocholin
DMSO	Dimethylsulfoxid
DNA	Desoxyribonukleinsäure
D_2O	Deuteriumoxid
DOPC	1,2-Dioleoyl-sn-Glycero-3-Phosphocholin

DOPE	1,2-di-(9Z-Octadecenoyl)-*sn*-Glycero-3-Phosphoethanolamin
DSP	Dithiobis(succinimidylpropionate)
DSPG	1,2-Distearoyl-sn-glycero-3-phospho-glycerol
DTT	Dithiothreitol
E	Glutaminsäure
EBD	Ethylenbindedomäne
EBF	*EIN3 Binding F-Box*
E. coli	*Escherichia coli*
EDTA	Ethylendiamintetraessigsäure
EGTA	Ethylenglycolbis(aminoethylether)-N,N,N′,N′-tetraessigsäure
EIL	*EIN3-Like*
EIN	*Ethylene Insensitive*
EIN2-CEND	Carboxy-terminales Ende von EIN2
ENAP	*EIN2 Nuclear Associated Protein*
EPR	*Electron Paramagnetic Resonance*
ER	Endoplasmatisches Retikulum
ERF	*Ethylene Response Factor*
ERS	*Ethylene Response Sensor*
ESI	*Electronical Stored Information*
et al.	*et aliae*
ETP	*EIN2 Targeting Protein*
ETR	*Ethylene Receptor*
ETR1 1-157ΔC	In ETR1 TMD wurden die Aminosäuren C4, C6, C65 und C99 durch Serin ersetzt
ETRs	Ethylenrezeptoren, *Ethylene Receptors*
EXFAS	*Extended X-ray Absorption Fine Structure*

EXP	Expansin-A
F	Phenylalanin
FRO	*Ferric Reductase Oxidase*
g	Gramm
G	Glycin
GAF	*cGMP-Specific pPhosphodiesterases, Adenyl Cyclases, Formate Hydrogen Lyase Transcriptional Activator*
GFP	Grün fluoreszierendes Protein
GHz	Giga Hertz
GPCR	*G-Protein Coupled Receptors*
GST	Glutathion-S-Transferase
h/ hr	Stunde
H	Histidin
H	Wasserstoff
HEPES	Hydroxyethylpiperazin-Ethansulfon-säure-Puffer
Hg_2Cl	Quecksilberchlorid
HIK2	Histidin-Kinase 2
HK	Histidin-Kinase
HMA	*Heavy Metal p-type ATPases*
H_2O	Wasser
HPLC	*High Pressure Liquid Chromatography*
HRP	Meerrettichperoxidase
Hz	Hertz
I	Isoleucin
IMAC	Immobilisierende-Metall-Ion-Affinitäts-chromatographie
IPTG	Isopropyl-β-D-thiogalactopyranosid
K	Lysin
K	Kelvin
KanR	Kanamycin Resistenz

Kb	Kilobasen
K_D	Dissoziationskonstante
kDa	Kilo Dalton
Kryo-EM	Kryoelektronenmikroskopie
L	Liter
L	Leucin
L	Load
LCP	*Lipidic Cubic Phase*
LLPs	*Lipid-Like Peptides*
LMNG	Lauryl Maltose Neopentyl Glycol
LUV	*Large Unilamellar Vesicles*
m	Meter
mm	Millimeter
mM	Millimolar
M	Methionin
M	Molarität
MAG	Monoacylglycerol
MBD	Metallbindedomäne
MD	*Molecular Dynamics*
mg	Milligramm
mHz	Millihertz
min	Minute
mL	Milliliter
mM	Millimolar
MMM	*Multiscale Modeling Of Macromole-cules Software*
MO	Monoolein
MOR244-3	*Mouse Olfactory Receptor244-3*
MP	Monopalmitolein
mRNA	*Messenger RNA*
MSP1D1	*Membrane Scaffold Protein D1*
MST	*Microscale Thermophoresis*

mT2	*Monomeric Turquoise2*
MTSSL	*Methanethiosulfonate Spin Label*
MW	Molekulargewicht
mW	milliWatt
n	Nano
N	Asparagin
N_2/N	Stickstoff
NaCl	Natriumchlorid
nanoDSF	*Nano Differential Scanning Fluorimetry*
NarQ	Nitrat/Nitrit Sensor Protein NarQ
NarX	Nitrat/Nitrit Sensor Protein NarX
NBD	2,5-Norbornadien
NIP-1	*NLS icosapeptide1*
nL	Nanoliter
NLS	*Nuclear Localization Sequence*
nm	Nanometer
nM	nanomolar
nmol	nanomol
NMR	*Nuclear Magnetic Resonance*
NOP-1	*NLS Octapeptide1*
ns	Nanosekunde
N-terminal	Amino-terminal
N-Terminus	Amino-Terminus
O/O_2	Sauerstoff
OD_{600}	bei 600 nm gemessene optische Dichte
Omp	*Outer Membrane Porin*
ORS	*Organ Size Related 1*
P	Prolin
PAB	*Poly(A)-Binding Protein*
P-Body/P-Bodies	Prozessierungskörperchen
P. communis	*Pyrus communis*

PCR	Polymerase-Kettenreaktion
PDB	Proteindatenbank
PEG	Polyethylenglycol
pI	isoelektrischer Punkt
pH	pH-Wert
PMSF	Phenylmethylsulfonylfluorid
POPC	1-Palmitoyl-2-Oleoyl-Glycero-3-Phos-phocholin
POPG	1-Palmitoyl-2-Oleoyl-sn-Glycero-3-Phosphatidylglycerol
Q	Glutamin
R	Arginin
Raf	*Rapidly Accelerated Fibrosarcoma*
RAN1	*Response To Antagonist 1*
RD	*Receiver*-Domäne
RNA	Ribonukleinsäure
ROS	*Reactive Oxygen Species*
rpm	*Revolutions Per Minute*
S	Serin
SAM	S-Adenosylmethionin
SAXS	*Small Angle X-Ray Scattering*
S. cerevisiae	*Saccharomyces cerevisiae*
SCF	*Skp1 Cullen F-Box*
SCF-E3	*Skp 1 Cullen F-Box* E3-Ubiquitin-Ligase-Komplex
SD/ SE	Standardabweichung
SDS-PAGE	Natriumdodecylsulfat-Polyacrylamide-lektrophorese
SDSL	*Site-Directed Spin Labelling*
SEC	Größenausschlusschromatographie
sec	Sekunde
sfGFP	*Superfolder Green Fluorescent Protein*

sfmT2	*Superfolder Monomeric Turquoise2*
sfmT2^{ox}	*Superfolder Monomeric Turquoise2,* stabil gegenüber oxidierenden Bedingungen
SI	*Stored Information*
SMA-Nanodisks	*Styrene Maleic Anhydrid Nanodisks*
T	Threonin
T	Tesla
Tab.	Tabelle
TBS	Tris gepufferte Kochsalzlösung
TBT	Tris gepufferte Kochsalzlösung mit Tween
TCEP	Tris(2-chlorehyl)phosphat
TCO	*trans*-Cycloocten
TEMED	Tetramethylethylendiamin
TKF	Transkriptionsfaktoren
TM	Transmembran
TMD	Transmembran-Domäne
TMH	Transmembran-Helix
TRIS	Tris(hydroxymethyl)-aminomethan
TTM	Ammoniumtetrathiomolybdat
TWT amplifier	*Traveling Wave Tube Amplifier*
u. a.	unter anderem
ÜN	Über Nacht
UPF	*Up-Frameshift Surpressor 1*
UTR	*Untranslated Region*
UV	ultraviolett
UZ	Ultrazentrifuge
V	Valin
V	Volt
v/v	*Volume Per Volume*
vgl.	vergleiche

Vol-%	Volumenprozent
W	Watt
W	*Wash*
WT	Wildtyp
w/v	*Weight Per Volume*
w/w	*Weight by Weight*
XAS	*X-ray Absorption Spectroscopy*
xg / g	Zentrifugalkraft/Beschleunigung
XRN4	Exoribonuklease 4
Y	Tyrosin
2YT	*2×Yeast Extract And Tryptone*
z. B.	Zum Beispiel
ZIP	*Zinc Transporter*
Zn	Zink
$ZnCl_2$	Zinkchlorid

9 Danksagung

Ich möchte mich beginnend bei Herr Prof. Dr. Groth bedanken. Georg, Du hast mir ermöglicht an diesem spannenden Thema zu arbeiten! Auch wenn Du immer viel zu tun hattest, hast Du immer sehr aufmerksam zugehört und konntest immer weiterhelfen. Zudem hast Du mir ermöglicht Teil des SFB1208 werden, wodurch viele Institute miteinander kooperieren konnten. Man konnte sein Wissen durch verschiedene Angebote erweitern und ausbauen. Ich bin dafür dankbar auch die Möglichkeit etwas anderes außerhalb der HHU zu sehen, erleben und lernen zu dürfen sei es mit dem Kooperationspartnern in Konstanz, der Aufenthalt am DESY oder die Konferenz in Toulouse. Hier möchte ich meinen Dank an die netten und fleißigen Kooperationspartner AG Drescher und Dr. Anandi Kugele aussprechen. Durch die Meetings und dem effizienten Arbeiten konnte ein gutes Paper geschrieben werden. Mein Dank richtet sich ebenfalls an die Postdocs Dr. Alexander Minges, Dr. Yvonne Thielmann und Dr. Raphael Eberle. Ihr wart immer an Ort und Stelle. Ich durfte von Euch tolle Techniken erlernen und Arbeitsweisen abschauen. Eure sehr wertvollen Tipps und Ideen haben mich immer weitergebracht. Auch hier möchte ich meine Wertschätzung und meinen Dank an die beiden technischen Assistenten Nicole und Kerstin aussprechen. Ihr beide habt mir immer großartig im Labor unter die Arme gegriffen und wenn es nicht das Labor war, waren es auch hier Hinweise und Ratschläge bei anderen Themen. Ihr seid die guten Feen, die alles am Laufen halten. Für die lustige Zeit möchte ich mich auch bei Ece, Denise, Marlene, Fabian und Meike bedanken. Ich bin sehr dankbar, dass Ihr die Mittagspausen und auch die sonstige Zeit mit Leben gefüllt habt! Vielen Dank für eure Unterstützung auf den letzten Metern, sei es z. B. bei der Ersatz-Betreuung von anderen Personen, mentalen Unterstützung oder beim Korrekturlesen. Der Aufenthalt im Institut war eine besondere Zeit und habe mich insgesamt sehr wohl gefühlt. Daran werde ich mich gerne zurück erinnern. Teilweise konnten sich unerwartete Freundschaften entwickeln und man selbst konnte nur durch seine Herausforderungen und Aufgaben wachsen. Zum Schluss möchte ich mich für die Geduld, die unterstützenden Worte und Liebe, die davor, aber in der stressigen Zeit gegeben wurde bei meinen Freunden, meiner Familie und meinem Mann bedanken. Ich bin froh, dass Alles, was nötig war mir mitgegeben wurde, damit ich das erreichen kann, was ich möchte.

10 Eidesstaatliche Erklärung

Ich versichere an Eides Statt, dass die Dissertation von mir selbständig und ohne unzulässige fremde Hilfe unter Beachtung der Grundsätze zur Sicherung guter wissenschaftlicher Praxis an der Heinrich-Heine-Universität Düsseldorf erstellt worden ist. Ich habe keine anderen als die angegebenen Quellen und Hilfsmittel benutzt. Die aus fremden Quellen direkt oder indirekt übernommenen Inhalte wurden als solche kenntlich gemacht. Darüber hinaus versichere ich, dass ich die Dissertation nur in diesem und keinem anderen Promotionsverfahren eingereicht habe und diesem Promotionsverfahren keine endgültig gescheiterten Promotionsverfahren vorausgegangen sind. Ich versichere weiterhin, dass alle von mir gemachten Angaben wahrheitsgemäß und vollständig sind.

_____ _____

Ort, Datum Buket Rüffer (geb. Uzun)